The HIPERC project has examined the effects of alloying elements and processing conditions in low carbon, < 0.09 wt %., niobium containing, 0.05 - 0.12 wt.%, steels. Laboratory-scale heats and pilot rolling trials simulating air and water-cooled plate production as well as hot-rolled strip production have been made. The effects of C, Mn, Ni, Cu, Cr, Mo, Nb, Ti and B, on transformation characteristics and temperatures of recrystallisation have been determined along with regression equations for characterisation of microstructure, tensile and impact properties, and for the weldability of these steels. The properties of products processed commercially to plate and coil-plate and made into pipe and to plate for structural use were determined and these compared well with the values predicted from the regression equations. The project has shown that excellent combinations of strength, toughness and weldability can be obtained using this steel type.

Additional experiences have been gained in the processing of these steels through three commercial rolling mills and benefits were seen with this steel type due to higher production rates and lower amounts of surface dressing compared with steels currently being used to satisfy equivalent property specifications. Recommendations on the limits for niobium in Euronorms have been proposed; concerns relating to weldability have been addressed by proposing varying limits based on the carbon and manganese contents of the steel. This report makes the output of this project available to CEN working groups to support the revision of Euronorms based on the gathered data.

Price (excluding VAT) in Luxembourg: EUR 8

Publications Office

ISBN 978-92-79-14438-7

KI-NA-24209-EN-C

EC

HIPERC: A novel, high performance, economic steel concept for linepipe and general structural use

EUR 24209

EUROPEAN COMMISSION

European Research Area

HIPERC: A novel, high performance, economic steel concept for linepipe and general structural use

Research Fund for Coal & Steel

Interested in European research?

RTD info is our quarterly magazine keeping you in touch with main developments (results, programmes, events, etc.). It is available in English, French and German. A free sample copy or free subscription can be obtained from:

Directorate-General for Research
Information and Communication Unit
European Commission
B-1049 Brussels
Fax (32-2) 29-58220
E-mail: research@ec.europa.eu
Internet: http://ec.europa.eu/research/rtdinfo/index_en.html

How to obtain EU publications

Free publications:

- via EU Bookshop (http://bookshop.europa.eu);
- at the European Commission's representations or delegations. You can obtain their contact details by linking http://ec.europa.eu or by sending a fax to +352 2929-42758.

Publications for sale:

- via EU Bookshop (http://bookshop.europa.eu);
- Priced subscriptions (Official Journal of the EU, Legal cases of the Court of Justice as well as certain periodicals edited by the European Commission) can be ordered from one of our sales agents. You can obtain their contact details by linking http://bookshop.europa.eu, or by sending a fax to +352 2929-42758.

EUROPEAN COMMISSION
Directorate-General for Research
Research Fund for Coal and Steel Unit

Contact: RFCS publications
Address: European Commission, CDMA 0/124, B-1049 Brussels
Fax (32-2) 29-65987; e-mail: rtd-steel@ec.europa.eu

European Commission

Research Fund for Coal and Steel

HIPERC: A novel, high performance, economic steel concept for linepipe and general structural use

L. J Drewett ([1]), S. Bremer ([2]), M. Liebeherr ([3]), W. De Waele ([4]), A. Martín-Meizoso ([5]), J. Brózda ([6]), B. Zeislmair ([7]), H. Morbacher ([8]), D. Porter ([9]), Dr N. Gubeljak ([10])

([1]) **Corus RD&T, Swinden Technology Centre —** Moorgate, Rotherham, South Yorkshire, S60 3AR, UNITED KINGDOM
([2]) **Salzgitter Mannesmann Forschung GmbH —** Eisenhüttenstraße 99, 38326 Salzgitter, GERMANY
([3]) **OCAS —** John Kennedylaan 3, B-9060 Zelzate, BELGIUM
([4]) **Laboratorium Soete, Gent University —** Sint-Pietersnieuwstraat 41, B-9000 Gent, BELGIUM
([5]) **Department of Materials, CEIT —** Paseo de Manuel Lardizábal, 15, 20018 San Sebastián, SPAIN
([6]) **Instytut Spawalnictwa (Institute of Welding) —** ul. Bł. Czesława 16/18, 44-100 Gliwice, POLAND
([7]) **IEHK, RWTH —** Intzestraße 1, 52072 Aachen, GERMANY
([8]) **Niobium Products Company —** Steinstraße 28, 40210 Düsseldorf, GERMANY
([9]) **Rautaruukki Oyj Ruukki Production, Research Centre —** P.O. Box 93, Rautaruukintie 155, FINLAND
([10]) **Faculty of Mechanical Engineering, University of Maribor —** Smetanova 17, Maribor, SLOVENIA

Contract No RFSR-CT-2005-00027
1 July 2005 to 31 December 2008

Final report

Directorate-General for Research

2010 EUR 24209 EN

Europe Direct is a service to help you find answers to your questions about the European Union

Freephone number (*)**:**

00 800 6 7 8 9 10 11

(*) Certain mobile telephone operators do not allow access to 00 800 numbers or these calls may be billed.

A great deal of additional information on the European Union is available on the Internet. It can be accessed through the Europa server (http://europa.eu).

Cataloguing data can be found at the end of this publication.

Luxembourg: Publications Office of the European Union, 2010

ISBN 978-92-79-14438-7

doi 10.2777/86748

ISSN 1018-5593

Printed in Luxembourg

PRINTED ON WHITE CHLORINE-FREE PAPER

Contents

1. Objectives

The main objectives set at the outset of the project concerned the metallurgy of niobium-alloyed, low-carbon bainitic steels and their use in three particular product areas. They were:

- To determine composition - microstructure - property relationships for this type of steel
- To define its limits in thick-walled pipe for X60 to X70 strength level
- To explore its exploitation for thinner-walled pipe made from hot-coiled plate. The strength levels aimed for were X70 to X100
- To determine its applicability for general use for steels with yield stress in the range 400 - 650 MPa, with particular regard to the weldability of the steel.
- To carry out cost - benefit analyses for each product area concerned.
- To identify and justify appropriate changes to the Euronorms concerned.

2. Comparison of initially planned activities and work accomplished

When the partners finalised the compositions and processing conditions to be included in the laboratory model, work-package 1, it was decided that four more elements, Mn, Cr, Cu and Ni, should be added to C, Nb, Mo and B in the experimental design and this resulted in 24 casts being made rather than the 10 in the initial plan. Six conditions were processed in the laboratory for each composition to simulate rolling reduction ratios of 2 and 4 below the no-recrystallisation temperature, with cooling rates between 850°C and 550°C, termed CR1, of 0.5°C/s, 10°C/s followed by air cooling, and 10°C/s followed by slow cooling, respectively. These conditions were selected to simulate the slow cooling conditions in heavy plate mills without accelerated cooling, faster cooling in heavy plate mills with accelerated cooling, and in hot strip mills with coiling after rolling.

It was decided that the most important properties to be determined on this increased number of compositions were those of tensile strength, impact toughness and weldability, and that fracture toughness testing would not be carried out. These changes increased the amount of work to be carried out in work-package 1 and a rearrangement of the activities of each partner was considered necessary. In particular, all the casts were made by OCAS and University of Maribor completed all of the tensile testing. For each type of test it was decided to carry out the testing in one laboratory to eliminate inter-laboratory scatter.

A breakdown in the first year on the vacuum furnace being used for steelmaking resulted in delays against the planned schedule for the laboratory model work-package. When the casts were made, the aluminium levels on the laboratory cast steels containing 2.1 wt. % Mn were higher than the aim of 0.03 wt. %, with levels in the range 0.057 – 0.096 wt. %, while one of the 1.5 wt. % Mn steels had a lower than planned level of 0.007 wt. %. It was decided to accept the higher than planned aluminium level, but two of the 2.1 wt. % Mn steels also missed their designed carbon contents, having levels of 0.09 wt. % instead of the planned 0.04 wt. %. These two casts were re-made and the ‘mis-casts’ were processed in the laboratory along with feedstock from three of the commercial casts from work-packages 3 and 4, and one conventional X70 steel, containing 0.08 C, 1.66 Mn, 0.04 Nb, 0.08 V, to give additional conditions for the validation of the models. These difficulties created subsequent scheduling issues through the test facilities, but the planned tests have all been completed.

Commercial rollings were made and processed with the following deviations from the initial plans. In work-package 2, on thick-walled welded pipe, the range of thickness planned was 15 – 35 mm, but no available orders were received for pipe above 25.4 mm wall thickness and so three plate thicknesses, 14.6 mm, 20.9 mm and 25.4 mm were processed and evaluated. In work-package 3, hot-coiled plate for pipe, three trial casts were made at Ruukki, with 14 strips being rolled, and two casts were produced in Salzgitter, resulting in 12 strips. Two strips were processed to high-frequency induction (welding process 291 to EN ISO 4063: 2000 [1]) welded pipes, one strip was rolled for structural application in work-package 4, and the remaining strips were processed to spiral pipe. Difficulties were experienced in completing girth-welding trials; girth welds without any visible surface defects were made on two pipes, but these were only completed in the final semester and it was only possible to complete a full evaluation of one spiral-welded pipe. In work-package 4, plate for general construction, it proved not to be possible for OCAS to obtain coil-plate through one of the Arcelor mills and coil-plate from Salzgitter has been evaluated in the assessment of weldability. Flat-rolled, air-cooled plate of 20 mm and 50 mm thickness was processed through one of the Corus plate mills.

3. Description of activities and discussion

The testing carried out in the laboratory consisted of processing plates to provide feedstock for material to be used in the determination of: CCT diagrams by dilatometry, recrystallisation temperatures using torsion tests, and weldability using a thermal cycle simulator to examine the effect of two cooling rates after reheating to 1250^{o}C. Plates were also processed to simulate six processing conditions that were evaluated by examination of the microstructure, using optical metallography and measurement of grain size using electron back-scattered diffraction, EBSD, and by determination of the tensile properties and impact toughness transition temperatures.

When all the laboratory test results were available, multiple regression analyses were carried out on each parameter measured to determine the factors having a high significance. This was done by calculating the p value, where this is defined as (Mean Square Regression / Mean Square Error), and including factors where $p < 0.1$ in the regression equations for each parameter. The regression analyses were carried out using the nine elements controlled in the experimental design, namely C, Mn, Ni, Cu, Mo, Cr, Cu, Nb, Ti and B, and the processing factors of $\log_{10}$CR1, where CR1 was the cooling rate between 850°C and 550°C, $\log_{10}$CR2, where CR2 was the cooling rate between 550°C and 20°C, the rolling reduction below the no-recrystallisation temperature, RR, and the finish cooling temperature, T_{FC}. The regression equations were validated by using six compositions, the two 'mis-casts' and material from four commercially produced casts, processed through the laboratory under the same processing conditions.

3.1. Microstructure

The characterisation of microstructures by metallography can be subjective. EBSD was used to quantify the grain size of the microstructure using boundary mis-orientation angles of 4^{o} and 15^{o} and the distribution of number fraction against mis-orientation boundary angle was recorded using mis-orientation angle maps. Ferritic and bainitic microstructures show characteristic maps. An approach was developed that classified the microstructures on the basis of the ratio of the grain sizes determined with these two mis-orientation angles. Ferritic microstructures were described as having a ratio $d_{15^o}/d_{4^o} < 1.25$, with a characteristic value of 1.125. Bainitic microstructures were described by a lower limit and a characteristic d_{15^o}/d_{4^o} ratio of 1.6 and 1.9 respectively. There were samples that presented a mixture of ferrite and bainite, and even with EBSD maps it is difficult to differentiate between such microstructures. They have been described as acicular ferrite and defined by $1.25 < d_{15^o}/d_{4^o} < 1.6$. The microstructures in the air-cooled condition were ferrite and pearlite in 37 out of the 52 samples from the experimental casts.

3.2. Transformation characteristics

Continuous cooling transformation diagrams were constructed using dilatometer studies; samples were heated to 1200°C at a heating rate of 5°C/s and held for 10 minutes. The samples were cooled at 5°C/s

to 1050°C and held for 3 s before applying a strain of 0.6, at a rate of 3/s, then cooled again at 5°C/s to 850°C when a second deformation of 0.6 strain was applied at 3/s. Nine cooling rates between 95°C/s and 0.3°C/s were applied and the hardness and microstructures were evaluated. A set of 29 CCT diagrams has been constructed and these are presented in Appendix A. Regression equations for the hardness of the formed microstructure were determined for three different cooling rate ranges and these have been described as applying to the cooling rates for formation of bainite, martensite and ferrite. Niobium was a significant factor in the bainite hardness equation. Martensite hardness is often considered to be a function only of the carbon content. The microstructures formed on applying the faster cooling rates, as given by the equation described as martensite hardness, were not necessarily martensitic and the inclusion of boron, molybdenum, manganese and chromium as significant factors in the regression analysis may be due to an effect of these elements on the hardenability of the steel. The hardness of the validation casts was well predicted by the equations, except at the slower cooling rates for ferrite formation where hardness was underestimated.

Temperatures of no-recrystallisation were determined from plots of the mean flow stress against the inverse of the absolute temperature following the procedure developed by Jonas and co-workers. This type of plot also allows the start, A_{r3}, and end, A_{r1}, temperatures for the austenite transformation to be determined. The mean flow stress has been defined as the area under each stress-strain curve divided by the pass strain determined from multi-pass torsion tests. A second method for the characterisation of the recrystallisation behaviour during the torsion tests was applied. From the stress-strain curves obtained in multi-pass tests, the anisothermal interpass fractional softening (FS) was determined following the procedure proposed by Liu and Akben [2]. From the plot of FS vs. Inverse Absolute Temperature two characteristic temperatures were derived, the recrystallisation limit temperature, RLT, indicating the temperature below which softening is less than 100%, and the recrystallisation stop temperature, RST, indicating the temperature below which no softening is observed between deformation passes. The findings showed that only boron had a significant effect on all of the recrystallisation temperatures, molybdenum was the only other significant factor on the RST and chromium the other significant factor on the RLT. The results of Djahazi et al. have demonstrated that boron accelerates the precipitation process by increasing the precipitation start temperature and reducing the precipitation start time. This means that precipitation is able to retard recrystallisation at higher temperatures than in steels containing only Nb, thus leading to an increase of the temperature of no-recrystallisation. The effects of Mo and Cr in retarding recrystallisation are due to solute drag. The absence of niobium as a significant factor may be due to saturation having already occurred at a niobium level of 0.05 wt. % in steels with these levels of alloying. A_{r3} and A_{r1} temperatures did show larger effects of composition with C and B have the strongest effects followed by Ni, Mn and Cu, all of which lowered the transformation temperatures.

3.3 Mechanical properties

Tensile testing was carried out using round tensile specimens with 25 mm gauge length and 5 mm diameter and an optical deformation and strain measurement system was used to determine the stress-strain curves. Duplicate specimens were taken from most plate conditions and there were some examples of markedly different tensile properties from within a plate, which may have been due to centre-line segregation. Repeat tests and some filtering of the results were carried out to remove results considered to be affected in this way. Seven out of nine of the alloying elements were found to be significant factors in the regression analysis for tensile strength and six were significant in the regression analysis for 0.2% proof stress. Copper was not found to be a significant factor in either proof stress or tensile strength. Correlation coefficients, R^2 adjusted, were high at 0.83 and 0.75 for tensile strength and proof stress respectively. The significant alloying elements all had positive constants indicating that they increased strength, and for both parameters niobium was a significant factor. The niobium constant was equivalent to 65 MPa increase in tensile strength per 0.1 wt. % addition and 50 MPa increase in proof stress per 0.1 wt. % addition. Faster cooling rates between 850°C and 550°C and slower cooling rates between 550°C and 20°C both increased strength. The rolling reduction ratio was not a significant factor on the strength.

Charpy impact tests were carried out to EN 10045 using an impact-testing machine with an energy capacity of 1448 J and an impact velocity of 7.74 m/s. The number of samples varied between 8 and 20

samples per plate. Impact transition curves were determined by means of the modified tanh-fitting algorithm of Wallin. Impact transition temperatures were calculated for two criteria; the first was for 27 J and the second was for half the upper shelf energy, described at 0.5Kvmax. For both values of impact transition temperature, niobium was not found to be a significant factor. Increasing C, B, Mn, Cr and Mo increased the impact transition temperatures while increasing Ni, Cu and rolling reduction ratio lowered the impact transition temperatures. The ability to predict impact transition temperature on the validation samples was less good on the higher carbon content steels. After casting, one of the steels produced was found to contain lower than planned levels of aluminium and titanium and the impact transition temperature of this steel was found to be ~ 50°C higher than the other steels with similar manganese content for all of the six rolled conditions. The cooling rate between 850°C and 550°C was not found to be a significant factor on the transition temperatures. Increasing the reduction ratio lowered the transition temperatures, while slower cooling from 550°C to 20°C raised them.

Summarising the findings of the significant factors in the tensile and impact analyses, the conclusions drawn were that increasing C, B, Mn, Mo and Cr increased strength while raising impact transition temperatures, increasing Ni and Ti tended to increase strength while lowering transition temperatures, increasing Nb increased strength but had little effect on transition temperatures, and increasing Cu had little effect on strength but lowered transition temperatures. Increasing the reduction ratio had little effect on strength but lowered transition temperatures, faster cooling rates between 850°C and 550°C increased strength but had little effect on transition temperatures, and slower cooling rate from 550°C to 20°C increased strength while raising transition temperatures.

Six casts were produced in total in the work-packages examining the commercial processing of steels and the tensile and impact toughness transition temperatures measured on these products were compared with the values predicted by the regression equations from the laboratory models. Tensile strength was well predicted for all of the steels, but the prediction of proof stress tended to higher than that measured. Impact transition temperatures were reasonably well predicted for four of the six casts, but for the other two steels the prediction was poor. Prediction of results from two published papers reporting other laboratory rolled plate experiments gave good agreement with the reported properties.

3.4 Weldability

Welds were made using various welding processes: submerged arc, reduced pressure power beam, autogenous laser and hybrid laser/MAG. The impact transition curves of specimens taken at various locations in the welds were determined and these showed that the steel had similar weldability to structural steels currently produced to S355 and S450 grades. Laboratory scale simulation of the weld HAZ has been carried out using a thermal cycle simulator to examine the effect of cooling rate. Samples were reheated to 1250°C and cooled at two controlled rates through the temperature range 800 – 500°C. The time taken through this temperature range is referred to as $t_{8/5}$ and the two times used in the simulations were 8 s and 30 s. Charpy impact tests were carried out on a machine with an energy capacity of 300 J and impact transition curves were determined by tanh fitting. Impact transition temperatures were determined as for the rolled conditions. Hardness values were measured for the rolled condition and the simulated welds. Ni and Mn were the only two elements that were significant in the regression equations for both 27 J ITT and 0.5Kvmax ITT, and both of these elements had negative constants indicating that increasing Ni and Mn had the beneficial effect of lowering the impact transition temperatures. For the 0.5Kvmax ITT, C was also a significant factor with a positive constant. Niobium was not a significant factor in either regression, but its constant was negative indicating that its tendency was not detrimental to weld toughness.

Properties considered to be of concern in downstream processes were identified and a limited number of results obtained for through thickness ductility, strain ageing, and post weld heat treatment. Through thickness ductility levels of > 60% were recorded and little effect of ageing was seen at 250°C. Post weld heat treatment did show that the impact transition temperature was increased, by as much as 50°C, but this effect is also seen in other micro-alloyed steels currently used.

4. Conclusions

The project has been successful in predicting properties in commercially rolled products on the basis of the models produced by multiple linear regression on the data determined from the laboratory rolled plates. It has demonstrated that a low-carbon, high-niobium chemistry allows the full-scale production of (1) S420ML in 50 mm thickness and S460ML in 20 mm thickness plate using lower levels of controlled rolling and with air-cooling, and (2) the properties of L450MB - L555MB to be achieved in a cost-effective way without the use of more expensive alloying elements such as molybdenum and vanadium.

The experience gained in the project has highlighted benefits in using low-carbon, high-niobium steels; of particular note was the good slab surface quality, the ability to process at higher temperatures and with shorter holding periods resulting in lower mill loads and higher productivity, and the achievement of specified properties with lower alloying cost.

The regression equations determined for the prediction of properties are shown below. These equations are applicable for cooling rate between 850 °C and 550 °C, CR1, of 0.5 °C/s and 17 °C/s, for cooling rate between 550 °C and 20 °C, CR2, of 0.008 °C/s and 0.25 °/s, and for rolling reduction ratio of 2 to 4.

Critical and Phase Transformation Temperature Models (T ^{o}C, weight %)

Recrystallisation limit temperature, RLT, ^{o}C	=	1034 + 12250B + 36Cr
Temperature of no recrystallisation, Tnr, ^{o}C	=	1014 + 18000B
Recrystallisation stop temperature, RST, ^{o}C	=	897 + 19000B + 70Mo
Ar3, ^{o}C	=	990 - 8600B - 550C - 90Mn - 75Ni - 26Cu
Ar1, ^{o}C	=	860 - 5500B - 390C - 65Ni - 56Mn

CCT hardness values

Three equations were determined that applied to different cooling rate ranges dependent on steel composition. For cooling rates less than that determined by logCR = 0.65 – 180B – 0.7Ni – 0.5Mn, use the equation described as ferrite hardness. Use the equation described as martensite hardness for cooling rates greater than that determined by logCR = 3 - 350B – 0.6Mn – 0.35Mo – 0.35Ni. Otherwise use the equation described as bainite hardness.

“Bainite Hardness”, HV10	=	80 + 10000B + 670C + 300Nb + 60Mo + 35Mn + 25Cr
		+ 5Cu + 5Ni + (20 + 150C -17Mo -7Mn)logCR
“Martensite Hardness”, HV10	=	50 + 90Mo + 60Mn + 50Cr + (14000B + 880C)logCR
“Ferrite Hardness”, HV10	=	25 + 14000B + 60Mn + 30Mo + (130000B – 800C)logCR

Microstructure – grain sizes in microns

(d_{4^o})	=	6 - 7C - 6Nb - 0.7Mo - 0.5Cu - 0.8*logCR*1 - 0.4*RR*
(d_{15^o})	=	5 + 450B - 7Nb + 1.3Mn + 1.2Cr - 0.6Cu + 0.2*logCR*2 - 0.8*RR*

Mechanical Properties

Proof stress, MPa	=	230 + 47000B + 1900Ti + 500Nb + 770C + 130Mo + 70Mn
		+ 68logCR1 - 27logCR2
Tensile strength, MPa	=	100 + 55000B + 2600C + 650Nb + 200Mo + 150Mn + 80Cr + 30Ni + 70logCR1 - 15logCR2

27J ITT, ^{o}C	=	50 + 14000B + 1050C - 40Ni + 33Mo - 33Cu + 15Cr + 13Mn - 14$logCR2 - 8(d_{15^o})^{-1/2}-9RR$ - 0.2T_{FC}
27J ITT, ^{o}C	=	- 60 + 20000B + 1100C - 40Cu - 40Ni + 40Mo + 30Cr + 30Mn - 20RR -10logCR2 - 0.2T_{FC}
0.5Kvmax ITT, ^{o}C	=	120 + 14500B + 1270C - 950Ti - 45Ni + 30Mn + 23Mo - 20Cu - 15$logCR2 - 10(d_{15^o})^{-1/2}$ - 0.3T_{FC}
0.5Kvmax ITT, ^{o}C	=	- 30 + 22500B + 1350C - 1400Ti + 50Mn - 50Ni - 30Cu + 27Mo + 25Cr - 16RR - 11logCR2 - 0.3T_{FC}

Weldability

27 J ITT, ^{o}C	= 10 - 45Ni - 40Mn - 30Cr
0.5Kvmax ITT, ^{o}C	= 480C - 45Ni - 30Mn
Parent metal hardness, HV5	= 13 + 27000B + 1020C + 50Mo + 60Mn + 50Ni
HAZ hardness, HV5	= 25 + 18000B + 1360C + 270Nb + 60Mo + 46Mn + 34Cr + 30log$CR_{8/5}$

5. Exploitation and impact of the research results

An important objective of the project was to justify changes to Euronorms relating to high-strength steels for linepipe and structural applications. The yield strength levels of the steels concerned range from 420 to above 700 MPa. Therefore, for structural steels, the Euronorm of interest is EN 10025-4 (Thermomechanically rolled structural steels). Though not specifically studied here, the steels covered by EN 10028-5 (Thermomechanically rolled pressure vessel steels) are closely related to the structural steels in EN 10025-4 and are similarly affected by the results of this project. High-strength steel for pipelines transporting combustible fluids is covered in EN 10208-2, in which the thermomechanically processed grades designated L415MB, L450MB, L485MB and L555MB are concerned here.

In these Euronorms, niobium microalloying is currently limited to a maximum of about 0.05. However, the maximum carbon levels allowed are about 0.16%. It has been shown within the project that much higher levels of niobium can be used to advantage provided the maximum carbon content is reduced below its current level. It has also been shown that levels of manganese higher than those currently allowed in the above standards are also advantageous in the case of lower carbon contents.

The reasons for the current limitations on niobium microalloying in the above Euronorms are unknown. Therefore, when proposing any increase in the maximum level of niobium allowed, it is necessary to address the possible objections that might be raised on the basis of current knowledge about niobium in steel. Areas of concern might be the properties and behaviour of the plate as delivered, after arc welding or after cold bending. This report addresses the influence of niobium in all these areas by making use of the results obtained in the project combined with information available in the literature concerning structural and linepipe steels containing more than 0.05% Nb. The following topics are treated: through-thickness ductility, strain ageing, hydrogen cracking, weld metal and HAZ toughness, and post-weld heat treatment.

On the basis of the survey, the following recommendations are made.

EN 10025-4: a footnote should be added to the table containing limits on alloying stating: “For each 0.01% reduction of the maximum carbon content, the maximum specified niobium content is increased by 0.01%, up to a maximum of 0.15%. In addition, for each 0.01% reduction of the maximum carbon content, the maximum manganese content is increased by 0.05% up to a maximum of 2.1%.”

EN 10208-2 should be changed to follow the harmonised API 5L/ISO 3183 with regard to the levels of microalloying allowed. The current separate limitations on niobium, vanadium and titanium should be replaced by a single condition Nb+Ti+V =< 0.15%.

EN 10028-5 should be changed in accordance with the above recommendation for EN 10025-4, together with an additional footnote stating that special care should be taken to ensure that toughness requirements are met in welds if post-weld heat treatment is prescribed in the case of high levels of microalloying.

Papers were presented by two of the partners during the course of the project; one on the use of EBSD to characterise the microstructures was presented at the Spanish National Congress [3] and the other on the evaluation of the weldability was presented at the 50th Annual Conference of the Polish Welding Institute [4]. It is expected that doctorate theses will be submitted as a result of the involvement of two of the partners; one from the University of Aachen on the work carried out on Charpy testing and the other on the microstructural characterisation carried out by CEIT. Conference papers are likely to be submitted to present the findings of the project.

6. Scientific and technical description of the results

6.1. Laboratory model

A principal objective of the project was to build models based on the chemical composition and processing conditions to predict bainite transformation, T_{nr} (no-recrystallisation temperature), strength and toughness. In order to investigate the influence of the alloying elements C, Mn, Nb, Cr, Mo, Ni, Cu and B with a minimum of laboratory casts the experimental set-up was designed based on a statistical approach by means of an intelligent design of experiments (DOE) using a three-stage approach. The first stage was a half fractional factorial design with variations in Mn, Cr, Mo, Ni and Cu at two levels to evaluate their effects and interactions on bainite formation and mechanical properties. The second stage was a full factorial design dedicated to the border conditions of the HTP concept and varies C and Nb at two levels. Finally, the third stage, which was also a full factorial design, investigated the influence of B by adding B and Ti at two levels.

Twenty-four casts were made to the aimed compositions of the three separate experimental designs and processed under six rolling schedules to simulate cooling of thick and thin products for both flat and coiled material. These conditions comprised reduction ratios below the no-recrystallisation temperature, of 2 (schedules C, E and G) and 4 (schedules D, F and H), with finish rolling temperatures of 850°C and cooling rates between 850°C/s and 550°C of 0.5°C/s (schedules C and D), 10°C/s followed by air cooling (schedules E and F), and 10°C followed by slow cooling, 30°C/hr (schedules G and H), respectively. These conditions are selected to simulate the slow cooling conditions in heavy plate mills without accelerated cooling, faster cooling in heavy mills with accelerated cooling, and in hot strip mills with coiling after rolling.

First of all, metallographic analyses were carried out for all casts and conditions. Complementing the light optical microscopy (LOM), EBSD measurements for all conditions were done to measure "bainitic" grain sizes. The effect of composition on the CCT behaviour with deformation was determined. To gain an overview about the softening behaviour of these HTP steels, the interaction of deformation and softening is investigated by torsion tests. Besides these microstructure analyses, the mechanical properties were characterised using tensile tests and impact transition curves. To complete the experimental analyses of the laboratory casts, the toughness behaviour of the materials after different welding procedures was examined. Finally, the plates processed in the laboratory were compared with commercial scale rolling of coil-plate and flat plate.

6.1.1. Set-up of lab simulations – design of experiments

The aim of work package 1 was to build a model based on the chemical composition predicting bainite transformation, T_{nr} (non recrystallisation temperature), strength and toughness.

The basic composition of the so-called high temperature processing, HTP, concept is low-carbon and niobium with some additions of titanium to bind nitrogen. Other alloying elements, usually denoted as hardening elements, are sometimes added depending on the steel processing.

The project partners agreed to investigate the influence of eight alloying elements, C, Mn, Nb, Cr, Mo, Ni, Cu and B, the assessment being based on a statistical approach by means of an intelligent design of experiments (DOE) using a three-stage approach. The first stage is a half fractional factorial design with variation of Mn, Cr, Mo, Ni and Cu at two levels to determine the effects of these elements with respect to bainite formation and mechanical properties. The second stage is a full factorial design dedicated to the border conditions of the HTP concept and varies C and Nb at two levels different to those in stage 1. The third stage, which is also a full factorial design, investigates the influence of B by adding B and Ti at two levels.

With this three-stage approach, it is possible to keep the number of casts to a reasonable value (24 casts) and, at the same time, to realize high-resolution designs that should enable revealing interactions between the factors (alloying elements). Table 1 summarises the design of the experiment and the planned compositions and its 3 stages.

Table 1: Design of experiment

Stage	Level	C	Nb	Ti	B	Mn	Ni	Mo	Cu	Cr
1	Low					1.5	0	0	0	0
	Base	0.04	0.10	0.015	0					
	High					2.1	0.5	0.3	0.5	0.5
2	Low	0.01	0.04							
	Base			0.015	0	1.8	0.25	0.15	0.25	0.25
	High	0.07	0.07							
3	Low			0.008	0.000					
	Base					1.8	0.25	0.15	0.25	0.25
	High			0.025	0.002					

In addition to selecting the chemical composition, the rolling and cooling conditions were varied during laboratory rolling trials in order to simulate the different processing routes of a heavy plate mill with air-cooling and with accelerated cooling, and a hot strip mill. Six different combinations were used with two reduction ratios and three sets of cooling conditions for each composition.

Some additional casts as well as industrial casts were used for the verification of the models. The laboratory simulations of the industrial casts also enabled the validation of the laboratory processing.

6.1.1.1 Stage 1 – Potential of HTP concept (Mn, Cr, Mo, Ni, Cu)

Stage 1 should give an idea of the potential of the HTP concept with respect to strength and toughness. The elements Mn, Cr, Mo, Ni and Cu were varied at two levels. With the given resolution, main effects are not confounded and 2-level interactions are confounded (aliased) only with 3-level interactions.

Factor:	const	const	const	1	2	3	4	5
	C	Nb	Ti	Mn	Cr	Mo	Ni	Cu
low (-1)				1.5	0	0	0	0
medium	0.04	0.1	0.015					
high (1)				2.1	0.5	0.3	0.5	0.5

DESIGN SUMMARY (standard design): 2**(5-1) design of resolution R = V
Number of factors (independent variables): 5
Number of runs (cases, experiments): 16
Number of blocks: 1
Fractional replications: 1/2 fractional factorial

	1	2	3	4	5			
Run	Mn	Cr	Mo	Ni	Cu		Factor	Alias
1	-1	-1	-1	-1	1		1	
2	-1	-1	-1	1	-1		2	
3	-1	-1	1	-1	-1		3	
4	-1	-1	1	1	1		4	
5	-1	1	-1	-1	-1		5	
6	-1	1	-1	1	1		1*2	3*4*5
7	-1	1	1	-1	1		1*3	2*4*5
8	-1	1	1	1	-1		1*4	2*3*5
9	1	-1	-1	-1	-1		1*5	2*3*4
10	1	-1	-1	1	1		2*3	1*4*5
11	1	-1	1	-1	1		2*4	1*3*5
	1	2	3	4	5			

Run	Mn	Cr	Mo	Ni	Cu		Factor	Alias
12	1	-1	1	1	-1		2*5	1*3*4
13	1	1	-1	-1	1		3*4	1*2*5
14	1	1	-1	1	-1		3*5	1*2*4
15	1	1	1	-1	-1		4*5	1*2*3
16	1	1	1	1	1			

6.1.1.2 Stage 2 – Limit conditions of HTP concept (C, Nb)

Stage 2, with combinations of low and high levels of C and Nb, was designed to check the limit conditions of the HTP concept. The amount of the alloying elements varied in stage 1 was set to intermediate levels. The design is full factorial; none of the effects are confounded.

Factor:	1	2	const	const	const	const	const	const
	C	Nb	Ti	Mn	Cr	Mo	Ni	Cu
low (-1)	0.01	0.03						
medium			0.015	1.8	0.25	0.15	0.25	0.25
high (1)	0.07	0.1						

DESIGN SUMMARY (standard design): 2**(2-0) design of resolution R = FULL
Number of factors (independent variables): 2
Number of runs (cases, experiments): 4
Number of blocks: 1

	1	2
Run	C	Nb
1	-1	-1
2	-1	1
3	1	-1
4	1	1

6.1.1.3 Stage 3 – Influence of B (B, Ti)

Stage 3 investigates the influence of B. Since only B in solid solution is effective for the phase transformation, the formation of BN must be avoided by means of Ti additions. The levels of Ti in stage 3 refer to Ti:N above and below the stoichiometric ratio assuming a N content of 40 ppm. The amount of the alloying elements varied in the other stages was set to intermediate levels. The design is full factorial; none of the effects are confounded.

Factor:	const	const	1	const	const	const	const	const	2
	C	Nb	Ti	Mn	Cr	Mo	Ni	Cu	B
low (-1)			0.008						0
medium	0.04	0.1		1.8	0.25	0.15	0.25	0.25	
high (1)			0.025						0.002

With an assumed N content of 40ppm, the targeted Ti:N ratios are, therefore:

	atomic ratio	mass ratio
low Ti	0.59	2
high Ti	1.83	6.25

DESIGN SUMMARY (standard design): 2**(2-0) design of resolution R = FULL
Number of factors (independent variables): 2
Number of runs (cases, experiments): 4
Number of blocks: 1

	1	2
Run	Ti	B
1	-1	-1
2	-1	1
3	1	-1
4	1	1

6.1.1.4 Definition of response variables

To get an overview of the microstructures, metallographic analyses using different etchants have been done, together with EBSD measurements. The means of assessing the effect of composition was to determine the CCT behaviour with deformation and the temperature of no-recrystallisation for each cast. The mechanical properties of the plates processed under the six conditions were determined by means of tensile tests and impact transition curves and the microstructures assessed. From these measurements models of the effect of composition and cooling rate on structure and properties have been constructed. The properties and microstructures of coil-plates and flat plates processed under commercial scale processes have then been used to validate these models.

Table 2 gives a list of the response variables being determined.

Table 2: Response variables

Technique	Response variable	tested per
Metallography	Phase components (only indicative)	plate
EBSD	grain size d_{4° and d_{15° (4° and 15° misorientation)	plate
Dilatometry	CCT diagram HV10 as function of cooling rate	cast
Torsion test	Tnr RLT RST Ar3 Ar1	cast
Welding simulation	8s ITT 0.5Kvmax 30s ITT 0.5Kvmax 8s HV5 30s HV5 8s 27J ITT 30s 27J ITT	cast
Charpy impact	ITT 0.5Kvmax ITT 27J Kvmax	plate
Tensile test	PS (proof stress) TS	plate

6.1.2 Set-up of Regression Analyses

A multiple linear regression technique was used to obtain a response equation for each of the different parameters measured. The sample was formed by the 24 designed casts. Only those parameters/variables considered in the three intelligent designs were taken into account (Mn, Ni, Mo, Cr, Cu, C, Nb, B and Ti) for the regression. Also, the rolling parameters play a role in the linear multiple regressions:

$\log_{10}CR_{800\text{-}550^oC}$ = *logCR1,* (*CR* = Cooling Rate (ºC/s))

$\log_{10}CR_{550\text{-}20^oC}$ = *logCR2*

Rolling Reduction = *RR* (below the no recrystallisation temperature)

Finish cooling temperature (ºC) = T_{FC}.

Exceptionally, other variables were also taken into consideration, when the literature describes and requires them for certain parameters. For example, in the response equation for toughness, grain size (d_{15^o}) was introduced as a regressor; for weldability, the Vickers hardness (*HV5*) and the cooling rate between 800 and 500ºC ($t_{8/5}$) were also introduced.

For each parameter, three equations have been fitted:

i) "Autofit" option is a back elimination procedure, removing those variables with significance $p > 0.1$,

ii) "Fit All" possible models are considered (for 9 variables there are 511 possible models) and the one with the largest adjusted determination (R^2_{adj}) coefficient is retained, and

iii) "Regress" on all the variables, irrespective of their significances. This method obtains the largest determination coefficient (maximum R^2).

The first option (Autofit) is the safest statistical approach. The second one is trying to detect some more effects, but the coefficients are not so sure. The smaller the significance parameter, *p*, the safer it is. The third option (regression to all variables) should be used with a lot of caution. It is the best fit to the experimental set of 24 considered casts, but one has to be aware of the uncertainty/significance of some coefficients. In the tables showing the regression results, those coefficients with significance, $p < 0.1$ (credible ones) are shown in bold.

Plots of experimental vs. predicted parameters are shown (only for the Autofit option) for the 24 casts used to compute the response equations. In Section 6.1.11, an additional plot shows the experimental vs. the predicted values for the 6 additional validation casts (not previously considered for the model generation).

6.1.3 Lab simulations

6.1.3.1 Lab casts

Twenty-four casts were planned in the three separate experimental designs. Two casts in the first stage contained carbon levels well above the aim of 0.04 wt. % at 0.09 wt. %. Theses two 'mis-casts', A039 and A040, were re-made and the two 'mis-casts' were processed to be used for the validation of the models, the compositions are shown in Table 3.

In total, 26 ingots of 100 kg each were cast in a vacuum furnace. Electrolytic iron was used as a basis in order to keep the S-content low. The chemical composition was analysed by means of SS-OES and combustion (only C, N and S). The range and average values of the uncontrolled elements in the stage 1 casts are shown in Table 4.

The phosphorous content was below 30ppm in all cases. The Si content was generally slightly higher than specified. Al was sometimes notably higher than specified and in the case of cast A029 it was exceptionally low at 70ppm. Cast A029 also showed an exceptionally low Ti content (50 ppm) and, consequently, a very low Ti:N ratio of 1.43. Cast A045 in the stage 2 design had a carbon content of 0.09 wt. %, above the aim of 0.07 wt. %, but it was decided to accept this and process the cast.

Table 3: Analyses (wt. %) obtained for the additional (verification) casts

		C	Mn	N	Ti	Nb	Ni	Mo	Cu	Cr	B	P	S	Si	Al	Ti/N
	aim	0.040	2.10	0.0040	0.015	0.10	0	0	0.50	0.50	0					
A039	actual	0.092	2.10	0.0051	0.014	0.11	0.004	0.022	0.50	0.50	0.0005	0.0023	0.0015	0.32	0.087	2.75
	aim	0.040	2.10	0.0040	0.015	0.10	0.50	0	0	0.50	0					
A040	actual	0.091	2.02	0.0036	0.018	0.12	0.53	0.025	0	0.50	0.0004	0.0015	0.0016	0.34	0.091	4.92

Table 4: Realisation range and average of uncontrolled elements

	P	S	Si	Al	N	Ti	V	Ti/N
aim			0.21	0.030	0.0040	0.015		
Average	0.0023	0.0014	0.31	0.052	0.0037	0.013	0.004	3.98
max	0.0028	0.0031	0.35	0.096	0.0059	0.021	0.009	6.77
min	0.0013	0.0006	0.21	0.007	0.0022	0.005	0.002	1.43

The aim and analysed chemical compositions of the casts are given in Table 5 through Table 7.

Table 5: Analyses (wt. %) obtained for the Stage 1 casts

		C	Mn	N	Ti	Nb	Ni	Mo	Cu	Cr	B	P	S	Si	Al	Ti/N
Run 1	aim	0.040	1.50	0.0040	0.015	0.10	0	0	0.50	0	0					
A027	actual	0.038	1.50	0.0032	0.016	0.11	0.01	0.01	0.48	0.01	0.0005	0.0021	0.0009	0.27	0.046	5.00
Run 2	aim	0.040	1.50	0.0040	0.015	0.10	0.50	0	0	0	0					
A028	actual	0.042	1.50	0.0059	0.014	0.11	0.44	0.01	0.01	0.01	0.0005	0.0022	0.0013	0.31	0.054	2.37
Run 3	aim	0.040	1.50	0.0040	0.015	0.10	0	0.30	0	0	0					
A029	actual	0.038	1.40	0.0037	0.005	0.10	0	0.32	0.01	0.01	0.0005	0.0026	0.0014	0.29	0.007	1.43
Run 4	aim	0.040	1.50	0.0040	0.015	0.10	0.50	0.30	0.50	0	0					
A030	actual	0.047	1.50		0.012	0.11	0.44	0.34	0.49	0.01	0.0006	0.0025	0.0031	0.26	0.047	
Run 5	aim	0.040	1.50	0.0040	0.015	0.10	0	0	0	0.50	0					
A031	actual	0.041	1.50	0.0032	0.017	0.11	0.01	0.01	0	0.47	0.0004	0.0013	0.001	0.34	0.062	5.31
Run 6	aim	0.040	1.50	0.0040	0.015	0.10	0.50	0	0.50	0.50	0					
A032	actual	0.042	1.50	0.0038	0.013	0.11	0.44	0.01	0.48	0.51	0.0007	0.0021	0.0014	0.28	0.046	3.42
Run 7	aim	0.040	1.50	0.0040	0.015	0.10	0	0.30	0.50	0.50	0					
A033	actual	0.041	1.50	0.0033	0.012	0.11	0.01	0.35	0.47	0.50	0.0007	0.0027	0.0017	0.30	0.014	3.64
Run 8	aim	0.040	1.50	0.0040	0.015	0.10	0.50	0.30	0	0.50	0					
A034	actual	0.042	1.50	0.004	0.013	0.10	0.43	0.35	0.02	0.52	0.0006	0.0027	0.0017	0.29	0.027	3.25
Run 9	aim	0.040	2.10	0.0040	0.015	0.10	0	0	0	0	0					
A035	actual	0.043	2.00	0.0037	0.011	0.10	0	0.01	0	0.02	0.0004	0.0021	0.0016	0.31	0.057	2.97
Run 10	aim	0.040	2.10	0.0040	0.015	0.10	0.50	0	0.50	0	0					
A036	actual	0.043	2.10	0.0039	0.013	0.11	0.43	0.01	0.50	0.02	0.0005	0.0023	0.0016	0.31	0.068	3.33
Run 11	aim	0.040	2.10	0.0040	0.015	0.10	0	0.30	0.50	0	0					
A037	actual	0.042	2.10	0.0040	0.014	0.11	0.01	0.35	0.49	0.01	0.0006	0.0027	0.0019	0.32	0.079	3.50
Run 12	aim	0.040	2.10	0.0040	0.015	0.10	0.50	0.30	0	0	0					
A038	actual	0.041	2.02	0.0038	0.016	0.11	0.52	0.33	0.01	0.02	0.0005	0.0014	0.0014	0.33	0.096	4.08
Run 13	aim	0.040	2.10	0.0040	0.015	0.10	0	0	0.50	0.50	0					
A202	actual	0.043	2.09	0.0031	0.021	0.12	0.01	0	0.56	0.48		0.0021	0.0006	0.21	0.032	6.77
Run 14	aim	0.040	2.10	0.0040	0.015	0.10	0.50	0	0	0.50	0					
A203	actual	0.042	2.07	0.0036	0.016	0.12	0.49	0	0.01	0.49		0.0019	0.0007	0.22	0.028	4.44
Run 15	aim	0.040	2.10	0.0040	0.015	0.10	0	0.30	0	0.50	0					
A041	actual	0.041	2.03	0.0042	0.016	0.12	0.01	0.33	0.01	0.49	0.0005	0.0017	0.0018	0.32	0.063	3.69
Run 16	aim	0.040	2.10	0.0040	0.015	0.10	0.50	0.30	0.50	0.50	0					
A042	actual	0.042	2.10	0.0033	0.015	0.11	0.45	0.34	0.53	0.51	0.0008	0.0028	0.0013	0.35	0.075	4.55

Table 6: Analyses (wt. %) obtained for the Stage 2 casts

		C	Mn	N	Ti	Nb	Ni	Mo	Cu	Cr	B	P	S	Si	Al	Ti/N
Run 1	aim	0.010	1.80	0.0040	0.015	0.04	0.25	0.15	0.25	0.25	0					
A043	actual	0.025	1.80	0.0028	0.009	0.05	0.24	0.17	0.27	0.25	0.0006	0.0028	0.0012	0.33	0.015	3.32
Run 2	aim	0.010	1.80	0.0040	0.015	0.07	0.25	0.15	0.25	0.25	0					
A044	actual	0.019	1.80	0.0035	0.013	0.08	0.24	0.17	0.29	0.24	0.0007	0.0019	0.0013	0.35	0.055	3.71
Run 3	aim	0.070	1.80	0.0040	0.015	0.04	0.25	0.15	0.25	0.25	0					
A045	actual	0.092	1.80	0.0022	0.011	0.05	0.24	0.16	0.30	0.25	0.0005	0.0025	0.0012	0.35	0.025	5.00
Run 4	aim	0.070	1.80	0.0040	0.015	0.07	0.25	0.15	0.25	0.25	0					
A046	actual	0.070	1.80	0.0034	0.014	0.08	0.23	0.18	0.28	0.24	0.0009	0.0023	0.001	0.33	0.047	4.12

Table 7: Analyses (wt. %) obtained for the Stage 3 casts

		C	Mn	N	Ti	Nb	Ni	Mo	Cu	Cr	B	P	S	Si	Al	Ti/N
Run 1	aim	0.040	1.80	0.0040	0.008	0.10	0.25	0.15	0.25	0.25	0					
A047	actual	0.042	1.80	0.0034	0.009	0.12	0.24	0.16	0.30	0.25	0.0008	0.0027	0.0015	0.35	0.057	2.50
Run 2	aim	0.040	1.80	0.0040	0.008	0.10	0.25	0.15	0.25	0.25	0.002					
A048	actual	0.043	1.80	0.0039	0.009	0.11	0.23	0.17	0.30	0.24	0.003	0.0026	0.0014	0.35	0.068	2.26
Run 3	aim	0.040	1.80	0.0040	0.025	0.10	0.25	0.15	0.25	0.25	0					
A049	actual	0.042	1.80	0.003	0.022	0.12	0.24	0.16	0.30	0.25	0.0006	0.0023	0.0013	0.35	0.051	7.33
Run 4	aim	0.040	1.80	0.0040	0.025	0.10	0.25	0.15	0.25	0.25	0.002					
A050	actual	0.042	1.90	0.0047	0.021	0.11	0.23	0.16	0.29	0.24	0.0028	0.0024	0.0013	0.31	0.060	4.47

6.1.3.2 Industrial casts

Industrially cast slab material was delivered by Ruukki and Salzgitter while Corus provided hot rolled plate in thickness 50mm. The chemical compositions were analysed on lab rolled plate by means of SS-OES and combustion (C, S and N), Table 8.

The Salzgitter materials supplied for rolling in the laboratory consisted of a conventional NbV-concept steel with relatively high, 0.08 wt. %, carbon content (cast 02098) and a low C-high Nb-Cr composition with moderate additions of Mo (cast 16685) fitting well with the design of the stage 1 laboratory casts. The materials provided by Corus and Ruukki also fitted well with the set-up of the experimental design. Both steels were alloyed with Ni, Mo and Cr; and the Ruukki steel contained higher levels of Mn and Cr.

Table 8: Analyses (wt. %) of the industrially cast materials

Cast	C	Mn	N	Ti	Nb	V	Ni	Mo	Cu	Cr	Ti/N
81351	0.042	1.97	0.0084	0.015	0.10	0.013	0.21	0.005	0.21	0.98	1.79
02098	0.079	1.66	0.0050	0.003	0.04	0.079	0.06	0.004	0.06	0.04	0.58
16685	0.047	1.73	0.0082	0.018	0.10	0.009	0.04	0.069	0.04	0.27	2.20
81913	0.05	1.58	0.0059	0.016	0.10	0.007	0.16	0.005	0.25	0.26	2.71

6.1.3.3 Rolling simulations

Nine blocks were cut from each ingot, Figure 1. Two blocks with dimensions 125 mm × 125 mm × 60 mm were rolled with no particular rolling schedule applied in order to supply one plate in thickness 15mm for dilatometer and torsion testing and one in thickness 12 mm for welding simulations.

Six blocks (an additional block was a spare in case of problems during processing) were rolled to plates using two different reduction ratios, *RR*, below an assumed no recrystallisation temperature, T_{nr}, of 1050°C, followed by three different cooling strategies to give six conditions for each chemistry. The cooling conditions were selected to simulate

- air-cooling of thick plate (AC)
- accelerated cooling at 10 °C/s of thick plate to 550°C followed by air cooling (ACC)
- accelerated cooling at 10 °C/s of hot strip (coil-plate) with coiling at 550°C followed by cooling at 30°C/h (ACC+coiling)

In order to give similar amounts of reduction in each pass during roughing of the laboratory plates, two different thicknesses of starting block were used for the reduction ratios, *RR*, of 2 and 4. In the case of *RR* = 2 (block dimension 125 mm × 100 mm × 50 mm), three roughing passes and four finishing passes were applied while in the case of *RR* = 4 (block dimension 125 mm × 90 mm × 80 mm), two roughing passes and five finishing passes were used.

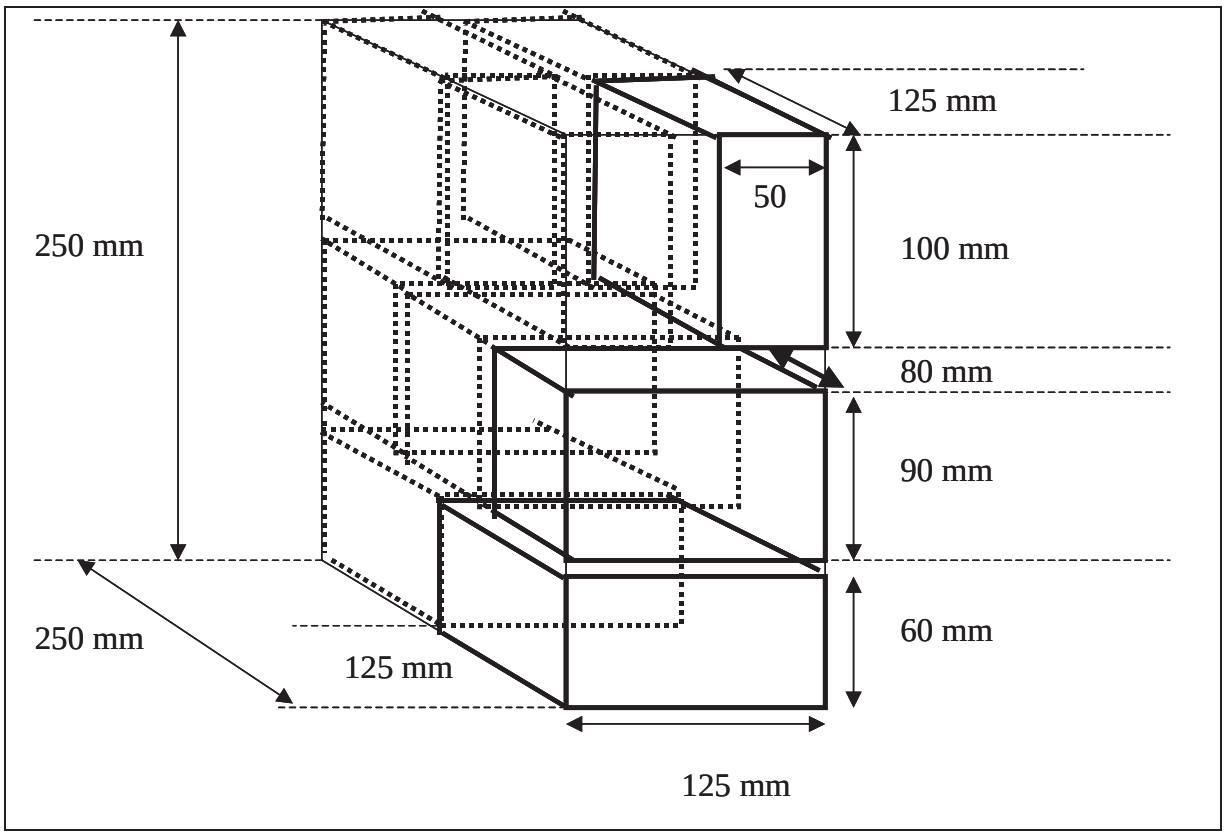

Figure 1: Cutting of ingots

Table 9: Rolling schedules and aimed rolling temperatures

RR at $T<T_{nr}$		Start	R1	R2	R3	Total in roughing	F1	F2	F3	F3/F4	F4/F5
2	Reduction (%)		22	22	22	52	16	16		16	16
	Thickness (mm)	50	39.1	30.7	24		20.2	17		14.3	12
4	Reduction (%)		23	23		40	24	24	24	24	24
	Thickness (mm)	80	62	48			36.4	27.6	20.9	15.8	12
Temp. (°C)		1200	1150	1100	1050		950	910	890	870	850

Blocks of the respective dimensions were taken from the industrially cast materials and rolled according to the same schedule. In the case of the 50 mm thick plate feedstock from Corus, the block dimensions and rolling schedule had to be adjusted for the higher reduction ratio. It was decided to reduce the rolling reduction during finishing from *RR* = 4 to *RR* = 3; the details are given in Table 10.

Table 10: Rolling schedules and aimed rolling temperatures for the Corus material

RR at $T<T_{nr}$		Start	R1	R2	R3	Total in roughing	F1	F2	F3	F3/F4	F4/F5
2	Reduction (%)		22	22	22	52	16	16		16	16
	Thickness (mm)	50	39.1	30.7	24		20.2	17		14.3	12
3	Reduction (%)		15	15		28	20	20	20	20	20
	Thickness (mm)	50	42.4	36			28.9	23.2	18.6	14.9	12
Temp. (°C)		1200	1150	1100	1050		950	910	890	870	850

The blocks were sorted according to the different combinations of rolling schedule and cooling strategy (designation A through H) and reheated in batches of no more than eight blocks. Block selection was random.

The reheating temperature was fixed to 1200°C for all but one cast composition; cast A046, run 4 in Stage 2. According to thermodynamic calculations, 1200°C is sufficient to dissolve all of the Nb. In the case of cast A046, which had the combination of 0.07% C and 0.07% Nb, a reheating temperature of 1250°C was used; however, the rolling schedule remained unchanged. After reheating, a thermocouple was introduced into a pre-drilled hole in the blocks allowing for temperature monitoring in the centre of the blocks during processing, i.e. rolling and cooling. The simulation of slow air-cooling in thick plate required a cooling rate of 0.5°C/s and this was achieved by covering the plate with two slices of refractory wool. Accelerated cooling, with an aim rate of 10°C/s, was obtained using a horizontal cooling table equipped with a sledge for passing the steel plate through a 4 m long array of water nozzles on bottom and topside. The water supply was stopped automatically when the temperature measured by the thermocouple reached the pre-defined stop cooling temperature. Due to a certain reaction time of the installation and due to the always slightly different position of the thermocouple with respect to the steel surface, the stop cooling temperature varied slightly from plate to plate. In order to be able to obtain a very narrow range of stop cooling temperatures it was decided to use a set temperature of 600°C and this resulted in a range of stop cooling temperatures between about 580ºC and 600°C.

Table 11 gives an overview of all plates processed and their designations. In the samples identified as E, 8 casts were processed after reheating to a higher temperature than planned, 1250°C, and the spare block from these casts was processed from the planned reheating temperature of 1200°C in the plates identified as code I.

The cooling conditions achieved for each plate were recorded and are summarised in Table 12 through to Table 16.

Table 11: Listing of plates rolled and their designation

Stage	Run	Cast	Rolling								
		No.	Dilatometry / Torsion 15 (mm)	Weld 12 (mm)	RR=2 AC	RR=4 AC	RR=2 ACC	RR=2 1250°C ACC	RR=4 ACC	RR=2 ACC+ coiling	RR=4 ACC+ coiling
1	1	A027	A	B	C	D	I	E	F	G	H
	2	A028	A	B	C	D	I	E	F	G	H
	3	A029	A	B	C	D	I	E	F	G	H
	4	A030	A	B	C	D	E		F	G	H
	5	A031	A	B	C	D	E		F	G	H
	6	A032	A	B	C	D	E			G	H
	7	A033	A	B	C	D	I	E	F	G	H
	8	A034	A	B	C	D	E		F	G	H
	9	A035	A	B	C	D	I	E	F	G	H
	10	A036	A	B	C	D	E		F	G	H
	11	A037	A	B	C	D	E		F	G	H
	12	A038	A	B	C	D	I	E	F	G	H
	13	A202	A	B	C	D	E		F	G	H
	14	A203	A	B	C	D	E		F	G	H
	15	A041	A	B	C	D	E		F	G	H
	16	A042	A	B	C	D	E		F	G	H
2	1	A043	A	B	C	D	E		F	G	H
	2	A044	A	B	C	D	I	E	F	G	H
	3	A045	A	B	C	D	E		F	G	H
	4	A046	A	B	C	D	E		F	G	H
3	1	A047	A	B	C	D	E		F	G	H
	2	A048	A	B	C	D	E		F	G	H
	3	A049	A	B	C	D	E		F	G	H
	4	A050	A	B	C	D	I	E	F	G	H
additional		A039	A	B	C	D	E		F	G	H
		A040	A	B	C	D	E		F	G	H
industrial		81351	14 (A)		15 (C)	10 (D)	16 (E)		13 (F)	17 (G)	11 (H)
		02098			F (C)		G (E)		E (F)	A,B (G)	D (H)
		16685	A	B	C	D	E		F	G	H
		81913	A	J (B)	C	D	E		F	G	H

The value of *T*-fc was the finish cooling temperature and, as the embedded thermocouple was not always in the middle of the plate, the thermocouple sometimes measured an increase in temperature after the water-cooling was stopped. In these cases the value of *T*-fc after recovery of this temperature was recorded.

Table 12: Temperatures during processing RR = 2 and ACC

Cast	Code	*T*-reheat (°C)	*T*-start cooling (°C)	cooling rate (°C/s)	*T*-fc (°C)	*T*-fc incl. reheat (°C)	CT (°C)
A027	I	1200	799	8.3	589	-	-
A028	I	1200	806	11.3	563	-	-
A029	I	1200	799	6.4	588	-	-
A030	E	1200	802	8.3	598	-	-
A031	E	1200	801	7.3	623	-	-
A032	E	1200	777	10.8	591	-	-
A033	I	1200	795	8.8	581	-	-
A034	E	1200	804	8.8	591	-	-
A035	I	1200	775	13.1	528	-	-
A036	E	1200	783	10.1	592	-	-
A037	E	1200	799	8.9	597	-	-
A038	I	1200	806	11.9	596	-	-
A039	E	1200	803	8.9	595	-	-
A202	E	1200	778	12.4	571	-	-
A040	E	1200	805	15.3	566	569	-
A203	E	1200	795	12.2	586	-	-
A041	E	1200	804	10.1	599	-	-
A042	E	1200	803	12.1	576	-	-
A043	E	1200	805	10	589	591	-
A044	I	1200	801	10.4	582	585	-
A045	E	1200	803	14.3	575	580	-
A046	E	1200	801	15.9	578	587	-
A047	E	1200	792	11.2	591	-	-
A048	E	1200	802	11.4	577	589	-
A049	E	1200	800	9.8	591	-	-
A050	I	1200	800	14.4	579	587	-
81351	E	1200	800	10.1	586	-	-
02098	E	1200	800	12.6	569	573	-
16685	E	1200	806	16.3	565	577	-
81913	E	1200	808	9.7	583	-	-

Table 13: Temperatures during processing RR = 2 and ACC; T-reheat of 1250°C

Cast	Code	*T*-reheat (°C)	*T*-start cooling (°C)	cooling rate (°C/s)	*T*-fc (°C)	*T*-fc incl. reheat (°C)	CT (°C)
A027	E	1250	797	13.5	528	-	-
A028	E	1250	799	10.3	582	-	-
A029	E	1250	798	16.9	566	598	-
A033	E	1250	786	11.1	545	-	-
A035	E	1250	800	11.2	578	-	-
A038	E	1250	-	-	-	-	-
A044	E	1250	779	16.3	506	-	-
A050	E	1250	803	10.8	581	589	-

Table 14: Temperatures during processing RR = 4 and ACC

Cast	Code	T-reheat (°C)	T-start cooling (°C)	cooling rate (°C/s)	T-fc (°C)	T-fc incl. reheat (°C)	CT (°C)
A027	F	1200	797	6.1	592	-	-
A028	F	1200	791	5.1	589	-	-
A029	F	1200	791	5.7	583	-	-
A030	F	1200	792	6.6	588	-	-
A031	F	1200	777	5.4	609	-	-
A032	F	1200	-	-	-	-	-
A033	F	1200	782	7.8	585	-	-
A034	F	1200	793	7	592	-	-
A035	F	1200	799	14.9	579	596	-
A036	F	1200	801	9.5	590		-
A037	F	1200	801	11.7	586	588	-
A038	F	1200	793	9.5	578	-	-
A039	F	1200	799	9.2	571	575	-
A202	F	1200	808	10.2	577	-	-
A040	F	1200	810	12.1	568	575	-
A203	F	1200	812	9	611	-	-
A041	F	1200	803	14.2	579	589	-
A042	F	1200	794	11.2	587	-	-
A043	F	1200	796	5.7	586	-	-
A044	F	1200	784	7.7	579	-	-
A045	F	1200	787	8	593	596	-
A046	F	1200	813	10.1	583		-
A047	F	1200	794	12.2	587		-
A048	F	1200	807	17.8	567	582	-
A049	F	1200	806	9.1	561	-	-
A050	F	1200	792	8.9	577	-	-
81351	F	1200	785	7.5	600	-	-
02098	F	1200	799	7	601	-	-
16685	F	1200	777	7.4	583	-	-
81913	F	1200	785	11.3	549	-	-

Table 15: Temperatures during processing RR = 2 and ACC+coiling

Cast	Code	T-reheat (°C)	T-start cooling (°C)	cooling rate (°C/s)	T-fc (°C)	T-fc incl. reheat (°C)	CT (°C)
A027	G	1200	800	8.4	582	592	550
A028	G	1200	807	8.9	589	-	550
A029	G	1200	804	6.3	593	-	550
A030	G	1200	810	12.7	578	-	550
A031	G	1200	791	10.6	576	579	550
A032	G	1200	803	8.8	583	-	550
A033	G	1200	806	7	593	-	550
A034	G	1200	815	8.3	588	-	550
A035	G	1200	806	8.1	533	-	550
A036	G	1200	803	10.3	591	-	550
A037	G	1200	-	-	-	-	550
A038	G	1200	806	10.5	584	-	550
A039	G	1200	804	7.8	590	-	550
A202	G	1200	802	9.2	602	-	550
A040	G	1200	809	13.2	572	-	550
A203	G	1200	798	13.9	586	601	550
A041	G	1200	811	10.5	596	-	550
A042	G	1200	806	14.3	569	-	550
A043	G	1200	806	10.7	594	603	550
A044	G	1200	808	10	602	607	550
A045	G	1200	806	11.1	585	-	550
A046	G	1200	807	10.4	582	583	550
A047	G	1200	768	10	584	-	550
A048	G	1200	810	9.5	583	594	550
A049	G	1200	786	10.8	572	-	550
A050	G	1200	793	9.3	582	-	550
81351	G	1200	811	11.5	589	-	550
02098	GA	1200	800	9.9	577	-	550
02098	GB	1200	803	5.8	591	-	550
16685	G	1200	803	7.7	634	-	550
81913	G	1200	748	13.1	584	581	550

Table 16: Temperatures during processing RR = 4 and ACC+coiling

Cast	Code	T-reheat (°C)	T-start cooling (°C)	cooling rate (°C/s)	T-fc (°C)	T-fc incl. reheat (°C)	CT (°C)
A027	H	1200	788	9.1	594	597	550
A028	H	1200	792	5.6	602		550
A029	H	1200	799	8.8	570		550
A030	H	1200	790	10.5	589	623	550
A031	H	1200	812	12.4	555	577	550
A032	H	1200	790	9.4	602		550
A033	H	1200	806	9.6	584		550
A034	H	1200	782	11.2	565		550
A035	H	1200	803	7.3	582		550
A036	H	1200	808	10.4	583		550
A037	H	1200	791	9.9	584		550
A038	H	1200	815	10.6	569		550
A039	H	1200	808	8.5	591		550
A202	H	1200	795	8.1	629		550
A040	H	1200	804	15.2	585	618	550
A203	H	1200	795	9.8	582		550
A041	H	1200	798	11	583	586	550
A042	H	1200	814	14.1	573	574	550
A043	H	1200	804	11	573		550
A044	H	1200	815	11.2	548		550
A045	H	1200	779	9	582	584	550
A046	H	1200	762	10.2	580	585	550
A047	H	1200	804	9.9	586	601	550
A048	H	1200	792	12.9	585		550
A049	H	1200	805	10.5	583		550
A050	H	1200	795	10.4	584	588	550
81351	H	1200	801	11.7	550		550
02098	H	1200	801	6.9	586		550
16685	H	1200	789	6.1	602		550
81913	H	1200	799	6.5	618		550

The realisation of the accelerated cooling (ACC) was very satisfactory. The average cooling rate was 10.2°C/s with a spread between 5.1 and 17.8°C/s, Figure 2. The average finish cooling temperature T-fc was 582°C with a spread between 506 and 634°C. The majority of the T-fc values fell in the range between 570 to 600°C, Figure 3. Only 10% of the plates had T-fc values higher than 610°C or lower than 560°C. The respective data sets are listed in Table 17.

The cooling rate during the air cooling simulation (AC) was estimated to be 0.5°C/s through the range 850 – 550°C and 0.08°C/s below 550°C; these values were based on readings from two long term data loggers on plates 81351-10 (C) and 81351-15 (D) where the reading time was about two hours.

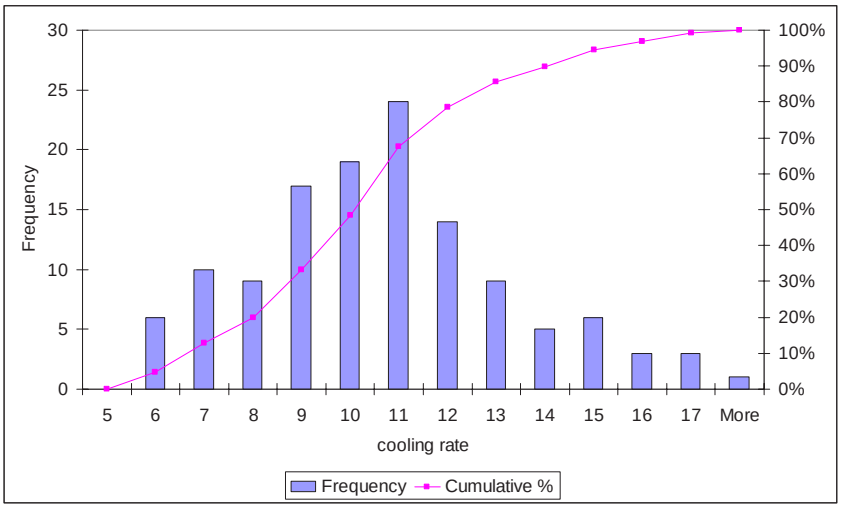

Figure 2: Histogram and cumulative percentage of the cooling rates achieved

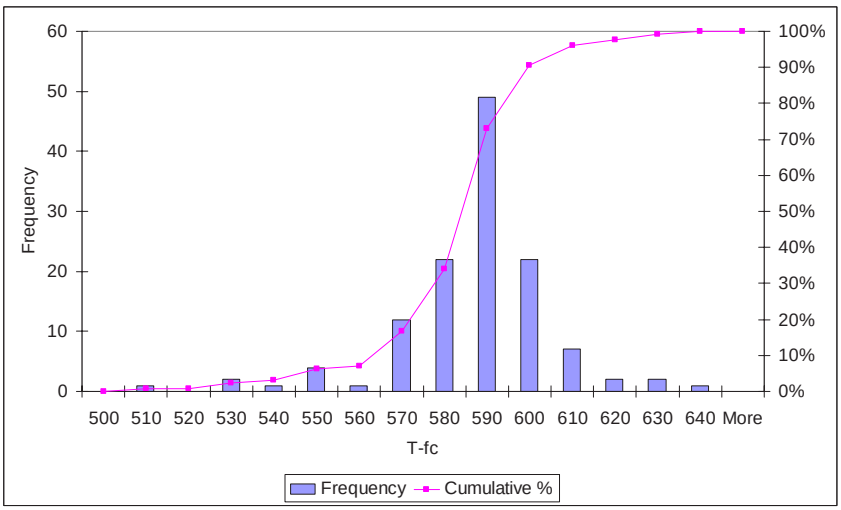

Figure 3: Histogram and cumulative percentage of the T-fc values achieved

Table 17: Plates with T-fc outside the range 560 to 610°C

Cast	Code	T-reheat (°C)	T-start cooling (°C)	cooling rate (°C/s)	T-fc (°C)	T-fc incl. reheat (°C)	CT (°C)
A044	E	1250	779	16.3	506	-	-
A035	I	1200	775	13.1	528	-	-
A027	E	1250	797	13.5	528	-	-
A035	G	1200	806	8.1	533	-	550
A033	E	1250	786	11.1	545	-	-
A044	H	1200	815	11.2	548		550
81913	F	1200	785	11.3	549	-	-
81351	H	1200	801	11.7	550		550
A031	H	1200	812	12.4	555	577	550
81913	H	1200	799	6.5	618		550
A031	E	1200	801	7.3	623	-	-
A202	H	1200	795	8.1	629		550
16685	G	1200	803	7.7	634	-	550

6.1.3.4 Sampling

All lab rolled plates were cut at OCAS by means of water-jet cutting and sawing. The initial sampling schedule is shown schematically in Figure 4; it concerns 2 transverse tensile specimens and about 16 transverse Charpy samples. However, only bars were cut (dotted lines) and sent to the partners, at Aachen and Maribor, where the samples were finished. Maribor used a smaller round bar tensile specimen and was able to take two or more samples from each delivered bar.

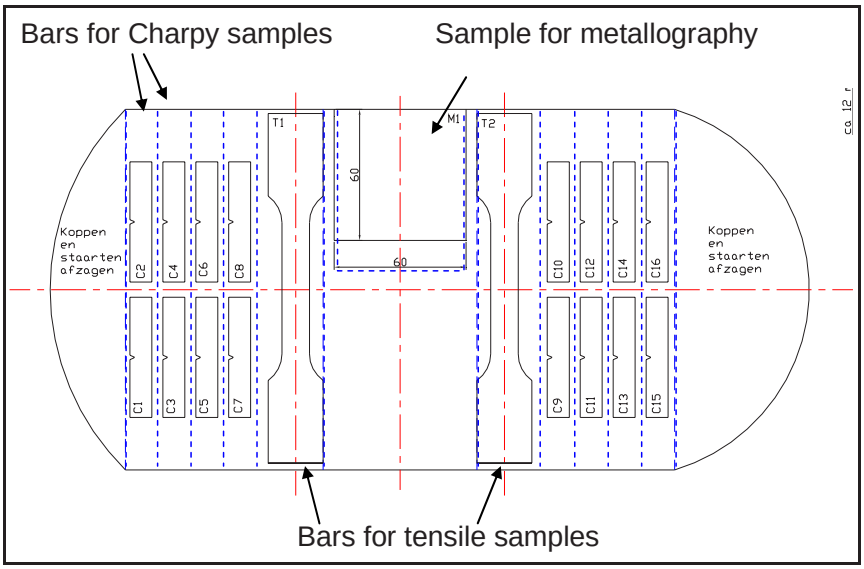

Figure 4: Sampling schedule for cutting

6.1.4 Metallography

Metallographic investigations were carried out on all the plate conditions. The accelerated cooled samples, E, F, G, and H, were examined to identify the multiphase microstructures by means of colour etchings. For the sake of completeness, the Nital etchings were repeated for imaging with magnifications 200x (overview) and 1000x (detail), respectively. The magnification for the colour etchings was always 1000x. The microstructures were examined at the quarter thickness of the plates.
After grinding and polishing of mounted samples, etching was performed as follows:

Etching with Nital 2 % for 10 seconds; this etchant was used to reveal the banded structure, and the grain boundaries and carbide containing phases.

After repolishing, etching with Le Péra reagent for 20 seconds was used to show up bainite, cementite and/or pearlite which appear dark and martensite and/or austenite which appear white.

After repolishing, etching with Picral 4% for 30 seconds followed by sodium bisulphite 10% for 7 seconds colours cementite, bainite and/or pearlite dark, while martensite colours a light brown and austenite white.

After repolishing, etching with sodium metabisulphite 10 % for 5 seconds and Klemm's reagent for 60 seconds causes the austenite to appear white. As an example, the microstructures seen in the F condition, which was accelerated cooled with a reduction ratio of 4, for steel A035 are shown in Figure 5.

A qualitative description of the microstructures is given in Table 18 through Table 22. As generally known, the low-carbon bainitic microstructures are often complex consisting of several phases with different crystallography, morphology and chemical composition. An attempt was made to apply the classification system proposed by the Bainite committee of ISIJ, [5] which recognises the following five morphologies:

- Polygonal ferrite (PF)
- Quasi-polygonal ferrite (QF)
- Widmanstätten ferrite (WF)
- Granular bainitic ferrite (GB)
- Bainitic ferrite (BF)

A quantitative evaluation of the amounts of second phases (austenite, A, and martensite, M) was not performed; the results are therefore only indicative. In the following tables, Table 18 through Table 22, the presence of the respective bainite morphologies and second phases is indicated. The letter P indicates the predominance of the specific bainite morphology and S indicates a notably large volume fraction of the identified second phase.

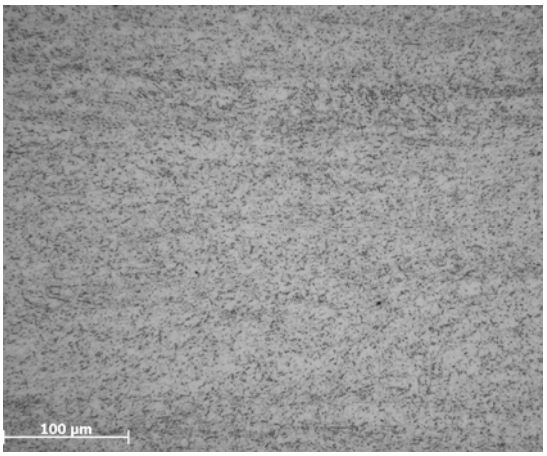

Overview sample etched in Nital

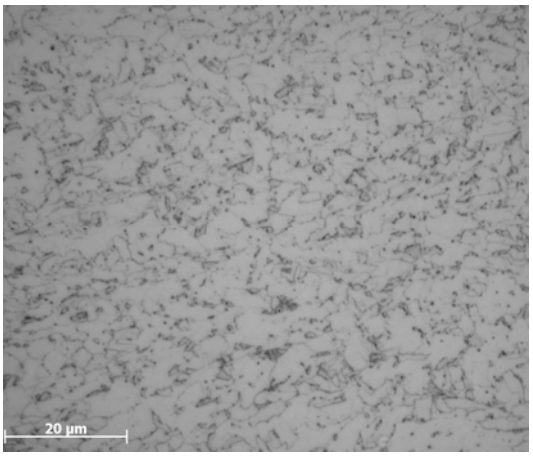

Detail sample etched in Nital

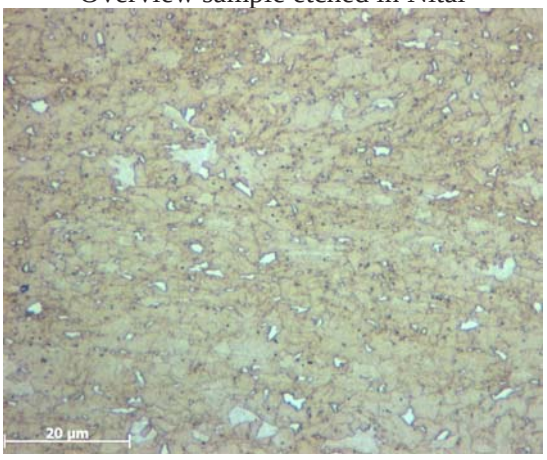

Le Pera

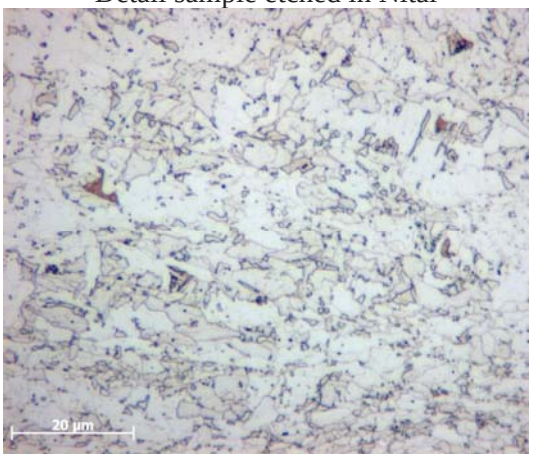

Picral+Sodiumbisulphite

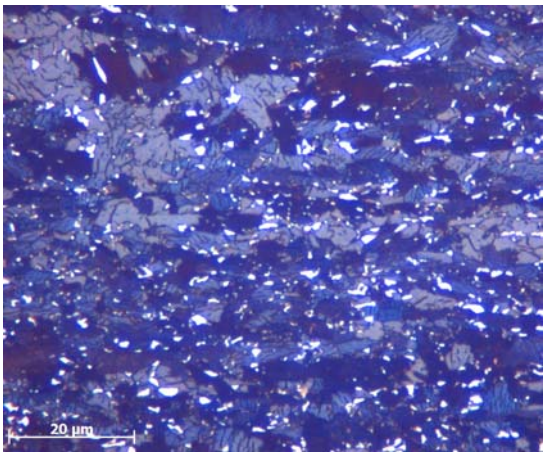

Sodiumbisulphite+Klemm's

Figure 5: Micrographs with different etchants in steel A035 for the F condition

Table 18: Description of microstructures, Stage 1

Cast/type	Code	PF	QF	GB	BF	A	M	No MA	Remark
A027 Cu	I								not investigated
	E		P	S		S			
	F	P	S			S			
	G		P	S	S			S	
	H		P					S	
A028 Ni	I								not investigated
	E		P	S	S	S	S		
	F		P			S	S		
	G		S	P	S			S	
	H		S	P				S	
A029 Mo	I								not investigated
	E	S	P			P	S		
	F	S	P		S	S			C-enriched phases in bands
	G		P	P		S			
	H	S	P		S			S	C-enriched phases in bands
A030 NiMoCu	E			P	S	S	S		
	F			P		S	S		
	G		P	S	S	S	S		
	H		S	P				S	
A031 Cr	E		S	P		P			
	F		S	P		P	S		
	G			S	P	P			
	H			P				S	
A032 NiCuCr	E			P	S	S	S		
	F								not processed
	G			P	S	S	S		
	H			P		few		~ S	
A033 MoCuCr	I								not investigated
	E			P	P	S			
	F		S	P		S			
	G		S	P		S	few		
	H		S	P		few			
A034 MoNiCr	E			P			P		
	F			P		S	P		
	G		S	P			P		
	H		S	P				S	
A035 Mn	I								not investigated
	E			P	S	P	S		
	F			P		P	S		
	G		S	P		few		~ S	
	H		S	P	S	S			
A036 MnNiCu	E		P	S		P	few		
	F		P			P			
	G		P			S			
	H		P		S	few		~ S	
A037 MnMoCu	E			P		P	P		
	F			P		S	P		
	G			P			P		

Cast/type	Code	PF	QF	GB	BF	A	M	No MA	Remark
	H			P		S			
A038 MnNiMo	I								not investigated
	E		S	P		S			
	F		S	P	S	S	S		
	G			P	S		S		
	H			P				S	
A202 MnCuCr	E			P	S	S			
	F			P		S	S		
	G			P		S	P		
	H			P	S	S	S		
A203 MnNiCr	E			P	S		P		
	F		S	P			P		
	G		S	P			P		
	H		S	P				S	
A041 MnMoCr	E			P	S	S	P		
	F			P	S		P		
	G			P	S		P		
	H			P			P		
A042 MnNiMoCuCr	E			P	P		P		
	F			P			P		
	G			P	S		P		
	H			P	S				

Table 19: Description of microstructures, Stage 2

Cast/type	Code	PF	QF	GB	BF	A	M	no MA	Remark
A043 lowC-lowNb	E		P	S	S	S			
	F		P	S			P		
	G		P	P			P		
	H		P						
A044 lowC-highNb	I								not investigated
	E		S	P	S	S			
	F		S	P			S		
	G		S	P			S		
	H			P				P	
A045 highC-lowNb	E			S	P	P	P		
	F			P	S	P	P		
	G			P	P	S			
	H			P		S			
A046 highC-highNb	E	S	P			S	P		
	F			P		S	P		
	G			P	P	S		S	
	H			P		S		S	

Table 20: Description of microstructures, stage 3

Cast/type	Code	PF	QF	GB	BF	A	M	no MA	Remark
A047 lowTi-lowB	E			P	S	S	P		
	F			P		S	S		
	G			P	S		P		
	H			P	S		P		
A048 lowTi-highB	E			P	S	S	P		
	F			P	S	S	P		
	G			P	S		P		
	H			P	S		S		
A049 highTi-lowB	E			P	S	S	S		
	F			P		S	S		
	G			P	S		S		
	H			P			S		
A050 highTi-highB	I								not investigated
	E			P	S	S	P		
	F			P	S		P		
	G			P	S		P		
	H			P	P	S	S		

Table 21: Description of microstructures, additional lab casts

Cast/type	Code	PF	QF	GB	BF	A	M	no MA	Remark
A039 C-MnCuCr	E			P	S	P	P		
	F			P	S	S	S		
	G			P	S	S	P		
	H			P	S			S	
A040 C-MnNiCr	E			P	S	S	P		
	F			P		S	P		
	G			P	S	S	P		
	H			P	S		P		

Table 22: Description of microstructures, industrial casts

Cast/type	Code	PF	QF	GB	BF	A	M	no MA	Remark
16685 Cr	E		S	P		S	S		
	F		S	P		P	S		
	G			P		S	S		
	H			P				S	
81913 NiCuCr	E		S	P		S			
	F		S	P		S			
	G		S	P		few			upper bainite/pearlite
	H		S	P				S	

6.1.5 Electron back-scattered diffraction, EBSD

6.1.5.1 Experimental method and results

Detailed microstructural information, at the scale of bainitic microstructures, was obtained using EBSD technique. EBSD is a tool that can quantify the misorientation between grains. The number and nature of boundaries in the microstructure obtained by EBSD mapping can be used to distinguish between

different phases. Clear differences are noted between ferrite and bainite. Ferrite has very few boundaries with low misorientation; in contrast with bainite, which contains a high proportion of low angle misorientations. Bainite characteristically forms with a high dislocation compared with allotriomorphic ferrite and thus a term for this strengthening is often incorporated. The bainite laths, separated by low misorientation angle boundaries, are arranged in packet or colonies, separated by high angle boundaries.

The samples for Electron Back-Scattered Diffraction (EBSD) observations were prepared from rolling-schedule samples of each different cast, taking into account the rolling direction. All the scans were obtained at the quarter plate thickness position. EBSD observations were carried out on a Philips XL30cp Scanning Electron Microscope (SEM). The EBSD specimen was tilted 75º from the horizontal, so that the surface was normal to the electron beam. The step size was 0.4 microns and scan size was 160 × 100 microns. Approximately 500 grains were examined in each scan.

TSL OIM Analysis 4.6 software was used to interpret the data. Pattern indexing is quite effective at identifying the orientation from a diffraction pattern, mainly in the samples with ferritic microstructure, but pattern indexing of orientations as at grain boundaries (where the patterns often are made up of two superposed diffraction patterns, from both crystal lattices separated by the grain boundary) are difficult. The grain size was determined with threshold misorientations of 4° and 15°, leading to the response variables d_{4^o} and d_{15^o}, respectively in Table 23.

Table 23: Grain size d_{4^o} and d_{15^o} of all plates

Stage	Run	Cast	Type	Mean grain size d_{4^o} and d_{15^o}, microns											
				C		D		E		F		G		H	
				4°	15°	4°	15°	4°	15°	4°	15°	4°	15°	4°	15°
1	1	A027	Cu	5.0	5.4	3.1	3.4	2.3	3.1	2.4	3.0	3.0	4.3	2.4	2.9
	2	A028	Ni	4.0	4.6	3.2	3.5	3.0	4.7	2.3	2.8	2.8	3.7	2.2	2.8
	3	A029	Mo	5.6	6.6	4.2	5.1	4.1	5.5	3.0	4.0	3.8	5.9	3.2	4.3
	4	A030	NiMoCu	3.0	3.5	3.2	3.6	3.0	4.8	2.1	2.8	2.2	3.3	2.2	3.4
	5	A031	Cr	4.1	4.7	3.0	3.6	2.9	4.3	2.6	3.1	3.0	4.3	2.4	2.9
	6	A032	NiCuCr	3.8	4.4	3.3	3.9	2.6	4.8			3.1	4.9	2.3	3.4
	7	A033	MoCuCr	3.8	4.4	3.4	3.9	2.9	5.8	2.3	3.9	3.0	4.9	2.0	2.9
	8	A034	MoNiCr	4.0	4.7	3.2	3.6	3.4	5.7	2.2	3.4	2.5	4.2	1.7	2.5
	9	A035	Mn	4.5	5.3	3.2	3.6	3.0	5.0	2.6	3.8	2.8	4.2	2.3	3.1
	10	A036	MnNiCu	4.0	4.7	3.1	3.5	3.1	5.3	2.0	2.8	2.7	4.4	1.9	2.7
	11	A037	MnMoCu	3.9	4.9	2.9	3.4	2.4	4.6	2.0	3.1	2.4	4.5	1.8	3.1
	12	A038	MnNiMo	3.3	4.9	2.7	3.2	3.4	7.1	2.5	4.5	2.7	4.9	1.9	3.2
	13	A202	MnCuCr	4.8	6.0	4.2	4.9	2.5	4.4	2.1	3.3	4.0	7.7	2.4	4.5
	14	A203	MnNiCr	5.2	7.7	3.9	4.4	3.6	6.4	3.1	5.1	4.4	7.5	2.9	4.4
	15	A041	MnMoCr	4.1	5.5	3.6	4.3	3.0	5.7	2.3	4.3	2.3	4.7	2.0	3.3
	16	A042	MnNiMoCuCr	2.9	5.4	2.9	6.0	3.3	6.7	2.3	4.7	2.8	6.0	2.2	4.6
2	17	A043	lowC-lowNb	5.4	6.0	3.9	4.4	4.2	7.1	2.8	3.7	3.8	5.8	2.5	3.6
	18	A044	lowC-highNb	4.1	4.8	3.1	3.5	2.7	4.9	2.5	3.9	3.4	5.9	2.3	3.2
	19	A045	highC-lowNb	4.7	6.4	3.7	4.4	2.6	5.0	2.2	3.6	2.7	5.0	2.2	3.2
	20	A046	highC-highNb	3.7	5.6	3.7	7.1	3.6	6.5	2.2	4.2	2.5	4.5	2.0	3.8
3	21	A047	lowTi-lowB	3.5	4.2	3.1	3.6	3.0	5.7	2.0	3.0	3.3	6.6	2.5	3.9
	22	A048	lowTi-highB	3.4	6.5	2.4	3.9	3.0	6.1	2.4	5.4	3.2	7.1	1.7	2.9
	23	A049	highTi-lowB	4.8	5.4	3.3	3.8	3.0	5.0	2.3	3.6	3.5	6.6	2.2	3.2

Stage	Run	Cast	Type	Mean grain size d_{4^o} and d_{15^o}, microns											
				C		D		E		F		G		H	
				4°	15°	4°	15°	4°	15°	4°	15°	4°	15°	4°	15°
	24	A050	highTi-highB	3.6	6.2	3.6	6.1	3.6	7.5	3.0	6.4	2.9	6.0	2.0	4.1
Additional		A039	C-MnCuCr	3.9	4.7	2.9	3.4	2.7	4.3	1.8	2.6	2.2	3.4	1.8	2.7
		A040	C-MnNiCr	3.6	4.8	2.8	3.3	2.4	4.0	1.8	2.8	2.3	3.9	2.0	2.6
Industrial		81351	MnNiCu-1Cr	4.0	4.5	3.1	3.6	2.5	4.1	2.0	2.7	2.8	4.8	2.0	2.8
		02098	Nb-V	5.2	5.7			3.6	5.0	3.0	3.9	4.0	5.3	2.8	3.3
		16685	Cr	4.6	5.3	3.5	3.9	3.4	4.8	2.8	3.9	3.3	4.7	2.2	3.2
		81913	NiCuCr	4.4	4.9	4.0	4.5	2.9	4.1	2.5	4.0	3.2	4.4	2.8	4.0

To estimate the strengthening due to grain size, boundaries with misorientations greater than 4º are used, and misorientation greater than 15º to quantify bainitic packets in relation with toughness.

The EBSD data clearly indicate that the change from ferrite to bainite alters the proportion of low and high angle grain boundaries. As shown in Figure 6, the low angle/lath boundaries dominate the microstructure of bainite while the microstructure of ferrite is composed of grains with high angle boundaries. These characteristic misorientation distributions allow ferritic and bainitic types of microstructure to be identified.

The ratio between average grain sizes of large angle (d_{15}) and low angle (d_4) grains was found to describe well the type of microstructure, the ratio d_{15}/d_4 being ~1 for ferrite and >>1 for bainite, respectively, compare Figure 7. The analysis of the EBSD data will be the subject of a PhD thesis from CEIT.

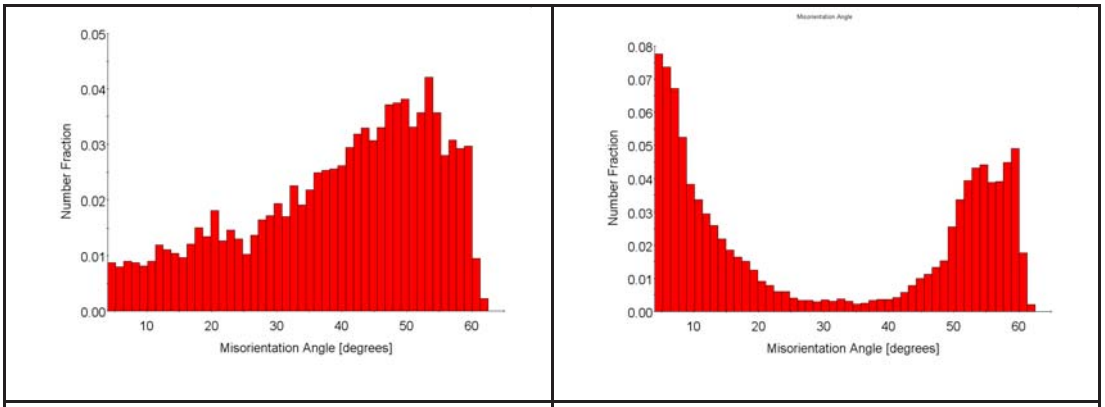

Typical distribution of ferrite | Typical distribution of bainite

Figure 6: Misorientation Angle Maps

The proportion of low angle misorientations (4º-15º) can be quantified by means of the d_{15^o}/d_{4^o} ratio, see Figure 7. This ratio is characteristic of each phase. For instance, the ferritic microstructure shows a ratio $d_{15^o}/d_{4^o} < 1.25$, with a characteristic value of 1.125. In the case of bainitic microstructure, the lower limit and characteristic ratio d_{15^o}/d_{4^o} are 1.6 and 1.9, respectively. Moreover, there are several samples which present a mixture of ferrite and bainite (sometimes it is hard, even with EBSD maps, to differentiate the type of microstructure). Such microstructures present the following limit ratios: $1.25 < d_{15^o}/d_{4^o} < 1.6$.

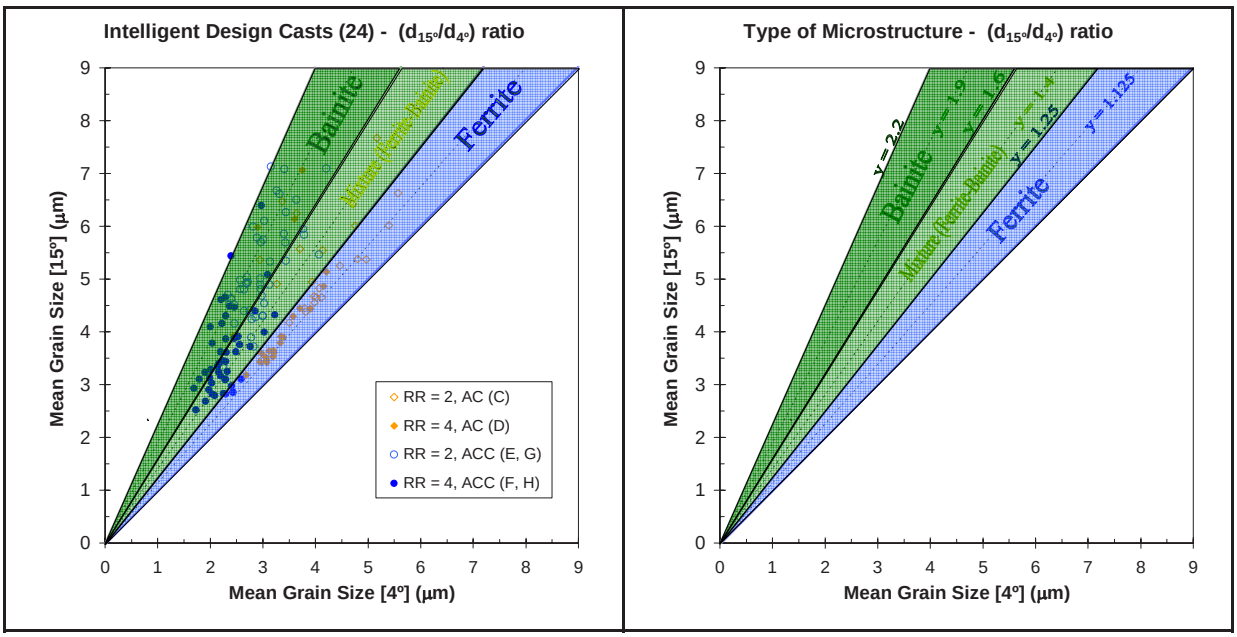

Figure 7: Microstructures as a function of $d_{15°}/d_{4°}$ ratio

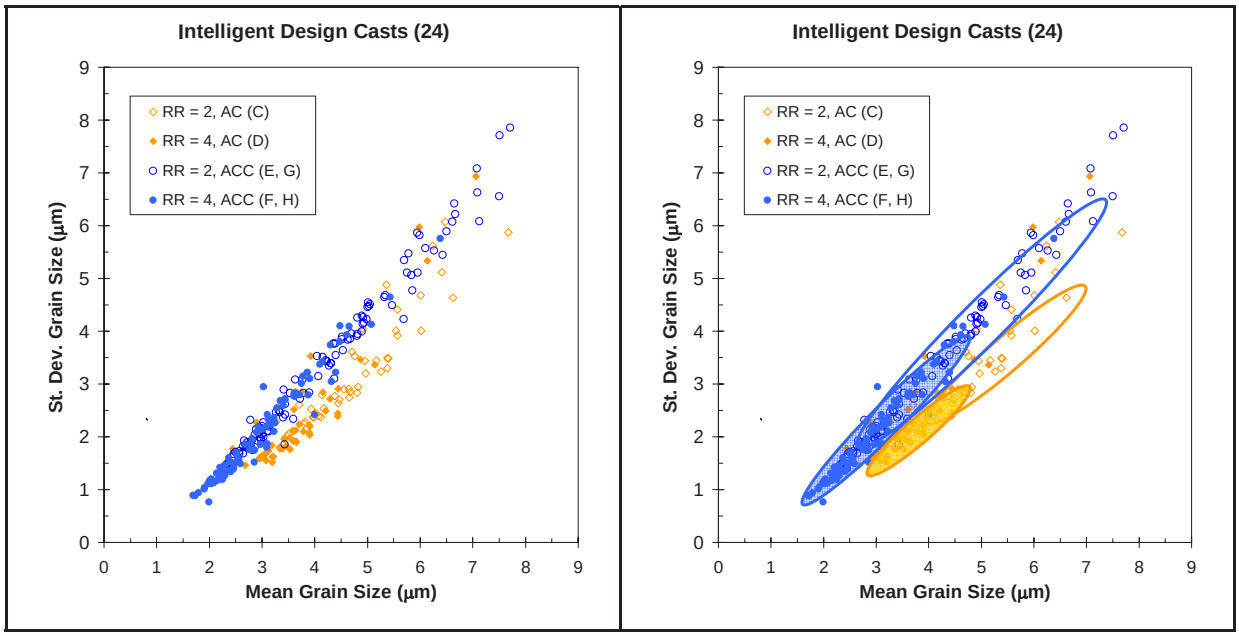

Figure 8: Standard Deviation vs. Mean Grain Sizes for the 24 Designed Casts

The rolling schedule parameters of reduction ratio and type of cooling (AC or ACC) showed a strong effect on the final microstructure, as shown in Figure 7 and Figure 8. Such conclusions will be confirmed by the response equations of multiple regressions. Note that ACC denotes *CR*1 ($CR_{800\text{-}550°C}$).

Figure 8 shows how each schedule is located in specific areas. These areas have been represented by means of ellipses. The ellipse size is a function of the dispersion in results, but mainly it is a function of the difference between measurements of $d_{4°}$ and $d_{15°}$. The measurement for 4° is smaller than for 15° of misorientation and the measurements of 4° are located to the left and lower than the values for 15°. The larger difference between these measurements, the more is the tendency towards bainitic microstructures ($d_{15°}/d_{4°} >> 1$).

If the ellipses which represent *RR* = 4 are compared with those for *RR* = 2, in Figure 8 (closed symbol ellipses vs. open symbol ellipses), the ellipses for *RR* = 4 show smaller grain sizes. It is well established

that the amount of rolling reduction below T_{nr} has a strong influence on the final microstructure by reducing the prior austenite grain size (d_γ) and by increasing the accumulated strain (ε_{acc}) before transformation, thus decreasing the final grain size [6], [7]

Comparing Air Cooling (AC) with. ACcelerated Cooling (ACC), it is possible to draw conclusions based on differences between measurements of d_{4^o} and d_{15^o}: The ellipses for AC (orange ellipses) are smaller than those ellipses corresponding to ACC (blue ellipses). It is possible to conclude that accelerated cooling (ACC) promotes bainitic microstructures and also has a refining effect on d_{4^o}. Accelerated Cooling schedules (ACC: E, F, G and H) resulted in smaller grain sizes when compared to Air Cooling schedules (AC: C & D), when the same reduction rate was considered, see Figure 8.

The main conclusions drawn from the analysis of the EBSD data were:

The amount of reduction below T_{nr} had a strong influence in the final microstructure by reducing the final grain size of both d_{4^o} and d_{15^o}.

ACC promoted bainitic microstructures and refined the microstructure, Figure 9, but, when ACC was applied with RR = 4, ferritic microstructures were promoted due to an additive effect of accumulated strain (ε_{acc}), specific grain boundary area (S_v) and prior austenite grain size (D_γ) with accelerated cooling (ACC) favouring a higher density of nucleation sites [8],[9].

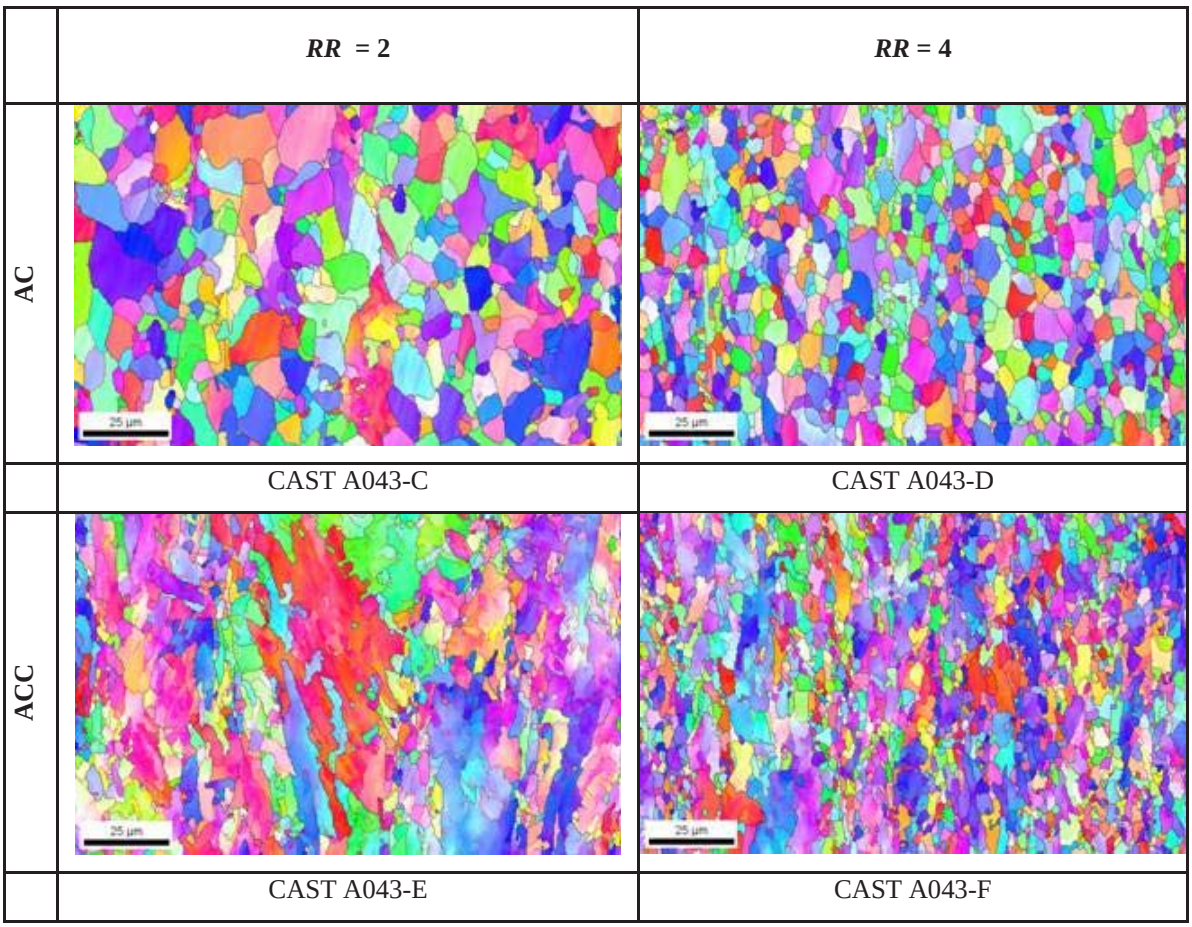

Figure 9: Inverse Pole Figures

The other rolling parameters ($CR_{550\text{-}20^oC}$, T_{FC}) and the chemical composition showed a weaker effect, even negligible in some cases, on the final microstructure; the effects were not as obvious as that of the reduction ratio and the cooling rate between 800 - 500^{o}C, $CR_{800\text{-}550\ ^oC}$. To quantify such effects multiple regression statistics have been used.

6.1.5.2 Regression analysis

The coefficients and significances of the factors, Table 24, showed their effects on the two measures of grain size (d_{4^o} and d_{15^o}); C, Nb, Mo, Cu, *RR* and *CR*1 reduced d_{4^o}, and Nb, Mn, Cu and *RR* reduced d_{15^o} while B, Cr and *CR*2 increased d_{15^o}. Only Nb and Cu refined both grain sizes. The effects of *RR* and *CR*1, mentioned previously, were very significant.

Table 24: Coefficients, Standard Errors and Significances of variables for the grain size measurements at 4° and 15° angle misorientation

MEAN 4° (24 casts)	Autofit			R^2_{adj} max			Regress, R^2max		
Term	Coefficient	Std Error	Significance	Coefficient	Std Error	Significance	Coefficient	Std Error	Significance
B							-55.070	56.160	0.329
C	-7.014	3.011	0.02123	-6.845	2.996	0.02382	-6.979	3.038	0.02311
Ti							-6.920	11.800	0.558
Nb	-6.121	1.986	0.00247	-6.252	1.979	0.00193	-5.918	2.184	0.00759
log *CR*1	-0.807	0.061	1.58E-26	-0.806	0.061	1.21E-26	-0.817	0.087	1.72E-16
Mo	-0.653	0.276	0.01922	-0.667	0.274	0.0161	-0.673	0.290	0.02167
Cu	-0.479	0.185	0.01048	-0.508	0.184	0.00646	-0.483	0.189	0.01157
RR	-0.386	0.037	5.38E-19	-0.387	0.037	3.30E-19	-0.388	0.038	9.34E-19
Ni				-0.265	0.201	0.19	-0.274	0.204	0.181
Constant	5.809	0.304	2.88E-41	5.814	0.304	3.95E-41	4.570	1.410	0.0015
T_{FC} (°C)							0.002	0.002	0.402
log *CR*2							0.066	0.061	0.281
Mn							0.137	0.167	0.413
Cr				0.304	0.188	0.109	0.318	0.199	0.112

MEAN 15° (24 casts)	Autofit			R^2_{adj} max			Regress, R^2 max		
Term	Coefficient	Std Error	Significance	Coefficient	Std Error	Significance	Coefficient	Std Error	Significance
Ti							-7.906	21.700	0.717
Nb	-6.754	3.495	0.05528	-7.068	3.493	0.0444	-6.713	4.032	0.09817
C							-1.148	5.608	0.838
RR	-0.755	0.068	6.24E-21	-0.771	0.069	2.86E-21	-0.772	0.070	9.23E-21
Cu	-0.566	0.341	0.099073	-0.592	0.340	0.08419	-0.573	0.349	0.103
log *CR*1				-0.254	0.158	1.09E-01	-0.260	0.161	1.08E-01
Constant	5.049	0.638	6.27E-13	1.696	2.550	5.07E-01	1.586	2.604	0.543
Ni							0.006	0.376	0.987
T_{FC} (°C)				0.006	0.004	0.175	0.006	0.005	0.17
Mo							0.166	0.535	0.756
log *CR2*	0.218	0.098	0.02738	0.179	0.110	0.108	0.179	0.112	0.113
Cr	1.220	0.346	0.000559	1.157	0.347	0.00109	1.185	0.367	0.00155
Mn	1.248	0.288	2.74E-05	1.295	0.288	1.47E-05	1.338	0.309	2.78E-05
B	449.770	101.770	1.94E-05	463.240	101.800	1.15E-05	460.120	103.690	1.86E-05

Nb has one of the most important roles of the microalloying elements in thermomechanically rolled steel. Its addition is considered to have three principal effects on refining the final grain size: (1) as an inhibitor of austenite grain coarsening during reheating, (2) retarding austenite recrystallisation prior to γ/α transformation, which provides more nuclei for the γ/α transformation and thus a finer grain size, through the strain induced precipitation of NbC and solute drag effect, and (3) as a consequence of the relatively large atom size of the Nb the transformation temperature (γ/α) decreases, thus increasing the ferrite nucleation rate as well.

Nb, Mn, C and surprisingly Cu play a similar role by retarding the γ/α transformation, which gives a further strength increase by refining the ferrite grains and promoting the formation of bainite. Note, from torsion tests results, that Cu addition reduces the phase transformation temperature (A_{3r}).

On the other hand, B is an efficient promoter of bainite as it suppresses the nucleation of ferrite by segregating to the austenite grain boundaries, thus retarding the transformation to ferrite. Such segregated atoms could affect the nucleation rate during phase transformation, increasing the final grain size d_{15^o}. Small B additions effectively reduce the formation of pearlite and quasi-polygonal ferrite and broaden the cooling rate region for bainite [10]. Small B additions also reduce both the A_{r3} and A_{r1} temperatures.

The efficiency of the B addition is usually considered to depend on an addition of Ti that combines with nitrogen thus preventing the formation of boron nitrides; the Ti addition therefore protects the B from precipitation. The level of Ti addition is controlled as a function of the N level, to ensure a stoichiometric Ti/N ratio, but, surprisingly, the results in this project did not show differences between the low and high levels of Ti.

Table 25: Regression equations to grain sizes from EBSD measurements.

Grain Sizes Models (microns, weight%, log°C/s,°C)		R^2	R^2_{adj}	p_{max}
MEAN[4°]	= **6** **-7C-6Nb-0.7Mo-0.5Cu** **-0.8*logCR*1** **-0.4*RR***	0.668	0.654	0.021
	= **6** **-7C-6Nb-0.7Mo-0.5Cu**+0.3Cr-0.3Ni **-0.8*logCR*1** **-0.4*RR***	0.678	0.660	0.190
	= **5** -55B-7Ti-**7C-6Nb-0.7Mo-0.5Cu**+0.3Cr-0.3Ni+0.14Mn **-0.8*logCR*1**+0.7log*CR*2-**0.4*RR***-0.002T_{FC}	0.686	0.656	0.558
MEAN[15°]	= **5+450B** **-7Nb+1.3Mn+1.2Cr** **- 0.6Cu** **+0.2*logCR*2-0.8*RR***	0.556	0.535	0.099
	= **2+460B** **-7Nb+1.3Mn+1.2Cr** **- 0.6Cu** -0.3*logCR*1+**0.2*logCR*2-0.8*RR***+0.006T_{FC}	0.565	0.537	0.175
	= **2+460B**-8Ti-**7Nb+1.4Mn+1.2Cr**-1.2C-**0.6Cu**+0.2Mo+0.01Ni-0.3*logCR*1+**0.2*logCR*2-0.8*RR***+0.006T_{FC}	0.566	0.525	0.838

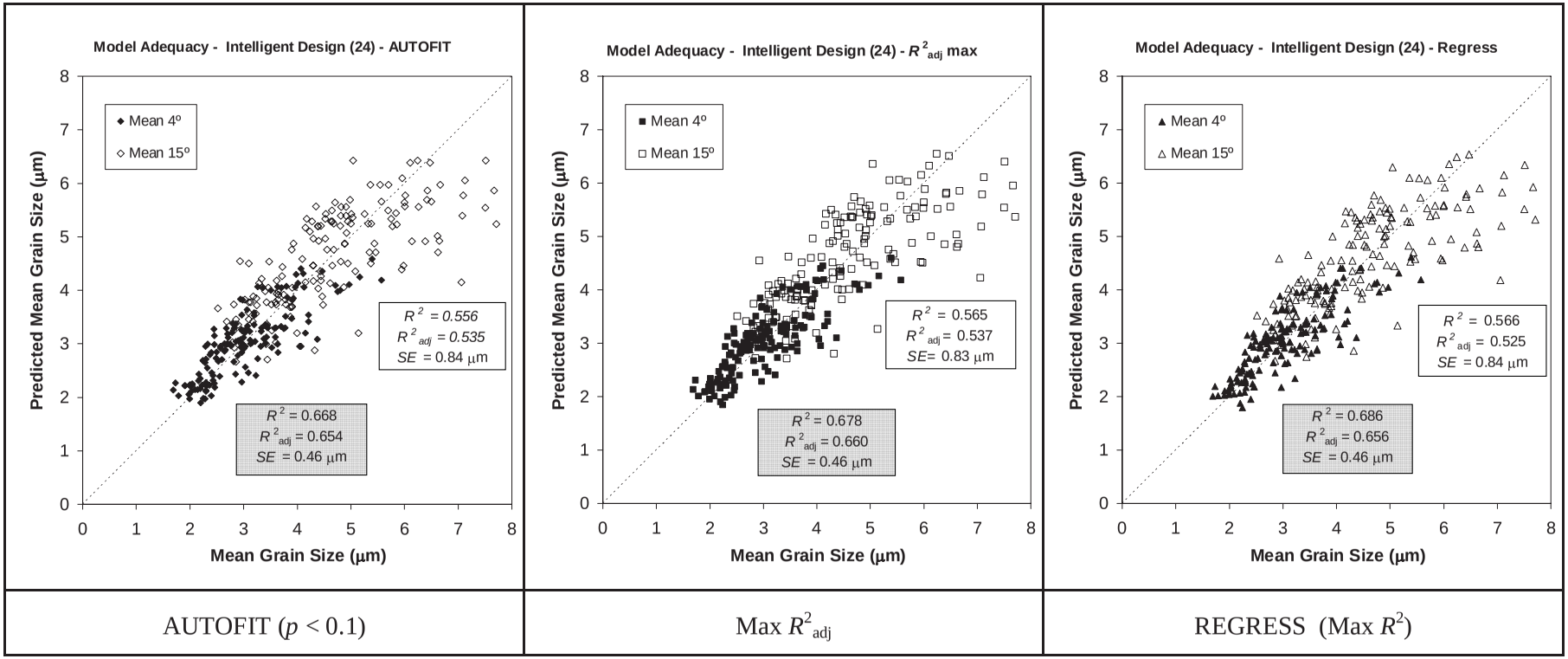

AUTOFIT ($p < 0.1$)	Max R^2_{adj}	REGRESS (Max R^2)

Figure 10: Experimental vs. predicted plot for grain size measurements for 4° and 15° for the 24 casts

6.1.6 Dilatometry

6.1.6.1 Experimental method and results

CCT diagrams were constructed for each cast using dilatometer studies. The heating and cooling rate up to the deformation steps was 5°C/s. The samples were heated to 1200°C and austenitised for 10 minutes. A holding time of 3s was applied before each of two deformation steps, where the rate of deformation was 3/s and the strain at both deformation steps was 0.6. This schedule is shown schematically in Figure 11.

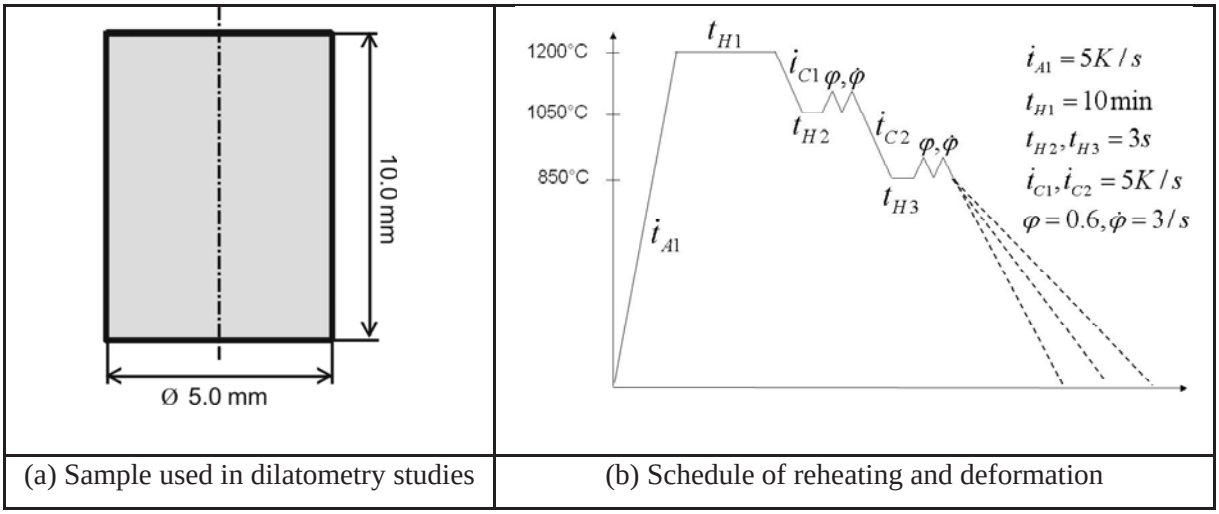

(a) Sample used in dilatometry studies | (b) Schedule of reheating and deformation

Figure 11: Detail of the dilatometry work for the determination of CCT diagrams

To produce CCT diagrams, the samples were analysed by light optical microscopy (LOM) and the hardness for all samples was measured. With this information, it is possible to gain an overview about the influence of different alloying elements on the phase transformation.

In Table 26, the values of hardness as a function of cooling rate are listed. Shaded squares indicate that 100% bainite was formed at the specified cooling rate. For most of the casts there were traces of residual austenite at slower cooling rates, but it was not possible to quantify the amount of this phase by LOM.

The main microstructure was bainitic, Table 26. In dependence of the alloying system, the critical temperature for 100 % bainite is shifted to lower or higher cooling rates.

For example at stage 1, for the higher Mn content of 2.1% there was a martensitic microstructure at the highest cooling rate. The same happened when C was added in stage 2, just with a higher effect. There was still martensitic microstructure at slower cooling, e.g. casts A045 and A046 and an increase in hardness with increases of Mn and C. Considering the increase of Nb content in stage 2, the table reveals that the ferrite/pearlite phase transformation is shifted to slower cooling rates. A decrease in the C- and Nb-content led to a constriction of the bainite phase transformation field. Regarding stage 3, it was noted that a variation of Ti and B content did not have a big influence on the kind of phase transformation but it did increase the hardness. Only in the case of the low B cast A047, ferrite formation appeared with slower cooling rates. In the case of high B content, martensite was formed in addition to bainite at slow cooling rates. Consequently, the hardness values for the casts A048 and A050 were at a high level.

Table 26: Hardness (HV10) as function of cooling rate (shaded squares = 100 % bainite)

Stage	Run	Cast	Type	Average cooling rate, °C/s								
				95.0	34.0	19.8	8.5	4.3	2.1	1.1	0.5	0.3
1	1	A027	Cu	224	222	216	215	213	213	205	182	165
	2	A028	Ni	235	222	219	217	211	211	208	197	169
	3	A029	Mo	228	220	219	218	217	207	188	175	169
	4	A030	NiMoCu	250	234	231	226	224	223	221	212	186
	5	A031	Cr	245	229	224	224	219	215	197	176	161
	6	A032	NiCuCr	260	248	237	236	230	229	223	210	183
	7	A033	MoCuCr	263	244	241	241	231	232	221	196	174
	8	A034	MoNiCr	253	246	237	237	237	245	230	202	181
	9	A035	Mn	237	234	223	223	218	214	211	184	174
	10	A036	MnNiCu	262	244	235	227	226	223	223	214	200
	11	A037	MnMoCu	283	258	254	254	250	246	244	239	205
	12	A038	MnNiMo	285	269	251	248	243	237	241	241	228
	13	A202	MnCuCr	278	254	244	242	237	237	232	217	197
	14	A203	MnNiCr	282	250	242	241	234	234	231	226	203
	15	A041	MnMoCr	309	271	254	253	250	250	250	245	226
	16	A042	MnNiMoCuCr	338	291	274	267	264	264	264	264	256
2	1	A043	lowC-lowNb	227	206	207	206	206	204	193	191	174
	2	A044	lowC-highNb	230	222	218	211	210	203	203	203	194
	3	A045	highC-lowNb	344	274	267	261	247	241	237	239	210
	4	A046	highC-highNb	364	295	266	253	250	250	250	244	226
3	1	A047	lowTi-lowB	301	273	262	251	248	240	238	237	211
	2	A048	lowTi-highB	331	307	287	259	250	250	250	250	248
	3	A049	highTi-lowB	263	247	247	242	238	237	237	219	192
	4	A050	highTi-highB	343	303	287	275	256	250	247	248	254
additional		A039	C-MnCuCr	383	309	291	276	269	264	264	254	224
		A040	C-MnNiCr	386	319	295	282	273	267	266	259	242
industrial		81351	MnNiCu-1Cr	303	269	263	251	254	245	244	224	206
		16685	Cr	268	231	231	222	216	213	202	184	164
		81913	NiCuCr	256	234	224	222	218	216	202	176	164

Comparing the laboratory casts with the industrial ones, it was noticeable that there was a high agreement between A031 and 16685. Slight differences in the content of Mn and Cr have not had a big influence on the phase transformation behaviour or on the hardness. Just at the highest cooling rate, the industrial cast showed a higher hardness value. Also, it is of interest to compare the industrial cast 81913 with A032. They differ in Ni, Cu and Cr content. This led to pearlite formation at slow cooling rates in the industrial cast while there was also a small martensitic transformation but mainly ferrite formation at the same rates in the laboratory cast. The decreases in hardness, 70 and 90 HV, from highest to slowest cooling rate was greater in the industrial cast.

6.1.6.2 Regression analysis

It was observed that the hardness was a linear function of logCR for the intermediate CRs, when the CR is higher than a certain value (upper limit) and lower than another (lower limit). These limit values were estimated by eye for all the 24 casts. At CRs lower than lower limit, the hardness drops below log-linear lines. Microstructurally, it is probable that this corresponds to the appearance of significant

amounts of polygonal ferrite. At cooling rates higher than the upper limit, the hardness increased above the log-linear lines, presumably due to the appearance of increasing amounts of martensite. Therefore lower limit and upper limit are related to the critical cooling rates for the appearance of martensite at one end and polygonal ferrite at the other. So, this analysis indicates that the central range of CR (lower limit CR < CR < upper limit CR) gives the hardness of bainite.

Two models have been generated to predict the upper and lower limits of cooling rates which define the central range (lower limit logCR < logCR < upper limit logCR). Once the limits have been established, the models for the three ranges have been applied:

- Lower range (log*CR* < lower limit *CR*),
- Central range (lower limit log*CR* < log*CR* < upper limit log*CR*) and
- Upper range (log*CR* > upper limit log*CR*).

Table 27: Coefficients, Standard Errors and Significances of variables for the Upper and Lower limit Cooling Rates from CCT diagrams

Lower Limit (24 casts)	*log CR* (Autofit)			*log CR* (Fit All, R^2_{adj} max)		
Term	**Coefficient**	**Std Error**	**Significance**	**Coefficient**	**Std Error**	**Significance**
B	-181.97	40.40	0.000216	-180.58	39.96	0.000235
Ni	-0.679	0.142	0.000113	-0.677	0.140	0.000118
Mn	-0.419	0.110	0.00106	-0.423	0.108	0.000959
Mo				-0.230	0.191	0.242
Constant	0.644	0.199	0.00412	0.689	0.200	0.00273
Upper Limit (24 casts)	*log CR* (Autofit)			*log CR* (Fit All, R^2_{adj} max)		
Term	**Coefficient**	**Std Error**	**Significance**	**Coefficient**	**Std Error**	**Significance**
B	-347.04	40.19	5.28595E-08	-353.18	34.77	2.20689E-08
Ti				-16.55	7.059	0.03230
Mn	-0.623	0.109	1.66166E-05	-0.563	0.100	3.85889E-05
Mo	-0.339	0.192	0.09281	-0.438	0.170	0.02055
Ni	-0.348	0.141	0.02326	-0.357	0.122	0.00958
Constant	3.204	0.201	1.90775E-12	3.019	0.198	5.96278E-11
Cr				0.235	0.116	0.06002
Nb				2.616	1.226	0.04858

Table 28: Coefficients, Standard Errors and Significances of variables for the Central Range hardness from CCT diagrams
(Lower Limit logCR < logCR < Upper Limit logCR)

Central Range (24 casts)	Hardness (Autofit)			Hardness (Fit All, R^2_{adj} max)		
Term	**Coefficient**	**Std Error**	**Significance**	**Coefficient**	**Std Error**	**Significance**
Ti**logCR*				-257.00	176.27	0.147
Mo*logCR	-17.45	5.430	0.00160	-19.49	5.564	0.000608
Mn*logCR	-6.845	3.171	0.03244	-5.659	3.267	0.08530
Constant	80.88	6.377	1.33385E-25	80.26	6.407	4.2857E-25
Cr**logCR*				4.613	3.714	0.216
Ni	5.240	2.605	0.04602	5.118	2.599	0.05080
Cu	4.945	2.366	0.03828	5.554	2.397	0.02185
logCR	20.96	6.035	0.000669	21.64	6.130	0.000551
Cr	25.41	2.367	2.31898E-20	22.99	3.542	1.1713E-09
Mn	34.01	3.131	1.05069E-20	33.89	3.125	1.37869E-20
Mo	59.42	5.315	1.4744E-21	59.39	5.298	1.44481E-21
C*logCR	156.75	57.05	0.00673	152.72	56.95	0.00815
Nb	287.37	25.15	3.25483E-22	298.66	26.20	4.48099E-22
C	670.83	47.80	3.1888E-29	676.88	47.79	1.89542E-29
B	9656.7	844.12	2.97547E-22	9534.6	844.78	8.99978E-22

Table 29: Coefficients, Standard Errors and Significances of variables for the Upper and Lower limit hardness from CCTs diagrams.

Lower Range(24 casts)	Hardness (Autofit)			Hardness (Fit All, R^2_{adj} max)		
Term	**Coefficient**	**Std Error**	**Significance**	**Coefficient**	**Std Error**	**Significance**
C*logCR	-833.87	232.25	0.00163	-9561.9	4182.2	0.03621
B*logCR	133100	27877.7	9.10951E-05	-7969.3	125870	0.950
C				-4942.6	2394.8	0.05564
Cu				-10.52	8.341	0.226
Constant	25.07	17.64	0.169	4.419	18.82	0.817
Mo	30.23	12.25	0.02188	32.76	11.34	0.01066
Mn	59.20	7.206	3.79321E-08	60.44	6.814	1.41757E-07
Ni				85.59	43.88	0.06887
Ni**logCR*				126.77	81.03	0.137
Nb				2442.7	938.12	0.01919
Nb**logCR*				4041.8	1638.4	0.02530
B	136859	23762.1	8.5634E-06	60875.9	69795.3	0.396

Upper Range (24 casts)	Hardness (Autofit)			Hardness (Fit All, R^2_{adj} max)		
Term	**Coefficient**	**Std Error**	**Significance**	**Coefficient**	**Std Error**	**Significance**
Constant	52.21	42.28	0.232	40.40	43.15	0.362
Cr	47.87	18.01	0.01553	47.69	17.85	0.01558
Mn	57.24	20.06	0.01015	60.61	20.10	0.00743
Mo	85.78	25.60	0.00336	88.58	25.50	0.00271
C*logCR	880.41	95.05	1.77989E-08	933.84	105.02	5.27232E-08
B*logCR	14155.5	1885.8	4.26072E-07	8652.9	5128.1	0.109
B				9576.3	8310.1	0.264

Table 30: Regression equations of Vickers hardness.

CCT Models (HV10, log(°C/s), weight %)	R^2	R^2_{adj}	p_{max}
Lower Limit *logCR* = **0.65-180B-0.7Ni-0.5Mn**	0.762	0.727	0.001
= **0.7 -180B-0.7Ni-0.5Mn**-0.25Mo	0.779	0.733	0.242
Upper Limit *logCR* = **3-350B -0.6Mn-0.35Mo-0.35Ni**	0.870	0.843	0.093
= **3-350B**-17Ti+2.5Nb-**0.6Mn-0.45Mo-0.35Ni**+0.25Cr	0.919	0.883	0.060
HV Central Range (lower Limit *logCR* < *logCR* < Upper Limit *logCR*)			
= **80+10000B+670C+300Nb+60Mo+35Mn+25Cr+5Cu+5Ni+(20 +150C-17Mo-7Mn)*logCR***	0.899	0.891	0.046
= **80+10000B+680C+300Nb+60Mo+35Mn+25Cr+6Cu+5Ni+(20**-260Ti+**150C-20Mo-6Mn**+5Cr)***logCR***	0.901	0.892	0.216
HV Lower Range (*logCR* < lower limit *logCR*)			
= **25+14000B +60Mn+30Mo+(130000B-800C)*logCR***	0.812	0.770	0.022
= **4+ 6000B**+2500Nb-5000C-10Cu+90Ni+**60Mn+35Mo**+(-10000C-**8000B**+4000Nb+125Ni)***logCR***	0.894	0.821	0.950
HV Upper Range (*logCR* > upper limit *logCR*)			
= **50 +90Mo+60Mn+50Cr+(14000B+880C)*logCR***	0.880	0.849	0.016
= **40**+9500B+**90Mo+60Mn+50Cr+(9000B+930C)*logCR***	0.888	0.851	0.264

The terms before the parenthesis of the HV formula predict the hardness for CR = 1 °C/s (log CR = 0). The terms within the parenthesis show the correction for other cooling rates: the more positive the terms in the parenthesis, the stronger the effect of the cooling rate.

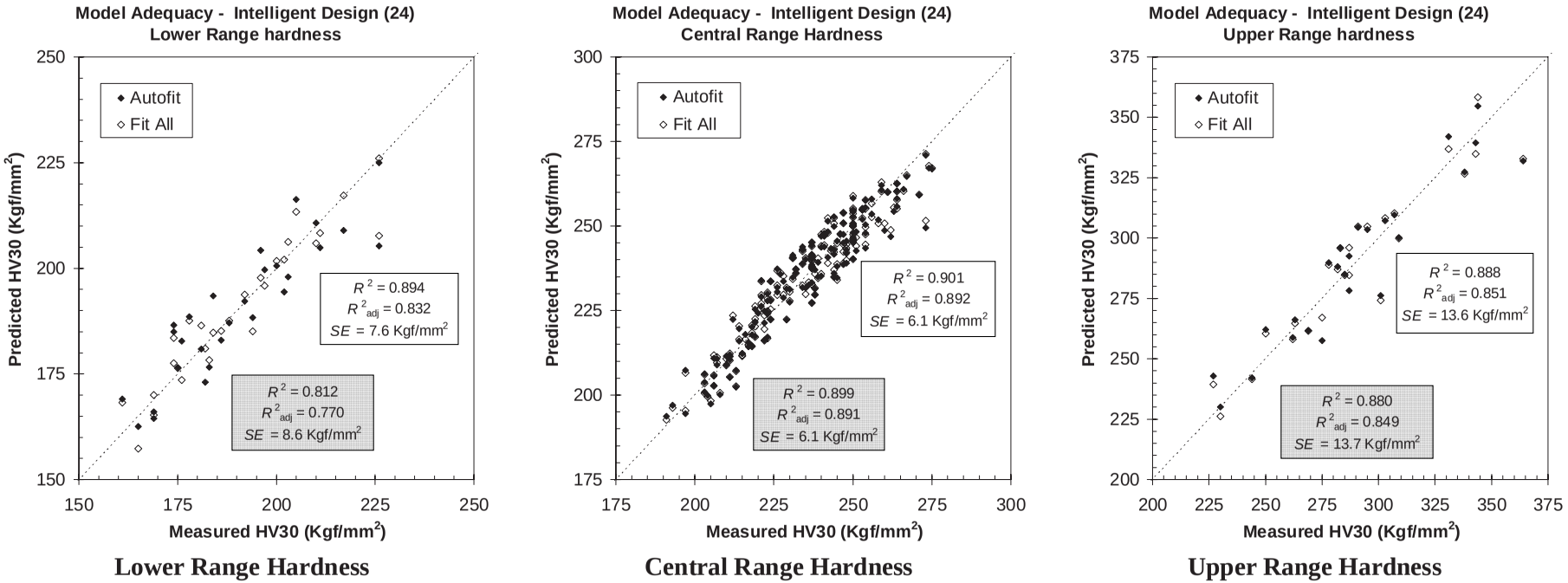

Figure 12: Experimental vs. predicted plots for CCT hardness for the 24 casts

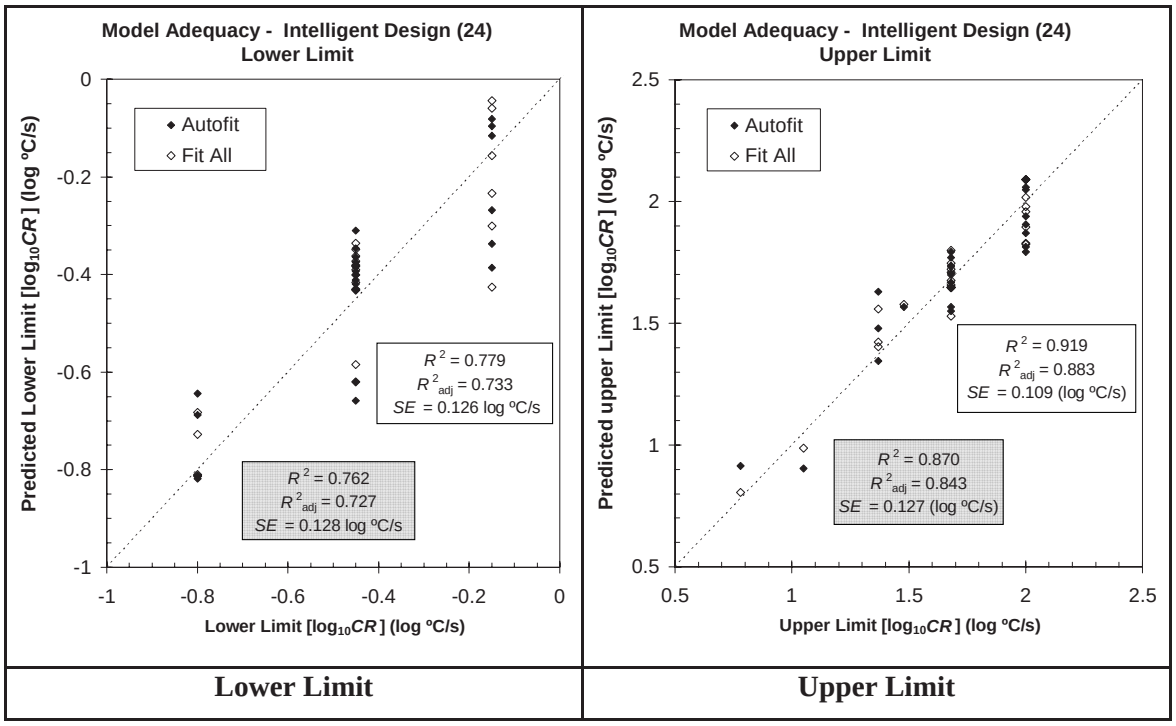

Figure 13: Experimental vs. predicted plots of Cooling Rates for upper and lower limit for the 24 casts

6.1.7 Torsion Tests

6.1.7.1 Experimental methods and results

The experimental procedure of multipass torsion tests, carried out for the determination of the no-recrystallisation temperature (T_{nr}) was as follows:

Specimens were reheated in an induction furnace to 1250ºC (soak temperature) for 15 minutes to dissolve almost all Nb. Then, the specimens were cooled down from 1250ºC to 1150ºC (first pass of deformation) at 1ºC/s. Deformation at constant temperature in steps of $\varepsilon = 0.3$ and at a strain rate $\dot{\varepsilon} = 1\,\mathrm{s}^{-1}$ was started at 1150ºC and continued until 690ºC. The number of passes was 24, the interpass time was 20 seconds and the temperature steps between passes was 20ºC (cooling at 1ºC/s). The schedule is shown schematically in Figure 14.

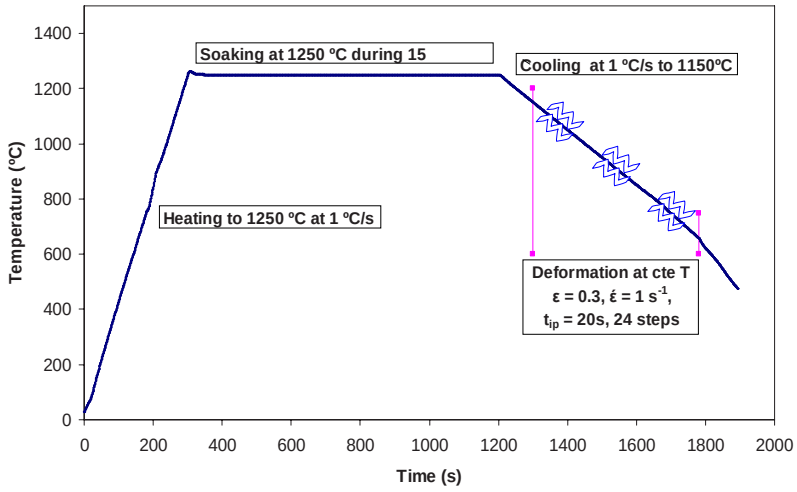

Figure 14: Thermal and mechanical cycle for multipass torsion tests

Stress-strain curves show that stress increases as the temperature drops, as well as a greater tendency towards hardening after approximately 10 passes. On the other hand a reduction in the level of stress can be observed, denoting the start of the $\gamma \rightarrow \alpha$ phase transformation, Figure 15 (a).

The T_{nr} values were calculated, following the procedure development by Jonas and co-workers [11] from the plot of Mean Flow Stress vs. Inverse Absolute Temperature. The Mean Flow Stress (MFS) corresponding to each pass has been calculated by numerical integration and plotted against the inverse absolute temperature. The MFS has been defined as the area under each stress-strain curve divided by the pass strain, Figure 15 (b).

Three different regions can be clearly distinguished:

- **Region I**: Where it is supposed that complete recrystallisation (100 %) occurs between passes and the stress increases from pass to pass are only due to the temperature drop.
- **Region II**: Where recrystallisation between passes is inhibited by strain induced precipitation. The stress increases more rapidly due to both, the temperature drop and the accumulation of strain.
- **Region III**: Corresponds to the austenite-ferrite region. The stress reduction from the start of the transformation of austenite to softer ferrite phase (A_{r3} temperature).

The T_{nr} value is determined from the intersection between the regression lines of the points corresponding to regions I and II.

Another useful parameter is the recrystallised fraction between passes, shown in Figure 15 (c). The anisothermal interpass fractional softening (FS) is determined from the stress-strain curves obtained in multipass tests using the following equation:

$$FS(\%) = \frac{\sigma_m^i - \sigma_y^{i+1}\dfrac{\sigma_0^i}{\sigma_0^{i+1}}}{\sigma_m^i + \sigma_0^i} \times 100$$

where σ^i_m and σ_y^{i+1} are the maximum and the yield stresses for both, the i-th (at temperature T_i) and the (i+1)st (at temperature T_{i+1}) passes respectively, while σ^i_o and σ_o^{i+1} are the yield stresses of a fully recrystallized material for the i-th and (i+1)st passes. The yield stresses are determined by the 2 % offset method. σ^i_m and σ_y^{i+1} are derived from the pass to pass flow curves, while σ^i_o and σ_o^{i+1} are determined from a relationship which has been derived from the values of yield stresses measured in the stress-strain curves corresponding to the range of complete recrystallisation.

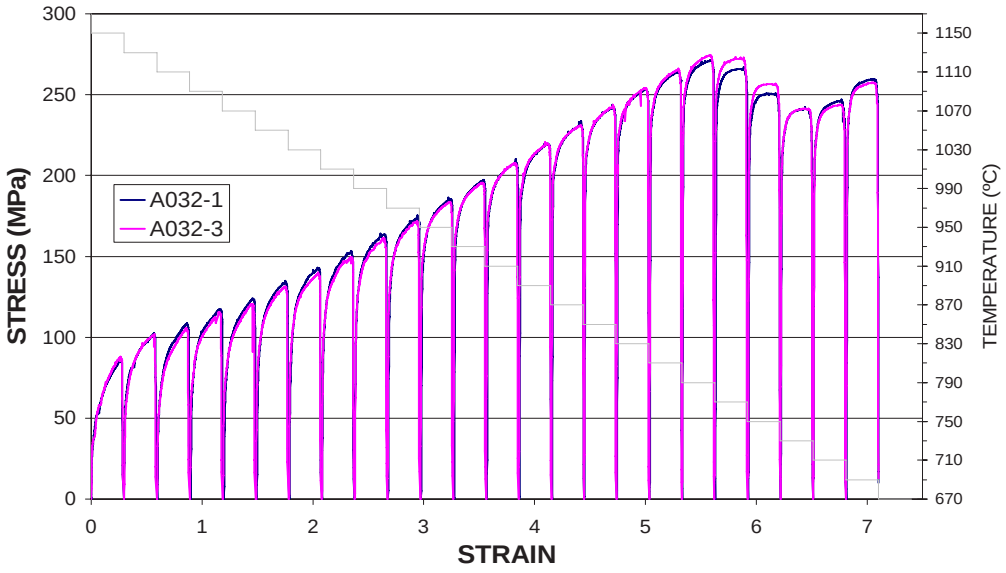

(a)

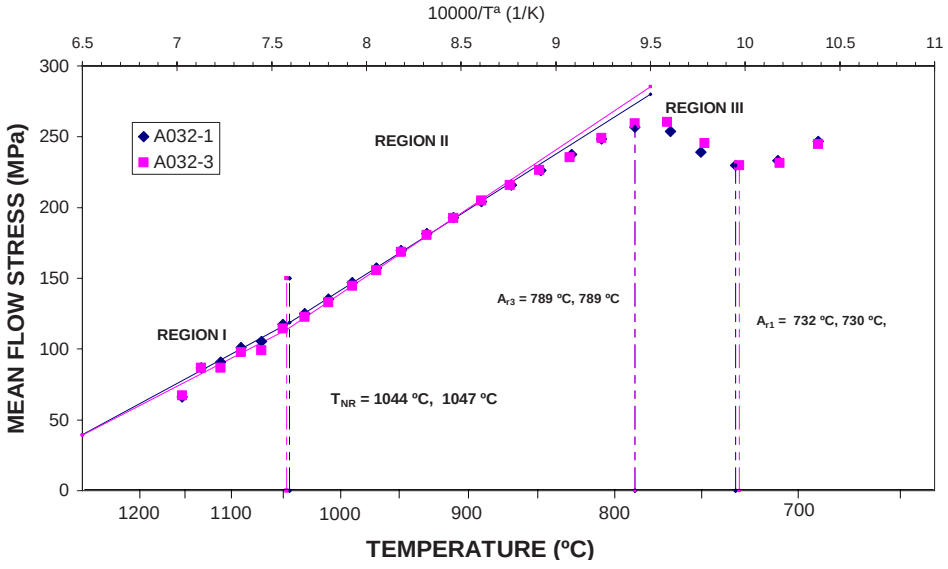

(b)

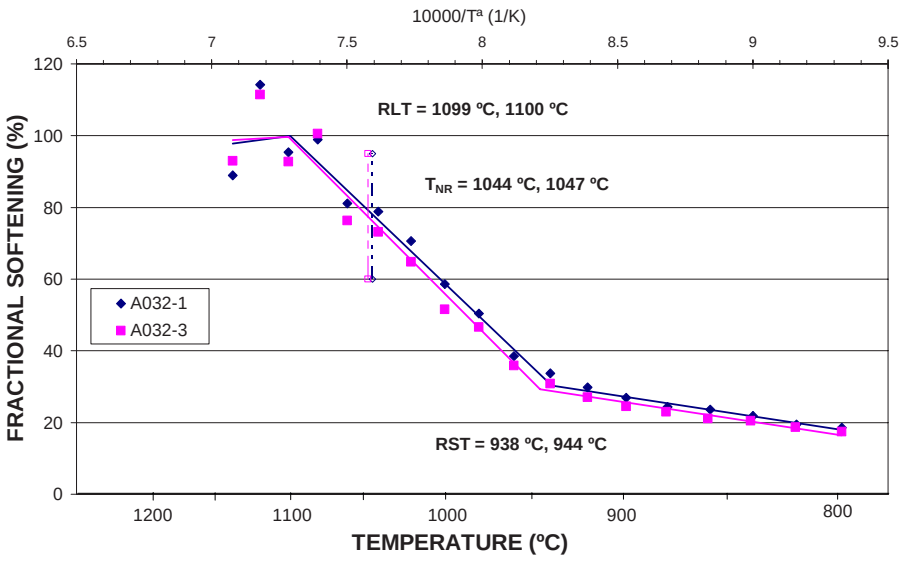

(c)

Figure 15: Curves of (a) stress vs. strain, (b) MFS vs. 1/T, and (c) FS vs. 1/T for cast A032

Table 31: Critical and phase transformation temperatures (ºC) from torsion tests.

Stage	Run	Cast	Type	RLT	TNR	RST	A3R	A1R
1	1	A027	Cu	1053	1022	920	810	752
	2	A028	Ni	991	983	867	790	728
	3	A029	Mo	1057	1030	937	830	773
	4	A030	NiMoCu	1055	1030	920	784	734
	5	A031	Cr	1060	1034	939	849	770
	6	A032	NiCuCr	1100	1045	941	789	731
	7	A033	MoCuCr	1051	1024	942	810	756
	8	A034	MoNiCr	1058	1038	940	790	728
	9	A035	Mn	1028	1027	900	780	730
	10	A036	MnNiCu	1048	1020	910	729	*
	11	A037	MnMoCu	1048	1020	912	770	730
	12	A038	MnNiMo	1056	1028	938	748	711
	13	A202	MnCuCr	1033	1014	898	748	*
	14	A203	MnNiCr	1030	1010	884	730	*
	15	A041	MnMoCr	1080	1037	930	788	730
	16	A042	MnNiMoCuCr	1072	1023	933	730	*
2	1	A043	lowC-lowNb	1033	1008	901	772	729
	2	A044	lowC-highNb	1069	1037	943	792	730
	3	A045	highC-lowNb	1040	1022	929	750	707
	4	A046	highC-highNb	1060	1060	930	750	708
3	1	A047	lowTi-lowB	1048	1028	939	770	710
	2	A048	lowTi-highB	1072	1053	947	750	712
	3	A049	highTi-lowB	1046	998	897	770	708
	4	A050	highTi-highB	1079	1072	976	750	712
additional		A039	C-MnCuCr	1058	1015	909	748	*
		A040	C-MnNiCr	1048	1018	886	720	*
		C228	all low					
Industrial		81913	NiCuCr	1023	1014	906	828	750
		16685	Cr	1046	1016	907	808	750
		81351	MnNiCu-1Cr	1005	1002	*	740	*
		02098	Nb-V	1030	1010	900	809	751

* Not observed

6.1.7.2 Regression analysis

Table 32: Coefficients, Standard Errors and Significances of variables for the Critical Temperatures (RLT, Tnr & RST) from Torsion tests.

RLT (ºC) (24 casts)	(Autofit)			(R^2_{adj} max)			(Regress)		
Term	Coefficient	Std Error	Significance	Coefficient	Std Error	Significance	Coefficient	Std Error	Significance
Ti							-272.48	1397.40	0.848
C							-110.6	352.7	0.758
Mn							-6.76	19.62	0.736
Ni							-1.2	23.832	0.961
Constant	1034.0	7.877	4.29E-32	1021.6	9.889	1.35E-27	1035.3	43.539	1.02E-12
Cu				19.73	18.91	0.310	21.61	22.10	0.345
Cr	36.40	19.92	0.082	35.67	19.07	0.077	36.76	22.74	0.128
Mo				47.43	28.10	0.108	45.54	33.34	0.194
Nb							65.76	252.68	0.798
B	12246.0	6126.6	0.059	11218.4	5901.7	0.073	11177.8	6802.5	0.123

Tnr (°C) (24 casts)	(Autofit)			(R^2_{adj} max)			(Regress)		
Term	**Coefficient**	**Std Error**	**Significance**	**Coefficient**	**Std Error**	**Significance**	**Coefficient**	**Std Error**	**Significance**
Ti							-377.33	1146.83	0.747
Nb							-23.1	207.4	0.913
Ni							-11.75	19.56	0.558
Mn							-2.6	16.105	0.873
Cu							-2.32	18.14	0.900
Constant	1013.7	4.899	1.10E-37	1009.5	6.176	4.31E-34	1013.0	35.732	9.10E-14
Cr							15.58	18.66	0.418
Mo				25.40	22.93	0.280	22.64	27.36	0.422
C							195.41	289.43	0.511
B	17644.0	4803.8	0.001	17451.1	4782.4	0.001	17721.4	5582.7	0.007

RST (°C) (24 casts)	(Autofit)			(R^2_{adj} max)			(Regress)		
Term	**Coefficient**	**Std Error**	**Significance**	**Coefficient**	**Std Error**	**Significance**	**Coefficient**	**Std Error**	**Significance**
Ti							-382.88	1348.64	0.781
Nb							-43.7	243.9	0.860
Mn				-19.91	15.53	0.215	-17.55	18.94	0.370
Ni							-13.2	23.000	0.575
Constant	897.2	7.578	3.74E-31	927.0	28.856	5.05E-18	930.8	42.020	2.68E-12
Cu							7.38	21.33	0.734
Cr				23.72	18.57	0.217	25.88	21.95	0.258
C							61.52	340.36	0.859
Mo	68.36	28.13	0.024	66.87	27.38	0.025	64.55	32.18	0.065
B	19016.8	5868.1	0.004	19108.0	5721.7	0.003	19164.2	6565.1	0.011

Table 33: Coefficients, Standard Errors and Significances of variables for the Phase Transformation Temperatures (RLT, Tnr & RST) from Torsion tests.

A_{r3} (°C) (24 casts)	(Autofit)			(R^2_{adj} max)			(Regress)		
Term	**Coefficient**	**Std Error**	**Significance**	**Coefficient**	**Std Error**	**Significance**	**Coefficient**	**Std Error**	**Significance**
B	-8586.72	2897.89	8.327E-03				-8828.68	3197.60	1.53E-02
C	-546.35	142.91	1.246E-03				-526.5	165.8	6.73E-03
Mn	-89.29	7.90	1.305E-09				-90.63	9.22	1.16E-07
Ni	-74.60	10.18	8.342E-07				-75.1	11.203	1.01E-05
Cu	-26.38	9.36	1.140E-02				-27.13	10.39	2.05E-02
Constant	988.62	15.30	9.161E-23	(Idem Autofit)			981.39	20.47	6.24E-17
Cr							3.5	10.7	0.745
Mo							11.0	15.673	4.94E-01
Nb							35.35	118.78	0.770
Ti							207.78	656.87	0.756

A_{r1} (°C) (24 casts)	(Autofit)			(R^2_{adj} max)			(Regress)		
Term	**Coefficient**	**Std Error**	**Significance**	**Coefficient**	**Std Error**	**Significance**	**Coefficient**	**Std Error**	**Significance**
B	-5453.16	2848.16	7.481E-02	-4505.3	2850.4	0.138	-4200.87	3297.82	2.32E-01
C	-388.46	137.43	1.275E-02	-368.37	135.05	0.01726	-372.3	159.4	4.17E-02
Ni	-63.40	11.48	5.875E-05	-64.78	11.26	6.68222E-05	-65.17	12.92	5.03E-04
Mn	-55.70	9.32	2.538E-05	-59.15	9.366	2.6792E-05	-60.4	11.744	4.37E-04
Nb							-14.83	122.13	0.906
Cu				-13.17	10.61	0.236	-13.57	12.10	2.88E-01
Ti							-13.0	673.603	9.85E-01
Cr							-6.03	12.17	0.631
Constant	860.45	16.98	3.440E-18	864.91	16.99	2.37834E-16	869.99	25.11	9.50E-12
Mo				17.50	15.40	0.276	18.5	18.3	0.337

Table 34: Regression equations of Critical and Phase Transformation Temperatures from torsion tests.

Critical and Phase Transformation temperatures Models (T^a, weight %)	R^2	R^2_{adj}	p_{max}
RLT (ºC) = **1034+12250B** **+36Cr**	0.268	0.198	0.082
= **1021+11200B** +47Mo**+36Cr**+20Cu	0.393	0.265	0.310
= **1035+11200B**-270Ti-110C+65Nb+45Mo**+37Cr**+20Cu-7Mn-1.2Ni	0.411	0.033	0.848
Tnr (ºC) = **1014+18000B**	0.380	0.352	0.001
= **1010+17500B** +25Mo	0.414	0.359	0.280
= **1013+18000B**-380Ti+200C-23Nb+23Mo+16Cr-12Ni-3Mn-2Cu	0.480	0.146	0.913
RST (ºC) = **897+19000B** **+70Mo**	0.447	0.395	0.024
= **927+19000B** **+70Mo** +24Cr-20Mn	0.527	0.427	0.217
= **930+19000B**-400Ti**+65Mo**+60C-44Nb+26Cr-18Mn-13Ni+7Cu	0.549	0.260	0.860
Ar3(ºC) = **990 -8600B-550C** **-90Mn-75Ni** **-26Cu**	0.933	0.914	0.001
= **990 -8600B-550C** **-90Mn-75Ni** **-26Cu**	0.933	0.914	0.001
= **980 -8800B-525C**+200Ti-**90Mn-75Ni**-35Nb-**27Cu**+11Mo+4Cr	0.937	0.896	0.770
Ar1 ºC) = **860 -5500B-390C -65Ni-56Mn**	0.847	0.807	0.075
= **865 -4500B-370C -65Ni-60Mn**+18Mo -13Cu	0.874	0.815	0.276
= **870 -4200B-370C -65Ni-60Mn**+19Mo-15Nb-14Cu-13Ti-6Cr	0.877	0.766	0.906

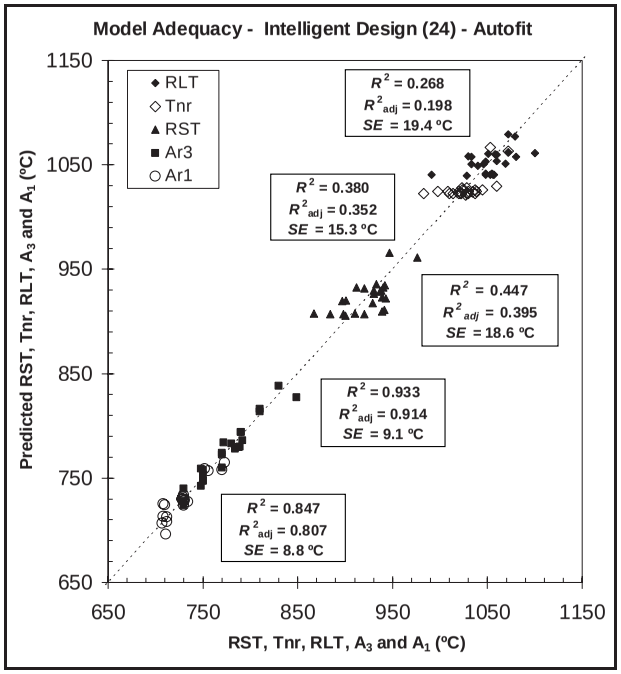

AUTOFIT ($p < 0.1$)

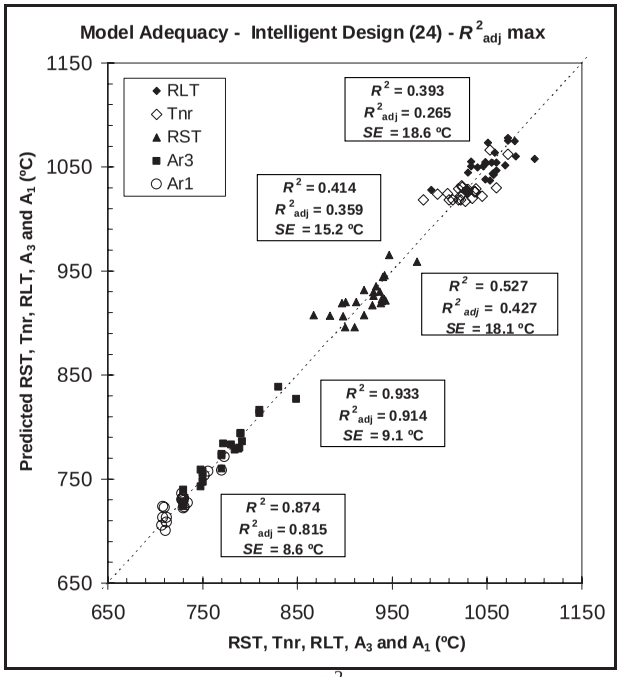

Max R^2_{adj}

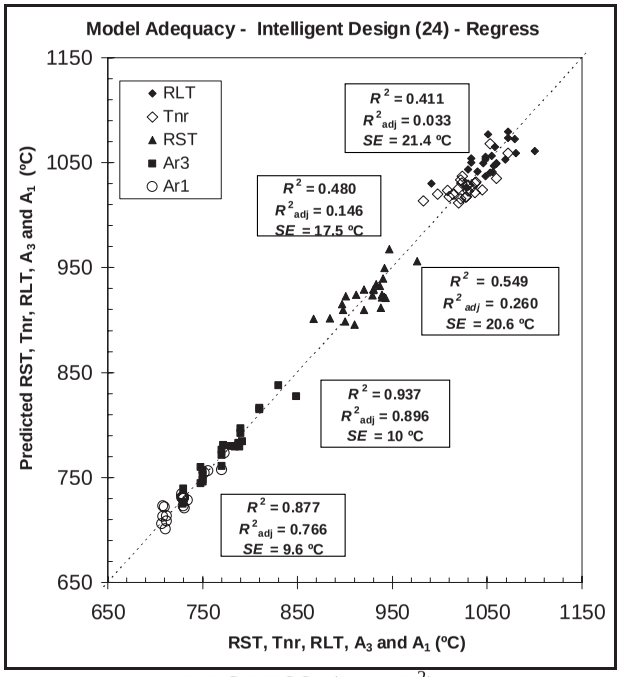

REGRESS (Max R^2)

Figure 16: Experimental vs. predicted plots for Critical and Phase Transformation Temperatures for the 24 casts

6.1.7.3 Summary of torsion test results

From the multipass torsion tests the critical temperatures of T_{nr}, *RLT* and *RST*, describing recrystallisation behaviour, as well as the critical temperatures of A_{r3} and A_{r1}, for phase transformation, were determined for all the casts.

The results have shown that there are not significant differences in the values of recrystallisation critical temperatures found for the different compositions. T_{nr} ranges between 983ºC and 1056ºC, minimum and maximum values, but most of the data are situated about 1020-1030ºC. A similar situation occurs with the *RLT* and *RST* temperatures. This means that these temperatures are not very sensible for the consideration of composition changes. This is clearly evident from the regression analysis of the results shown in Table 27. In the calculated response equations only the effect of boron addition, increasing all the recrystallisation critical temperatures, appears clearly. Beyond this element some influence of Cr and Mo, also in the same direction, is observed. The higher values of T_{nr}, *RLT* and *RST* reached when boron is added to the steel can be explained in part in terms of the influence of boron on the precipitation kinetics of Nb(C,N); a contribution may also be made by the non-equilibrium segregation of boron to austenite grain boundaries. The results of Djahazi et al.[12] and [13] demonstrated that boron addition accelerates the precipitation process by increasing the precipitation start temperature and decreasing the precipitation start time. This means that precipitation is able to retard recrystallisation at higher temperatures than in steels containing only Nb, thus leading to an increase of the T_{nr}.

On the other hand the influence of Mo and Cr may be understood in terms of their effect in retarding recrystallisation by solute drag. Surprisingly the regression equations did not show any effect of Nb. This is probably due to the range of Nb additions considered, between 0.05% and 0.12% Nb. The present results suggest some saturation of the effect of Nb in retarding recrystallisation at these high Nb levels occurs. Similar results can be found in the work of Bai et al. [14]

In contrast A_{r3} and A_{r1} temperatures show bigger differences with the composition. C and B have the strongest effect followed by alloying elements, mainly Ni, Mn and Cu, all of them depressing the transformation temperatures.

6.1.8 Tensile tests

6.1.8.1 Experimental method and results

Round tensile test specimens with 25mm gauge length and 5mm cross section diameter, Figure 17, were machined from the bars so that it was in most cases possible to get out more than 1 sample from each bar. Testing was performed to the requirements of EN 10002-1: 2001 with an INSTRON 1255 servo hydraulic testing machine supported by Control Panel 8500+. An optical deformation and strain measurement system ARAMIS was used to determine the stress-strain curves.

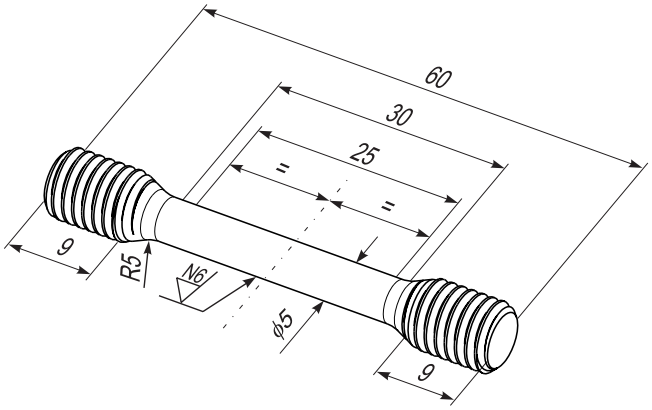

Figure 17: Geometry of round tensile test specimen

Sample preparation and testing was completed in several batches and some problems arose with material supply resulting in missing conditions. Based on the review of all tensile data, a number of tensile curves and data sets were disregarded in the analysis of the experimental design due to large scatter in results, some of which was due to segregation in the plate.

The average proof stress values, after reviewing ('filtering'), are shown in Table 35 and the tensile strengths are shown in Table 36.

Table 35: Proof stress values

Stage	Run	Cast	Type	Proof Stress, MPa					
				C	D	E	F	G	H
1	1	A027	Cu	460	454	567	605	577	630
	2	A028	Ni	476	471	544	598	566	626
	3	A029	Mo	490	479	580	557	581	608
	4	A030	NiMoCu	493	499	560	602	576	720
	5	A031	Cr	511	516	555	562	617	651
	6	A032	NiCuCr	461	469	535		616	636
	7	A033	MoCuCr	455	495	605	615	633	
	8	A034	MoNiCr	447	452	580	616	589	687
	9	A035	Mn	446	482	564	609	628	643
	10	A036	MnNiCu	470	508		575	573	
	11	A037	MnMoCu	516	497	671	682	708	676
	12	A038	MnNiMo	577	520	624	632	674	703
	13	A202	MnCuCr	522	480	639	599	623	483
	14	A203	MnNiCr	560	492	582	605	616	660
	15	A041	MnMoCr	574	538	649	643	753	662
	16	A042	MnNiMoCuCr	691	710	696	694	763	712
2	1	A043	lowC-lowNb	473	526	529	525	526	560
	2	A044	lowC-highNb	448	493	599	591	618	667
	3	A045	highC-lowNb	520	462	570	708	665	642
	4	A046	highC-highNb	581	525	596	605	635	690
3	1	A047	lowTi-lowB	521	470	631	609	653	655
	2	A048	lowTi-highB	673	681	713	660	744	727
	3	A049	highTi-lowB	474		605	655	643	702
	4	A050	highTi-highB	673	680	702	663	767	736
additional		A039	C-MnCuCr	540	502	650	647	623	626
		A040	C-MnNiCr	558	554	635	670	606	622
industrial		81351	MnNiCu-1Cr	530	446	607	589	641	649
		02098	Nb-V	478		536	568	554	561
		16685	Cr	460	484	470	518	579	603
		81913	NiCuCr	457	463	555	566	581	593

Table 36: Tensile strength values

Stage	Run	Cast	Type	R_m, MPa					
				C	D	E	F	G	H
1	1	A027	Cu	520	512	634	649	648	689
	2	A028	Ni	530	516	655	665	634	658
	3	A029	Mo	537	521	684	639	661	664
	4	A030	NiMoCu	593	606	692	731	759	778
	5	A031	Cr	540	551	661	666	711	716
	6	A032	NiCuCr	548	551	701		700	716
	7	A033	MoCuCr	554	609	722	698	780	
	8	A034	MoNiCr	577	587	716	761	743	747
	9	A035	Mn	507	544	681	720	679	681
	10	A036	MnNiCu	626	581		696	715	
	11	A037	MnMoCu	659	608	785	820	857	839
	12	A038	MnNiMo	751	685	767	747	805	802
	13	A202	MnCuCr	673	624	775	743	790	629
	14	A203	MnNiCr	713	654	743	746	769	755
	15	A041	MnMoCr	731	730	797	786	856	830
	16	A042	MnNiMoCuCr	850	873	841	851	910	849
2	1	A043	lowC-lowNb	539	572	635	655	654	650
	2	A044	lowC-highNb	537	542	680	695	698	712
	3	A045	highC-lowNb	809	721	774	834	787	820
	4	A046	highC-highNb	771	741	792	808	818	843
3	1	A047	lowTi-lowB	698	635	786	762	813	797
	2	A048	lowTi-highB	829	843	833	811	866	805
	3	A049	highTi-lowB	605		731	737	754	778
	4	A050	highTi-highB	834	866	824	834	873	849
additional		A039	C-MnCuCr	781	747	727	877	765	750
		A040	C-MnNiCr	789	804	864	854	838	822
industrial		81351	MnNiCu-1Cr	656	633	743	779	807	812
		02098	Nb-V	553		694	662	678	661
		16685	Cr	551	544	712	695	690	676
		81913	NiCuCr	525	531	650	655	667	650

6.1.8.2 Regression analysis

Table 37: Coefficients, Standard Errors and Significances of variables for Proof stress and Tensile strength.

Proof Stress (24 casts)	Proof Stress (Autofit)			Proof Stress (R^2_{adj} max)			Proof Stress (Regress, R^2max)		
Term	Coefficient	Std Error	Significance	Coefficient	Std Error	Significance	Coefficient	Std Error	Significance
log CR2	-26.470	5.771	1.05E-05	-27.040	5.739	6.37E-06	-26.980	5.768	7.43E-06
Cu							-12.740	17.670	0.472
T_{FC}(°C)				-0.274	0.233	0.241	-0.278	0.234	0.238
Constant	229.100	35.400	1.80E-09	361.800	132.990	0.00743	363.560	133.720	0.00748
RR				6.035	3.484	0.08562	5.995	3.502	0.08939
Ni							8.086	19.060	0.672
Cr				23.160	18.490	2.13E-01	22.640	18.600	2.26E-01
Mn	71.450	15.610	1.09E-05	69.840	15.530	1.54E-05	70.260	15.670	1.63E-05
log CR1	67.820	6.493	6.49E-19	73.890	8.161	2.06E-15	73.940	8.210	2.98E-15
Mo	131.990	26.990	2.93E-06	126.450	27.000	7.14E-06	126.920	27.210	7.83E-06
Nb	497.610	199.050	0.01367	529.020	198.350	0.00865	520.330	199.600	0.01025
C	769.970	276.450	0.00615	806.550	275.750	0.00408	809.100	277.920	0.00426
Ti	1862.200	1063.800	0.08241	1527.100	1097.500	0.167	1641.000	1113.000	0.143
B	46881.400	5169.600	1.61E-15	46575.400	5139.500	1.96E-15	46967.900	5214.400	2.97E-15

Tensile Strength (24 casts)	Tensile Strength (Autofit)			Tensile Strength (R^2_{adj} max)			Tensile Strength (Regress, R^2 max)		
Term	Coefficient	Std Error	Significance	Coefficient	Std Error	Significance	Coefficient	Std Error	Significance
log CR2	-15.160	5.668	0.00846	-15.160	5.668	0.00846	-15.140	5.746	0.00948
RR							-0.884	3.489	0.8
T_{FC}(°C)							-0.005	0.233	0.982
Constant	97.430	34.720	0.0058	97.430	34.720	0.0058	105.240	133.220	0.431
Cu							6.027	17.600	0.733
Ni	32.900	18.720	0.08125	32.900	18.720	0.08125	33.570	18.990	0.07952
log CR1	70.790	6.377	1.63E-20	70.790	6.377	1.63E-20	70.800	8.179	2.05E-14
Cr	81.460	17.500	7.92E-06	81.460	17.500	7.92E-06	76.490	18.530	6.64E-05
Mn	153.170	14.590	5.08E-19	153.170	14.590	5.08E-19	148.090	15.610	2.05E-16
Mo	197.380	25.560	2.76E-12	197.380	25.560	2.76E-12	204.290	27.110	8.53E-12
Nb	650.270	179.970	0.000432	650.270	179.970	0.000432	576.200	198.850	0.00444
Ti							1035.900	1108.800	0.352
C	2630.400	270.840	4.52E-17	2630.400	270.840	4.52E-17	2601.200	276.870	3.46E-19
B	55063.400	5081.200	7.44E-20	55063.400	5081.200	7.44E-20	54857.200	5194.700	5.04E-19

Table 38: Regression equations for proof stress and tensile strength.

Proof Stress and Tensile Strength Models (MPa, weight %, log(ºC/s), ºC)	R^2	R^2_{adj}	p_{max}
Proof Stress			
= **230+47000B+1900Ti+500Nb+770C+130Mo+70Mn** **+68*logCR*1-27*logCR*2**	0.764	0.750	0.082
= **360+47000B+1500Ti+530Nb+800C+130Mo+70Mn**+23Cr **+74*logCR*1-27*logCR*2**+6*RR*+0.3T_{FC}	0.774	0.754	0.241
= **365+47000B+1600Ti+520Nb+800C+130Mo+70Mn**+23Cr-13Cu+8Ni **+74*logCR*1-27*logCR*2**+6*RR*+0.3T_{FC}	0.775	0.752	0.672
Tensile Strength			
= **100+55000B+2600C** **+650Nb+200Mo+150Mn+80Cr+30Ni** **+70*logCR*1-15*logCR*2**	0.846	0.835	0.081
= **100+55000B+2600C** **+650Nb+200Mo+150Mn+80Cr+30Ni** **+70*logCR*1-15*logCR*2**	0.846	0.835	0.081
= **100+55000B+2600C**+1000Ti**+675Nb+200Mo+150Mn+80Cr+30Ni**+6Cu**+70*logCR*1-15*logCR*2**-1*RR*+0.01T_{FC}	0.847	0.831	0.982

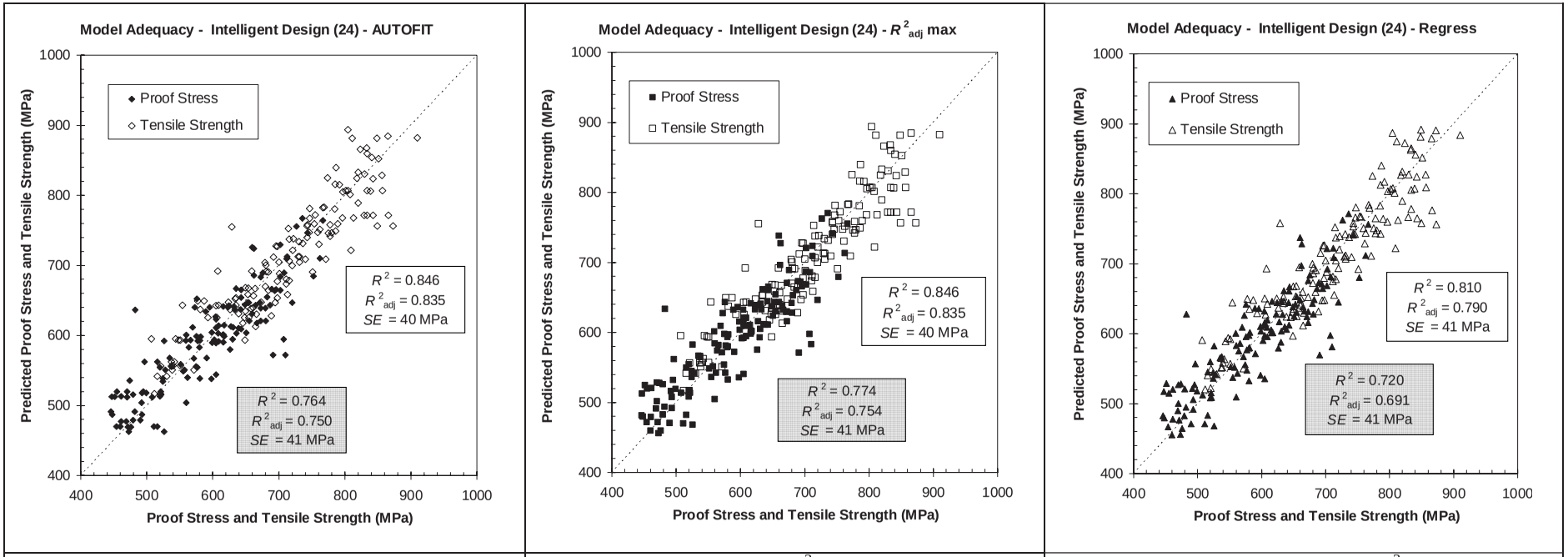

AUTOFIT ($p < 0.1$)	Max R^2_{adj}	REGRESS (Max R^2)

Figure 18: Experimental vs. predicted plot for Proof stress and Tensile strength for the 24 casts

6.1.9 Charpy impact test

6.1.9.1 Experimental method and results

Charpy impact tests were carried out on 2 mm V notched specimens to EN 10045 using an impact testing machine with an energy capacity of 1448 J and an impact velocity of 7.74 m/s. The number of samples varied between 8 and 20 samples per plate. Impact transition curves were determined by means of the modified tanh fitting algorithm of Wallin [15].

The response variables of the Charpy impact tests are listed in Table 39, for ITT 27J, Table 40 for ITT 0.5Kvmax and Table 41, for Kvmax.

Table 39: 27J impact transition temperatures of all plates

Stage	Run	Cast	Type	ITT 27J, °C					
				C	D	E	F	G	H
1	1	A027	Cu	-130	-152	-135	-165	-133	-140
	2	A028	Ni	-147	-156	-167	-173	-142	-166
	3	A029	Mo	-50	-87	-62	-93	-55	-81
	4	A030	NiMoCu	-131	-170	-156	-177	-129	-123
	5	A031	Cr	-119	-136	-127	-151	-92	-116
	6	A032	NiCuCr	-123	-161	-141		-143	-178
	7	A033	MoCuCr	-133	-151	-133	-167	-102	-155
	8	A034	MoNiCr	-127	-152	-121	-157	-115	-127
	9	A035	Mn	-91	-144	-130	-144		-156
	10	A036	MnNiCu	-139	-187	-136	-179	-131	-171
	11	A037	MnMoCu	-127	-145	-114	-174	-133	-152
	12	A038	MnNiMo	-96	-156	-98	-152	-86	-121
	13	A202	MnCuCr	-62	-124	-98	-134	-78	-118
	14	A203	MnNiCr	-70	-123	-96	-141	-72	-139
	15	A041	MnMoCr	-79	-124	-81	-125	-82	-99
	16	A042	MnNiMoCuCr	-52	-100	-73	-111	-46	-106
2	1	A043	lowC-lowNb	-111	-187	-112	-183	-108	-145
	2	A044	lowC-highNb	-146	-171	-138	-162	-125	-126
	3	A045	highC-lowNb	-45	-91	-77	-107	-41	-93
	4	A046	highC-highNb	-42	-85	-44	-106	-57	-94
3	1	A047	lowTi-lowB	-110	-146	-100	-145	-101	-135
	2	A048	lowTi-highB	-63	-123	-68	-93	-62	-83
	3	A049	highTi-lowB	-101	-150	-123	-154	-79	-142
	4	A050	highTi-highB	-68	-109	-51	-98	-32	-81
additional		A039	C-MnCuCr	-99	-140	-103	-136	-104	-165
		A040	C-MnNiCr	-96	-147	-92	-142	-100	-130
industrial		81351	MnNiCu-1Cr	-109	-173	-146	-161	-99	-155
		02098	Nb-V	-94	-128	-133	-122	-104	-128
		16685	Cr	-119	-143	-118	-155	-108	-151
		81913	NiCuCr	-105	-111	-117	-122	-93	-105

Table 40: Ductile to brittle transition temperature of all plates

Stage	Run	Cast	Type	ITT 0.5Kvmax, °C					
				C	D	E	F	G	H
1	1	A027	Cu	-96	-141	-126	-121	-106	-123
	2	A028	Ni	-120	-138	-134	-151	-109	-131
	3	A029	Mo	-24	-47	-27	-58	-29	-42
	4	A030	NiMoCu	-101	-128	-110	-155	-107	-86
	5	A031	Cr	-99	-125	-98	-126	-59	-76
	6	A032	NiCuCr	-81	-136	-121	-138	-123	-154
	7	A033	MoCuCr	-87	-138	-118		-67	-137
	8	A034	MoNiCr	-99	-139	-112	-141	-101	-114
	9	A035	Mn	-55	-126	-114	-97		-111
	10	A036	MnNiCu	-89	-134	-115	-144	-82	-139
	11	A037	MnMoCu	-90	-101	-85	-110	-76	-89
	12	A038	MnNiMo	-74	-115	-74	-123	-52	-80
	13	A202	MnCuCr	-29	-78	-69	-98	-28	-77
	14	A203	MnNiCr	-41	-87	-66	-105	-45	-102
	15	A041	MnMoCr	-58	-77	-52	-91	-46	-69
	16	A042	MnNiMoCuCr	-22	-66	-40	-78	-15	-68
2	1	A043	lowC-lowNb	-68	-115	-93	-127	-66	-118
	2	A044	lowC-highNb	-133	-151	-122	-146	-114	-103
	3	A045	highC-lowNb	-26	-38	-29	-69	-16	-47
	4	A046	highC-highNb	26	8	-5	-63	-30	-43
3	1	A047	lowTi-lowB	-76	-96	-66	-84	-64	-85
	2	A048	lowTi-highB	-29	-69	-34	-49	-19	-22
	3	A049	highTi-lowB	-58	-107	-104	-140	-66	-128
	4	A050	highTi-highB	-32	-69	-21	-56	-8	-54
additional		A039	C-MnCuCr	-55	-63	-59	-82	-49	-99
		A040	C-MnNiCr	-38	-40	-32	-105	-41	-35
industrial		81351	MnNiCu-1Cr	-82	-129	-120	-138	-55	-110
		02098	Nb-V	-57	-101	-106	-91	-88	-101
		16685	Cr	-104	-136	-93	-116	-77	-128
		81913	NiCuCr	-81	-88	-69	-95	-74	-72

Table 41: Kvmax of all plates

Stage	Run	Cast	Type	Kvmax, J					
				C	D	E	F	G	H
1	1	A027	Cu	284	282	280	301	271	260
	2	A028	Ni	270	302	334	283	302	281
	3	A029	Mo	245	235	206	169	137	168
	4	A030	NiMoCu	287	314	314	296	278	236
	5	A031	Cr	304	304	301	278	282	244
	6	A032	NiCuCr	289	302	282		288	307
	7	A033	MoCuCr	334	286	259	289	277	278
	8	A034	MoNiCr	336	310	297	298	291	271
	9	A035	Mn	363	322	288	324		316
	10	A036	MnNiCu	297	304	288	313	314	310
	11	A037	MnMoCu	290	284	285	316	324	314
	12	A038	MnNiMo	270	254	275	237	276	280
	13	A202	MnCuCr	249	272	294	290	255	252
	14	A203	MnNiCr	254	267	276	280	258	294
	15	A041	MnMoCr	243	256	276	253	242	256
	16	A042	MnNiMoCuCr	245	244	270	258	253	227
2	1	A043	lowC-lowNb	290	299	248	302	284	282
	2	A044	lowC-highNb	349	348	296	304	302	296
	3	A045	highC-lowNb	91	120	235	161	223	208
	4	A046	highC-highNb	211	206	216	299	231	235
3	1	A047	lowTi-lowB	222	221	275	233	249	216
	2	A048	lowTi-highB	224	221	245	213	214	177
	3	A049	highTi-lowB	282	282	289	262	245	269
	4	A050	highTi-highB	240	252	248	242	154	244
additional		A039	C-MnCuCr	114	131	231	140	203	200
		A040	C-MnNiCr	120	137	255	155	226	216
industrial		81351	MnNiCu-1Cr	228	240	281	256	264	226
		02098	Nb-V	268		214	195	218	213
		16685	Cr	291	296	248	293	312	284
		81913	NiCuCr	303	284	279	277	244	280

It can be seen that the higher reduction ratio resulted in better impact toughness; both ITT 27J and ITT 0.5Kvmax were shifted to lower temperatures for all three cooling conditions with RR=4 (conditions D, F, and H) compared to RR = 2 (conditions C, E, and G).

The values of Kvmax should be used with caution, because the high toughness of most of these steels resulted in specimens that did not break-through, they deformed sufficiently to pass through the abutment of the impact-testing machine. For this reason, regression analysis was not carried out for Kvmax as a measured parameter.

The Charpy test results will be the subject for a PhD thesis at RWTH Aachen.

6.1.9.2 Regression analysis

Two approaches were undertaken in the regression analysis; one was to force the grain size to be in the regression and the other was to use only the composition and processing conditions.

Toughness –considering the grain size of 15°

Table 42: Coefficients, Standard Errors and Significances of variables for ITT 27J and 0.5Kvmax. including grain size of 15° as a parameter

ITT 27J (24 casts)	ITT 27J (Autofit)			ITT 27J (R^2_{adj} max)			ITT 27J (Regress, R^2max)		
Term	Coefficient	Std Error	Significance	Coefficient	Std Error	Significance	Coefficient	Std Error	Significance
Ti							-96.69	481.37	0.8410
Ni	-38.64	8.31	8.10E-06	-38.36	8.29	8.97E-06	-38.52	8.34	9.33E-06
Cu	-32.48	7.77	5.26E-05	-32.35	7.75	5.41E-05	-32.10	7.82	7.26E-05
log *CR2*	-13.92	2.45	8.39E-08	-12.93	2.56	1.44E-06	-13.01	2.57	1.45E-06
$d_{15^\circ}^{-1/2}$	-7.74	1.19	1.65E-09	-7.92	1.20	8.99E-10	-8.09	1.23	9.84E-10
RR	-8.60	2.18	0.00013	-8.20	2.20	0.000285	-7.95	2.23	0.000516
T_{FC} (°C)	-0.21	0.08	0.01331	-0.29	0.11	0.00634	-0.30	0.11	0.00533
Constant	55.73	50.57	0.2720	107.43	64.12	0.0963	108.46	64.46	0.09492
log *CR1*				4.77	3.65	0.194	5.02	3.68	0.175
Mn	13.36	6.86	0.05353	12.39	6.88	0.07392	11.87	7.31	0.107
Cr	15.01	8.01	0.06335	15.29	8.00	0.05809	15.01	8.42	0.07709
Mo	33.81	11.31	0.00334	32.07	11.36	0.00551	31.57	11.90	0.009
Nb							72.38	89.06	0.418
C	1045.40	115.67	1.92E-15	1050.70	115.43	1.41E-15	1083.30	122.63	7.00E-15
B	13984.20	2499.10	1.25E-07	13672.20	2503.80	2.35E-07	13381.50	2542.20	5.84E-07

ITT 0.5Kvmax (24 casts)	ITT 0.5Kvmax (Autofit)			ITT 0.5Kvmax (R^2_{adj} max)			ITT 0.5Kvmax (Regress, R^2 max)		
Term	Coefficient	Std Error	Significance	Coefficient	Std Error	Significance	Coefficient	Std Error	Significance
Ti	-938.12	489.76	0.05761	-949.86	487.68	0.0536	-1271.60	557.51	0.0242
Ni	-44.98	9.63	7.39E-06	-45.46	9.60	5.59E-06	-45.75	9.66	5.72E-06
Cu	-19.39	8.96	0.03224	-21.11	9.00	0.02045	-20.72	9.06	0.02387
log *CR2*	-15.47	2.80	1.73E-07	-14.81	2.82	6.17E-07	-14.67	2.98	2.60E-06
$d_{15^\circ}^{-1/2}$	-10.74	0.94	2.00E-21	-9.36	1.32	8.53E-11	-9.35	1.42	1.05E-09
RR				-3.63	2.48	0.145	-3.58	2.58	0.169
T_{FC} (°C)	-0.26	0.09	0.00644	-0.26	0.09	0.00722	-0.29	0.12	0.02006
Constant	121.83	57.30	0.0354	103.96	58.33	0.0771	112.32	74.66	0.1350
log *CR1*							1.16	4.26	0.787
Cr							6.66	9.76	0.496
Mo	22.63	13.55	0.09737	23.68	13.51	0.08207	21.29	13.78	0.125
Mn	26.77	8.07	0.00117	29.75	8.29	0.000466	30.03	8.47	0.000547
Nb							105.02	103.15	0.311
C	1270.50	134.08	1.52E-16	1278.80	133.61	9.44E-17	1327.50	142.03	4.00E-16
B	14502.60	2799.00	8.17E-07	15552.90	2877.90	3.01E-07	15260.60	2944.30	8.35E-07

Table 43: Regression equations to ITT 27J and 0.5Kvmax., including grain size of 15° as a parameter

Toughness: ductile to brittle transition temperature Models (ºC, weight %, mm, °C/s, ºC)	R^2	R^2_{adj}	p_{max}
ITT(27J) = **50+14000B+1050C** **-40Ni+33Mo-33Cu+15Cr+13Mn-14*logCR*2 -8$d_{15^\circ}^{-1/2}$-9*RR*** **-0.2T_{FC}**	0.775	0.756	0.063
= **100+14000B+1050C** **-40Ni+32Mo-32Cu+15Cr+12Mn-13*logCR*2 -8$d_{15^\circ}^{-1/2}$-8*RR***+5*logCR*1**-0.3T_{FC}**	0.778	0.758	0.194
= **110+14000B+1100C** -100Ti +70Nb**-40Ni+32Mo-32Cu+15Cr+12Mn-13*logCR*2 -8$d_{15^\circ}^{-1/2}$-8*RR***+5*logCR*1**-0.3T_{FC}**	0.779	0.755	0.841
0.5Kvmax = **120+14500B+1270C -950Ti** **-45Ni+30Mn+23Mo-20Cu** **-15*logCR*2-10$d_{15^\circ}^{-1/2}$** **-0.3T_{FC}**	0.743	0.724	0.097
= **100+15500B+1280C -950Ti** **-45Ni+30Mn+24Mo-20Cu** **-15*logCR*2- 9$d_{15^\circ}^{-1/2}$**-4*RR* **-0.3T_{FC}**	0.747	0.726	0.145
= **110+15000B+1330C-1270Ti**+100Nb**-45Ni+30Mn+21Mo-20Cu**+7Cr **-15*logCR*2- 9$d_{15^\circ}^{-1/2}$**-4*RR*+1*logCR*1**-0.3T_{FC}**	0.750	0.723	0.787

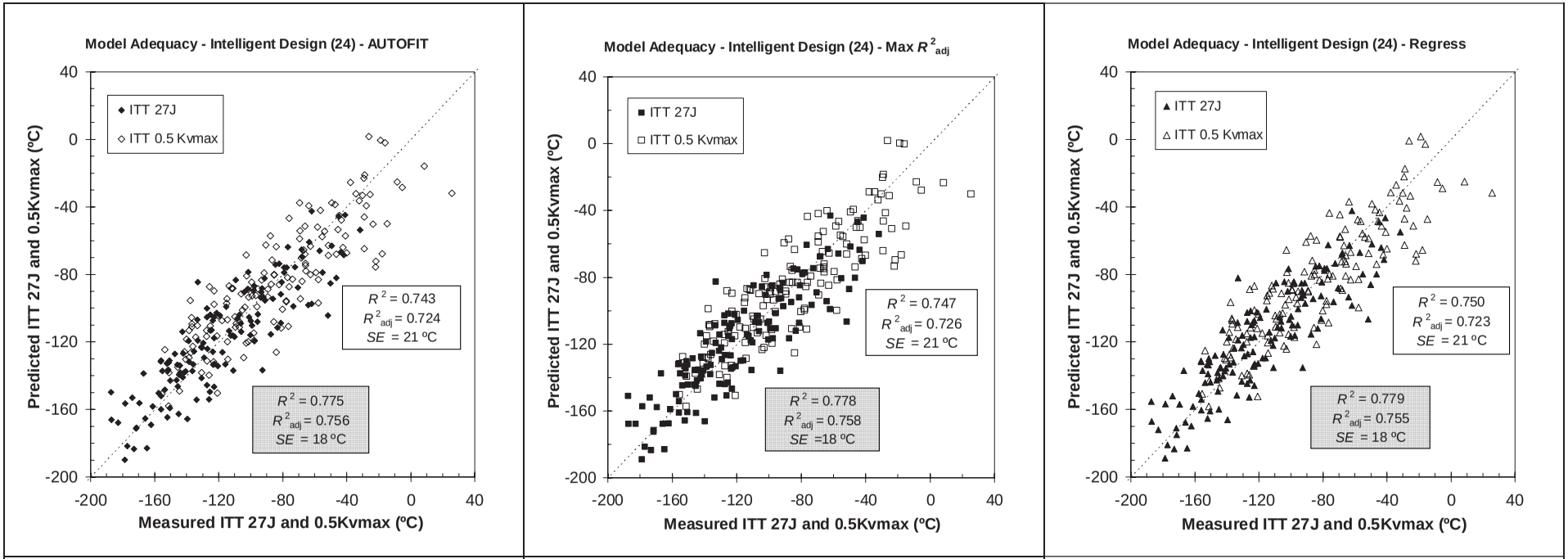

AUTOFIT ($p < 0.1$)	Max R^2_{adj}	REGRESS (Max R^2)

Figure 19: Experimental vs. predicted plot for ITT 27J and 0.5Kvmax. of 15° as a parameter for the 24 casts, including grain size

Toughness – without considering the grain size of 15°

Table 44: Coefficients, Standard Errors and Significances of variables for ITT 27J and 0.5Kvmax.

ITT 27J (24 casts)	ITT 27J (Autofit)			ITT 27J (R^2_{adj} max)			ITT 27J (Regress, R^2max)		
Term	Coefficient	Std Error	Significance	Coefficient	Std Error	Significance	Coefficient	Std Error	Significance
Ti				(Idem Autofit)			-197.388	555.493	0.723
Cu	-41.264	8.766	6.297E-06				-40.907	8.902	1.021E-05
Ni	-40.183	9.524	4.549E-05				-40.081	9.625	5.699E-05
Nb							-20.509	101.538	0.840
RR	-18.782	1.736	6.971E-20				-18.717	1.760	2.531E-19
log*CR2*	-10.311	2.735	2.457E-04				-9.874	2.919	9.534E-04
T_{FC}	-0.212	0.094	0.026				-0.247	0.123	0.047
Constant	-58.706	54.328	0.282				-36.199	70.000	0.606
log*CR1*							1.927	4.216	0.648
Mn	28.335	7.400	1.986E-04				29.200	7.880	3.125E-04
Cr	29.187	8.839	1.236E-03				30.597	9.335	1.348E-03
Mo	39.203	12.930	2.930E-03				36.968	13.709	7.950E-03
C	1094.998	132.297	1.267E-13				1085.562	141.586	3.864E-12
B	19765.693	2676.438	1.583E-11				19746.949	2716.042	3.150E-11

TT 0.5Kvmax (24 casts	ITT 0.5Kvmax (Autofit)			ITT 0.5Kvmax (R^2_{adj} max)			ITT 0.5Kvmax (Regress, R^2 max)		
Term	Coefficient	Std Error	Significance	Coefficient	Std Error	Significance	Coefficient	Std Error	Significance
Ti	-1391.577	586.218	1.907E-02	(Idem Autofit)			-1387.952	643.018	0.033
Ni	-47.433	11.058	3.464E-05				-47.551	11.141	3.807E-05
Cu	-30.936	10.231	3.008E-03				-30.903	10.304	3.255E-03
RR	-15.932	2.016	1.005E-12				-16.019	2.037	1.339E-12
log*CR2*	-10.501	3.175	0.001				-11.043	3.379	1.391E-03
logCR1							-2.423	4.880	0.620
Nb							-2.345	117.537	0.984
T_{FC}	-0.271	0.109	0.014				-0.226	0.143	0.115
Constant	-30.082	63.189	0.635				-54.885	81.030	0.499
Cr	24.987	10.701	0.021				24.675	10.806	0.024
Mo	26.691	15.625	0.090				27.526	15.870	0.085
Mn	49.743	9.035	1.890E-07				50.060	9.121	2.092E-07
C	1334.527	153.731	1.410E-14				1330.185	163.895	3.437E-13
B	22522.588	3107.195	3.347E-11				22617.925	3143.986	4.698E-11

Table 45: Regression equations for ITT 27J and 0.5Kvmax.

Toughness: ductile to brittle transition temperatures Models (ºC, weight %, °C/s, ºC)	R^2	R^2_{adj}	p_{max}
ITT 27J = **-60+20000B+1100C -40Cu-40Ni+40Mo+30Cr+30Mn -20*RR*-10*logCR2* -0.2T_{FC}**	0.702	0.680	0.026
= **-60+20000B+1100C -40Cu-40Ni+40Mo+30Cr+30Mn -20*RR*-10*logCR2* -0.2T_{FC}**	0.702	0.680	0.026
= **-35+20000B+1100C** -200Ti-**40Cu-40Ni+37Mo+30Cr+30Mn**-20Nb-**20*RR*-10*logCR2***+2*logCR1*-**0.2T_{FC}**	0.704	0.674	0.840
0.5Kvmax = **-30+22500B+1350C-1400Ti+50Mn-50Ni-30Cu+27Mo+25Cr -16*RR*-11*logCR2* -0.3T_{FC}**	0.664	0.636	0.090
= **-30+22500B+1350C-1400Ti+50Mn-50Ni-30Cu+27Mo+25Cr -16*RR*-11*logCR2* -0.3T_{FC}**	0.664	0.636	0.090
= **-55+22600B+1350C-1400Ti+50Mn-50Ni-30Cu+30Mo+25Cr** -2Nb-**16*RR*-11*log*CR2**-2*logCR1*-**0.2T_{FC}**	0.665	0.631	0.984

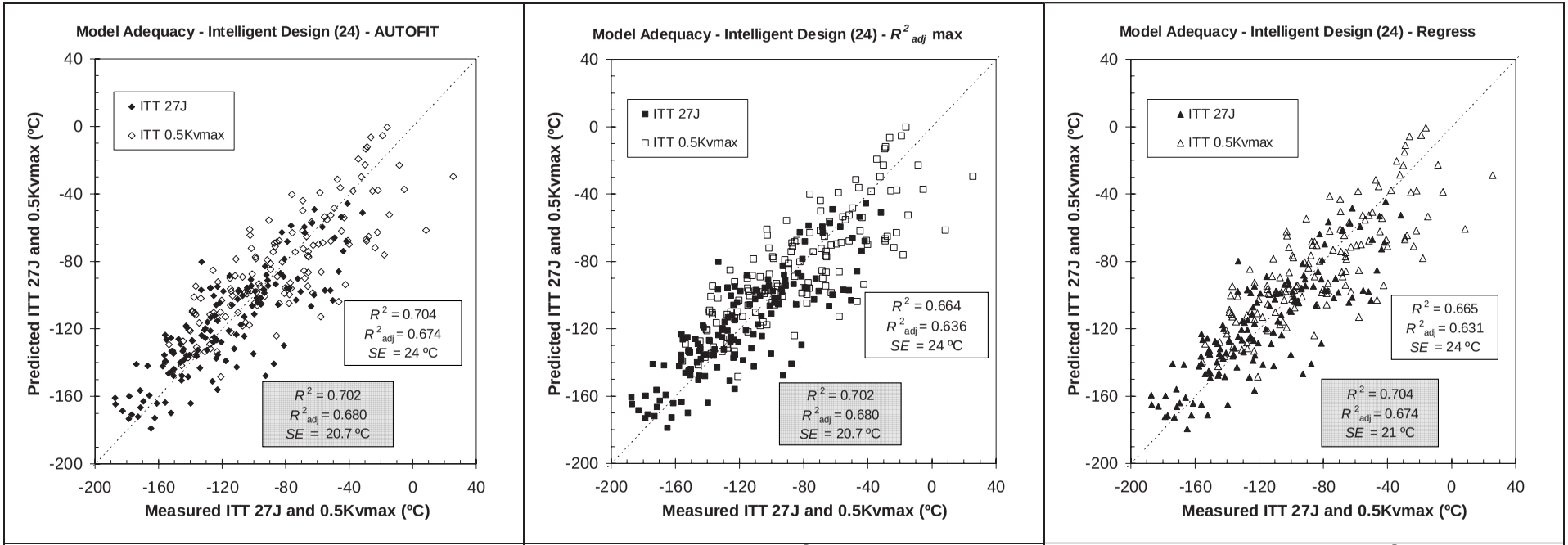

AUTOFIT ($p < 0.1$) | Max R^2_{adj} | REGRESS (Max R^2)

Figure 20: Experimental vs. predicted plot for ITT 27J and 0.5Kvmax , for the 24 casts

6.1.10 Welding simulations

6.1.10.1 Experimental method and results

Weld simulation was carried out by reheating to 1250°C followed by controlled cooling. Two cooling conditions were used having cooling times of 8 s and 30 s through the range 800 - 500 °C. Brittle fracture resistance was determined on parent and simulated HAZ material from laboratory rolled test plates by producing Charpy V notch impact transition curves and determining the transition temperatures and measuring the hardness of the microstructure, Table 46. The duplication of hot rolled plate transition curves, which should have been consistent with the properties of air-cooled plate, enabled the mis-identification of two plates to be realised and corrected. The results of cast A029 show higher transition temperatures; this steel was the one found on analysis to have low aluminium and titanium contents.

Table 46: Hardness and toughness of welding tests

Cast	8s ITT 0.5Kvmax (°C)	30s ITT 0.5Kvmax (°C)	Parent (HV5)	8s (HV5)	30s (HV5)	8s 27J ITT (°C)	30s 27J ITT (°C)
A027	-40	-48	184	236	215	-60	-65
A028	-60	-56	168	231	224	-79	-80
A029	20	28	170	238	214	7	13
A030	-50	-46	186	252	242	-90	-80
A031	-33	-27	164	249	240	-92	-48
A032	-51	-49	194	273	252	-100	-78
A033	-40	-31	184	249	248	-90	-75
A034	-54	-65	198	255	228	-85	-78
A035	-38	-60	184	226	230	-58	-95
A036	-45	-67	206	257	239	-97	-98
A037	-51	-63	202	261	256	-95	-83
A038	-70	-55	232	293	294	-98	-85
A202	-48	-42	181	266	250	-85	-82
A203	-50	-55	236	265	245	-100	-85
A041	-47	-61	213	295	279	-97	-90
A042	-70	-68	275	331	300	-100	-98
A043	-46	-47	169	239	203	-84	-87
A044	-53	-50	176	241	228	-78	-79
A045	0	4	256	312	286	-37	-39
A046	-52	-72	222	335	322	-98	-95
A047	-70	-48	207	306	296	-102	-79
A048	-82	-45	259	304	281	-98	-71
A049	-41	-33	202	299	258	-78	-58
A050	-19	-13	270	314	295	-61	-20
Validation casts							
A039	-17	-13	266	337	291	-67	-39
A040	-33	-25	224	365	319	-85	-38
81913	-65	-60	175	256	218	-75	-72
16685	-33	-13	181	288	252	-65	-50
30257	-30	-45	212	259	247	-70	-70

6.1.10.1.1 Regression analysis

Table 47: Coefficients, Standard Errors and Significances of variables for parent material hardness.

HV5 (24 casts)	HV5 Parent Material (Autofit)			HV5 Parent Material (R^2_{adj} max)			HV5 Parent Material (Regress, R^2 max)		
Term	Coefficient	Std Error	Significance	Coefficient	Std Error	Significance	Coefficient	Std Error	Significance
Cu							-2.17	16.24	0.8954
Constant	13.09	25.39	0.6122	8.60	24.79	0.7330	-3.19	31.99	0.9220
Ti							5.95	1026.61	0.9955
Cr				21.83	14.84	0.1597	21.26	16.71	0.2239
Mo	47.77	22.57	0.0485	47.34	21.88	0.0450	47.73	24.50	0.0717
Ni	50.57	16.63	0.0070	50.18	16.12	0.0063	49.39	17.51	0.0136
Mn	60.03	12.84	0.0002	59.60	12.44	0.0002	58.52	14.42	0.0012
Nb							118.49	185.63	0.5336
C	1021.39	233.25	0.0004	1024.76	226.08	0.0003	1081.95	259.09	0.0009
B	26731.78	4714.84	2.23E-05	26449.88	4573.67	2.21E-05	26230.96	4997.47	1.23E-04

Table 48: Coefficients, Standard Errors and Significances of variables for Heat Affected Zone (HAZ) hardness.

HV5 (24 casts)	HV5 HAZ (Autofit)			HV5 HAZ (R^2_{adj} max)			HV5 HAZ (Regress, R^2 max)		
Term	Coefficient	Std Error	Significance	Coefficient	Std Error	Significance	Coefficient	Std Error	Significance
Cu							4.131	13.75	0.766
Ni				22.11	14.53	0.136	22.37	14.83	0.140
Constant	24.76	29.49	0.406	23.93	29.02	0.415	25.43	29.69	0.397
log*CR*	29.18	9.414	0.00354	29.18	9.262	0.00313	29.18	9.446	0.00380
Cr	33.57	13.59	0.01784	33.30	13.37	0.01713	30.99	14.15	0.03490
Mn	45.90	11.46	0.000262	44.90	11.30	0.000295	42.14	12.21	0.00141
Mo	59.30	20.00	0.00509	58.91	19.68	0.00478	61.99	20.75	0.00496
Nb	266.22	144.50	0.07286	253.85	142.42	0.08246	215.61	157.22	0.179
Ti							517.39	869.45	0.555
C	1359.8	216.82	1.9622E-07	1336.5	213.89	2.3394E-07	1319.8	219.43	5.9988E-07
B	18021.3	4195.5	0.000108	17909.2	4128.8	9.853E-05	17759.6	4232.5	0.000163

Table 49: Regression equations for welding parameters.

Weldability: Hardness Models (kgf/mm^2, weight %, s)	R^2	R^2_{adj}	p_{max}
HV5 PM = **13+27000B+1020C** **+50Mo+60Mn** **+50Ni**	0.843	0.799	0.049
= **9+26500B+1025C** **+50Mo+60Mn**+20Cr **+50Ni**	0.860	0.811	0.160
= **-3+26000B+1080C** +6Ti+120Nb **+50Mo+60Mn**+20Cr **+50Ni**-2Cu	0.865	0.779	0.996
HV5 HAZ = **25+18000B+1360C** **+270Nb+60Mo+46Mn+34Cr** **+30*logCR***	0.730	0.683	0.073
= **24+18000B+1340C** **+250Nb+60Mo+45Mn+33Cr**+22Ni **+30*logCR***	0.745	0.693	0.136
= **24+18000B+1340C**+520Ti**+215Nb+60Mo+42Mn+30Cr**+22Ni+4Cu**+30*logCR***	0.749	0.681	0.766

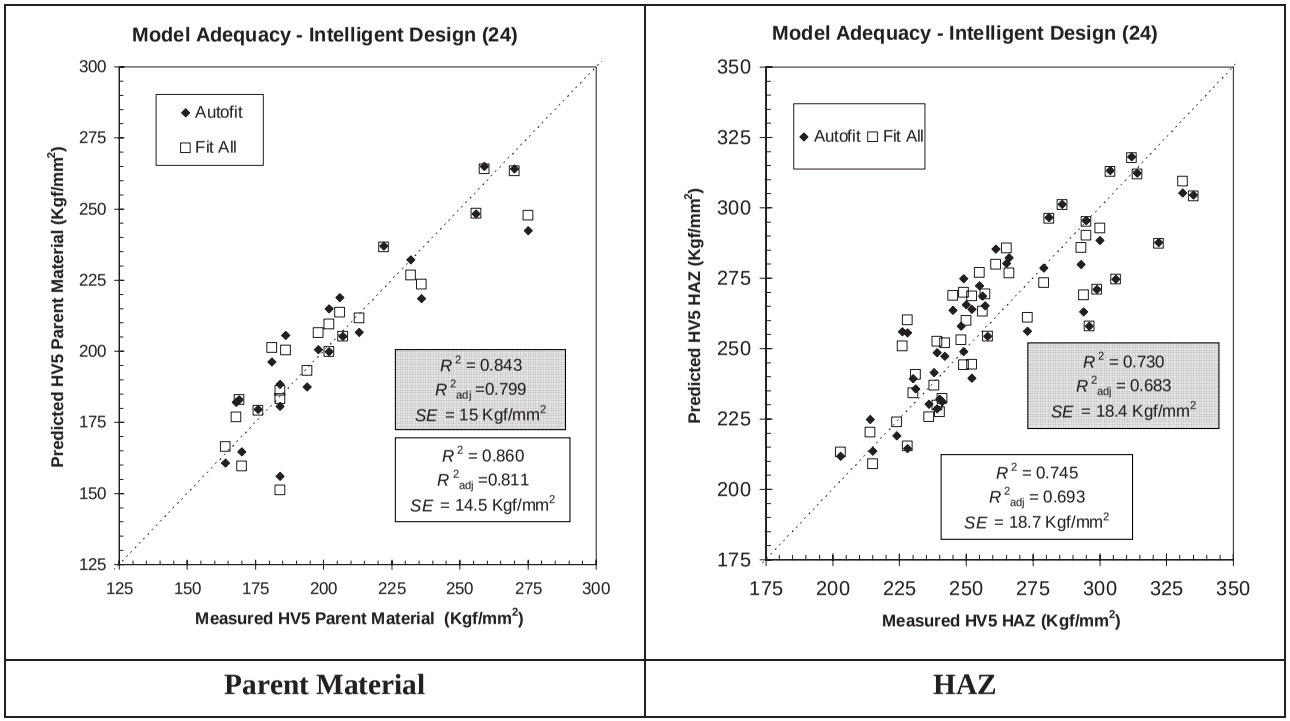

Figure 21: Experimental vs. predicted plots for Parent material and HAZ hardness, for the 24 casts

Table 50: Coefficients, Standard Errors and Significances of variables for the transition temperatures (ITT 27J and 0.5Kvmax) of welds

ITT 27J (24 casts)	ITT 27J (Autofit)			ITT 27J (R^2_{adj} max)			ITT 27J (Regress, R^2_{max})		
Term	Coefficient	Std Error	Significance	Coefficient	Std Error	Significance	Coefficient	Std Error	Significance
Nb				-123.82	164.09	0.4550	-141.65	185.93	0.4511
Ni	-42.86	17.44	0.0180	-45.07	16.74	0.0104	-41.63	17.62	0.0237
Mn	-38.87	13.45	0.0060	-36.59	13.07	0.0079	-33.31	16.20	0.0470
Cr	-29.54	16.07	0.0728	-29.10	15.39	0.0661	-27.65	17.35	0.1197
Cu				-25.77	15.39	0.1019	-26.73	15.88	0.1010
HV5							-0.156	0.190	0.4172
Constant	10.02	24.55	0.6850	-0.50	30.55	0.9871	12.28	34.95	0.7273
$t_{8/5}$				0.42	0.28	0.1422	0.298	0.319	0.3560
Mo							20.96	26.67	0.4370
C				303.26	246.85	0.2266	493.50	356.00	0.1742
Ti							842.88	1007.8	0.4085
B				6782.13	4773.87	0.1634	9513.6	5931.8	0.1175

ITT 0.5Kvmax (24 casts)	ITT 0.5Kvmax (Autofit)			ITT 0.5Kvmax (R^2_{adj} max)			ITT 0.5Kvmax (Regress, R^2 max)		
Term	Coefficient	Std Error	Significance	Coefficient	Std Error	Significance	Coefficient	Std Error	Significance
Nb				-179.15	145.83	0.2260	-174.19	170.57	0.3140
Ni	-44.96	15.01	0.0045	-43.87	14.95	0.0053	-40.43	16.17	0.0171
Mn	-31.21	11.56	0.0098	-29.22	11.61	0.0156	-23.06	14.86	0.1294
Cu							-14.58	14.57	0.3237
Cr							-6.53	15.91	0.6839
HV5							-0.18	0.17	0.3027
$t_{8/5}$							-0.10	0.29	0.7376
Constant	0.74	22.45	0.9739	18.96	26.80	0.4831	34.47	32.07	0.2895
Mo							17.19	24.46	0.4867
C	472.67	210.50	0.0298	388.86	220.14	0.0844	632.84	326.60	0.0605
Ti							707.41	924.60	0.4492
B							5449.35	5441.97	0.3233

Table 51: Regression equations for the transition temperatures of welds

Weldability: ductile to brittle transition temperatures Models (ºC, weight %, °C/s, ºC, kgf/mm^2)	R^2	R^2_{adj}	p_{max}
ITT 27J = **10** **-45Ni-40Mn-30Cr**	0.305	0.258	0.073
= **-0.5** +6800B +300C-125Nb **-45Ni-40Mn-30Cr**-26Cu	0.437	0.322	0.455
= **12** +9500B+850Ti+500C-140Nb **-40Ni-30Mn-30Cr**-27Cu+20Mo+0.3$t_{8/5}$-0.2*HV5*	0.458	0.292	0.451
ITT 0.5Kvmax = **0.8** **+480C** **-45Ni-30Mn**	0.326	0.280	0.030
= **20** **+390C** -180Nb **-45Ni-30Mn**	0.349	0.289	0.226
= **35** +5500B+700Ti **+630C**-175Nb **-40Ni-25Mn** -7Cr-15Cu+17Mo-0.1$t_{8/5}$-0.2*HV5*	0.401	0.218	0.738

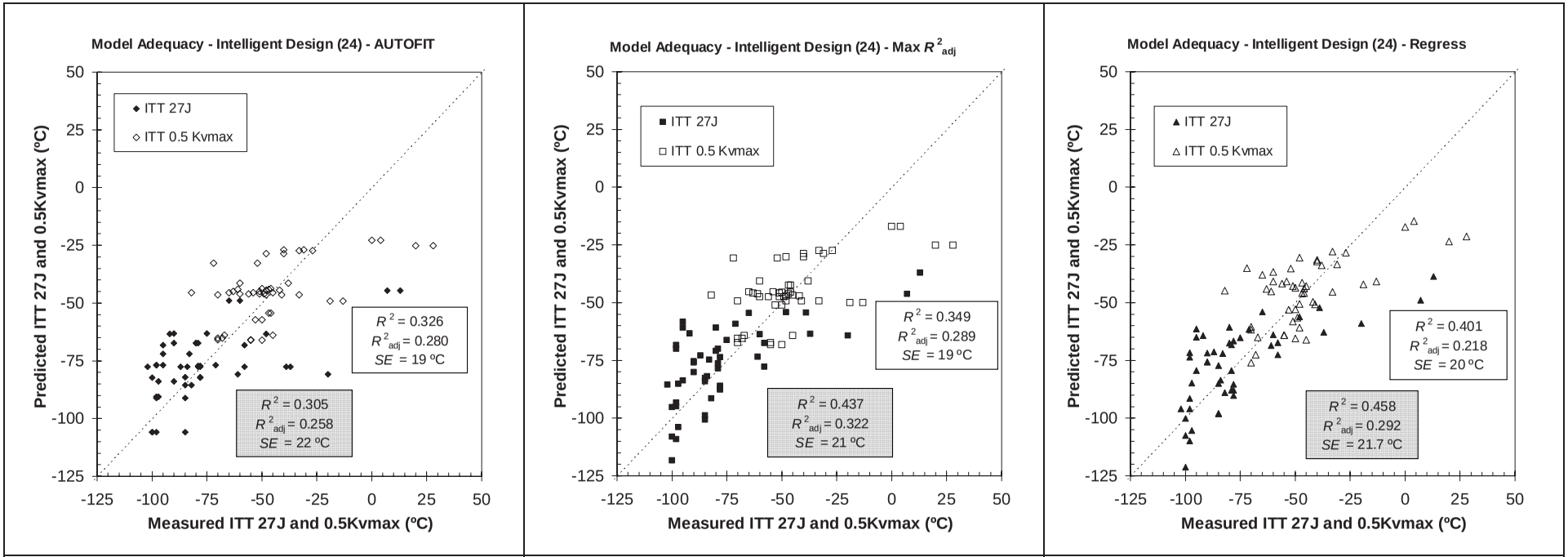

AUTOFIT ($p < 0.1$)	Max R^2_{adj}	Regress (Max R^2)

Figure 22: Experimental vs. predicted plot for ITT 27J and 0.5Kvmax, for the 24 casts

6.1.11 Validation of lab simulations

6.1.11.1 EBSD measurements

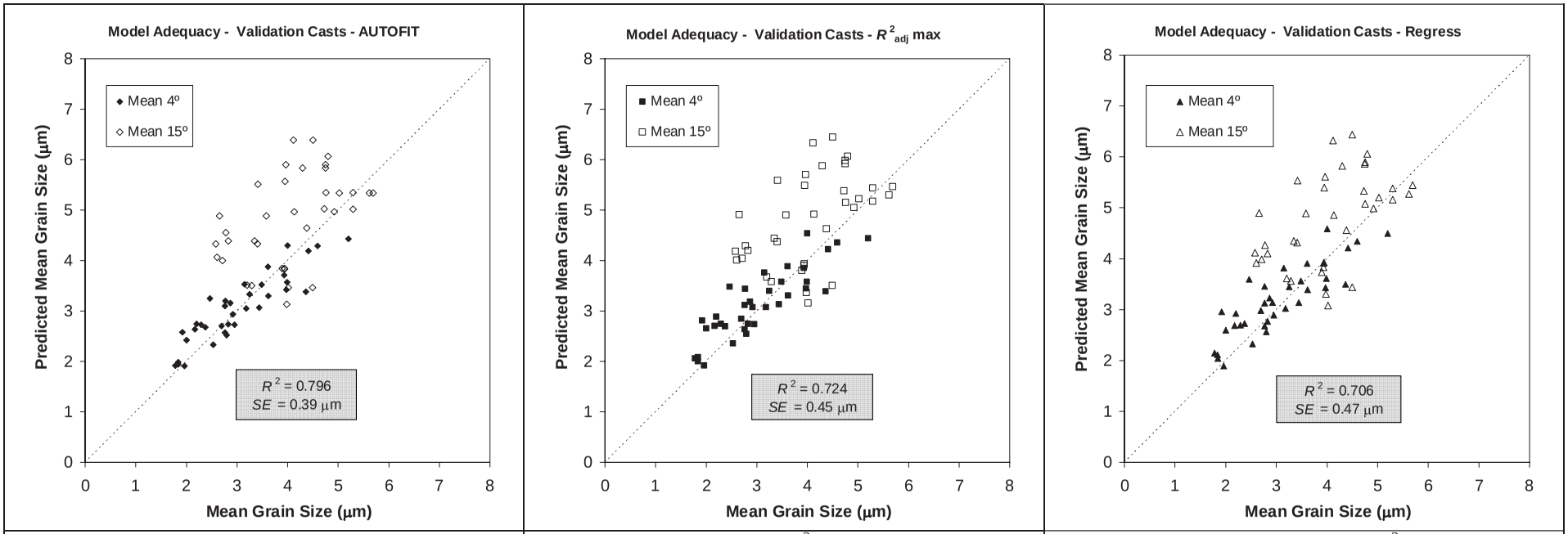

AUTOFIT ($p < 0.1$)	Max R^2_{adj}	REGRESS (Max R^2)

Figure 23: Experimental vs. predicted plot for grain size measurements of 4º and 15º, for the 6 validation casts

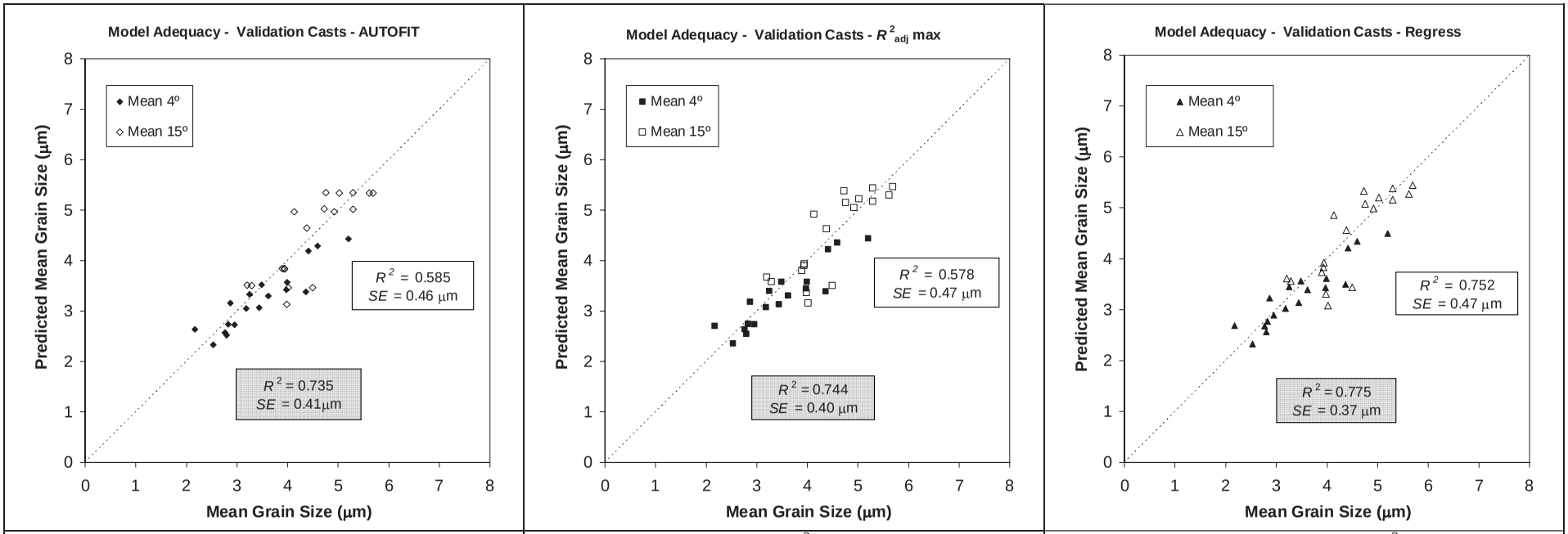

AUTOFIT ($p < 0.1$)	Max R^2_{adj}	REGRESS (Max R^2)

Figure 24: Experimental vs. predicted plot for grain size measurements of 4º and 15º, only for casts: 81913, 16685 and 02098 (validation casts)

6.1.11.2 Dilatometry

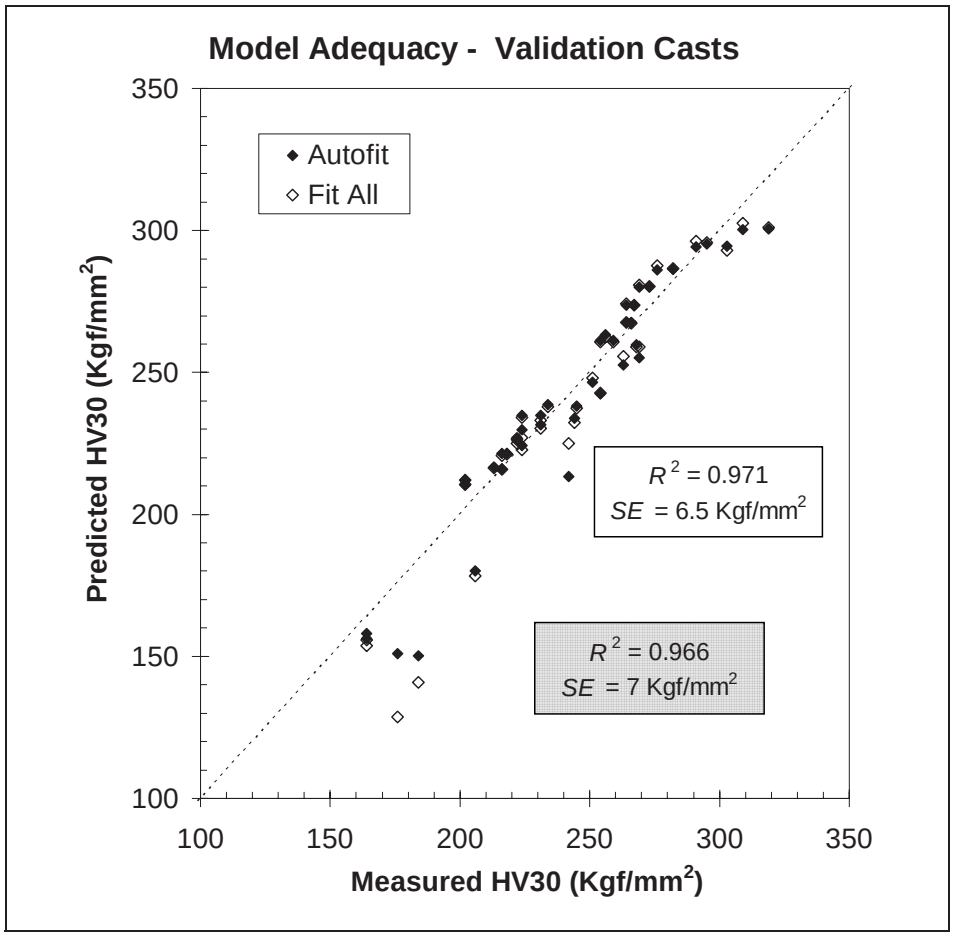

Figure 25: Experimental vs. predicted plots for CCT hardness, for the validation casts

The predictions for the 24 casts and the 6 validation casts show that the models obtained are able to predict hardness fairly accurately.

6.1.11.3 Torsion tests

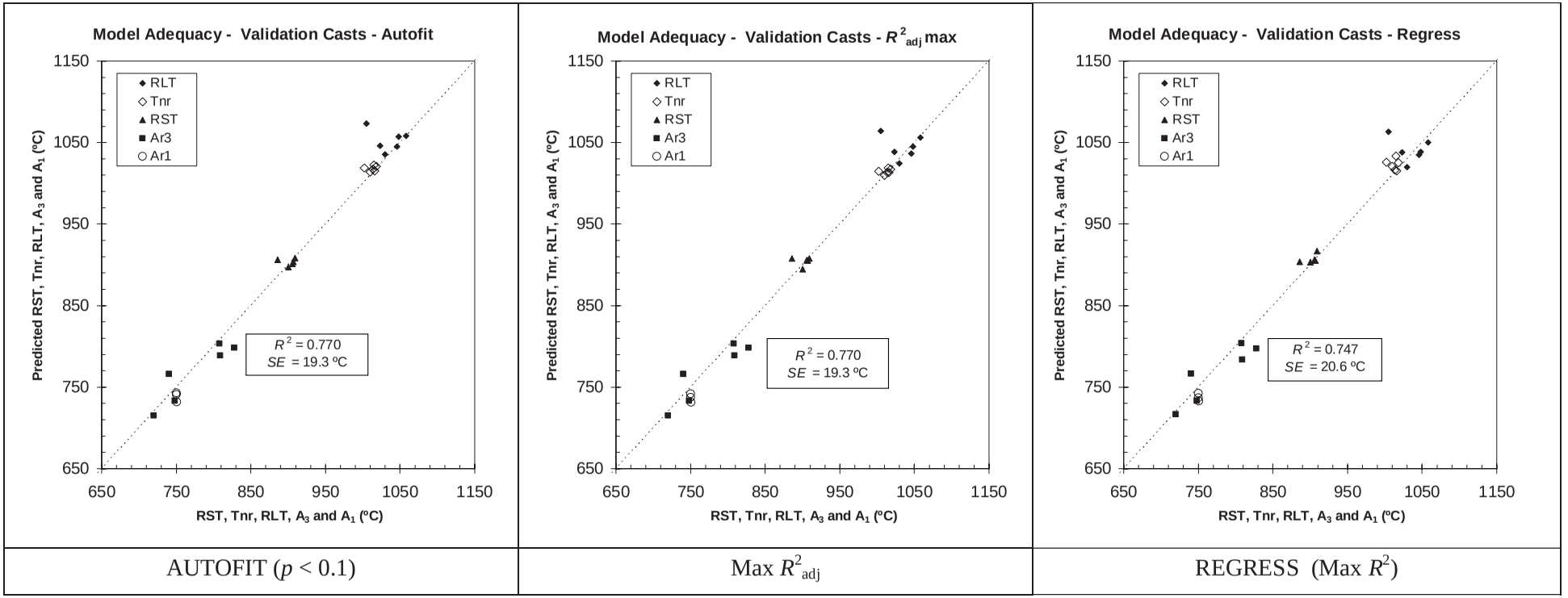

AUTOFIT ($p < 0.1$)	Max R^2_{adj}	REGRESS (Max R^2)

Figure 26: Experimental vs. predicted plots for Critical and Phase Transformation Temperatures, for Validation casts

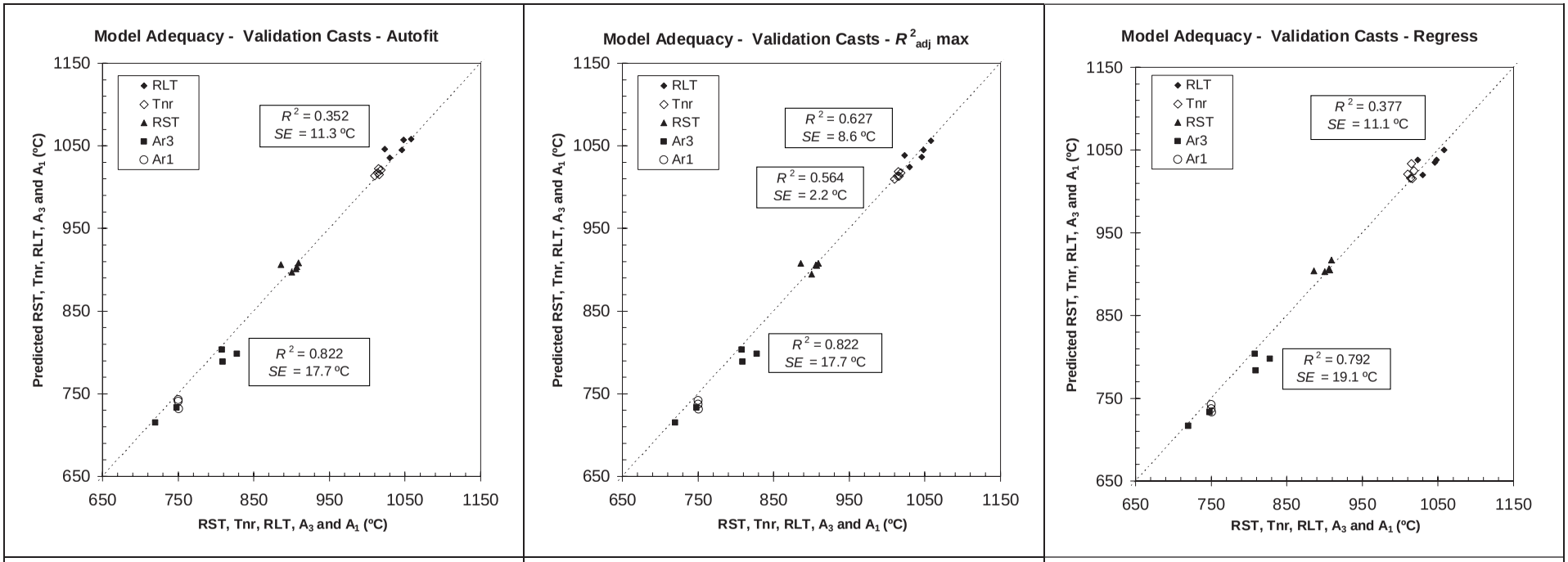

AUTOFIT ($p < 0.1$)	Max R^2_{adj}	REGRESS (Max R^2)

Figure 27: Experimental vs. predicted plots for Critical and Phase Transformation Temperatures, for Validation casts (excluding Ruukki cast 81351)

6.1.11.4 Tensile tests

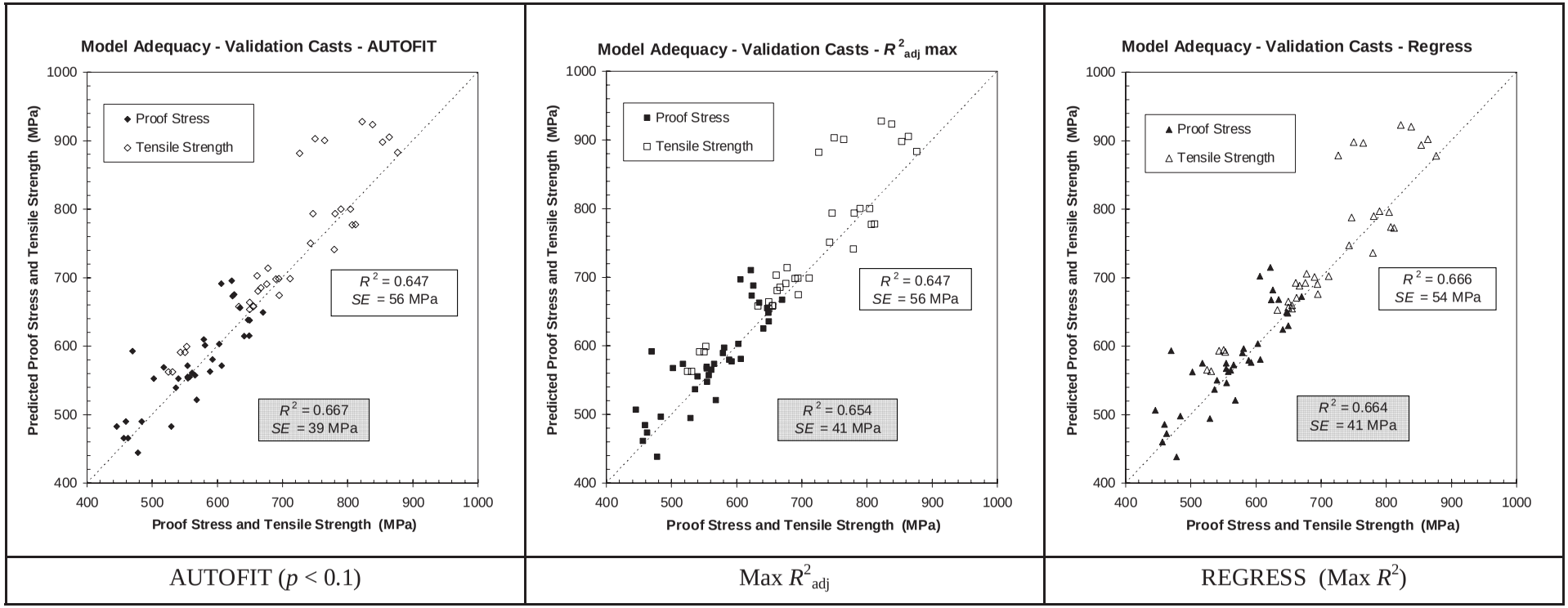

AUTOFIT ($p < 0.1$)	Max R^2_{adj}	REGRESS (Max R^2)

Figure 28: Experimental vs. predicted plot for Proof stress and Tensile strength, for validation casts

6.1.11.5 Charpy impact tests

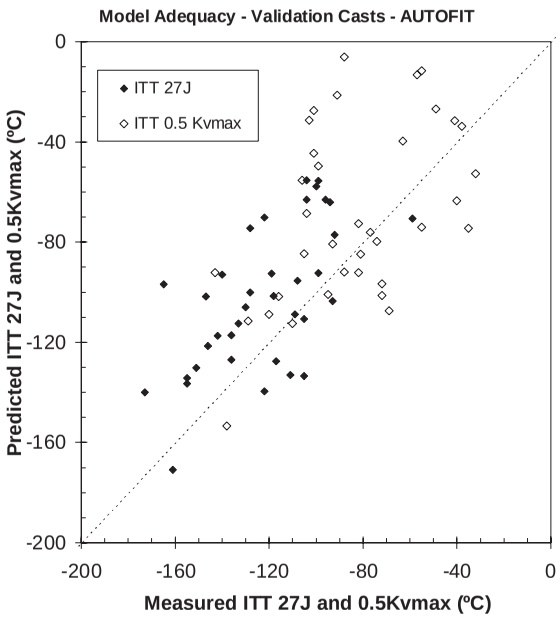

AUTOFIT ($p < 0.1$)

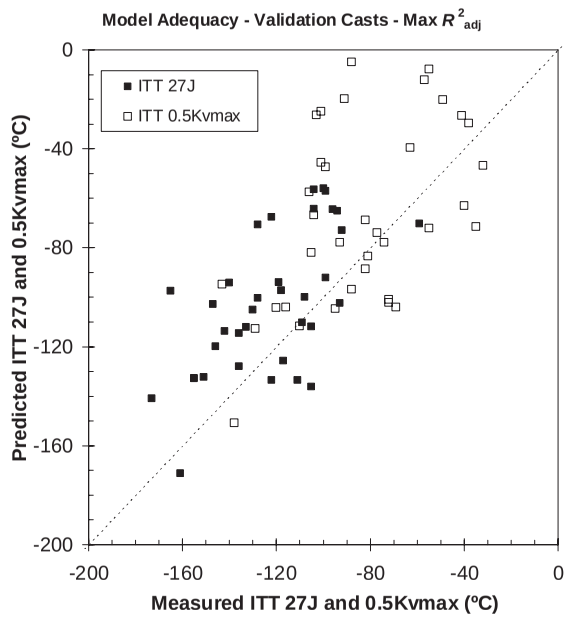

Max R^2_{adj}

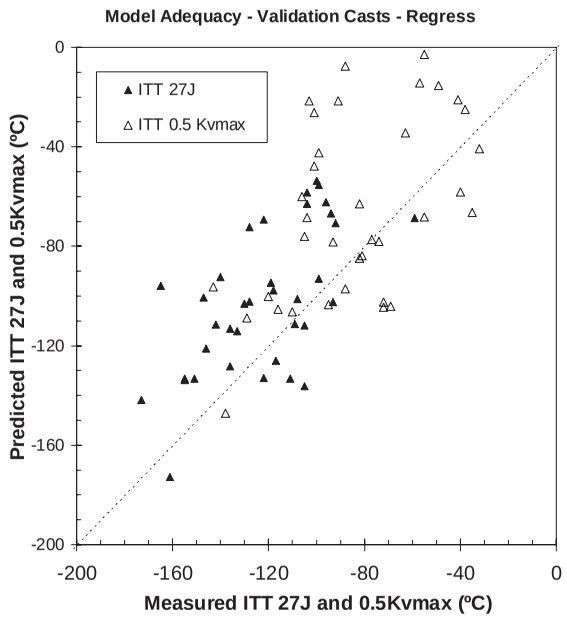

REGRESS (Max R^2)

Figure 29: Experimental vs. predicted plot for ITT 27J and 0.5Kvmax, for the validation casts

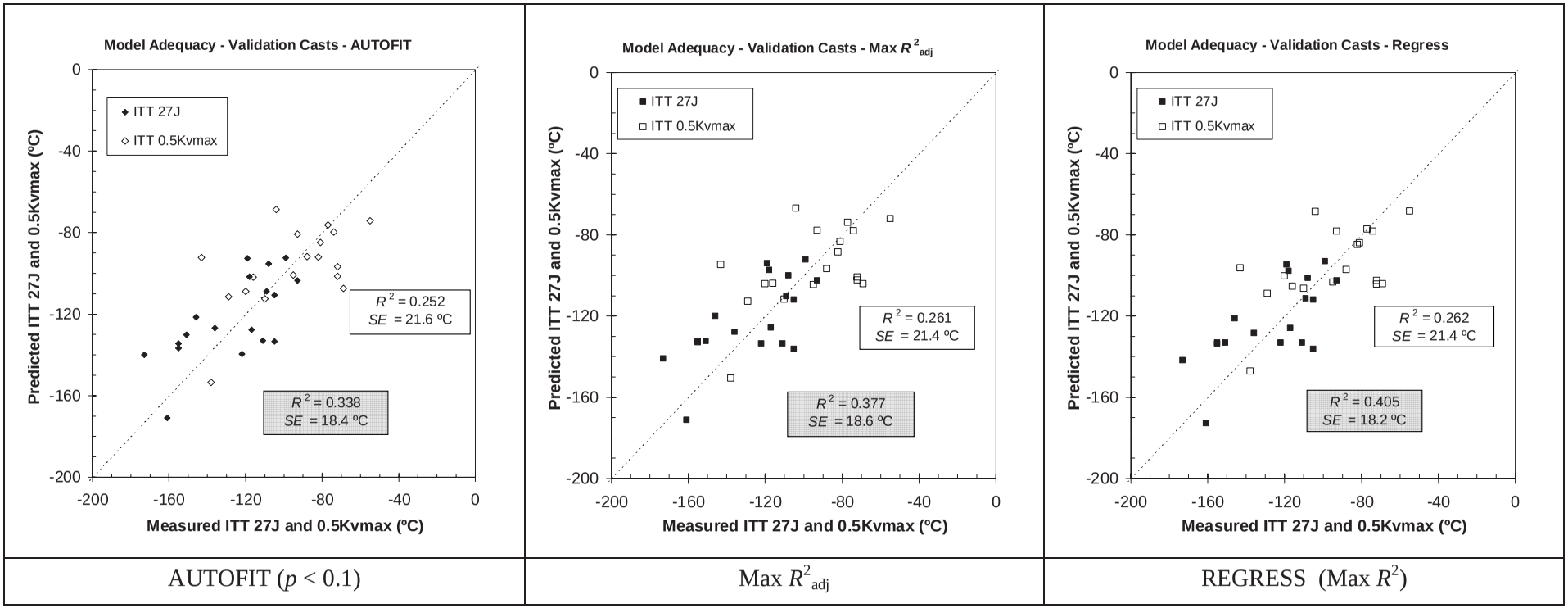

AUTOFIT ($p < 0.1$)	Max R^2_{adj}	REGRESS (Max R^2)

Figure 30: Experimental vs. predicted plot for ITT 27J and 0.5Kvmax , only for 81913, 16685 and 81351 casts (validation casts)

6.1.11.6 Welding simulation

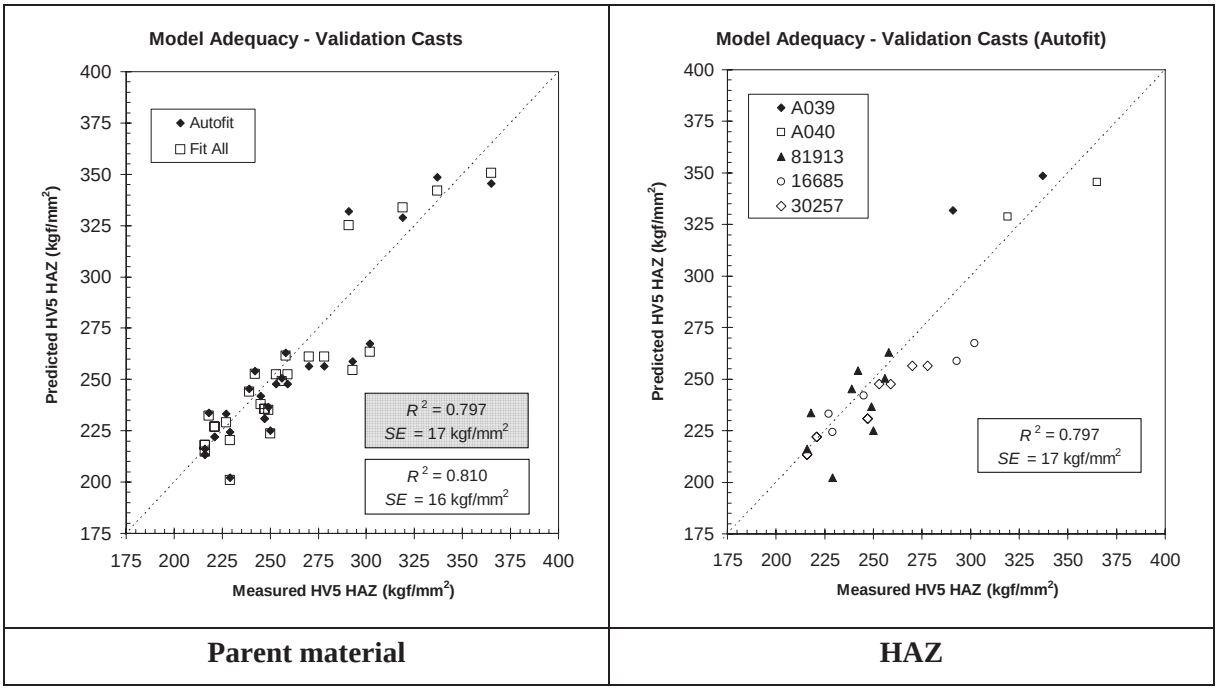

Figure 31: Experimental vs. predicted plots for parent material and HAZ hardness, for the validation casts

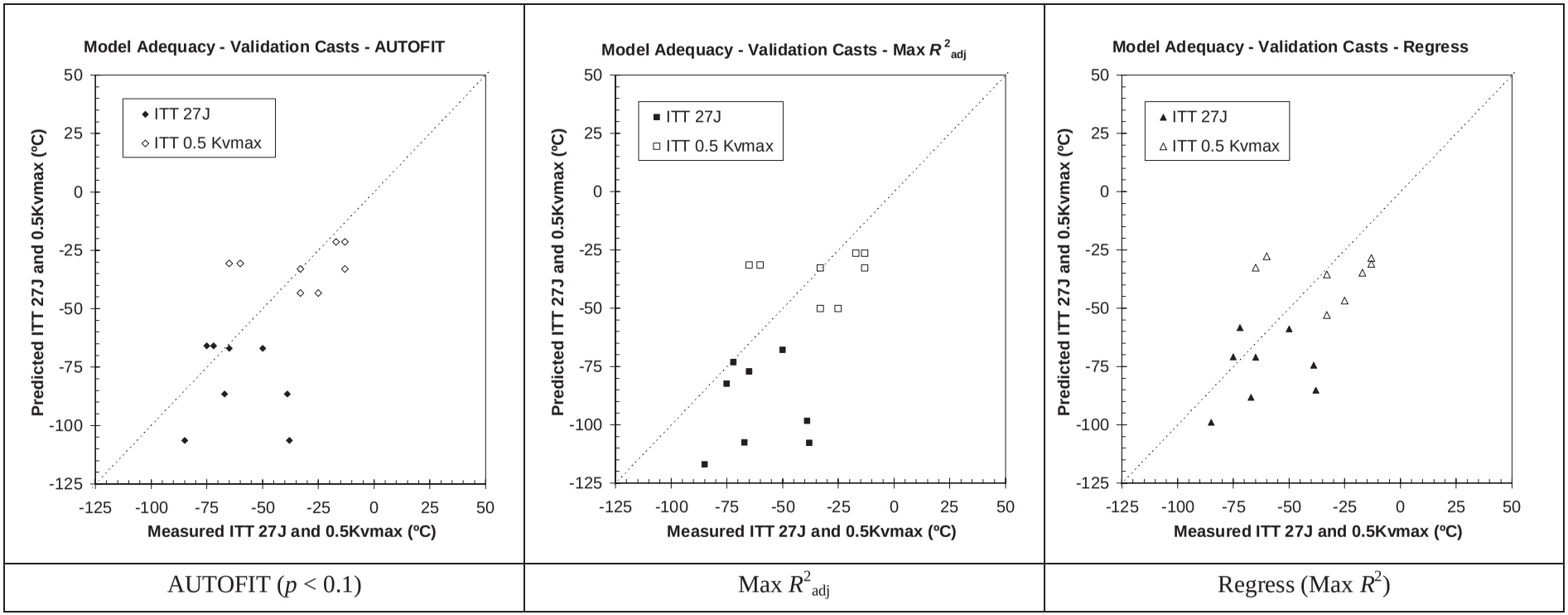

AUTOFIT ($p < 0.1$)	Max R^2_{adj}	Regress (Max R^2)

Figure 32: Experimental vs. predicted plot for ITT 27J and 0.5Kvmax, for the validation casts

6.1.12 Conclusions from the regression analyses

The regression analyses have shown that equations based on the results of the twenty-four compositions under the six rolling conditions could be used to predict the results of other compositions processed in the laboratory under similar conditions by using the logarithms of the cooling rates between 850°C and 550°C, logCR1, and between 550°C and 20°C.

6.2 Thick-walled welded pipe

The aim of this work-package was to determine the properties that could be obtained in plates processed in the air-cooled condition. Plates of 14.6 mm, 20.9 mm and 25.4 mm thickness were produced and processed to pipe using the UOE forming method.

6.2.1 Composition and Processing

All of the plates were produced from cast 81913, which had the analysis shown in Table 52.

Table 52: Composition of cast 81913

C	Si	Mn	P	S	Al	Nb	V	Cu
0.053	0.18	1.59	0.013	0.0038	0.037	0.097	0.001	0.23
Cr	Ni	N	Mo	Ti	Ca	B	Pcm	CEV
0.26	0.17	0.006	0.002	0.016	0.0013	-	0.17	0.40

The processing conditions are summarised in Table 53.

Table 53: Details of the evaluated plates and pipes

Product ID	Slab size (mm)	Transfer bar thickness (mm)	SRT (°C)	EHT (°C)	FRT (°C)	Plate thickness (mm)	Reduction Ratio	Processed to pipe	Pipe outer diameter (mm)
PE111	230 x 1610	54.3	1198	859	775	14.6	3.7	YBWA1	610
PB329	230 x 1970	86.3	1236	798	708	20.9	4.1	YBRP2	914
PA665	230 x 1970	80	1182	798	720	25.4	3.1	YBRM1	914
PA666	230 x 1970	80	1196	780	715	25.4	3.1	YBRM3	914
PC943	230 x 1970	105	1195	824	712	25.4	4.1		

The steel was also processed on a laboratory mill to produce three 20 mm thick plates to study the effect of finish rolling temperature on the microstructure and mechanical properties in the air-cooled condition. Feedstock from the 50 mm thick plate rolled in work-package 4 was reheated to 1220°C and rolled to 20 mm thickness with pass exit thickness values of 40, 32, 27, 23 and 20 mm. The finish rolling temperatures were 880, 950 and 1031°C.

6.2.2 Mechanical Properties

The measured tensile, impact and drop weight tear test properties of the commercially processed plates and pipes are shown in Table 54. Elongation, A, values on plate material are for a 200 mm gauge length while those for pipe are for a 50 mm gauge length.

Table 54: Mechanical properties of commercially processed plates and pipes

Product ID	Product	t (mm)	RR	FRT (°C)	$R_{t0.5}$ (MPa)	R_m (MPa)	A (%)	R_t/R_m	27 J ITT (°C)	0.5Kvmax ITT (°C)	DWTT (°C)
PE111	Plate	14.6	3.7	775	439	533	26	0.82	-110	-90	-60
PB329	Plate	20.9	4.1	708	533	592	18	0.90	-100	-85	-40
PA665	Plate	25.4	3.1	720	479	541	18	0.89		-85	
PA666	Plate	25.4	3.1	715	512	581	23	0.88	-90	-75	-10
PC943	Plate	25.4	4.1	712	496	543	22	0.91	-140	-140	-35
YBWA1	Pipe	14.6	3.7		564	579	41	0.97	-110	-90	-60
YBRP2	Pipe	20.9	4.1		513	611	44	0.84	-100	-85	-45
YBRM1	Pipe	25.4	3.1		478	554	51	0.86			
YBRM3	Pipe	25.4	3.1		488	586	45	0.83	-90	-75	-15

The impact transition curves are shown in Figure 33 and the drop weight tear test transition curves are shown in Figure 34.

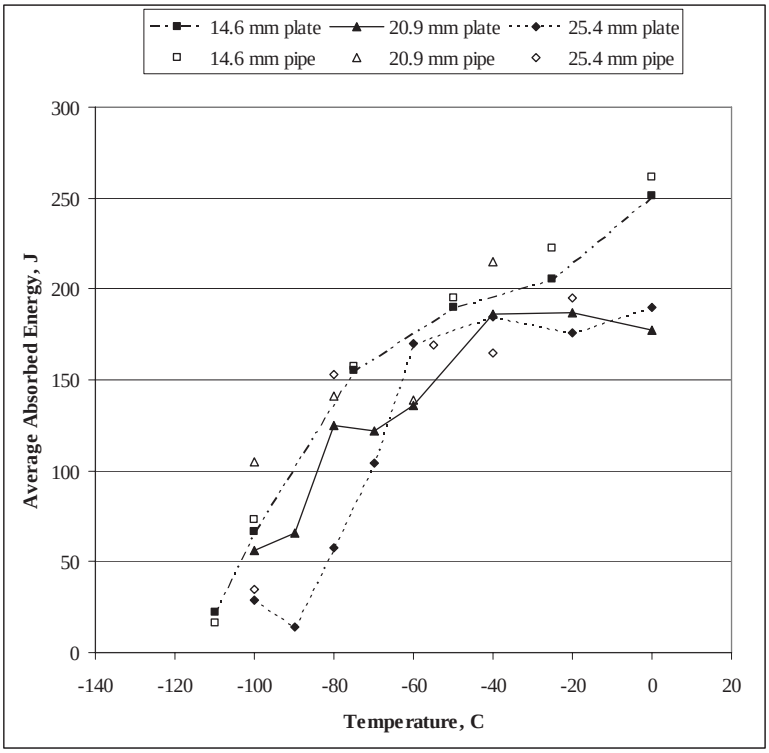

Figure 33: Impact transition curves for average values of absorbed energy in the transverse orientation

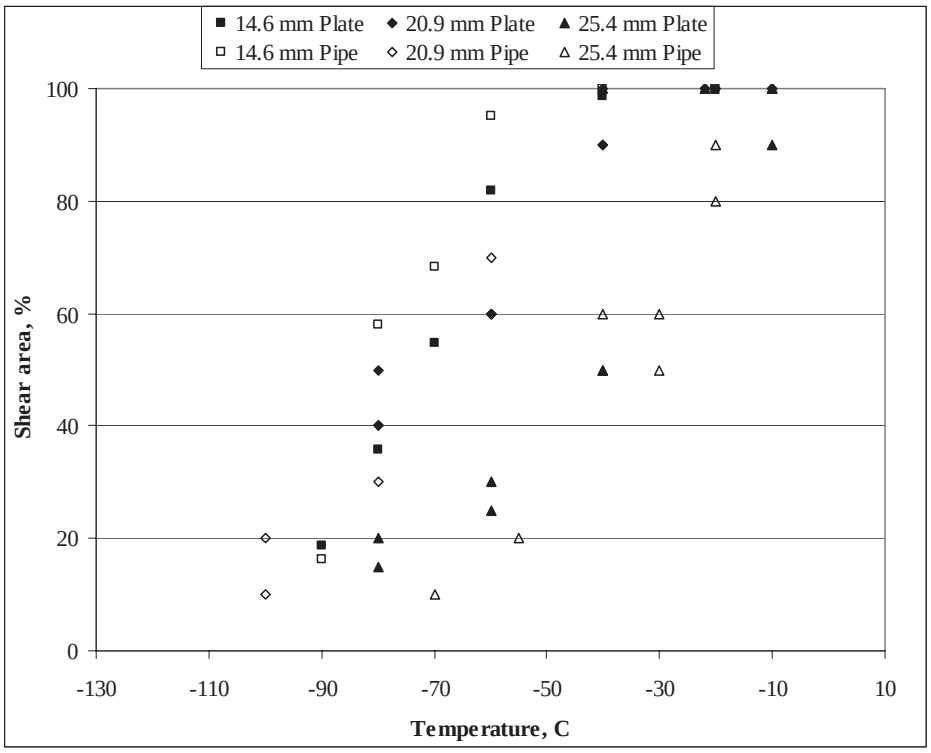

Figure 34 Drop weight tear test transition curves

The impact transition and DWTT transition curves showed that there was little effect of the pipe forming operation on the transition temperatures.

The tensile and impact properties of the laboratory rolled plates are shown in Table 55.

Table 55: Tensile and impact transition temperatures of laboratory rolled plates

Code	FRT (°C)	Mean $R_{t0.5}$ (MPa)	Mean R_m (MPa)	Mean Rt/Rm	27 J ITT (°C)
7JE119	1031	504	639	0.79	20
7JE118	950	493	648	0.76	-10
7JE117	880	454	611	0.74	-40

A limited amount of fracture toughness testing to BS 7448 was carried out to determine a crack tip opening displacement, CTOD, transition curve for specimens taken from the 25.4 mm thick plate, PA665, and the results are shown in Table 56 and Figure 35.

Table 56: Fracture toughness parameters measured from 25.4 mm thick plate

Specimen orientation	Test temp. (°C)	CTOD (mm)	J (J/mm²)	K_J (MPa√m)	Result type	Valid to BS7448
Transverse	20	1.42	1.303	545.7	m	y
	-20	0.304	0.243	235.7	c (type II pop-in)	y
	-40	0.475	0.378	293.9	c (type II pop-in)	y
	-80	0.07	0.058	115.1	c (type II pop-in)	y
	-100	0.06	0.056	113.1	c	y
	-100	0.046	0.039	94.4	c	y
	-100	0.029	0.025	75.6	c	y
	-100	0.103	0.091	144.2	c	y
	-100	0.063	0.052	109.0	c	y
	-100	0.069	0.059	116.1	c	y
	-100	0.066	0.048	104.7	c	y
Longitudinal	20	2.476	1.465	578.7	m	y
	-40	2.094	1.903	659.5	m	y
	-80	0.18	0.139	178.2	u	y
	-120	0.019	0.016	60.5	c	y
	-100	0.123	0.092	145.0	c (type II pop-in)	y
	-110	0.06	0.05	106.9	c	y
	-110	0.059	0.052	109.0	c	y
	-110	0.127	0.11	158.6	c (type II pop-in)	y
	-110	0.238	0.189	207.8	c	y
	-120	0.018	0.017	62.3	c	y
	-90	0.155	0.116	162.8	c (type II pop-in)	y
	-60	0.71	0.63	379.5	c (type II pop-in)	y

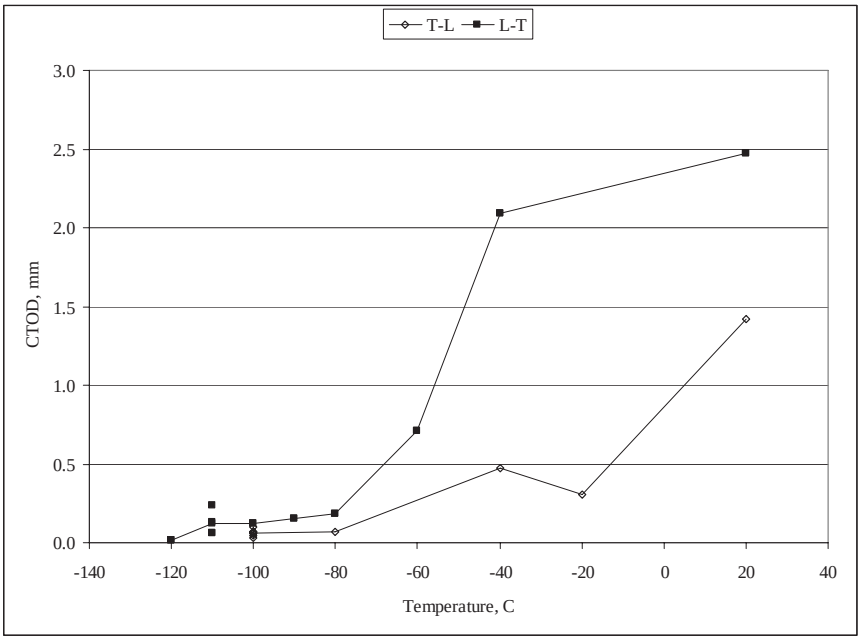

Figure 35: CTOD transition curve for 25.4 mm thick plate

6.2.3 Microstructure

The grains sizes for the plates are shown in Table 57.

Table 57: Grain sizes of hot-rolled plates from cast 81913

	PE111	PB329	PA665	PA666	PC943	7JE117	7JE118	7JE119
Thickness, mm	14.6	20.9	25.4	25.4	25.4	20	20	20
FRT, ^{o}C	775	708	720	715	712	880	950	1031
$d^{-1/2}$, $mm^{-1/2}$	13.0	14.6	13.9	-	15.2	8.9	7.5	6.1

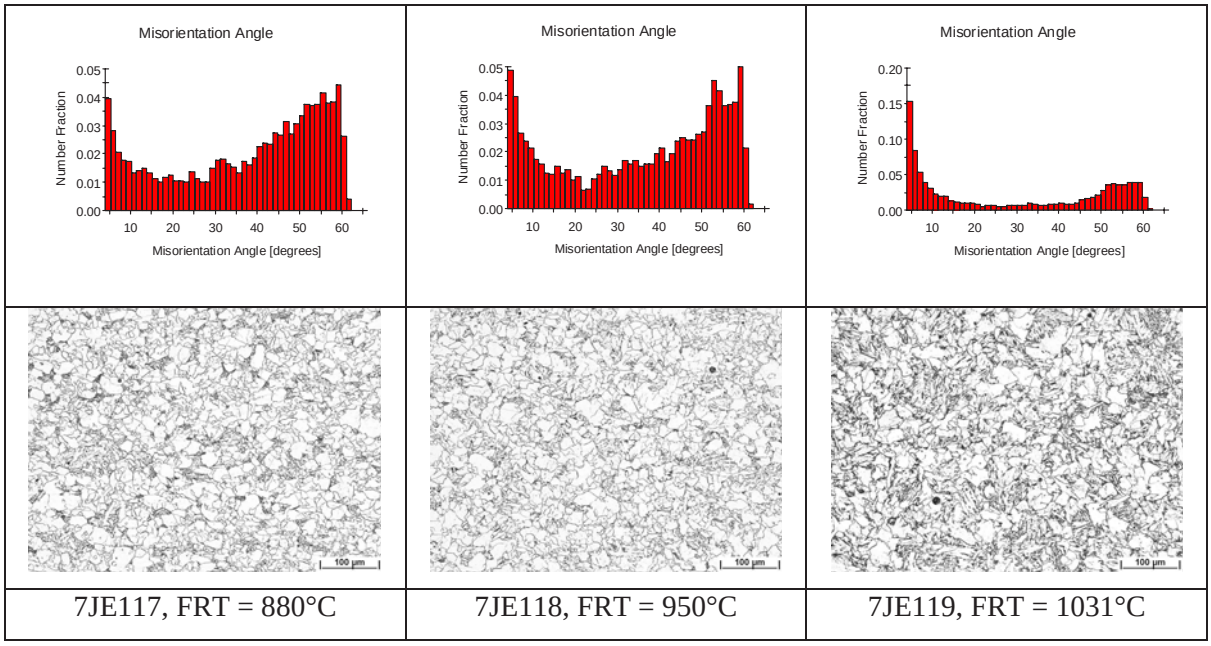

7JE117, FRT = 880°C | 7JE118, FRT = 950°C | 7JE119, FRT = 1031°C

Figure 36: Number fraction distribution and microstructures of laboratory rolled plates

6.2.4 Weldability

6.2.4.1 Thermal simulation

Weld simulation was carried out by reheating to 1250^{o}C followed by controlled cooling through the range 800 - 500^{o}C and the impact energy absorbed at +20^{o}C and -40^{o}C for each condition was measured along with the hardness of the microstructure, Figure 37.

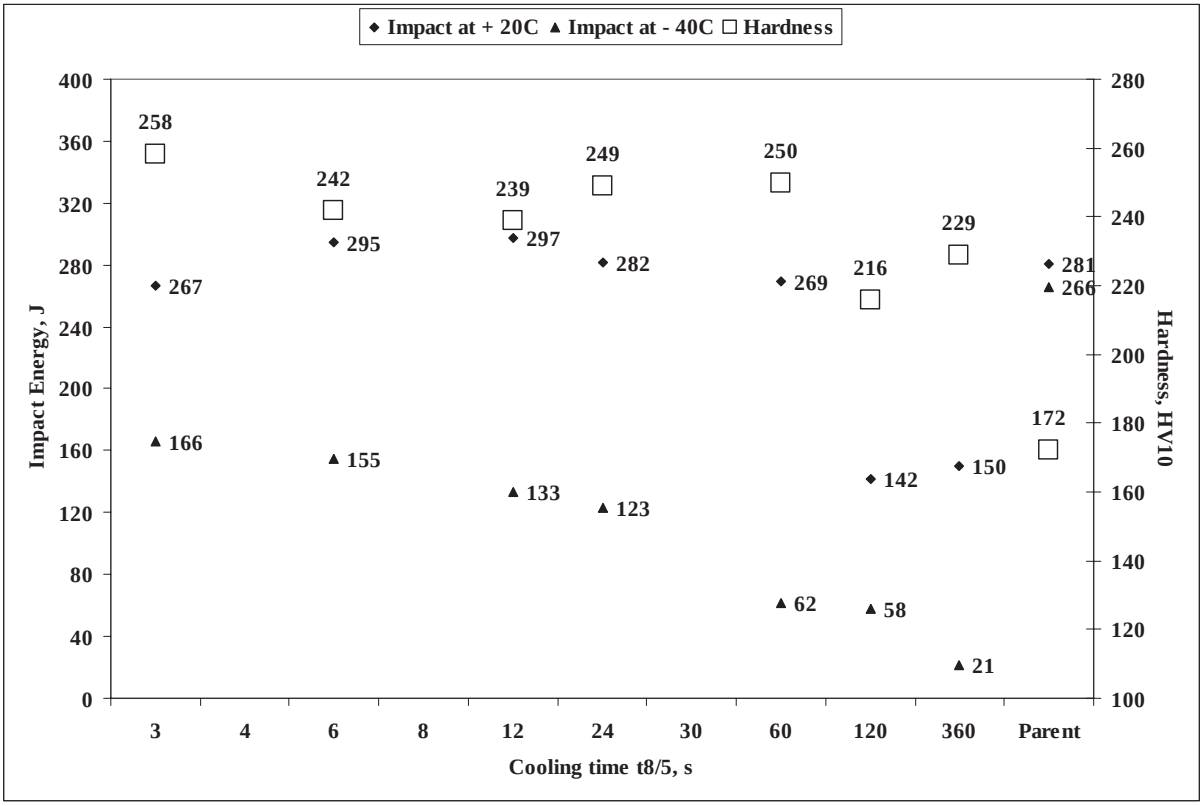

Figure 37: Toughness and hardness of simulated weld HAZ microstructures in plate PC943

6.2.4.2 Tekken test

Tekken tests were carried out to EN ISO 17642-2 to establish preheating requirements to avoid hydrogen cracking.

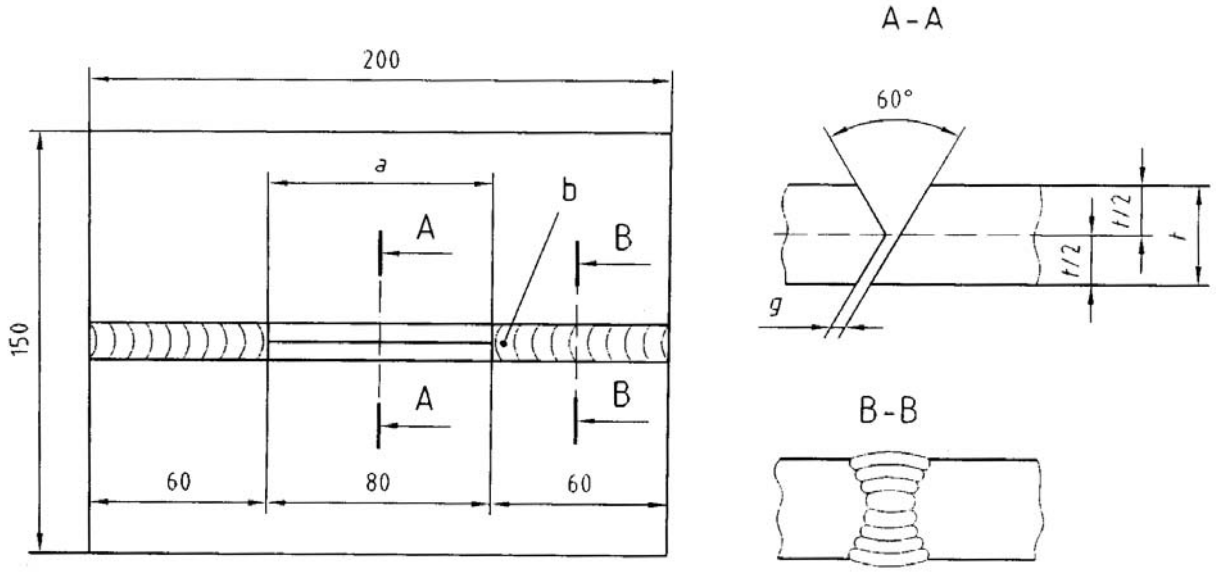

Figure 38: Schematic of the Tekken test weld

The properties of the electrodes and welding wire used in the Tekken tests are shown in Table 58.

Table 58: Welding wire and electrodes used in the Tekken tests

Brand	Classification	Weld metal properties			Diffusible hydrogen	
		$R_{p0.2}$ (MPa)	R_m (MPa)	A (%)	Glycerine method	Mercury method
Covered electrodes					ml/100 g	ml/100 g
SL 12G Basic very low hydrogen	EN 1599-97: E Mo B 32 H5	550	610	25	1.65	2.50
Pipeliner 8P+ Cellulosic	EN 499-94: E 46 4 1Ni C25	460 - 559	550 - 676	19 - 27	24.8	37.7
Welding wire						
IMT NiMoCr	EN 12534 Mn3NiCrMo	> 620	> 700	> 17		

Examination of the weld microstructures after welding in the Tekken test identifies the welding conditions under which cracking occurs with the different consumables. The Tekken test welding parameters and results for these two steels are shown in Table 59.

Table 59: Tekken test results on material from plate PC943

	Current	Voltage	Speed	Heat Input	Preheat temperature	Result
	A	Volts	cm/s	kJ/cm	C	
SL 12G	144	23.5	0.34	8.0	20	No cracks in 4 slices examined
Pipeliner 8P+	118	24.5	0.34	6.7	20	Cracks in weld for all 4 slices
Pipeliner 8P+	118	24.5	0.34	6.7	100	No cracks in 4 slices examined
Pipeliner 8P+	118	24.5	0.34	6.7	150	No cracks in 4 slices examined

Four slices through the weld were examined and these examinations showed that cracking did not occur in the HAZ of the welds even with high levels of diffusible hydrogen, Figure 39.

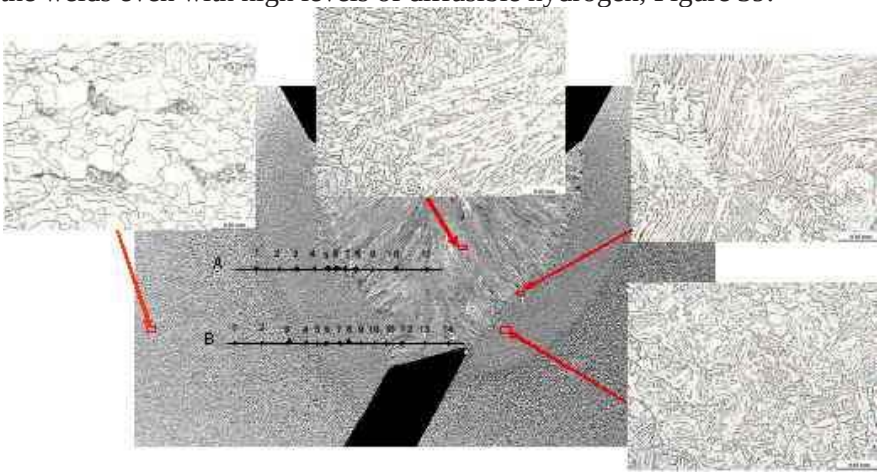

Indentation number	1	2	3	4	5	6	7	8	9	10	11	12	13	14
Row A	205	210	217	229	234	257	269	224	234	245	242	Parent = 164		
Row B	159	178	185	185	214	219	221	251	245	245	251	242	245	257

Figure 39: Tekken test on plate PC943 with SL12G electrode

Cracking of the weld metal did occur with diffusible hydrogen levels of 37 ml/100 g when no pre-heating temperature was applied, Figure 40.

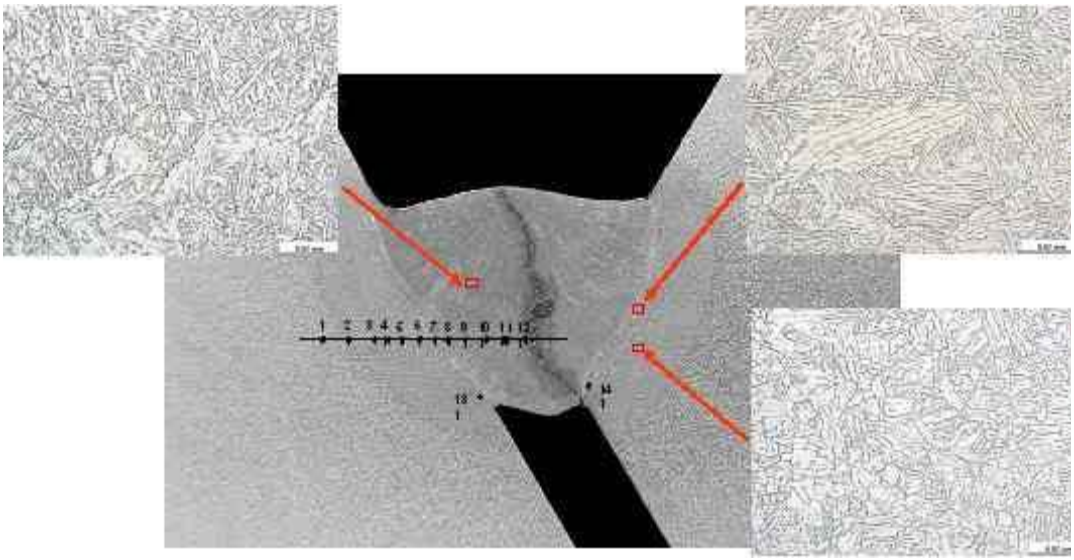

Indentation number	1	2	3	4	5	6	7	8	9	10	11	12	13	14
Hardness, HV1	156	171	217	234	245	283	276	283	251	276	269	276	272	272

Figure 40: Tekken test on plate PC943 with Pipeliner 8P+ electrode with no pre-heat

6.2.4.3 Girth Welding

A girth weld was made in the 14.6 mm thick, 610 mm diameter pipe, identified as YBWA1. The girth welding was coordinated and monitored [16] by Smart Engineering BV (the Netherlands) and was executed by MultiMetaal Constructie BV (the Netherlands) following a proposed welding procedure specification (pWPS), shown in Appendix B1. The two welders who performed the welding were asked to comment on the performance of the wires with the material and to provide comments on the weldability of the parent material. After the root run was completed they reported that the "new material" was similar to welding 13Cr or Duplex, when using gas tungsten arc welding, GTAW, which is welding process reference number 141. The weld showed no surface defects under visual inspection.

6.3 Hot-coiled plate for pipe

Within work-package 3, the industrial implementation of different low carbon bainitic steels and their processing routes have been realised at two steel plants. The idea was to develop high strength linepipe steel more cost effectively and with more reliability on the mechanical properties compared with ferritic-pearlitic materials. The resulting mechanical properties have been studied for hot strip material and for large diameter linepipe material. EBSD characterisation of the strip microstructure was used. Simulation on the material behaviour for different welding conditions and for girth welding has been carried out. Three trial heats were made at Ruukki, being rolled to 14 strips and two casts were produced in Salzgitter, resulting in 12 strips. One slab each was exchanged and mutually hot-rolled. The strips have mainly been formed into spiral pipes, two strips were processed to high-frequency induction welded pipes and one strip was rolled for structural application.

6.3.1 Steel compositions and processing conditions

6.3.1.1 Steel compositions

With the aim of achieving pipe steels with different strength levels, all containing a partly bainitic microstructure, the following casts were produced.

Table 60: Compositions of casts for commercial rollings

Cast	C	Si	Mn	P	S	Al	Nb	V	Cu	
81351	0.043	0.20	1.96	0.007	0.0009	0.027	0.104	0.008	0.21	
17721	0.033	0.22	1.82	0.005	0.0015	0.027	0.052	0.004	0.02	
30619	0.042	0.30	1.81	0.006	0.0024	0.036	0.056	0.009	0.21	
30257	0.040	0.20	1.49	0.012	0.0040	0.031	0.068	0.005	0.49	
16685	0.050	0.32	1.75	0.009	0.0010	0.030	0.098	0.005	0.04	
Cast	Cr	Ni	Ce	N	Mo	Ti	Ca	B	Pcm	CEV
81351	1.01	0.22	0.003	0.0075	0.000	0.014	0.0018	0.0003	0.22	0.64
17721	0.21	0.05	0.006	0.0070	0.003	0.013	0.0026	0.0003	0.14	0.38
30619	0.21	0.20	0.007	0.0061	0.001	0.013	0.0019	0.0003	0.17	0.37
30257	0.04	0.41	0.003	0.0046	0.008	0.014	0.0013	0.0019	0.16	0.35
16685	0.27	0.04		0.0070	0.070	0.020	0.0012	0.0001	0.174	0.42

Carbon was kept at a low level to prevent the formation of pearlite. Niobium was varied up to a level of 0.10% to promote the formation of bainite during cooling and to increase the recrystallisation stop temperature. Chromium was added in one cast to retard transformation and enable bainite formation during cooling. Boron was alloyed for a similar purpose.

A major aim was to keep the alloying costs low, and for that reason vanadium and molybdenum were not used in the alloy designs.

6.3.1.2 Processing conditions

When rolling high-strength linepipe steels with high toughness requirements on the hot strip mill, the roughing temperature is usually controlled by a holding period before or in between roughing rolling. Such pause or holding periods increase the production times and thus, lead to a lower production capacity. With the chemical compositions given above, production times should be accelerated.

The layouts of the hot strip mills are as shown in Figure 41 for the Ruukki mill and in Figure 42 for Salzgitter's.

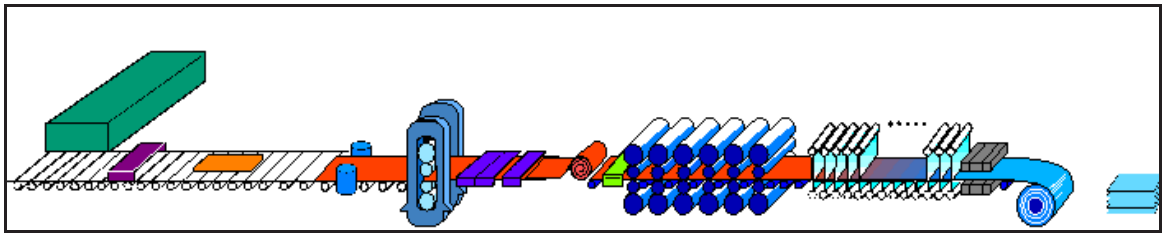

Figure 41: Layout of Ruukki`s hot strip mill

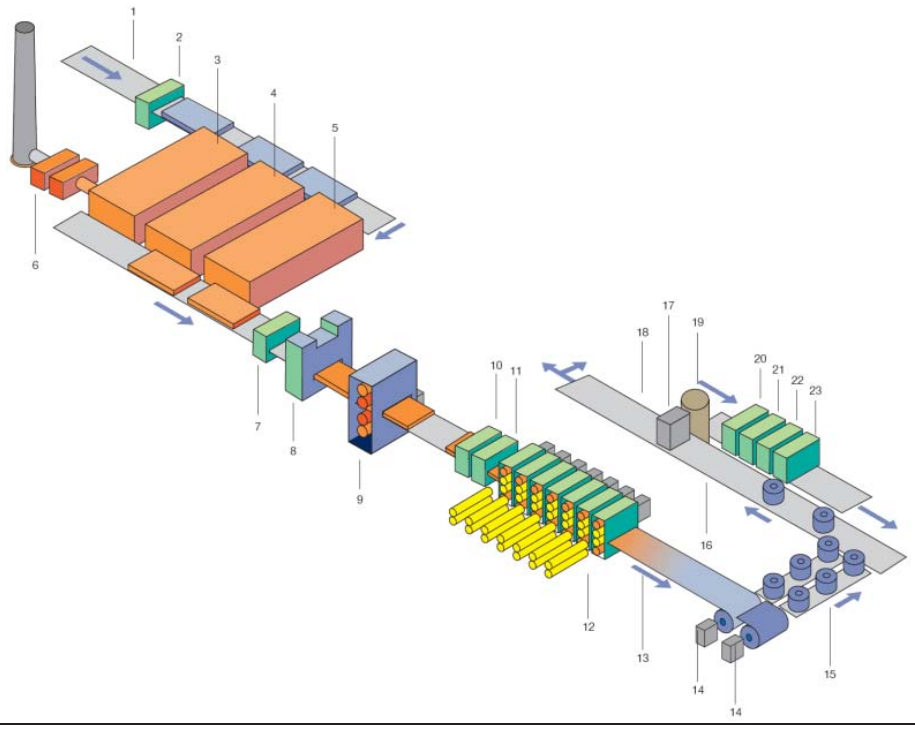

1 Slab roller table, 2 Deburring device, 3-5 Reheating furnaces, 6 Waste gas heat recovery, 7 High-pressure water descaler, 8 Sizing press, 9 Roughing train, 10 Crop shears, 11 High-pressure water descaler, 12 Finishing train, 13 Runout table/strip cooling, 14 Downcoilers, 15 Transverse transport of coils, 16 Longitudinal transport of coils, 17 coil weighing machine, 18 Walking beam conveyer, 19 V-plate conveyer, 20 Shears for cropping and sampling, 21 Outer coil binding, 22 Binding through coil eye, 23 Finish coil weighing machine

Figure 42: Layout of Salzgitter`s hot strip mill

Mean rolling parameters of the trial strips are given in Table 61. Slab sizes, transfer bar thickness, slab reheating temperature, final roughing temperature, final strip rolling temperature, cooling rate, coiling temperatures, strip thickness and the pipe diameter are given.

Table 61: Processing conditions and dimensions for the commercial rollings

Product ID	Cast	Slab size (mm)	Transfer bar thickness (mm)	SRT (°C)	RFT (°C)	FRT (°C)	CR (°C/s)	CT (°C)	Plate thickness (mm)	Reduction Ratio	Pipe outer diameter (mm)
31	81351	210 x 1275	38		1113	866	33	579	10	3.8	813
41	81351	210 x 1275	38		1111	855	39	599	10	3.8	813
51	81351	210 x 1275	38		1125	905	24	550	10	3.8	813
61	81351	210 x 1275	38		1141	871	32	562	10	3.8	813
41	17721	210 x 1275	42		1051	894	18	482	12	3.5	813
51	17721	210 x 1275	42		1056	886	16	553	12	3.5	813
21	17721	210 x 1275	42		1004	891	15	505	16	2.6	1220
69	17721	210 x 1275	42		996	877	13	547	16	2.6	1220
21	30619	210 x 1520	42		1054	856	-	609	14	3.0	813
31	30619	210 x 1520	42		1116	865	-	639	14	3.0	813
41	30619	210 x 1520	42		1011	843	-	548	14	3.0	813
61	30619	210 x 1520	42		1106	861	-	536	14	3.0	813
71	30619	210 x 1520	42		1014	851	-	572	14	3.0	813
79	30619	210 x 1520	42		1020	841	-	582	14	3.0	813
2101	30257SZ	250 x 1553	38		1059	843	-	551	10	3.8	610
783077	30257	250 x 1552	49	1220	950	810	5.4	575	14.1	3.5	1067
783078	30257	250 x 1551	49	1220	950	810	4.6	600	14.1	3.5	1067
783079	30257	250 x 1544	49	1220	950	810	3.4	650	14.1	3.5	1067
783080	30257	250 x 1559	49	1220	950	810	4.4	600	14.1	3.5	1067
937683	30257	250 x 1474	42	1220	1070	800	6.0	560	11	3.8	473
837482	30257	250 x 1547	45	1250	1130	820	10.0	450	8	5.6	-
883756	D81351	210 x 1262	42	1265	1050	830	9.9	450	11	3.8	403
246062	16685	250 x 1555	48.5	1250	1000	840	10.9	450	14.1	3.4	1067
246063	16685	250 x 1555	48.5	1250	1000	840	11.7	450	14.1	3.4	1067
246064	16685	250 x 1555	48.5	1250	1000	840	11.7	450	14.1	3.4	1067
246065	16685	250 x 1555	48.5	1250	1000	840	11.7	450	14.1	3.4	1067
246066	16685	250 x 1555	48.5	1250	1000	840	11.7	450	14.1	3.4	1067
246067	16685	250 x 1555	48.5	1250	1000	840	11.7	450	14.1	3.4	1067

The slabs at Ruukki were extracted from the furnace at a temperature of approximately 1250°C. All strips of cast 81351 rolled at Ruukki were rolled without holding periods during roughing. Roughing should be finished relatively high at temperatures above 1100°C. Hot rolling schedules for cast 81351 were designed with different aim finish rolling temperatures (850°C and 890°C). One further target coiling temperature (500°C) could not be reached. Due to the automation system, heat 17721 was rolled with a pause during roughing so that the coiling temperatures were reached. The strips of cast 30619 were rolled with different final roughing temperatures in order to investigate the influence of the final roughing temperature on the toughness: every second strip was roughed at a higher temperature. No intermediate stand cooling was used.

Cast 30257 was rolled with different coiling temperatures to investigate the effect of coiling plus boron on temperature on the strength and toughness. The roughing finishing temperature has not been measured due to scale and water remaining on the transfer bar, the values given were estimated. A holding period after slab extraction has been realised. The Ruukki slab being rolled in Salzgitter was cooled to 450°C to compare the properties with the higher cooling temperatures gained at Ruukki. Cast 16685 has been extracted from the furnace and roughed at higher temperatures due to the higher amount of Nb and additionally the final strip rolling temperature was increased. No holding period was used. Also for the strips being rolled for HFI-pipe forming, no holding time was applied.

All of the strips rolled at Ruukki were processed to spiral pipes at Oulainen pipe mill. The strips hot-rolled in Salzgitter have either been processed to spiral pipes at Salzgitter Großrohr or to longitudinal welded HFI-pipes at Salzgitter Mannesmann Linepipe. Strip 837482 was used for structural application.

Figures 43 and 44 show the two types of pipe forming process.

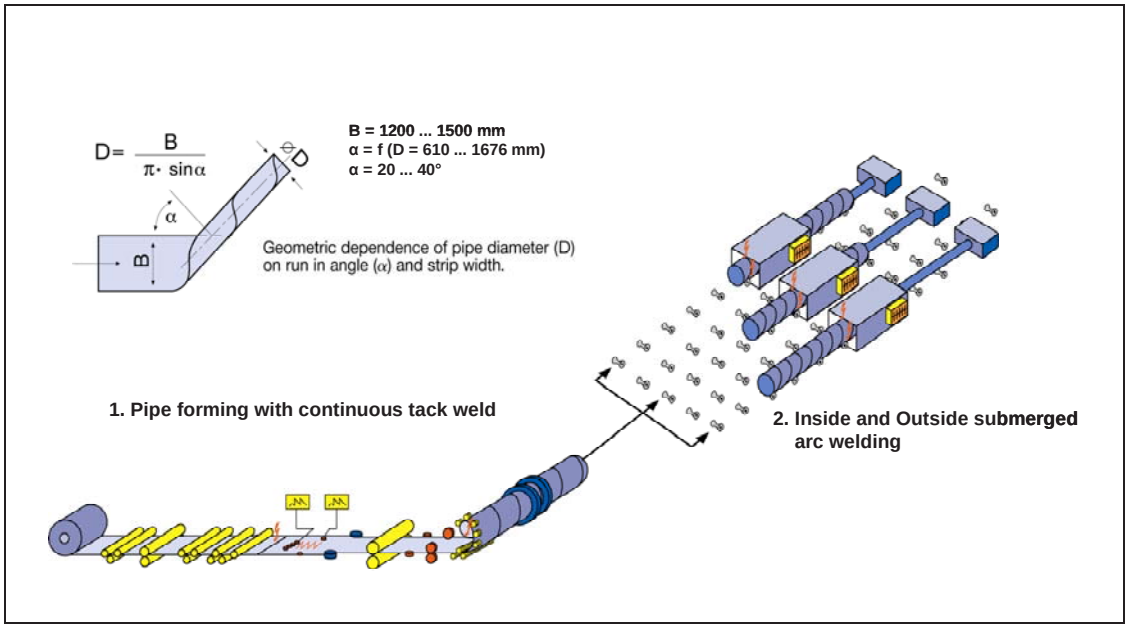

Figure 43: Schematic figure of spiral pipe forming

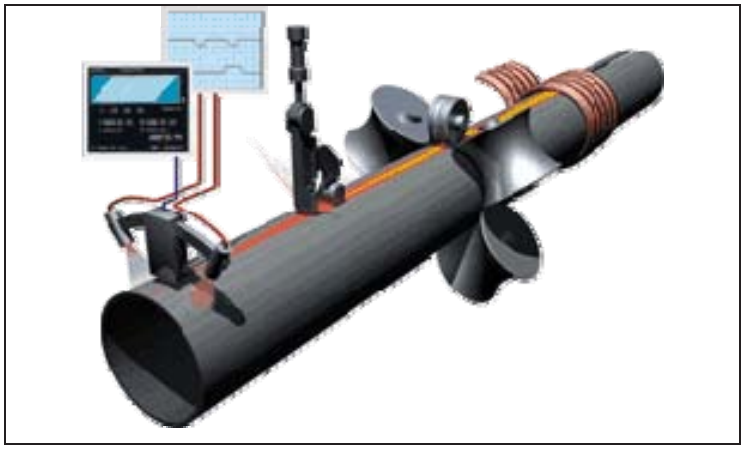

Figure 44: Schematic figure of HFI-pipe forming

Welding parameters of Ruukki's pipe mill are given in Table 62.

Table 62: Welding wire, flux and arc energy of Ruukki`s welding process

Heat	Strip mm	Thick mm	Dia	Wire	Flux	Arc energy, kJ/mm			
						Inside (6 o'clock)		Outside (12 o'clock)	
						DC	AC	DC	AC
81351	41	10	813	OK 13.43	OK 10.71	0.8	0.6	0.9	0.4
	61	10	813	OK 13.43	OK 10.71	0.8	0.6	0.9	0.4
	31	10	610	Weld not tested					
	51	10	610						
17721	41	12	813	OK 12.20	OK 10.71	0.9	0.8	1.0	0.4
	51	12	813	OK 12.20	OK 10.71	0.9	0.8	1.0	0.4
	21	16	1220	OK 12.24	OK 10.71	1.3	0.9	1.4	0.6
	69	16	1220	OK 12.24	OK 10.71	1.3	0.9	1.4	0.6
30619	21	14	813	OK 12.24	OK 10.71	1.0	0.9	1.2	0.5
	31	14	813	OK 12.24	OK 10.71	1.0	0.9	1.2	0.5
	41	14	813	OK 12.24	OK 10.71	1.0	0.9	1.2	0.5
	61	14	813	OK 12.24	OK 10.71	1.0	0.9	1.2	0.5
	71	14	813	OK 12.24	OK 10.71	1.0	0.9	1.2	0.5
	79	14	813	OK 12.24	OK 10.71	1.0	0.9	1.2	0.5
30257S	2101	10	610	Weld not tested					

Table 63: Heat treatment after HFI-pipe forming

Heat	Coil	Post-heat treatment of weld and HAZ	Annealing of weld and HAZ
30257	937683	950°C, water quenching	590°C, air cooling
D81351	883756	920°C, air cooling	

The welding process has not been recorded for cast 30257 for spiral pipes.

Table 64: Processing conditions for the spiral pipes of Salzgitter (cast 16685)

	Inside	Outside
Wire	EN 756-S0	EN 756-S0
Flux	EN 760-SA CS1	EN 760-SA AB1
Arc energy (kJ/mm)	2.1	1.7

6.3.2 Mechanical properties

6.3.2.1 Tensile properties

Tensile test results of the pipe base material are given in Table 65. Samples were taken transverse to the pipe axis (hoop direction). All values are average values of two resp. three tensile samples. All samples were prepared according to EN 10002, showing a rectangular cross section. Samples taken from HFI-pipes were positioned at 3 o'clock for the transverse direction. Additionally, the local coiling temperatures are given for the different positions of the pipe rings with regard to the strip length. Strength classes of the materials are estimated according to the $R_{t0.5}$ values.

Table 65: Tensile properties of pipe samples

Cast	Coil	t (mm)	CT (°C)	CR (°C/s)	Specimen and orientation		$R_{p0.2}$ (MPa)	$R_{t0.5}$ (MPa)	R_m (MPa)	A (%)	R_t/R_m	R_m*A
81351	31	10	579	33	pipe ML*	trans	640	604	782	21	0.77	16422
	41	10	600	39	pipe ML	trans	562	560	707	24	0.79	16969
	51	10	550	24	pipe ML	trans	624	584	810	19	0.72	15390
	61	10	580	32	pipe ML	trans	613	604	787	19	0.77	14953
	61	10	550		pipe ML	trans	656	629	822	19	0.77	15618
17721	41	12	482	18	pipe ML	trans	451	465	564	30	0.82	16920
	51	12	553	16	pipe ML	trans	458	471	560	33	0.84	18480
	21	16	510	15	pipe ML	trans	475	487	561	24	0.87	13464
	21	16	510		pipe ML	trans	474	477	551	30	0.87	16530
	21	16	450		pipe ML	trans	498	503	584	23	0.86	16352
	69	16	580	13	pipe ML	trans	476	477	554	28	0.86	15512
	69	16	570		pipe ML	trans	478	481	550	27	0.87	14850
	69	16	480		pipe ML	trans	484	490	550	26	0.88	14300
30619	21	14	600		pipe ML	trans	496	501	604	24	0.83	14496
	31	14	640		pipe ML	trans	475	484	576	25	0.84	14400
	41	14	550		pipe ML	trans	481	490	596	26	0.82	15496
	61	14	530		pipe ML	trans	479	488	593	23	0.82	13639
	71	14	570		pipe ML	trans	484	492	599	23	0.82	13777
	79	14	570		pipe ML	trans	488	495	603	25	0.82	15075
30257SZ	2101	10	570		pipe ML	trans	642	630	727	17	0.87	12359
30257	783077	14.1	545	6.4	pipe ML	trans	568	569	663	18	0.86	11934
			545	6.4	strip ML	30°	556	559	646	20	0.86	12920
			575	5.5	pipe head	trans	-	-	-	-	-	-
			575	5.5	strip head	30°	612	608	688	13	0.88	8944
			530	6.5	pipe tail	trans	542	546	636	14	0.86	8904
			530	6.5	strip tail	30°	570	574	682	17	0.84	11594
30257	783078	14.1	540	6.2	pipe ML	trans	513	522	630	18	0.83	11340
			540	6.2	strip ML	30°	539	544	637	20	0.85	12740
			600	4.4	pipe head	trans	498	510	624	21	0.82	13104
			600	4.4	strip head	30°	557	561	649	17	0.86	11033
			555	5.6	pipe tail	trans	457	471	595	23	0.79	7735
			555	5.6	strip tail	30°	514	519	633	18	0.82	11394
30257	783079	14.1	590	4.2	pipe ML	trans	545	547	645	17	0.85	10965
			590	4.2	strip ML	30°	523	528	620	18	0.85	11160
			650	2.7	pipe head	trans	440	450	566	27	0.79	15282
			650	2.7	strip head	30°	466	470	576	26	0.82	14976
			570	4.9	pipe tail	trans	484	495	618	17	0.80	10506
			570	4.9	strip tail	30°	529	533	631	22	0.84	13882
30257	783080	14.1	575	4.8	pipe ML	trans	492	503	611	19	0.82	11609
			575	4.8	strip ML	30°	534	538	628	19	0.86	11932
			600	4.4	pipe head	trans	529	537	639	18	0.84	11502
			600	4.4	strip head	30°	557	561	644	19	0.87	12236
			570	5.1	pipe tail	trans	479	493	618	18	0.80	11124
			570	5.1	strip tail	30°	560	563	654	15	0.86	9810
30257	937683	11.0	560	5.7	pipe ML	trans	597	600	720	13	0.83	9360
			560	5.7	strip ML	trans	-	-	-	-	-	-
			560	5.7	pipe ML	long	658	655	713	14	0,92	9982
			560	5.7	strip ML	long	-	-	-	-	-	-
			535	6.3	pipe head	trans	663	660	708	12	0.93	8496
			535	6.3	strip head	trans	624	627	705	14	0.89	9870
			535	6.3	pipe head	long	629	628	731	8	0.86	5848
			535	6.3	strip head	long	573	578	679	14	0.85	9506
			510	7.3	pipe tail	trans	611	617	724	11	0.85	7964

			510	7.3	strip tail	trans	594	599	711	17	0.84	12087
			510	7.3	pipe tail	long	598	622	744	14	0.84	10416
			510	7.3	strip tail	long	534	544	687	19	0.79	13056
30257	837482	8.0	420	13.0	strip tail	trans	713	716	818	8		6544
			420	13.0	strip tail	long	665	669	754	16		12064
D81351	883756	11.0	420	10.4	pipe ML	trans	-	643	796	14	0.81	11144
			420	10.4	pipe ML	long	-	621	799	18	0.79	14382
			440	10.0	pipe head	trans	-	674	806	13	0.84	10478
			440	10.0	pipe head	long	-	659	817	12	0.81	9804
			245	15.3	pipe tail	trans	-	640	784	16	0.82	12544
			245	15.3	pipe tail	long	-	639	776	19	0.82	14744
16685	246062	14.1	390	12.8	pipe ML	trans	526	532	641	18	0.83	11538
			390	12.8	strip ML	30°	-	-	-	-	-	-
			525	8.4	pipe head	trans	535	543	642	20	0.84	12840
			525	8.4	strip head	30°	525	535	641	20	0.83	12820
			305	16.5	pipe tail	trans	547	555	665	17	0.83	11305
			305	16.5	strip tail	30°	540	547	651	18	0.84	11718
16685	246063	14.1	390	13.6	pipe ML	trans	543	548	672	18	0.82	12096
			390	13.6	strip ML	30°	-	-	-	-	-	-
			540	8.3	pipe head	trans	541	550	646	20	0.85	12920
			540	8.3	strip head	30°	-	-	-	-	-	-
			275	18.4	pipe tail	trans	537	549	652	17	0.84	11084
			275	18.4	strip tail	30°	-	-	-	-	-	-
16685	246064	14.1	440	12.2	pipe ML	trans	540	546	657	22	0.83	14454
			440	12.2	strip ML	30°	-	-	-	-	-	-
			555	7.7	pipe head	trans	-	-	-	-	-	-
			555	7.7	strip head	30°	560	569	671	19	0.85	12749
			405	14.1	pipe tail	trans	552	563	670	17	0.84	11390
			405	14.1	strip tail	30°	561	564	649	18	0.87	11682
16685	246065	14.1	450	11.8	pipe ML	trans	510	524	646	21	0.81	13566
			450	11.8	strip ML	30°	-	-	-	-	-	-
			470	10.4	pipe head	trans	530	537	653	19	0.82	12407
			470	10.4	strip head	30°	550	557	652	18	0.85	11736
			445	13.7	pipe tail	trans	-	-	-	-	-	-
			445	13.7	strip tail	30°	566	571	661	21	0.86	13881
16685	246066	14.1	460	11.7	pipe ML	trans	528	535	646	21	0.83	13566
			460	11.7	strip ML	30°	-	-	-	-	-	-
			545	8.5	pipe head	trans	529	538	647	21	0.83	13587
			545	8.5	strip head	30°	560	565	654	19	0.86	12426
			400	14.9	pipe tail	trans	529	539	658	18	0.82	11844
			400	14.9	strip tail	30°	565	570	661	16	0.86	11898
16685	246067	14.1	480	11.0	pipe ML	trans	530	544	664	21	0.82	13944
			480	11.0	strip ML	30°	563	573	664	20	0.86	13280
			560	7.6	pipe head	trans	533	543	658	20	0.82	13160
			560	7.6	strip head	30°	566	568	658	22	0.86	14476
			400	14.0	pipe tail	trans	520	540	654	21	0.83	13734
			400	14.0	strip tail	30°	563	567	655	19	0.87	12445

* ML means „mid-length“

Cast 81351 resulted in an X80 grade, considering the lowest value of strip no. 41. Cast 17721 and 30619 reached X65 grade. The coiling temperature for casts 17221 and 30619 did not have an influence on the material's strength. Furthermore, there was no correlation between the cooling rate and the strength level of the pipes. Cast 17721 showed a big $R_{t0.5}/R_m$ ratio.

Lowering the coiling temperature for cast 81351 seemed to increase $R_{t0.5}$ and R_m. It is likely that the strength could have been improved further if coiling at 500°C was reached due to hardening effects and a low phase transformation temperature for this material. This cast shows very good $R_{t0.5}/R_m$ ratios. The

properties of strip 51 are questionable since the $R_{t0.5}$ value was very low and the graph of the tensile curve showed irregularities. Within the microstructure, MA-constituents were found which may have resulted in dual phase behaviour of the material.

Cast 30257 showed a very strong influence of the coiling temperature on the strength level. A high coiling temperature leads to the formation of ferrite and pearlite, in combination with bigger grain sizes. Lower coiling temperatures lead to a bainitic microstructure and higher yield strength. The strength levels varied between X75 and X60 grade.

Cast 16685 seemed to be unaffected by the coiling temperature. All yield strength and elongation values were uniform over the strip length and also between different strips. The grade reached a very good X70 level.

For cast 81351, the dependency of strength and coiling temperature is shown in Figure 45.

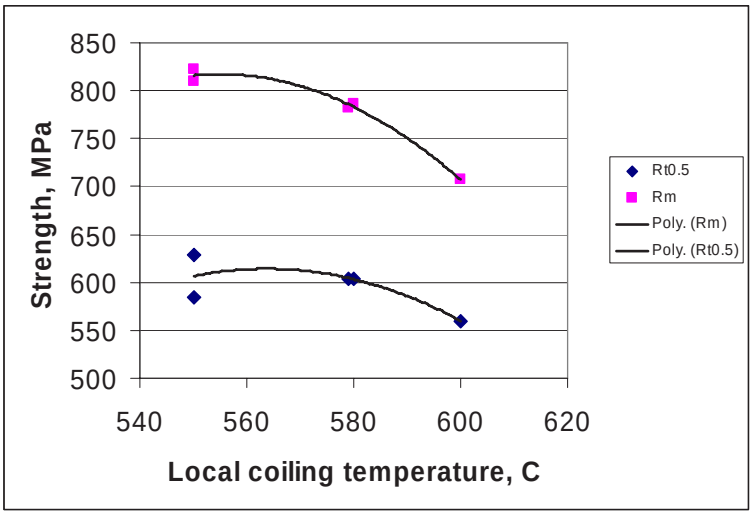

Figure 45: Yield and tensile strength of cast 81351 vs. coiling temperature

Coiling at higher temperatures led to lower strength. This effect is based on the fact that grain refinement and precipitation hardening of the ferrite grains seems to be less effective than transformation hardening.

For the same cast, strip samples were taken at the head, centre and tail position of strips 41 and 61. The head of the strips showed a higher strength than the centre and the tail. Strip and pipe values at similar positions (strip 30° to rolling and pipe transverse) were similar, Figure 46.

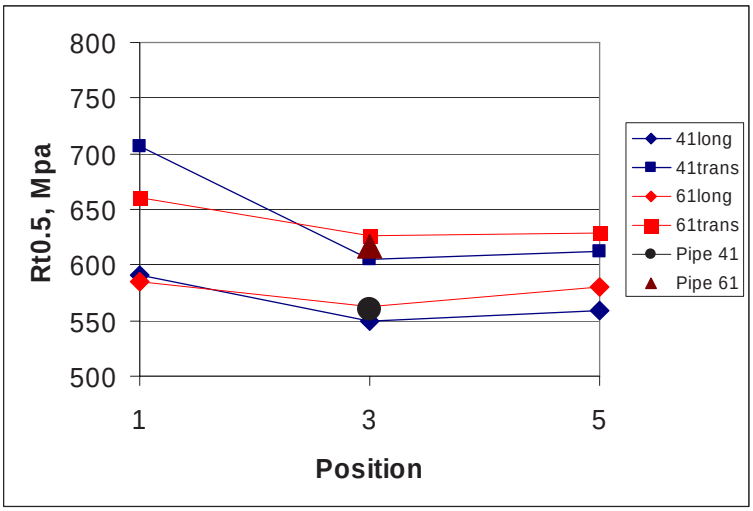

Figure 46: Yield strength of coils 41 and 61 of cast 81351

Comparisons of different tensile samples were carried out. Four different kinds of specimen have been investigated:

(F) = Flattened transverse flat/rectangular specimen

(L) = Longitudinal flat/rectangular specimen

(R) = Transverse round bar specimen (not flattened)

(A) = Flattened transverse aged specimen (ageing at 200°C for 30 min, coating simulation)

The results are shown in Table 66.

Table 66: Comparison of tensile testing specimen, average values of two samples

Coil	Aim Grade	Thick (mm)	Dia. (mm)	$R_{t0.5}$ (MPa)				R_m (MPa)				R_t / R_m			
				(F)	(L)	(R)	(A)	(F)	(L)	(R)	(A)	(F)	(L)	(R)	(A)
81351-41	X100	10	813	560	583	534	550	707	700	702	679	0.79	0.83	0.76	0.81
17721-41	X70	12	813	465	514	476	462	564	568	557	549	0.82	0.90	0.85	0.84
17721-51	X70	12	813	471	523	511	474	560	579	595	561	0.84	0.90	0.86	0.84
17721-21	X70	16	1220	477	517	486	443	551	576	554	556	0.87	0.90	0.88	0.80
17721-69	X70	16	1220	481	518	489	456	550	568	550	553	0.87	0.91	0.88	0.82
X70 Mean				474	518	489	456	556	573	564	555	0.85	0.90	0.87	0.82
30257-2101	X90	10	610	630	708	694	644	727	757	757	727	0.87	0.94	0.92	0.89
16685	X80	14.1	1067	541	-	562	-	656	-	664	-	0.82	-	0.85	-

Flattening of transverse pipe samples normally lowers the yield strength because of residual stress and small cold deformation ratios. The concave shape of the specimen may also change the shape of the tensile graph (stress-strain-curve) compared with the un-deformed round bar specimen. The difference between flattened specimen (F) and round bar specimen (R) was 15 - 20 MPa. Longitudinal samples that had not been flattened (L) showed a 44 MPa higher yield strength than the flattened transverse sample. The effect of ageing is shown by comparing (F) and (A) results and these showed that the $R_{t0.5}$ values tended to decrease with ageing.

6.3.2.2 Charpy impact transition curves

Specimen sizes for Charpy testing varied from the standard samples (10 x 10 mm) to 10 x t mm for cast 81351 and 30257 SZ and 7.5 x 10 mm for 17221- 41 and -51.

Charpy V-notched impact energies of the pipes in transverse direction of cast 81351 are shown in Figure 47, along with energies of the strip samples.

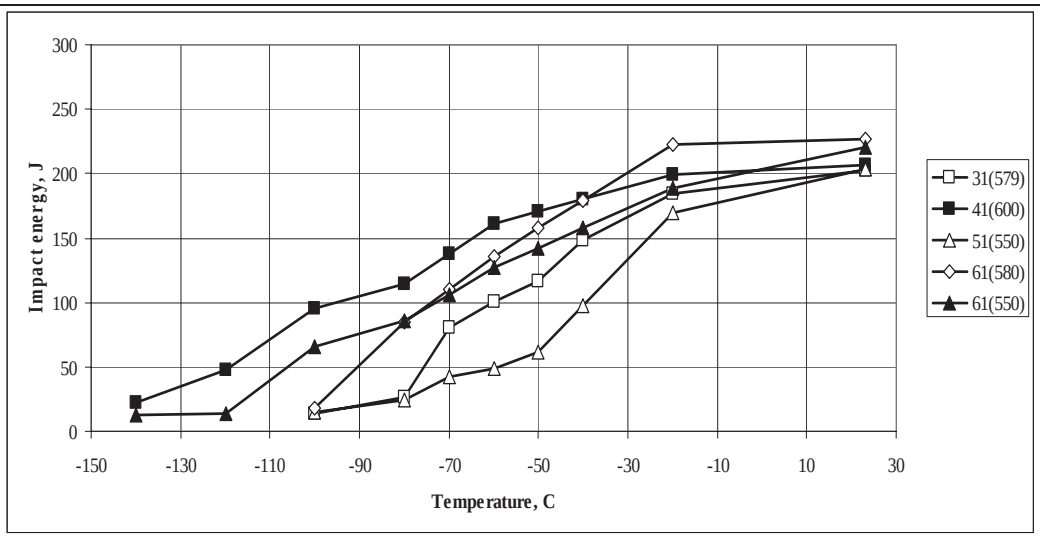

a)

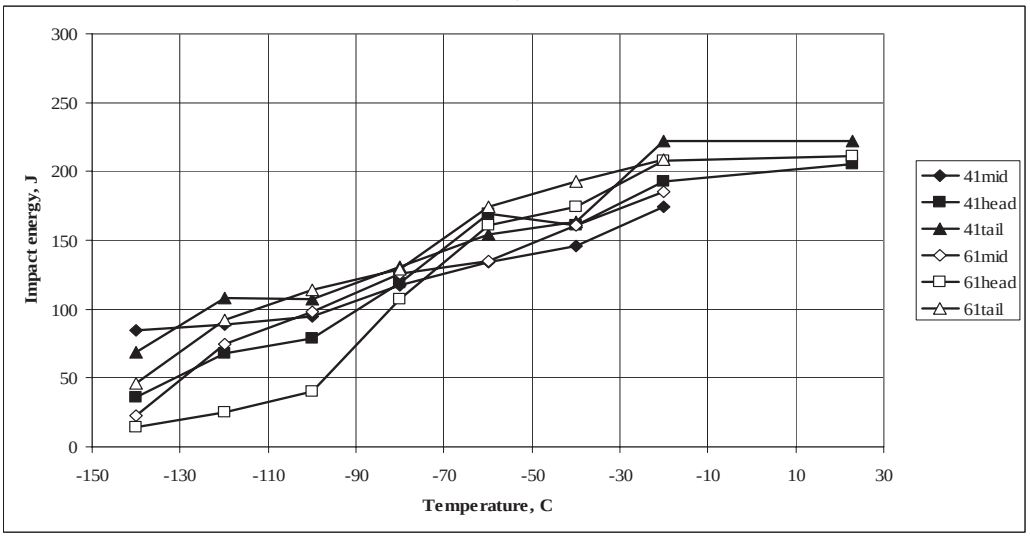

b)

a) Pipe samples b) Strip samples (head, centre, tail)

Figure 47: Impact toughness of pipes from cast 81351, specimen size 10 x 10 mm

The shape of the transition curves was similar for the different coiling temperatures and the upper shelf extended down to -30°C. The slope of strip 51 was steeper than the other strips and the transition temperature was -40°C.

Figure 48 shows the impact energy curves for pipes from cast 17221 material.

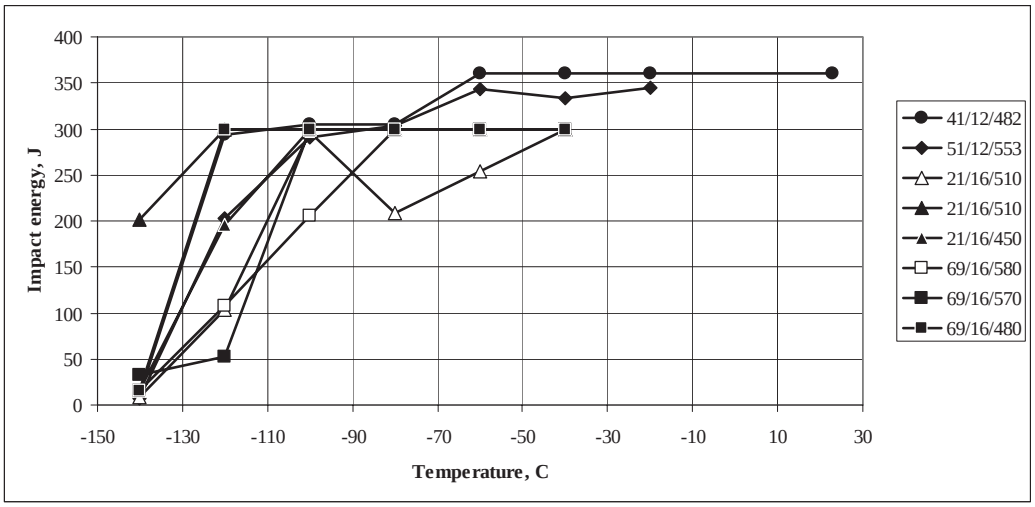

Figure 48: Charpy energy curves of pipes from cast 17221, specimen 10 x 10 mm

The thinner material (12 mm) had a higher upper shelf energy and its transition is moved to lower temperatures compared to the thicker wall thickness (16 mm). All pipes showed impact energies > 200 J down to -100°C.

Charpy energies of cast 30619 are displayed in Figure 49.

(a)

(b)

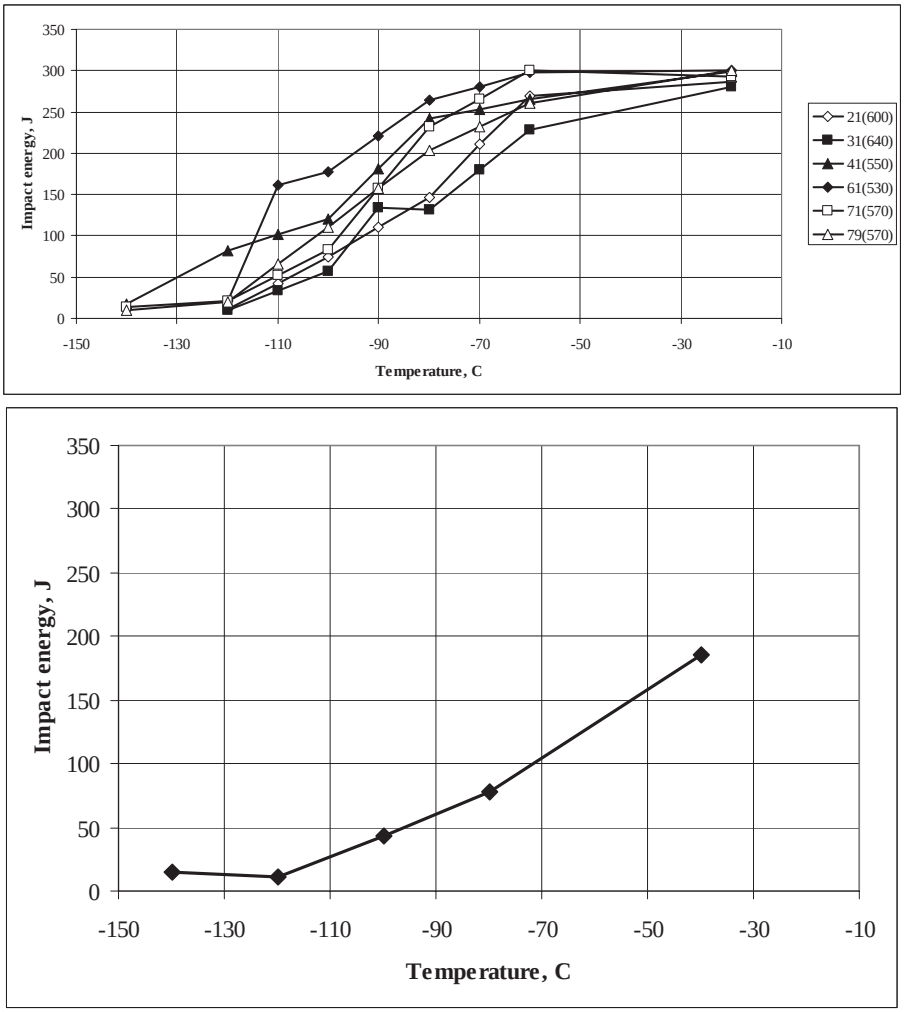

a) Cast 30619 b) Cast 30257 SZ

Figure 49: Charpy energy curves of pipes from cast 30619 and 30257 SZ, specimen 10 x 10 mm

All of the slopes for the pipe material of cast 30619 were similar. Cast 30257 SZ showed good impact energies down to -75°C. A comparison of strip and pipe samples of strips 783077 and 783080 of cast 30257 is shown in Figure 50.

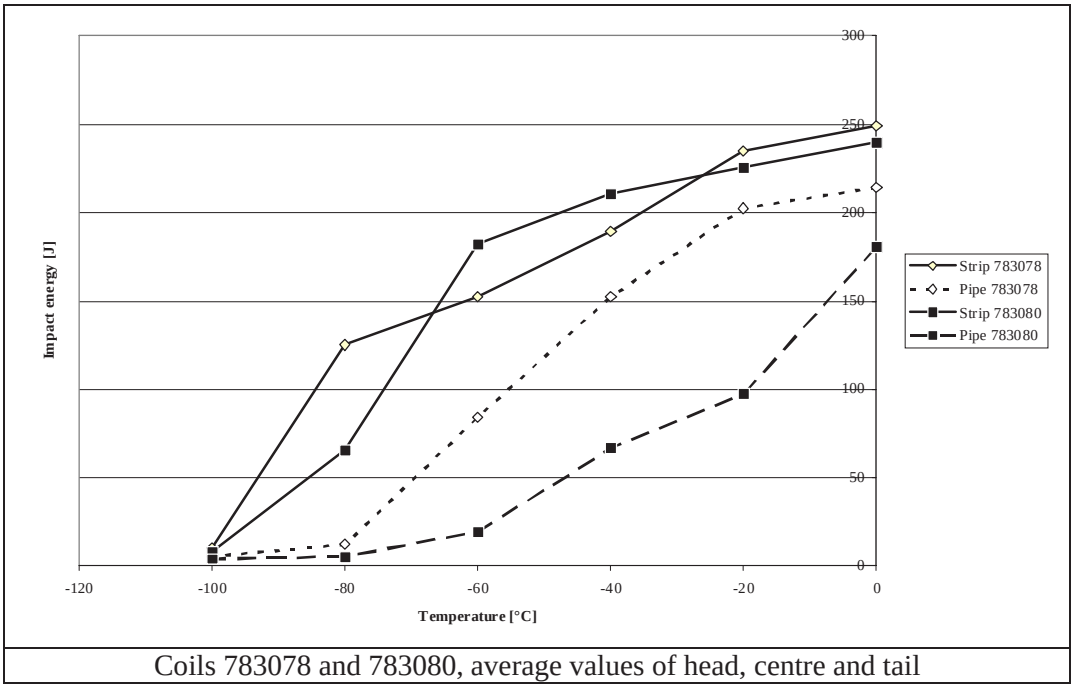

Figure 50: Charpy impact curves for strip and pipes made from cast 30257

Both graphs for the strip material had higher upper shelf energy levels than the pipes. The poor values of pipe 783080 are based on the calculation of the average values. Figure 51 shows the impact energy curves for cast 16685 for all coils (head and tail) and pipes (head, centre and tail).

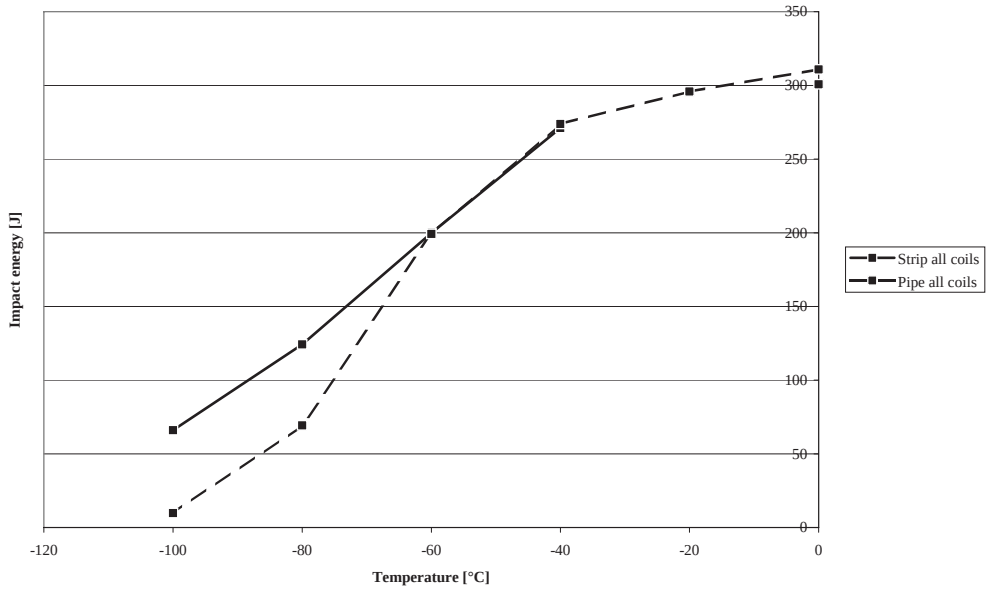

Figure 51: Charpy impact curves for mean values of all strip and pipes made from cast 16685

Strip and pipe values were almost equal, the upper shelf energy was higher than 300 J and the transition started at approx. -40°C. The Charpy impact transition temperatures for spiral pipes produced in Salzgitter are given in Table 67 for spiral pipes and in Table 68 for HFI-pipes.

Table 67: Charpy V impact toughness of spiral pipes processed at Salzgitter

Cast	Coil	t (mm)	CT (local) (°C)	CR (°C/s)	$R_{t0.5}$ (MPa)	R_m (MPa)	Grade Approx	Position	ITT 27J (°C)	ITT 0.5Kvmax (°C)	Kvmax (J)
30257	783077	14.1	573	5.5	-	-	X75	Head	-39	-31	205
	783077	14.1	544	6.4	569	663	X75	Centre	-58	-49	235
	783077	14.1	528	6.6	546	636	X75	Tail	-73	-54	248
	783078	14.1	604	4.4	471	595	X65	Head	-46	-43	230
	783078	14.1	538	5.9	522	630	X65	Centre	-60	-44	218
	783078	14.1	553	5.6	510	624	X65	Tail	-74	-57	233
	783079	14.1	650	2.7	450	566	X60	Head	-60	-44	227
	783079	14.1	588	4.0	475	587	X60	Centre	-34	-33	
	783079	14.1	569	5.0	495	618	X60	Tail	-50	-39	220
	783080	14.1	560	4.4	537	639	X65	Head	-38	-20	191
	783080	14.1	576	4.8	503	611	X65	Centre	-43	-24	230
	783080	14.1	568	5.1	493	618	X65	Tail	-55	-34	219
16685	246062	14.1	525	8.4	535	641	X75	Head	-115	-93	299
	246062	14.1	390	12.8	543	642	X75	Centre	-84	-60	299
	246062	14.1	305	16.5	555	665	X80	Tail	-86	-74	303
	246063	14.1	540	8.3	550	646	X75	Head	-	-	-
	246063	14.1	390	13.6	548	672	X75	Centre	-88	-63	309
	246063	14.1	275	18.4	549	652	X75	Tail	-	-	-
	246064	14.1	555	7.7	-	-	-	Head	-80	-73	291
	246064	14.1	440	12.2	546	657	X75	Centre	-78	-61	294
	246064	14.1	405	14.1	563	670	X80	Tail	-70	-59	306
	246065	14.1	470	10.4	537	653	X75	Head	-82	-62	302
	246065	14.1	450	11.8	524	646	X75	Centre	-83	-69	316
	246065	14.1	445	13.7	-	-	-	Tail	-88	-50	334
	246066	14.1	545	8.5	538	647	X75	Head	-81	-64	321
	246066	14.1	460	11.7	535	646	X75	Centre	-93	-63	340
	246066	14.1	400	14.9	539	658	X75	Tail	-81	-63	315
	246067	14.1	560	7.6	543	658	X75	Head	-77	-58	292
	246067	14.1	480	11.0	544	664	X75	Centre	-79	-59	309
	246067	14.1	400	14.0	540	654	X75	Tail	-97	-76	292

Table 68: Charpy V impact toughness of HFI-pipes processed at Salzgitter, transverse/hoop direction

Heat	Coil	t (mm)	CT (local) (°C)	CR (°C/s)	$R_{t0.5}$ (MPa)	R_m (MPa)	Grade Approx	Position	ITT 27J (°C)	ITT 0.5Kvmax (°C)	Kvmax (J)
30257	937683	11.0	535	6.3	660	708	X90	Head	-74	-47	228
	937683	11.0	560	5.7	600	720	X90	Centre	-46	-12	175
	937683	11.0	510	7.3	617	724	X90	Tail	-75	-60	222
D81351	883756	11.0	440	10.0	674	806	X100	Head	-73	-64	97
	883756	11.0	420	10.4	643	796	X100	Centre	-108	-86	95
	883756	11.0	245	15.3	640	784	X100	Tail	-128	-99	105

Heat	Coil	t (mm)	CT (local) (°C)	CR (°C/s)	$R_{t0.5}$ (MPa)	R_m (MPa)	Grade Approx	Position	Impact Energy at 0°C (J)	Impact Energy at -40°C (J)
30257	937683	11.0	535	6.3	660	708	X90	Head	176	50
	937683	11.0	560	5.7	600	720	X90	Centre	75	35
	937683	11.0	510	7.3	617	724	X90	Tail	106	24
D81351	883756	11.0	440	10.0	674	806	X100	Head	96	78
	883756	11.0	420	10.4	643	796	X100	Centre	94	79
	883756	11.0	245	15.3	640	784	X100	Tail	105	93

6.3.2.3 Drop weight tear tests

Drop Weight Tear Test, DWTT, transition tests were carried out and transition curves plotted. DWTT transition temperatures for 85% shear appearance were determined, Table 69, and these have been plotted as a function of strip coiling temperature in Figure 52.

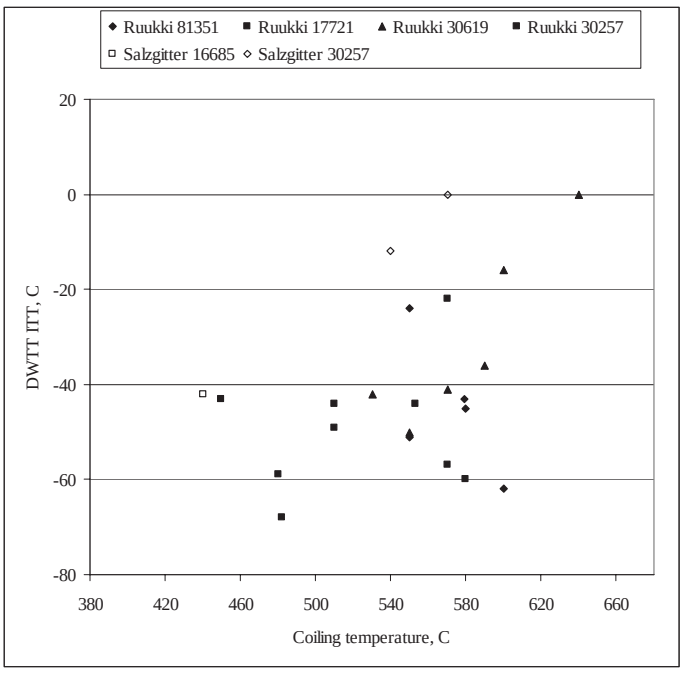

Figure 52: DWTT transition temperature plotted as a function of coiling temperature

The toughness of cast 81351 was very good in spite of roughing rolling being carried out without any holding period. DWTT values (shear area) can be raised when the coiling temperature is somewhat higher.

According to the toughness results of heats 17721 and 30619, the DWTT toughness deteriorated when the coiling temperature was higher than 600°C. Below 580°C the coiling temperature seemed to have no influence on the DWTT toughness. So, both toughness and strength seem to be insusceptible against the variation of the coiling temperature for heats 17721 and 30619. The DWTT toughness of coil 61, which was rolled without waiting in roughing, was as good as that of the coils rolled with waiting during roughing. The mean DWTT transition temperature of heat 17721 was 21°C lower than that of ordinary X70 pipes, although the wall thickness of most of the 17721 coils were 16 mm compared with 13 mm for the ordinary X70 trial pipes. The mean transition temperature of heat 30619 besides coils 21 and 31 was 10°C lower than that of ordinary X70 pipes. The DWTT transition temperature of heat 30257 (SZ) was 10°C higher than that of the ordinary X70 pipes. The reason for this poorer toughness is probably the B-alloying.

Table 69: DWTT transition temperatures of pipes made at Ruukki

Heat	Coil	Thickness, (mm)	T_{rough} (°C)	T_{Cmean} (°C)	T_{Clocal} (°C)	Cooling rate (°C/s)	$T_{trans(85\%)}$ (°C)
81351	31	10	1113	579		33	-43
	41	10	1111	599	600	39	-62
	51	10	1125	550		24	-24
	61	10	1141	562	580	32	-45
	61	10	1141	562	550	32	-51
	Mean						-45
17721	41	12	1051	482		18	-68
	51	12	1056	553		16	-44
	21	16	1004	505	510	15	-49
	21	16	1004	505	510	15	-44
	21	16	1004	505	450	15	-43
	69	16	996	547	580	13	-60
	69	16	996	547	570	13	-57
	69	16	996	547	480	13	-59
	Mean						-53
30619	41	14	1011	548	550		-50
	61	14	1106	536	530		-42
	71	14	1014	572	570		-41
	79	14	1020	582	570		-36
	Mean						-42
30619	21	14	1054	609	600		-16
	31	14	1116	639	640		> 0
30257 SZ	2101	10	1059	551	570		-22
Conventional X70	Mean						-32

Drop weight tear properties were rather poor for cast 30257. At 0°C, strips and pipes of coil 783078 achieved the requirements of the standards, but coil 783080 failed. The microstructure of the pipes showed segregation bands at the core of the wall thickness that, in addition to some retained austenite, may be the reason for its low toughness.

Both curves for strip and pipe samples of cast 16685 were similar and the transition temperature was approx. -40°C for all samples. The properties measured were similar with a very small scatter band. Table 70 shows the values for the spiral pipes and Table 71 shows the HFI-pipe properties.

Table 70: DWTT toughness of spiral pipes processed at Salzgitter

Cast	Coil	t (mm)	CT (local) (°C)	CR (°C/s)	$R_{t0.5}$ (MPa)	R_m (MPa)	Grade approx	Position	Shear area at 0°C (%)	Shear area at -10°C (%)
30257	783077	14.1	573	5.5	-	-	X75	Head	58	25
	783077	14.1	544	6.4	569	663	X75	Centre	23	0
	783077	14.1	528	6.6	546	636	X75	Tail	100	98
	783078	14.1	604	4.4	471	595	X65	Head	95	25
	783078	14.1	538	5.9	522	630	X65	Centre	93	25
	783078	14.1	553	5.6	510	624	X65	Tail	100	53
	783079	14.1	650	2.7	450	566	X60	Head	100	100
	783079	14.1	588	4.0	475	587	X60	Centre	83	30
	783079	14.1	569	5.0	495	618	X60	Tail	95	100
	783080	14.1	560	4.4	537	639	X65	Head	10	25
	783080	14.1	576	4.8	503	611	X65	Centre	30	20
	783080	14.1	568	5.1	493	618	X65	Tail	100	65
16685	246062	14.1	525	8.4	535	641	X75	Head	100	100
	246062	14.1	390	12.8	543	642	X75	Centre	100	100
	246062	14.1	305	16.5	555	665	X80	Tail	100	100
	246063	14.1	540	8.3	550	646	X75	Head	-	-
	246063	14.1	390	13.6	548	672	X75	Centre	100	100
	246063	14.1	275	18.4	549	652	X75	Tail	-	-
	246064	14.1	555	7.7	-	-	-	Head	100	100
	246064	14.1	440	12.2	546	657	X75	Centre	100	100
	246064	14.1	405	14.1	563	670	X80	Tail	100	100
	246065	14.1	470	10.4	537	653	X75	Head	-	-
	246065	14.1	450	11.8	524	646	X75	Centre	100	100
	246065	14.1	445	13.7	-	-	-	Tail	-	-
	246066	14.1	545	8.5	538	647	X75	Head	100	100
	246066	14.1	460	11.7	535	646	X75	Centre	100	100
	246066	14.1	400	14.9	539	658	X75	Tail	100	100
	246067	14.1	560	7.6	543	658	X75	Head	100	95
	246067	14.1	480	11.0	544	664	X75	Centre	100	98
	246067	14.1	400	14.0	540	654	X75	Tail	100	100

Table 71: DWTT toughness of HFI-pipes processed at Salzgitter, transverse/hoop direction

Cast	Coil	t (mm)	CT (local) (°C)	CR (°C/s)	$R_{t0.5}$ (MPa)	R_m (MPa)	Grade Approx	Position	Shear area at 0°C (%)	Shear area at -10°C (%)
30257	937683	11.0	535	6.3	660	708	X90	Head	100 (coil)	100 (coil)
	937683	11.0	560	5.7	600	720	X90	Centre	-	-
	937683	11.0	510	7.3	617	724	X90	Tail	100 (coil)	100 (coil)
D81351	883756	11.0	440	10.0	674	806	X100	Head	100	100
	883756	11.0	420	10.4	643	796	X100	Centre	100	100
	883756	11.0	245	15.3	640	784	X100	Tail	100	100

6.3.2.4 Hydrogen induced cracking testing

Hydrogen induced cracking, HIC, resistance of the base materials was tested according to the test standard NACE TM 0284 (pH = 3.4) at Ruukki. A summary of the test results is presented in Table 72. The HIC test values are determined from three test samples each coil and from three surfaces per test sample. In total, 9 surfaces were examined per coil. The mean longitudinal CLR-values per one surface for every coil and the maximum value per one surface for every coil are presented in the table. The C-, Mn-, and S-contents, which have been noticed to be essential for the HIC resistance, are given in Table 72. Casts 81351 and 30619 are not HIC resistant at all. However, the HIC test results of the base material of cast 17721 are good. The possible reason for the better HIC test results of this cast compared with the others is its low C- and S-content. On the other hand, the good HIC test results are astonishing, because high Mn-content has been noticed to be detrimental to HIC resistance in ordinary sour service grades. Probably the low C-content improves the HIC resistance.

Table 72: Summary of the HIC test results

Coil	C	Mn	S	CLR mean / max.
81351-41	0.043	1.96	0.0009	54.1 / 113.4
81351-61				46.3 / 126.1
17721-21	0.033	1.82	0.0015	0.0 / 0.0
17721-41				0.0 / 0.3
17721-51				2.0 / 12.0
17721-69				0.7 / 5.9
30619-21	0.042	1.81	0.0024	39.6 / 65.6
30619-31				29.6 / 45.9
30619-41				27.4 / 61.8
30619-61				26.1 / 70.3
30619-71				41.0 / 78.3
30619-79				68.9 / 103.6

6.3.3 Microstructural examination

The microstructures of the commercially produced strips and pipes have been quantified by light microscopy etched with Nital in order to characterise the phases. Electron back-scattered diffraction has been used to determine grain sizes and distinguish between ferrite, pearlite and bainite based on different grain boundary misorientations.

6.3.3.1 Conventional etchings

Low CT mixture of bainite (acicular ferrite) and ferrite

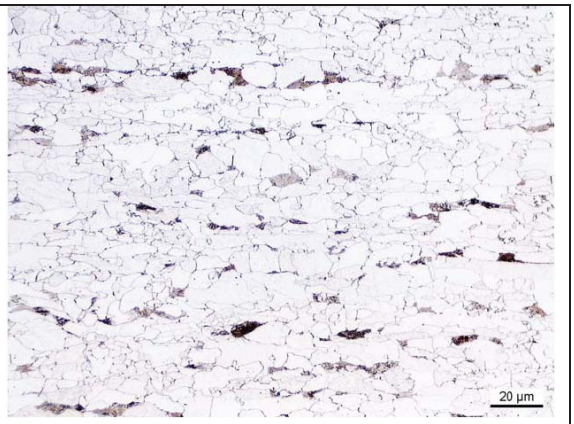

High CT: mainly ferrite with pearlite islands (5%)

Figure 53: Pipe base material for cast 30257 produced in Salzgitter after Nital etching

Mixture of bainite (acicular ferrite) and ferrite

Figure 54: Pipe base material for cast 16685 produced in Salzgitter after Nital etching

6.3.3.2 EBSD characterisation

In order to evaluate microstructure – mechanical properties relationships on the commercially rolled products, it is necessary to have a technique for determining a grain size for microstructures that may vary from ferrite – pearlite to bainitic microstructures. The approach taken has been to use Electron back-scattered diffraction technique to quantify the grain size. This approach has allowed the grain sizes based on different angles of grain misorientation to be assessed.

The number and nature of boundaries in the microstructure obtained by EBSD mapping provides a means of distinguishing between different phases. Clear differences were noted between ferrite and bainite. Ferrite has very few boundaries with low misorientation, in contrast with bainite, which contains a high proportion of low angle misorientations. Bainite characteristically forms with a high dislocation compared with allotriomorphic ferrite and thus a term for this strengthening is often incorporated. The bainite laths, separated by low misorientation angle boundaries, are arranged in packets or colonies, separated by high angle boundaries.

To estimate the strengthening due to grain size, boundaries with misorientations greater than 4º are going to be used, and misorientations greater than 15º to quantify bainitic packets in relation with

toughness. The high-angle boundaries provide effective barriers to cleavage fracture and a smaller grain size promotes lower toughness transition temperatures. On the other hand, low-angle misorientation (4º) grain size (effective grain size) is one of the factors that controls the proof and tensile strength of steel, because such misorientation is expected to be effective in opposing dislocation movement.

Graphs of standard deviation of the grain size plotted against the mean grain size and of mean grain size of 15º against the grain size of 4º of misorientation have been used to present the results.

Plots of number fraction and area fraction against misorientation angle have been used to characterize the microstructures as well. It is quite interesting the last plot (area fraction) because it allows detecting the coarse grain sizes (tails in the grain sizes distributions) due to its harmful effect in toughness.

The EBSD measurements, shown in Table 73 and Figure 55, have been performed at the quarter thickness for all the samples .

Table73: Grain sizes measurements and 15º/4º factors of commercially rolled products.

Cast	Pipe / Strip	Coil	Mean 4º microns	Mean 15º microns	15º / 4º
81351	603745	81351-61	2.375	3.697	1.557
81351	603752	81351-41	2.645	3.140	1.187
30257	SO 52	783078	2.672	5.203	1.947
30257	SO 64	783080	3.502	6.258	1.787
17721	614531	17721-21	3.473	4.670	1.345
17721	614534	17721-69	3.239	4.263	1.316
30619	623899	30619-79	2.855	3.873	1.357
30619	623909	30619-61	3.580	5.499	1.536
16685	264035	SZ	2.280	3.417	1.499

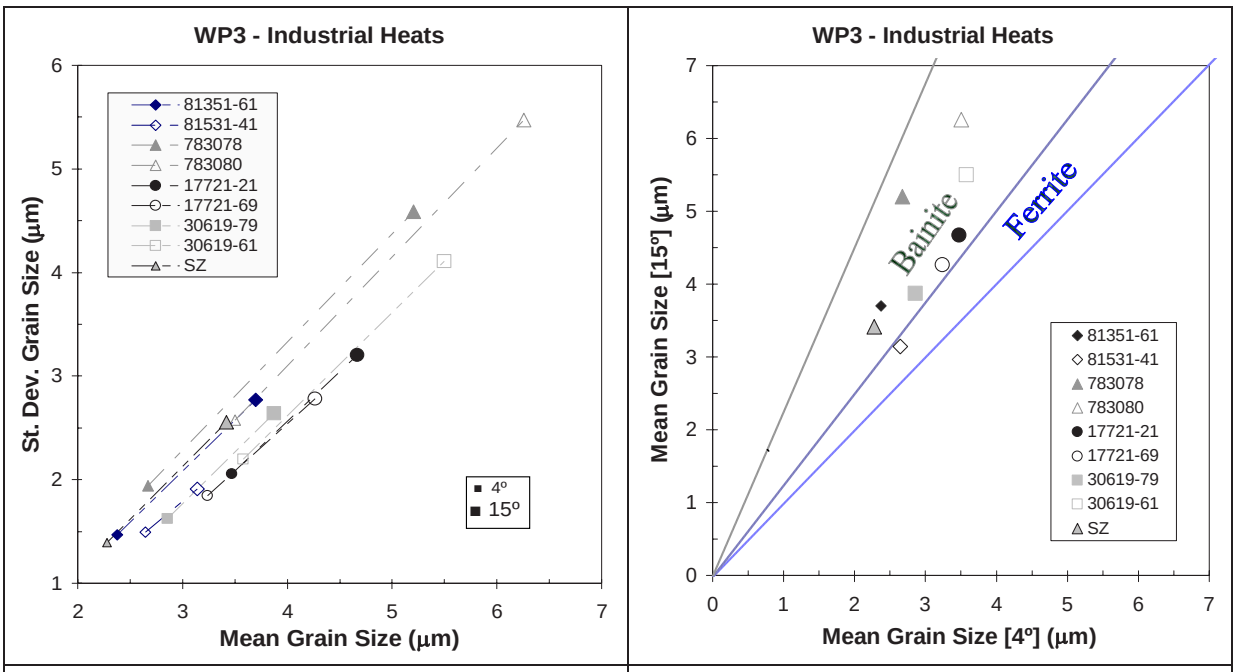

(a) Standard deviation of the grain size plotted against the mean grain size

(b) Mean grain size of 15º against the grain size of 4º

Figure 55 : Grain size measurements by EBSD

Examples of the crystal orientations, and misorientation grain boundaries, indicated in red or black, as a function of the misorientation angle are shown in Figure 56 for coils 81351-41 and 81351-61.

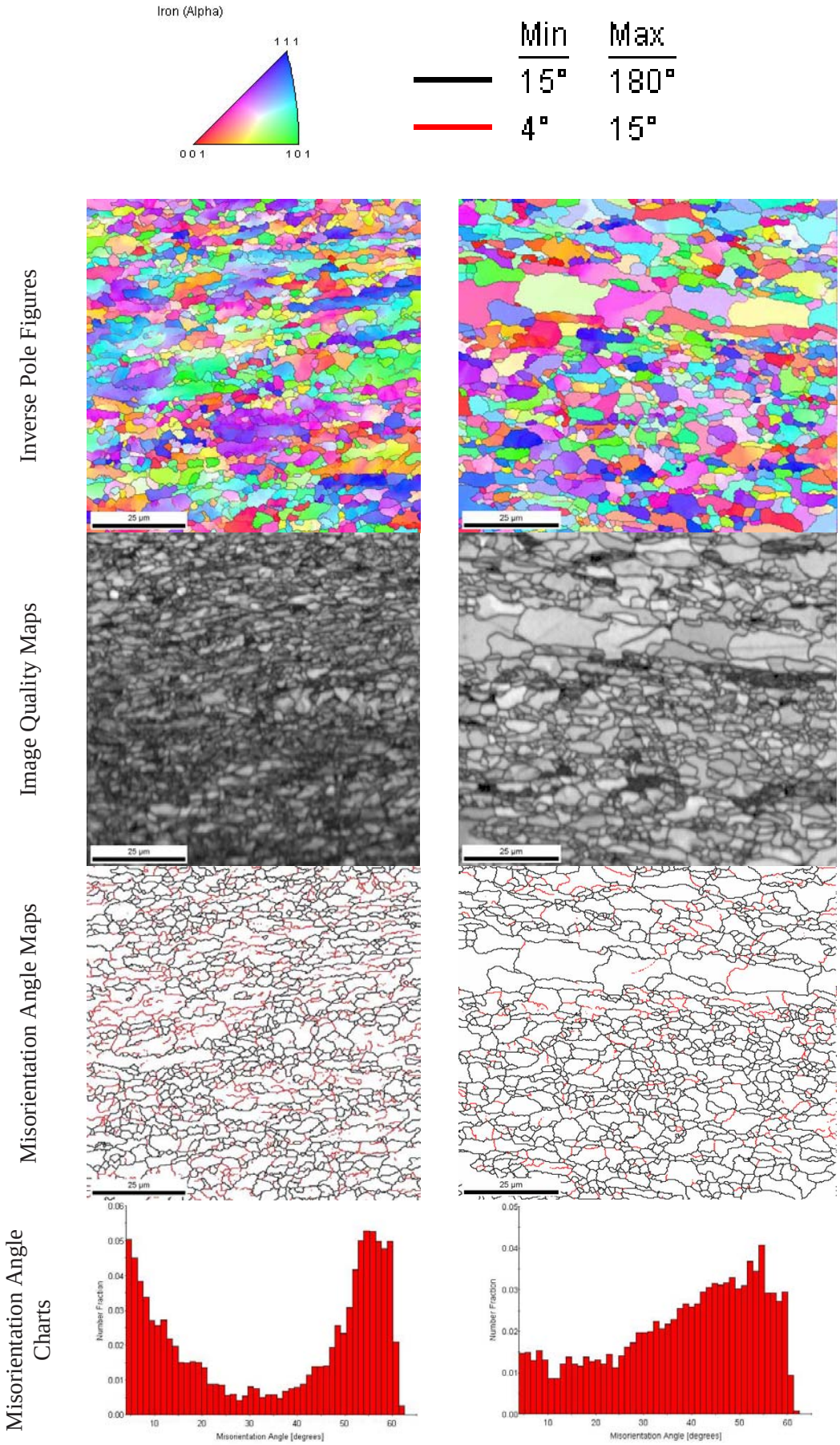

Coil nº 81351-61 Coil nº 81351-41

Figure 56: Microstructural details obtained by EBSD on coils 81351-41 and 81351-61

Plots of number fraction and area fraction against misorientation angle have also been used to characterise the microstructures. The examples for coils 81351-41 and 81351-61 are shown in Figure 57; the area fraction distribution shows the coarse grain sizes (tails in the grain sizes distributions) that may cause poor toughness.

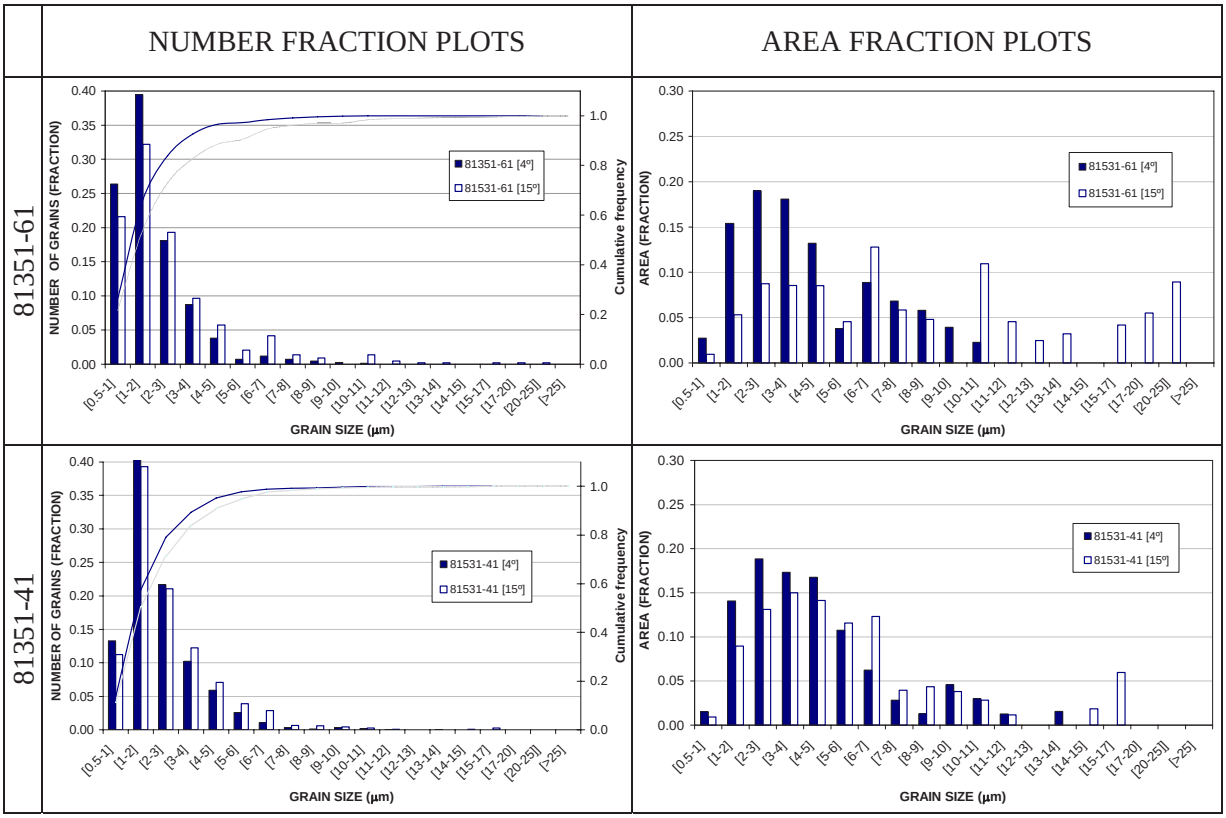

Figure 57: Number fraction and area fraction distributions for coils 81351-41 and 81351-61.

6.3.4 Weldability

6.3.4.1 Mechanical properties of spiral SAW and longitudinal HFI-welds

Tensile test were made on the welded joints and for the weld metal of the spiral-welded and HFI-pipes; the results for the spiral-welded pipes are shown in Table 74and those for the HFI-pipes are given in Table 75. The welding process reference numbers are 121 for spiral welding and 291 for HFI welding.

Table 74: Cross and all weld tensile properties for spiral-welds

Cast	Coil	t (mm)	CT (local) (°C)	Grade approx	Cross-weld			All Weld Metal		
					$R_{t0.5}$ (MPa)	R_m (MPa)	Fracture position	$R_{p0.2}$ (MPa)	R_m (MPa)	A %
81351	41	10	600	X70	637	796	FL	669	823	18
	61	10	550	X85	590	752	FL	633	784	19
17721	21	16	450	X65	519	615	Base	543	614	22
	41	12	482	X65	526	610	Base	553	638	25
	51	12	553	X65	538	624	Base	544	615	21
30619	21	14	600	X65	554	650	Base		736	22
	31	14	640	X65	518	618	Base	594	690	25
	41	14	550	X65	538	639	Base	611	708	23
	61	14	530	X65	536	639	Base	572	656	25
	71	14	570	X65	538	630	Base	589	681	24
	79	14	570	X65	560	659	Base	589	681	24

30257	783077	14.1	544	X75	568	667	Weld	-	-	-
	783079	14.1	588	X60	549	652	Base	-	-	-
16685	246066	14.1	460	X75	645	712	Base	-	-	-
	246067	14.1	480	X75	657	718	Base	-	-	-

According to the tensile results the welding consumables were deemed to be suitable for the material. For cast 81351 the strength of the weld metal was similar to the strength of the base material, a little higher strength would have been beneficial. All other casts showed suitably overmatching weld strengths.

Table 75: Cross weld tensile properties for HFI-welds

Cast	Coil	t (mm)	CT (local) (°C)	Grade approx	Cross-weld		
					$R_{p0.2}$ (MPa)	R_m (MPa)	Fracture position
30257	937683	11	560	X80	633	735	Weld
81351	883756	11	420	X85		754	Weld

The bending test of cast 30257 failed, cracks were observed. The tensile strength of both HFI-welds is very good but the fracture position is placed in the welded area.

Charpy V-notched samples have been used to determine toughness properties of the welds. For the tests, the notch was positioned in the weld, in the fusion line, in the fusion line +2 mm, in the fusion line +5 mm and in the base material (in cross weld direction) for the samples tested in Salzgitter, Table 76. At Ruukki, the notch was placed in the weld, in the fusion line, in the fusion line + 1.0 mm and in the fusion line +2.5 mm.

Table 76: Cross weld Charpy V-notch impact toughness for spiral-welds (Salzgitter)

Cast	Coil	t (mm)	CT (local) (°C)	Grade	Notch position	Cross-weld toughness (J)	
						-20°C	-40°C
30257	783077	14.1	544	X75	Weld	43	32
					FL	97	25
					FL+2 mm	162	108
					FL+5 mm	189	166
					Base	148	116
30257	783079	14.1	588	X60	Weld	79	34
					FL	57	59
					FL+2 mm	80	78
					FL+5 mm	118	92
					Base	78	48
16685	246066	14.1	460	X75	Weld	104	71
					FL	170	194
					FL+2 mm	240	241
					FL+5 mm	250	247
					Base	302	303
16685	246067	14.1	480	X75	Weld	70	74
					FL	106	36
					FL+2 mm	197	76
					FL+5 mm	249	232
					Base	202	187

Cast 30257 showed low values for the weld and the fusion line samples for -40°C. The microstructure in the weld and FL tended to coarsen in grain size and the microstructure was an inhomogeneous mixture of ferrite/pearlite and bainite. The arc energy may have been too high or the welding speed too low. Cast 16685 delivered good results for -20°C for all notch positions. At lower temperatures, the fusion line notched-samples were poor.

For HFI-pipes, Charpy samples were taken for notch positions in the weld, at the fusion line + 2 mm, and in the base metal. Table 77 presents the energies absorbed at - 20°C and - 40°C.

Table 77: Cross weld Charpy V-notch impact toughness for HFI-welds (Salzgitter)

Cast	Coil	t (mm)	CT (local) (°C)	Grade	Notch position	Cross-weld toughness (J)	
						-20°C	-40°C
30257	937683	11	560	X80	Weld	77	59
					FL+2 mm	109	99
					Base	161	157
81351	883756	11	420	X85	Weld	16	23
					FL+2 mm	-	-
					Base	-	-

The impact toughness of cast 30257 was similar to the results of the spiral-welded pipes. Both temperatures tested delivered good values. The very poor cross-weld toughness of cast 81351 may be related to the weld heat-treatment, which was done without annealing. A common practice for the weld and the HAZ is re-heating to austenitising temperature of 950°C and water quenching, followed by annealing at approx. 600°C. In the case of heat 81351, the weld was re-heated to 920°C and air cooled. Due to the alloying elements such as chromium, air-hardening may have occurred and the microstructure in the weld was martensitic/bainitic and thus, very brittle.

Impact toughness of the welds of casts 81351, 17221 and 30619 are shown in Figures 58 to 60. The test specimen for cast 81351 was 5 x 10 mm, the other specimens were 10 x 10 mm.

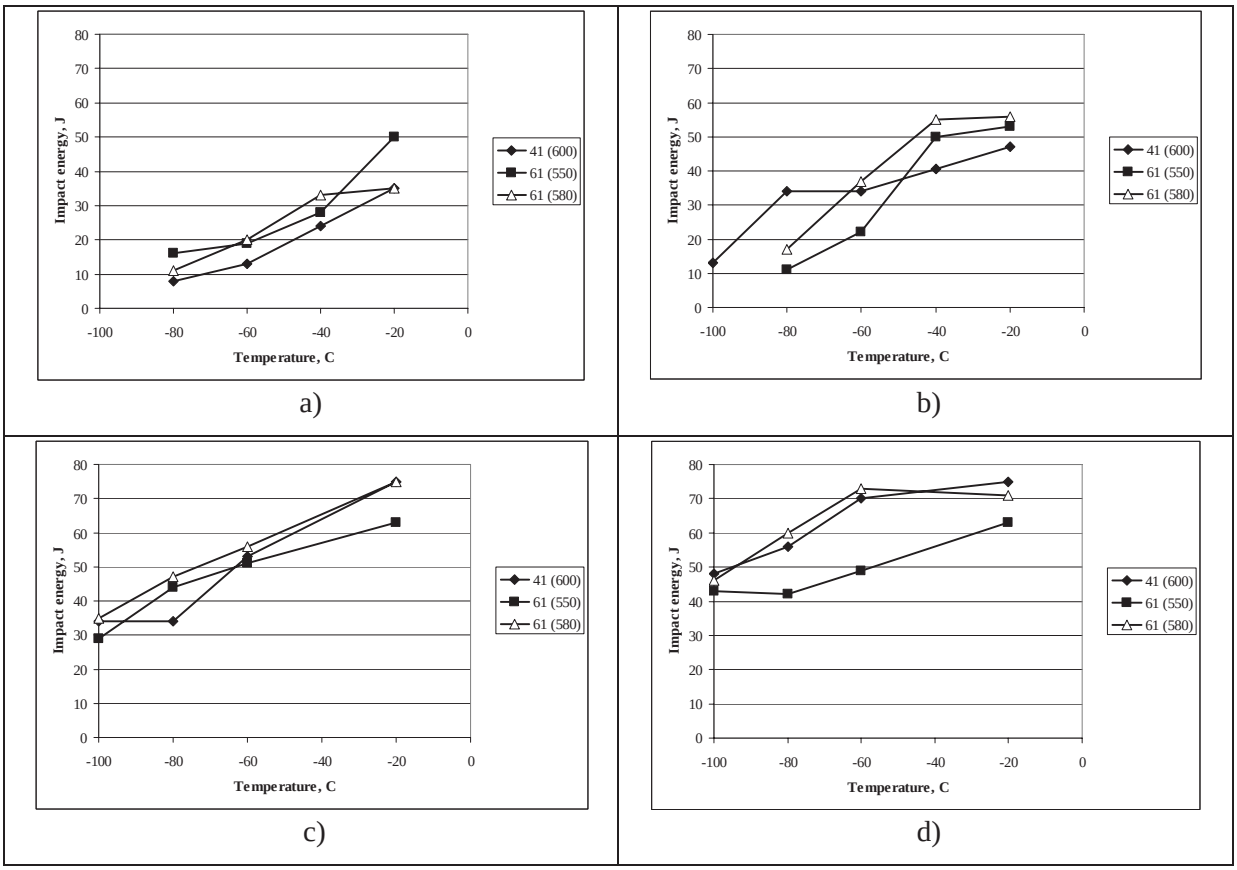

Figure 58: Cast 81351 a) Weld metal, b) FL, c) FL + 1 mm, and d) FL + 2.5 mm

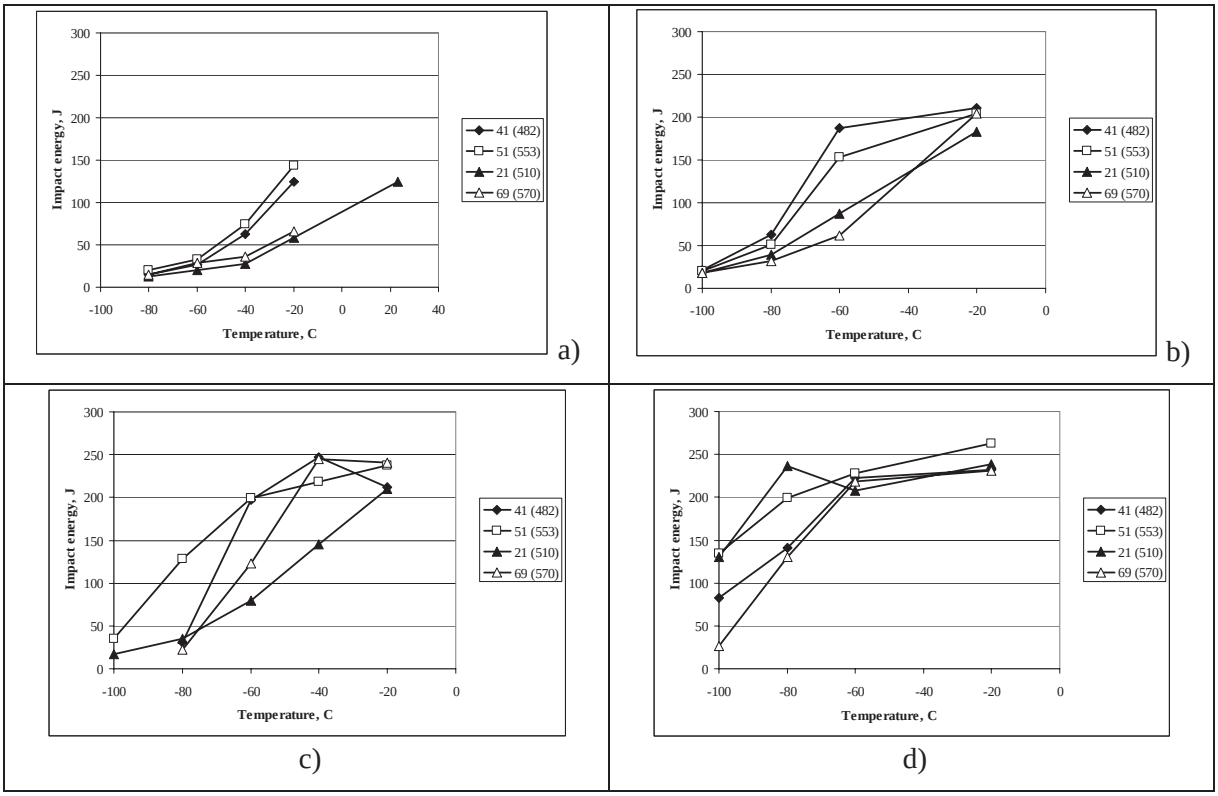

Figure 59: Cast 17221 a) Weld metal, b) FL, c) FL + 1 mm, and d) FL + 2.5 mm

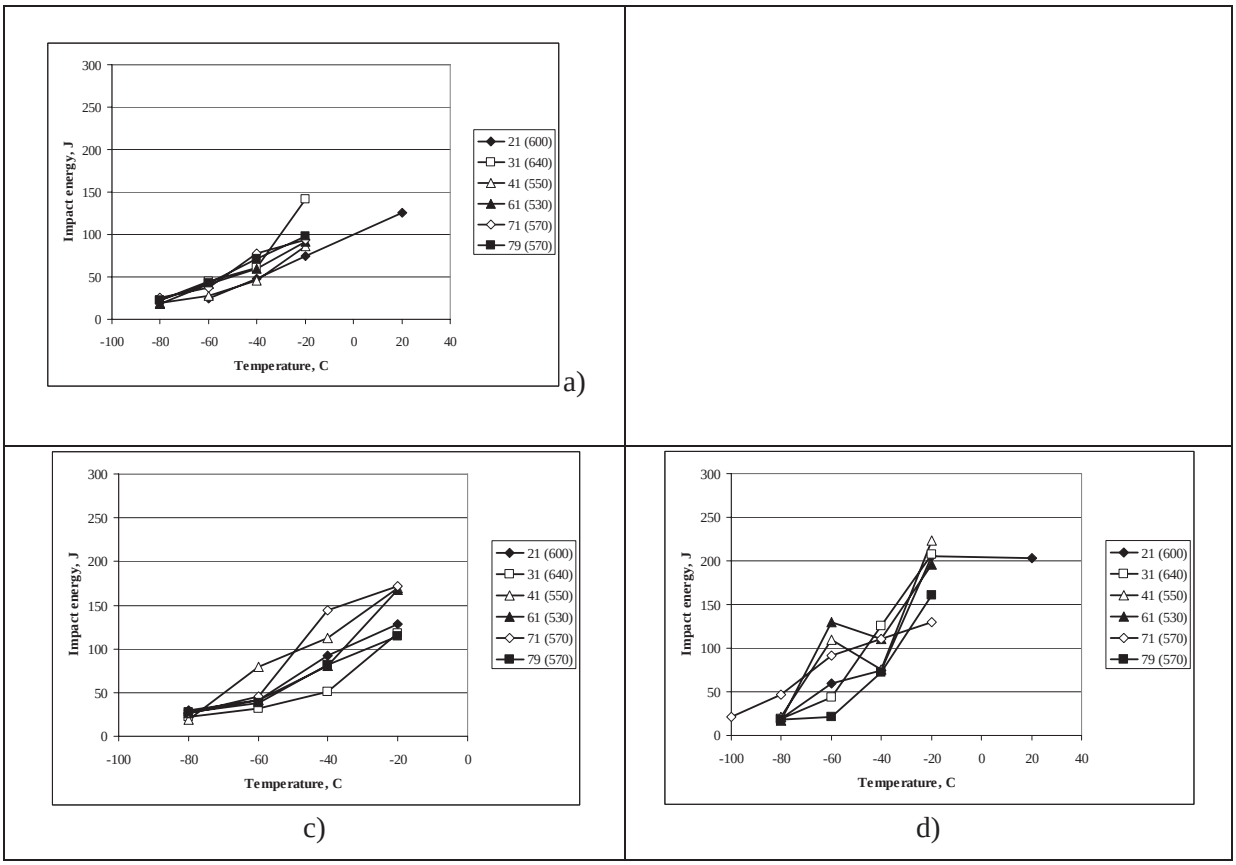

Figure 60: Cast 30619 a) Weld metal, c) FL + 1 mm, and d) FL + 2.5 mm

According to the standard EN 10208, the weld toughness requirement for specimen 10 x 10 mm is 40 J and for 5 x 10 mm specimen 20 J. Cast 81351 fulfils this requirement for all the different positions of the notch, even at temperatures of -40°C in the weld.

Cast 17221 also meets the requirements for all positions for -30°C and cast 30619 for -40°C.

Additionally, the hardness of the welds has been measured, Table 78 and Table 79.

Table 78: Cross weld hardness (HV10) for spiral welds (Salzgitter)

Position	Coil	Base metal	HAZ	Weld	HAZ	Base metal
1.5+/-0.5mm	246066	210	210	221	206	238
7.05mm			206	245	206	
13.1+/-0.5mm		206	221	226	221	210
1.5+/-0.5mm	783077	206	213	206	206	221
7.05mm			221	206	199	
13.1+/-0.5mm		206	224	193	228	206

Table 79: Cross weld hardness (HV10) for HFI-welds (Salzgitter)

Position	Coil	Base metal	HAZ+2mm	Weld	HAZ+2mm	Base metal
1.5+/-0.5mm	937683	213	240	254	258	221
7.05mm		221	228	226	236	224
10+/-0.5mm		221	228	213	221	228

All of the hardness measured for spiral pipes and HFI-pipes are quite similar. No hardness increase was observed. Figure 61 shows both types of welds.

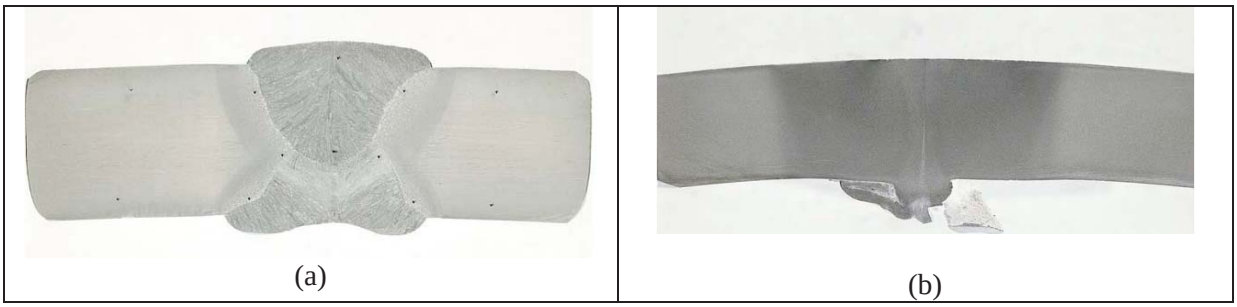

(a) (b)

Figure 61: (a) spiral pipe cast 30257, coil 783077, and (b) HFI-pipe cast 30257, coil 937683

The hardness of casts 81351, 17221 and 30619 is displayed in Figure 62. Hardness has been measured using HV10 along the centreline and at a distance of 2 mm from the outer and inner surface.

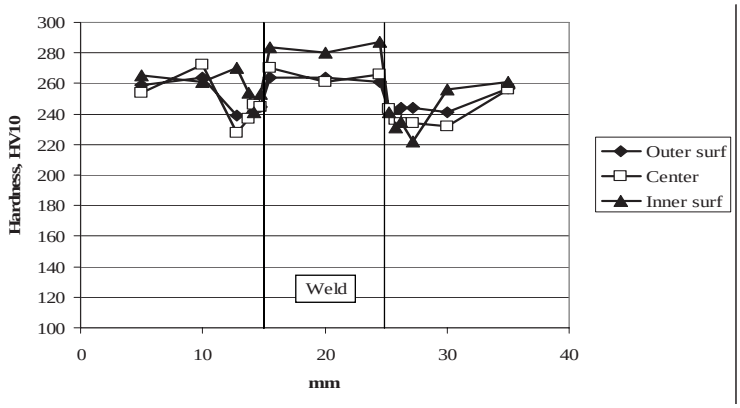

cast 81351, coil 41

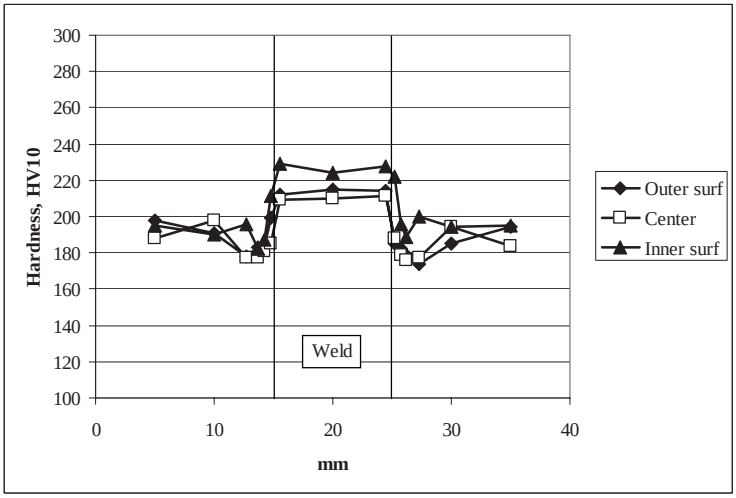

cast 17221, coil 41

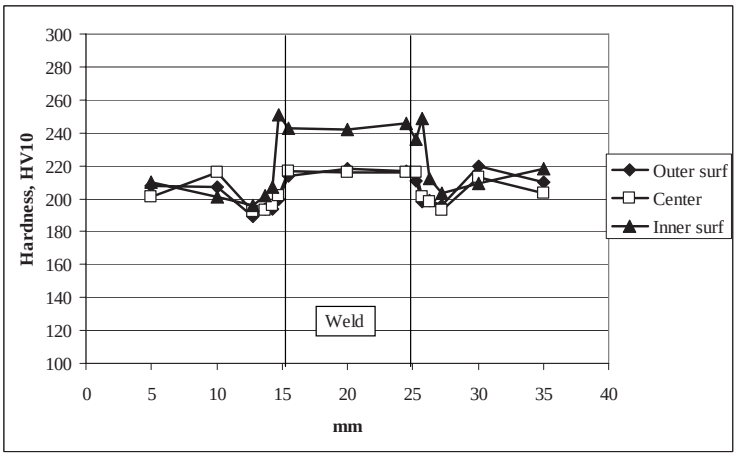

cast 30619, coil 41

Figure 62 Hardness profiles

All of the hardness profiles are good. Some minor softening of the fusion line can be observed but is smaller than compared to standard X60/X70 grades.

6.3.4.2 Tekken test

Tensile testing has been carried out in the longitudinal and transverse directions to rolling on the parent material for both compositions along with Charpy V notch impact tests. For welding simulations, 8 samples for the Tekken test were taken, samples for HAZ simulations trials were prepared and two

plates each for MMA and GMA welding have been cut. The processing parameters applied for MMA, reference number 111, and GMA, reference number 135, welding for cast 30257 and cast 16685 are shown in Table 80 and macrographs for cast 30257 are shown in Figure 63.

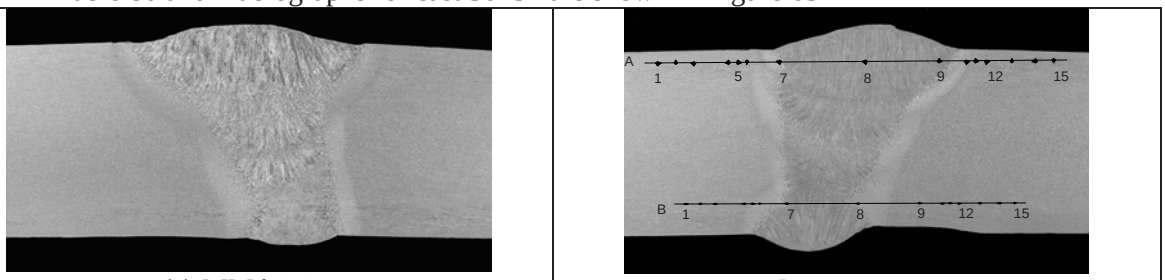

(a) MMA joint (b) GMA joint

Figure 63: Macrographs of welds in cast 30257

Table 80: Welding parameters for MMA and GMA welding trials

Welding method	Filler metal	Bead no.	Welding current (A)	Voltage (V)	Welding speed (cm/s)	Heat input E (kJ/cm)
MMA (111) Cast 30257	Electrode SL12G Φ 4.0 mm EN 15997-97 E Mo B 32 HB	1	93	22.0	0.153	13.7
		2	140	24.0	0.211	15.4
		3	147	26.0	0.193	19.8
		4	147	26.0	0.191	20.0
		5	152	26.0	0.202	19.6
					Mean value	17.7
GMA (135) Cast 30257	IMT NiMoCr Φ 1.2 mm + M21 EN 12534 Mn3Ni1CrMo	1	120	19.5	0.175	13.4
		2	168	23.0	0.438	8.8
		3	176	23.0	0.410	9.8
		4	182	23.0	0.379	11.0
		5	195	24.0	0.299	15.6
					Mean value	11.1
GMA (135) Cast 16685	IMT NiMoCr Φ 1.2 mm + M21 EN 12534 Mn3Ni1CrMo	1	200	20.0	0.42	9.5
		2	235	22.0	0.50	10.3
		3	235	22.0	0.50	10.3
		4	235	22.0	0.50	10.3
		5	260	24.5	0.60	10.6
		6	260	24.5	0.75	8.5
					Mean value	9.9

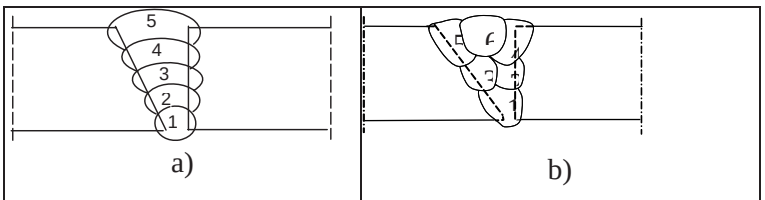

a) Cast 30257 and b) Cast 16685

Figure 64: Position of beads

Hardness measurements have been carried out for HV5 for both welding processes and are displayed in Table 81.

Table 81: Hardness distribution across both welds (MMA and GMA) of cast 30257 and 16685

	Indention No.														
	1	2	3	4	5	6	7	8	9	10	11	12	13	14	15
MMA	30257														
A	221	223	210	208	210	214	180	190	190	221	199	201	210	212	210
B	199	208	210	197	229	236	206	208	221	246	244	212	216	214	221
GMA	30257														
A	206	214	219	206	236	271	262	265	268	280	236	210	223	221	210
B	197	219	206	249	246	257	257	249	260	262	244	227	199	208	197
GMA	16685														
A	233	239	239	228	239	259	257	258	250	252	243	234	243	243	237
B	228	227	227	226	250	272	246	234	234	254	224	220	234	239	234

The MMA weld showed a hardness decrease in the weld whereas the GMA weld tended to excessive hardening in the weld. Mechanical properties of the weld have been characterised by tensile specimen, bending tests and Charpy V testing for different temperatures. The samples were all positioned across the weld, Table 82.

Table 82: Mechanical properties of the MMA and GMA welds

Welded test plate	Tensile test		Bend test			Impact strength KV (J) of HAZ			
	Rm (MPa)	Remark	In tension	Bending angle	Remark	+20°C	-40°C	-60°C	-80°C
MMA (30257)	593	Fracture in weld	face	180°	without cracks	191	181	68	88
						184	174	178	64
			root	180°	without cracks	186	184	82	78
						187	180	109	76
GMA (30257)	513	Fracture in weld	face	180°	without cracks	186	140		68
						189	126	51	70
			root	180°	without cracks	193	152	179	66
						189	139	105	68
GMA (16685)	727	Fracture in base/parent metal	face	180°	without cracks	288		88	61
						286		72	66
			root	180°	without cracks	224		86	58
						266		82	62

Tekken testing has been performed according to EN ISO 17642-2. Electrodes and welding wires applied for Tekken are shown in Table 83 and the processing parameters and results are shown in Table 84.

Table 83: Welding wires and electrodes used in Tekken testing

Brand	Classification	Mechanical properties of all weld metal			Diffusible hydrogen [ml/100g]	
		$R_{p0.2}$ (MPa)	Rm (MPa)	Elongation (%)	Glycerine method	Mercury method
Covered electrodes						
SL 12G Basic, very low hydrogen	EN 1599-97: E Mo B 32 H5	550	610	25	1.65	2,50
Pipeliner 8P+ Cellulosic	EN 499-94: E 46 4 1Ni C25	460-559	550-676	19-27	24.8	37.7
Welding wire						
IMT NiMoCr	EN 12534 Mn3Ni1CrMo	> 620	> 700	A_5 >17 %		

Table 84: Welding parameters for Tekken testing and metallographic investigations

Filler material	Welding parameters			Heat input	Temperature	Results of metallographic examination (sections)			
	I (A)	U (V)	v (cm/s)	(kJ/cm)	(°C)	1	1	1	1
30257									
Electrode SL12G Φ 4.0 mm	148	22.5	0.33	10.1	RT	No crack	No crack	No crack	No crack
IMT NiMoCr wire Φ 1.2 mm + M21	136	18.8	0.35	7.3	RT	No crack	No crack	No crack	No crack
Pipeliner 8P+ Φ 4.0 mm	116	24.6	0.34	8.4	RT	Crack in weld	Crack in weld	Crack in weld	Crack in weld
					65	Crack in weld	No crack	No crack	No crack
					100	No crack	No crack	No crack	No crack
16685									
Electrode SL12G Φ 4.0 mm	150	22.5	0.33	10.2	20	No crack	No crack	No crack	No crack
Pipeliner 8P+ Φ 4.0 mm	120	24.5	0.34	8.7	20	Crack in weld	Crack in weld	Crack in weld	Crack in weld
					60	Crack in weld	Crack in weld	Crack in weld	Crack in weld
					90	No crack	No crack	No crack	No crack

The conclusion can be drawn that the material 30257 is characterised by a high brittle fracture resistance at room-temperature and even at low temperatures. Cast 16685 also delivered very good results for brittle fracture resistance down to -100°C. The impact strength of the welded joints in the HAZ was good for both casts.

The material was resistant to cold cracking in the HAZ, even with a high level of diffusible hydrogen present in the weld metal (37 ml/100g).

6.3.4.3 Girth weld testing

A girth weld was made in the 14.2 mm thick, 1067 mm diameter pipe, identified as 925332, following the welding procedure specification shown in Appendix B2. The goal was to obtain an overmatch level of about 5 to 10% in weld metal yield strength compared to the X80 longitudinal properties of the pipe material. No specific weld pre-qualification program was conducted to optimise the level of strength mismatch. However, the selected consumables and welding procedure ensured that the transverse weld tensile test met the API requirements.

The pipe coupon was cut in two and bevelled according to the welding procedure specification. The girth weld was made by manual gas-shielded flux cored arc welding, FCAW (136). The weld bevel preparation had a V-shape with a nominal angle of 60° and a root opening of 1 mm; the chosen filler material was Lincoln Outershield 550-H with a wire thickness of 1.2 mm. The product conformance report gave the following overview of the mechanical properties of the weld metal:

Table 85: Mechanical properties of weld metal, Lincoln Outershield 550H

Room temperature properties			Charpy Energy at -40°C (J)
R_{el} (MPa)	R_M (MPa)	A5 (%)	
695	738	19	58

Shortly after beginning the hot pass at the six o'clock position, one of the welders burned through in two positions due to excessive grinding of the root and this area was repaired by grinding and re-welding from the inside once the entire weld had been completed.

EPRG toughness requirements [17] state that girth weld failure by the onset of remote yielding (remote = 0.5%) can be ensured when Charpy energy values of a minimum of 30 J and an average of 40 J are obtained at the design temperature.

Wide plate specimens were extracted by flame cutting in the axial (longitudinal) direction, Figure 65. These specimens had nominal dimensions for the overall width (arc length) of 400 mm and length of 1200 mm, with the weld at the mid-length. After flame cutting, the longitudinal edges within the prismatic (test) section were machined straight and parallel to each other. The prismatic part was machined to a width (arc length) of nominally 300 mm and a length of 900 mm, with the weld at mid-length, see Figure 66.

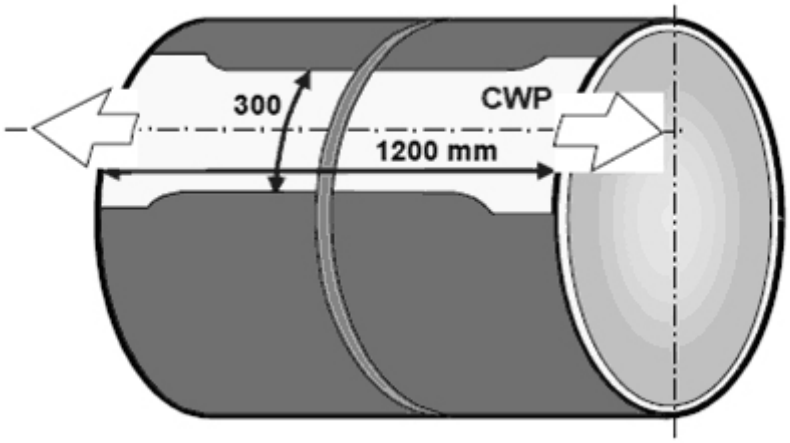

Figure 65: Illustration of a curved wide plate extracted from a large diameter pipe in the axial direction

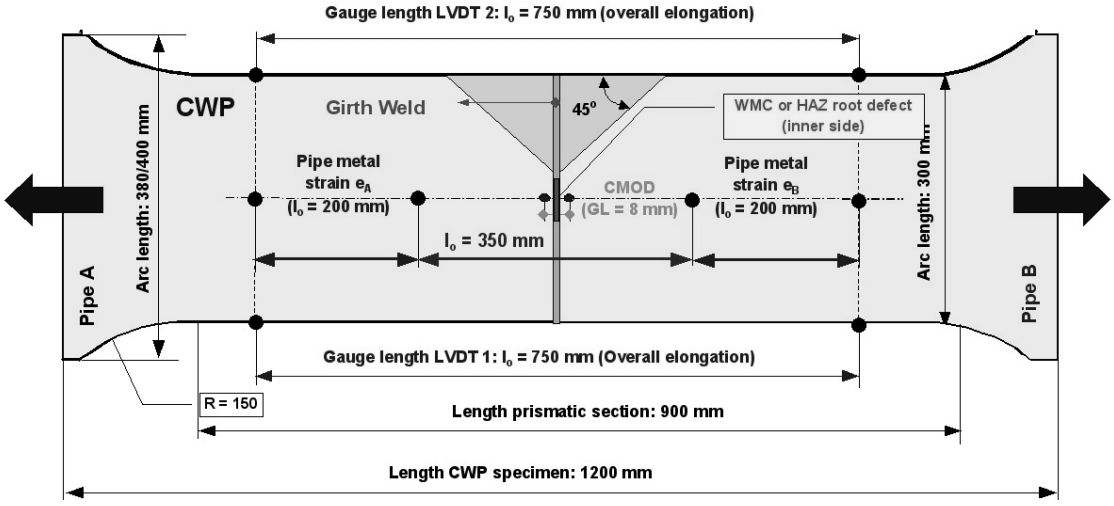

Figure 66: Curved wide plate specimen dimensions and instrumentation

The pipe sections were not flattened, that is the curvature was retained, and the weld reinforcements were not removed, except at the location where the surface breaking root defect was to be introduced. At this location, the root overfill was ground flush with the surfaces, during which care was exercised to respect the wall thickness at either side of the weld. Sharp surface breaking notches were introduced by means of a cutting wheel with a diameter of 63 mm and a blade thickness of 0.15 mm. This resulted in a notch-acuity of 0.15 mm. The defect depth was 3.0 mm, and the defect length was 50 mm. In selecting the notch dimensions, consideration was given to the fact that defect-area-ratios of less than 3% ensure remote plastic strains [18]. It should be noted that, owing to the finite diameter of the cutting

wheels, the surface notches had a semi-circular shape towards their extremities. Within the central portion, the notches were flat bottomed with a depth equal to the target values to within 0.05 mm. This is illustrated in Figure 67. Prior to notching, the weld root was locally ground, polished and macro etched in 5% Nital, which allowed the fusion boundaries at the inner pipe walls to be seen so that a notch could be located in the root at the weld metal centreline, identified as WMC, or at the heat affected zone/fusion line, identified as HAZ.

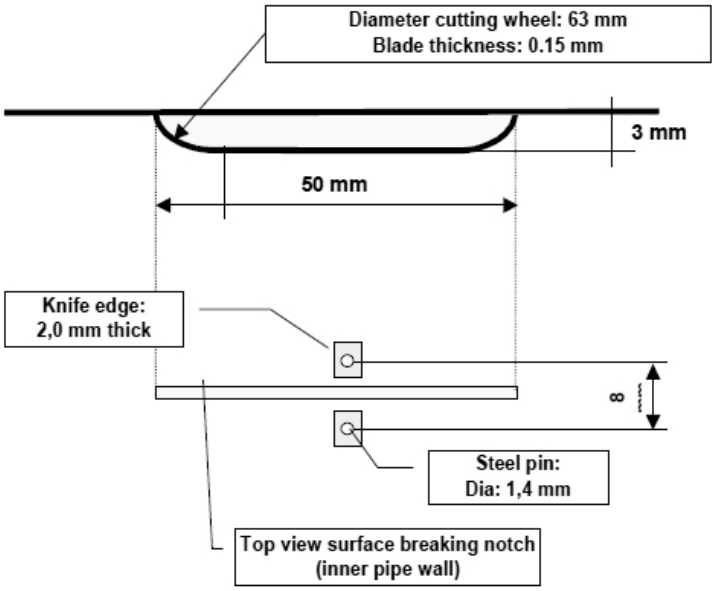

Figure 67: Wide plate notch details and CMOD measurements

After notching, the wide plates were manually welded at their extremities to heavy loading lugs, having a curvature matching the pipe curvature. Care was exercised during welding to ensure that the centroïd of the cross sectional area of the test section coincided with the load application line. The assembly was mounted, by means of the holes in the loading lugs and heavy steel pins, horizontally in three elements of the 8000 kN testing machine, Figure 68. The machine consists of four individual loading elements, each capable of developing 2000 kN. The framework of each element consists of two vertical I beams between which two servo-hydraulic actuators are mounted. Each actuator has a capacity of 1000 kN and a stroke of 750 mm. The machine is equipped with a closed loop control system allowing operation either in load or displacement-control. The load is measured by means of calibrated load cells mounted on the piston rods of the individual actuators.

Tests were carried out at -20^{o}C; this temperature was achieved and maintained for at least one hour before tensile loading was started by circulating refrigerated methanol, through specially designed cooling boxes having the same curvature as the pipe and firmly clamped against the outer walls at either side of the weld. As the fluid is directly in contact with the pipe walls and is circulated at high speed, a uniform temperature is obtained throughout the prismatic test section. The specimen temperature was continuously monitored by means of a chromel-alumel thermocouple, spot-welded to the inner wall in the near vicinity of the artificial defect.

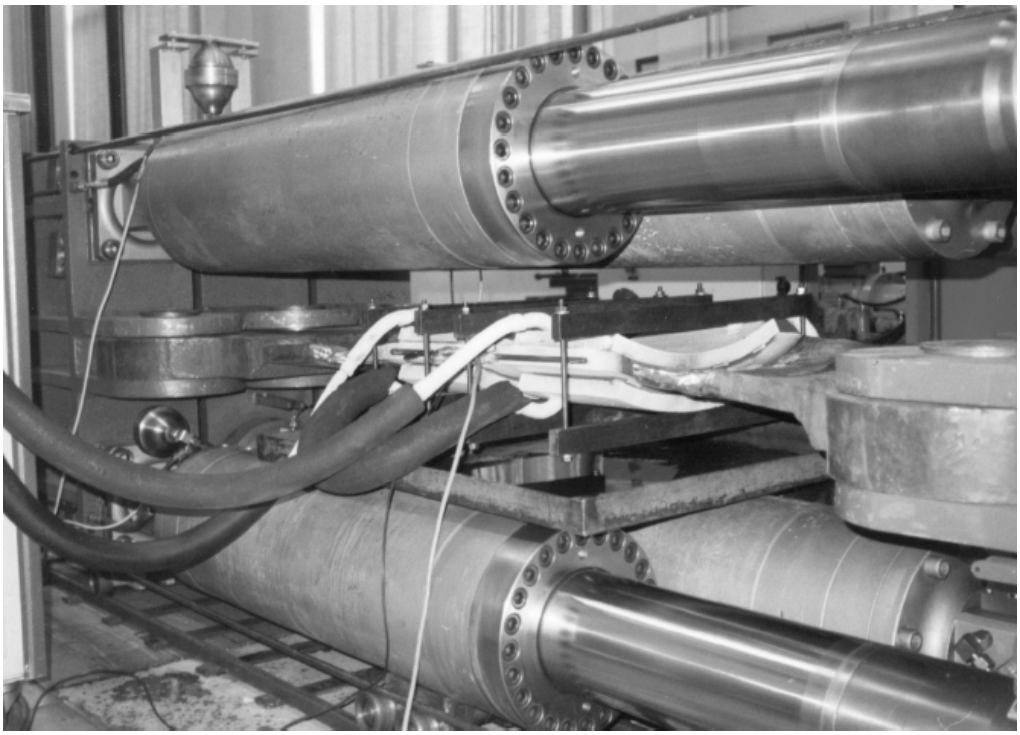

Figure 68: Wide plate specimen with cooling boxes mounted in the 8000 kN tensile testing rig

The overall elongation (Δl) was measured on a gauge length of 750 mm by means of two spring loaded Linear Variable Differential Transformers, LVDTs, which follow the relative displacement of two pairs of steel pins spot-welded 8.0 mm apart straddling the surface notch at the mid-length, see Figure 66. The use of two LVDTs is intended to compensate for any effect of in-plane bending that might occur as a result of any unwanted eccentricity of the load application line. The LVDTs had a linear stroke of nominally 40.0 mm and an accuracy of better than 0.01 mm. At either side of the weld, the elongations of the pipe sections were measured at the inner surface on a gauge length of 200 mm using similar LVDTs. The crack mouth opening displacement (CMOD) was measured at the root side on a gauge length of 8.0 mm by means of a clip-on measuring device, similar to that used for CTOD bend testing, which follows the relative displacement of the two steel pins. The clip-on gauge was mounted between knife edges having a height of 2.0 mm and it had a linear stroke of 8.0 mm with an accuracy of better than 0.005 mm.

Table 86 shows the values of the gross section stress, gross (overall) strain, CMOD value, the remote pipe metal strain, and the failure condition at the maximum load recorded during the curved wide plate tests.

Table 86: Summary of CWP test results at maximum load

Notch position	Gross failure stress, MPa	Overall failure strain, %	CMOD mm	Pipe metal failure strain, %	Wide plate performance
WMC	688	4.6	3.89	4.1	GSY
HAZ / FL	670	3.6	2.24	3.3	GSY
HAZ / FL	645	1.4	1.50	1.2	GSY

The curved wide plate specimen with the notch at the weld metal centreline failed at a remote strain of 4.1% while the HAZ-notched specimens survived remote strains of 3.3% and 1.2% respectively. The measured CMOD-values were in line with these observations. Instability at maximum load was seen in the weld metal centreline test and the specimen finally failed by unstable pop-through,

The fracture face of the test with the notch at the weld metal centre-line, Figure 69, shows the artificial weld defect, at the top of the fractograph, followed by tearing (black arrow) and final 45° shear failure (white arrow).

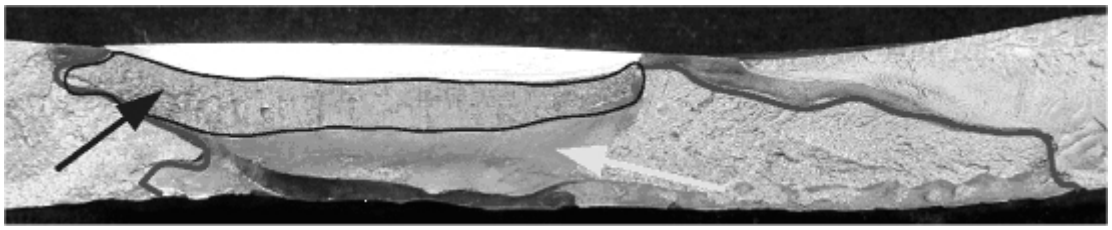

Figure 69: Fracture face of the specimen with the notch at the weld centre-line

The first specimen with a notch in the heat affected zone also failed by maximum load instability followed by unstable fracture whilst the other failed by unstable fracture initiation. The plots of gross stress and CMOD are shown, as an example, for this specimen, Figure 70.

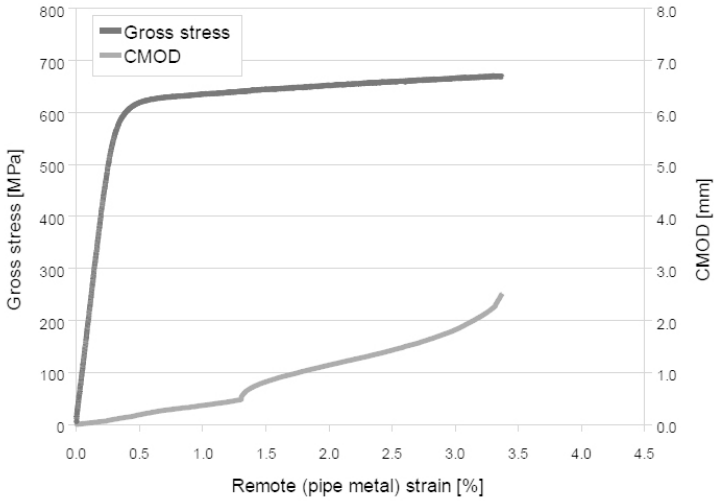

Figure 70: Gross stress and CMOD as a function of pipe metal strain for the first curved wide plate specimen notched in the heat affected zone

The fracture faces of the tests with the notch in the heat affected zone are shown in Figure 71 and Figure 72, where the grey arrows indicate the zones of insignificant pop-in adjacent to the artificial defects, and the black arrows point to the zones of stable crack extension.

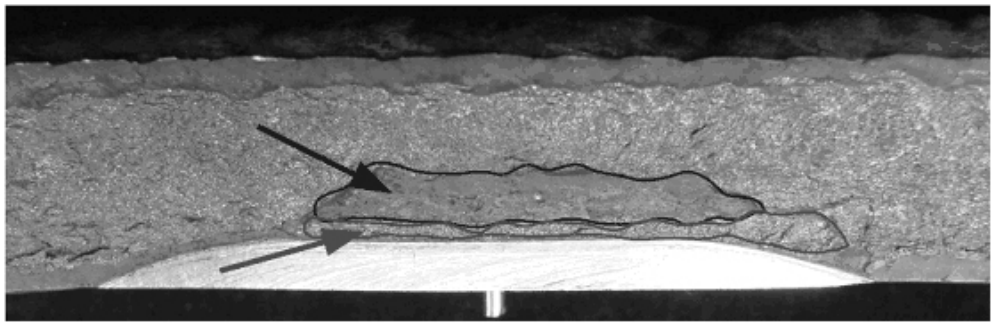

Figure 71: Fracture face of the first specimen with the notch in the heat affected zone

The difference between the results for these two specimens was attributed to the presence of weld porosity at the artificial crack tip, indicated by the white arrow in Figure 72, which has been attributed to the burning through and repair actions reported in the description of the welding procedure.

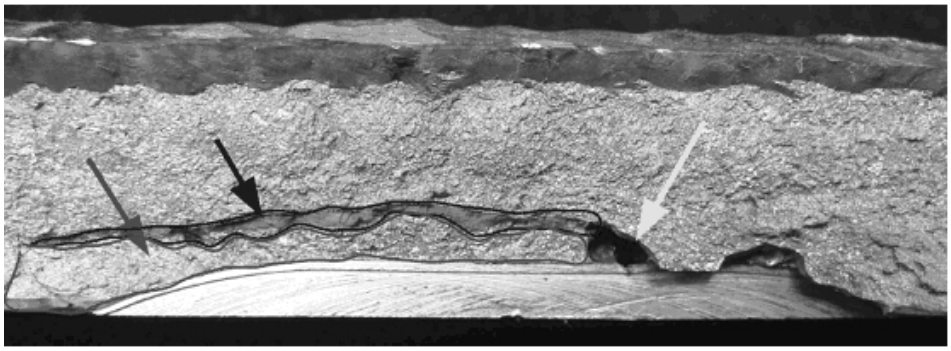

Fracture 72: Fracture face of the second specimen with the notch in the heat affected zone

In all three cases, the remote applied (gross) failure stress exceeded the pipe metal yield stress and the pipe metal strains measured at failure were all in excess of 0.5%. These observations indicate that gross section yielding has been reached for all three specimens and this performance has been attributed to the beneficial effect of weld metal strength overmatching that shields defects from the applied deformation [19]. The values in Table 86 indicate that the remote applied strains were mainly consumed by the pipes at either side of the weld.

Despite the incidence of pop-in, it was shown that the girth weld had adequate flaw tolerance, with respect to fracture initiation, for low temperature application. It was concluded that the FCAW girth weld in the high Nb alloyed X80 pipe can, at a temperature of -20 °C, tolerate at least 3.3 % strain with a 3 x 50 mm circumferential surface breaking defect present in the weld root. In the presence of weld porosity the strain limit was reduced to 1.2 %.

6.4 Plate for general construction

The aim of this work-package was to assess the capability of the steel type in the rolled condition when processed with lower levels of controlled rolling and without the use of accelerated cooling, and to assess the effect of post-production processes on the performance of these steels.

6.4.1 Composition and processing

Air-cooled plates of 20 mm and 50 mm thickness were rolled in the Corus Scunthorpe Plate Mill from cast 81913. The plate processing details are given in Table 87, and lower amounts of controlled rolling were used than that in plate for pipe production.

Table 87: Processing of plate for structural use

Plate ID	Slab size (mm)	Transfer bar thickness (mm)	SRT (°C)	EHT (°C)	FRT (°C)	Plate thickness (mm)	Reduction Ratio
FO922	230 x 1610	50	1225	970	896	20	2.5
GR184	230 x 1970	110	1234	920	825	50	2.2

6.4.2 Mechanical properties

Tensile, Charpy impact and drop weight tear tests were carried out on the plates and toughness transition temperatures determined. DWTT is not a requirement of Euronorms relevant to structural use, but the information was of interest to determine the effect of lower levels of controlled rolling on this test parameter.

Table 88: Mechanical properties of structural plates rolled from cast 81913

Plate ID	$R_{p0.2}$ (MPa)	R_m (MPa)	A (%)	R_p/R_m	0.5Kvmax ITT (°C)	27 J ITT (°C)	DWTT ITT (°C)
FO922	484	540	25	0.89	-90	-130	-40
GR184	410	521	21	0.79	-70	-110	-20

The strength requirements in EN 10025-4: 2004 are dependent on plate thickness; the properties in Table 88 satisfy S420ML in the 50 mm thickness, failing only on yield strength, and S460ML in the 20 mm thickness. Considering the low level of controlled rolling in both of these plates, good strength

and excellent toughness were obtained. This may allow higher production rates to be employed as holds to lower finish rolling temperatures are minimised.

6.4.3 Microstructure

The microstructures are shown for the quarter and mid-thickness of the plate in Figure 73.

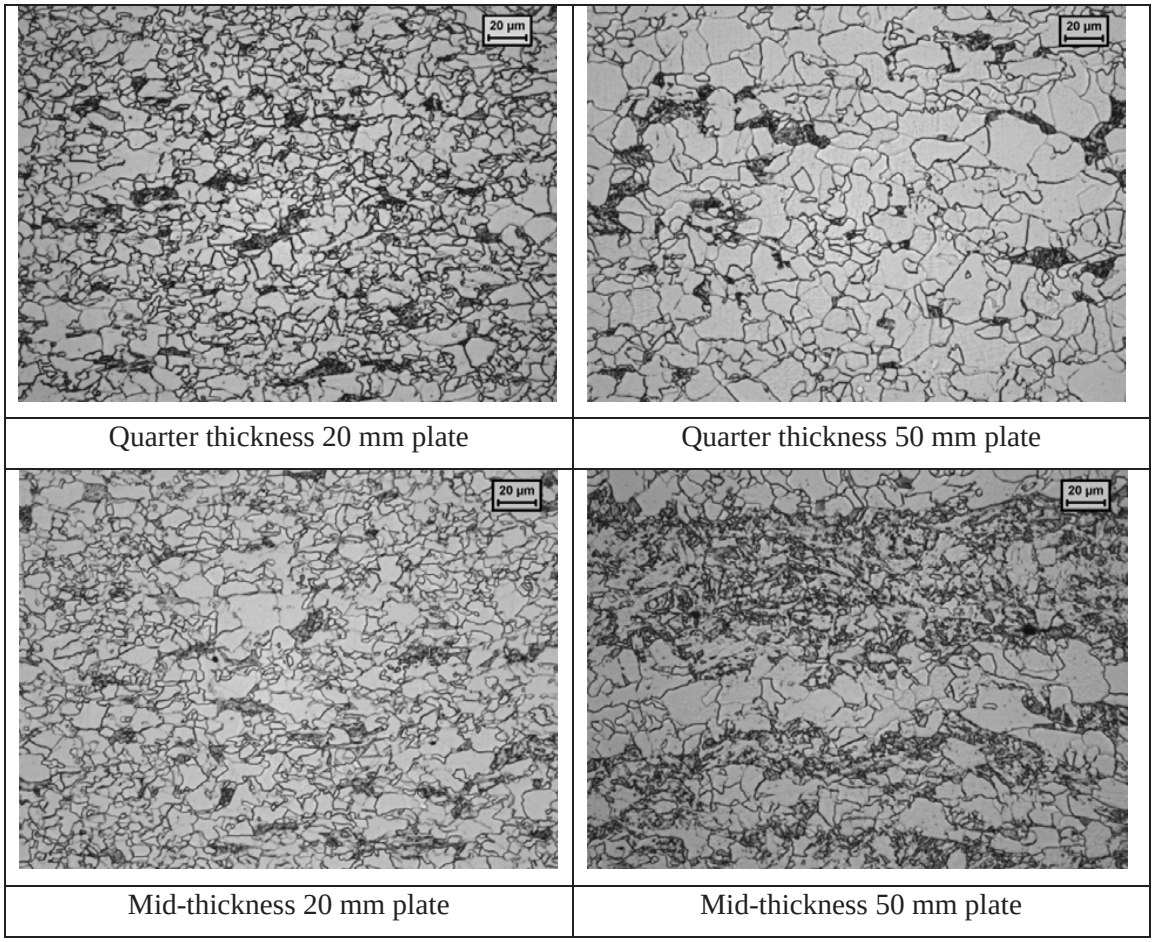

Figure 73: Microstructures of 20 mm and 50 mm structural steel plates

EBSD was used to determine the grain sizes with 4^o and 15^o boundary angles and the values for the quarter thickness location are shown in Table 89.

Table 89: Mean grain sizes in 20 mm and 50 mm structural steel plates

Plate thickness, mm	Mean 4^o Grain size		Mean 15^o Grain size		Mean 15^o/Mean 4^o
	microns	$mm^{-1/2}$	microns	$mm^{-1/2}$	
20	5.8	13.1	6.8	12.1	1.17
50	7.3	11.7	8.8	10.7	1.20

6.4.4 Weldability

6.4.4.1 Weld properties

Welding process are shown as three digit reference numbers according to EN ISO 4063: 2000 [1]. Welds were made by submerged arc, SAW (121), reduced pressure electron beam, RPEB (512), autogenous laser welding and hybrid laser/MAG processes (522) and the properties of the welds assessed by determination of Charpy impact transition curves for different notch locations. The results have been compared with conventional S355 and S450 grade welds.

6.4.4.1.1 Submerged arc welds

Submerged arc, butt welds were made in 25.4 mm and 50 mm thick plates. The 25.4 mm plate was welded in 5-passes with a heat input of 4.5 kJ/mm and the 50 mm thick plate was welded in 21-passes with a heat input of 3.5 kJ/mm. The welding procedures are shown in Appendix B3 and B4. Macrographs of the two welds are shown in Figure 74.

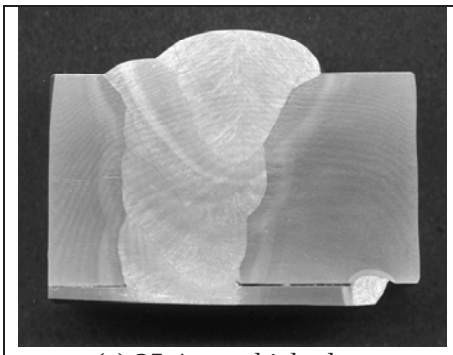

(a) 25.4 mm thick plate

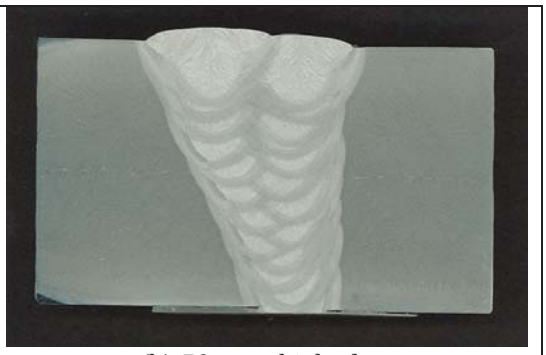

(b) 50 mm thick plate

Figure 74: Macrographs of submerged arc welds

The welding procedures for the S355EMZ and S450EMZ are shown in Appendix B5.

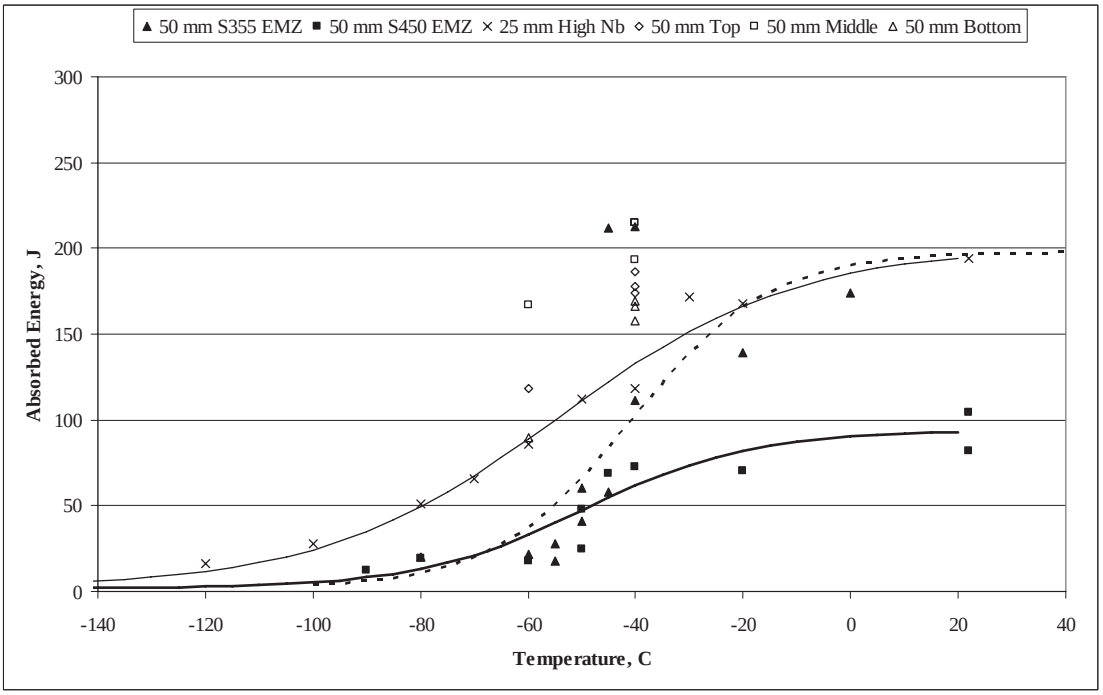

(a) Notch at weld fusion-line

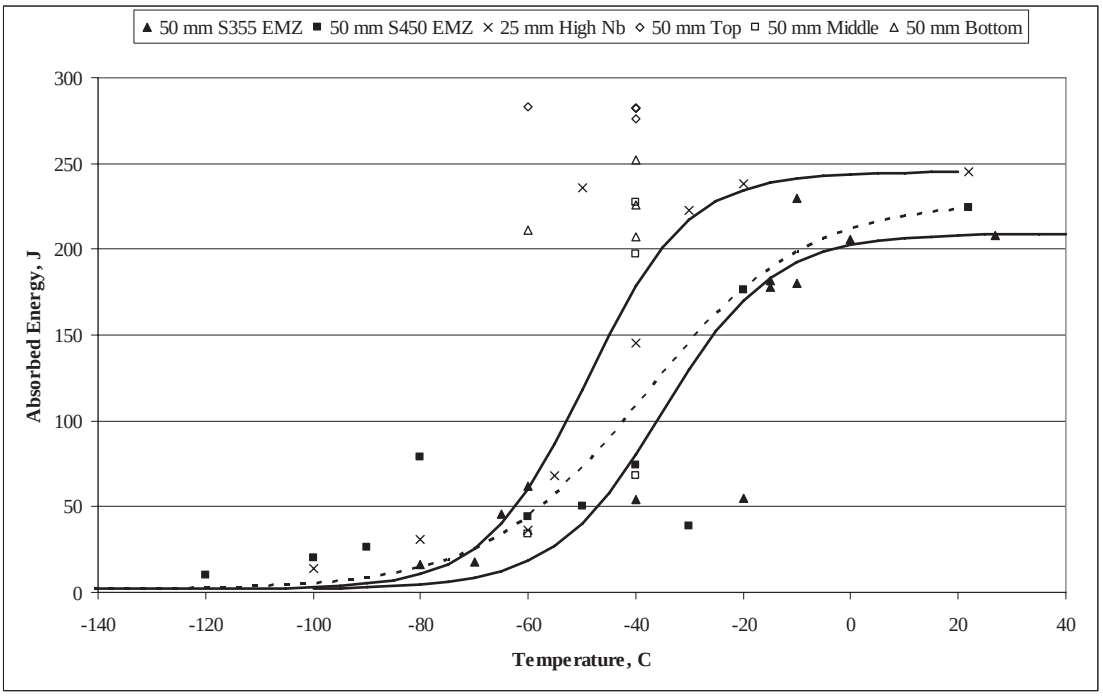

(b) Notch in heat affected zone

Figure 75: Impact transition curves for submerged arc welds

The transition curves, Figure 75, showed that the high-Nb steel had transition temperatures lower than the S355 EMZ and S450 EMZ steels.

6.4.4.1.2 Reduced pressure electron beam weld

Reduced pressure electron beam welding was performed to make a butt-weld in the 25.4 mm thickness plate using a beam of electrons from an electron gun having a power up to 100 kW at a pressure of 10^{-5}-10^{-2} mbar. The weld macrograph is shown in Figure 76 and the transition curve is shown in Figure 77.

Figure 76: RPEB weld in 25 mm thick plate

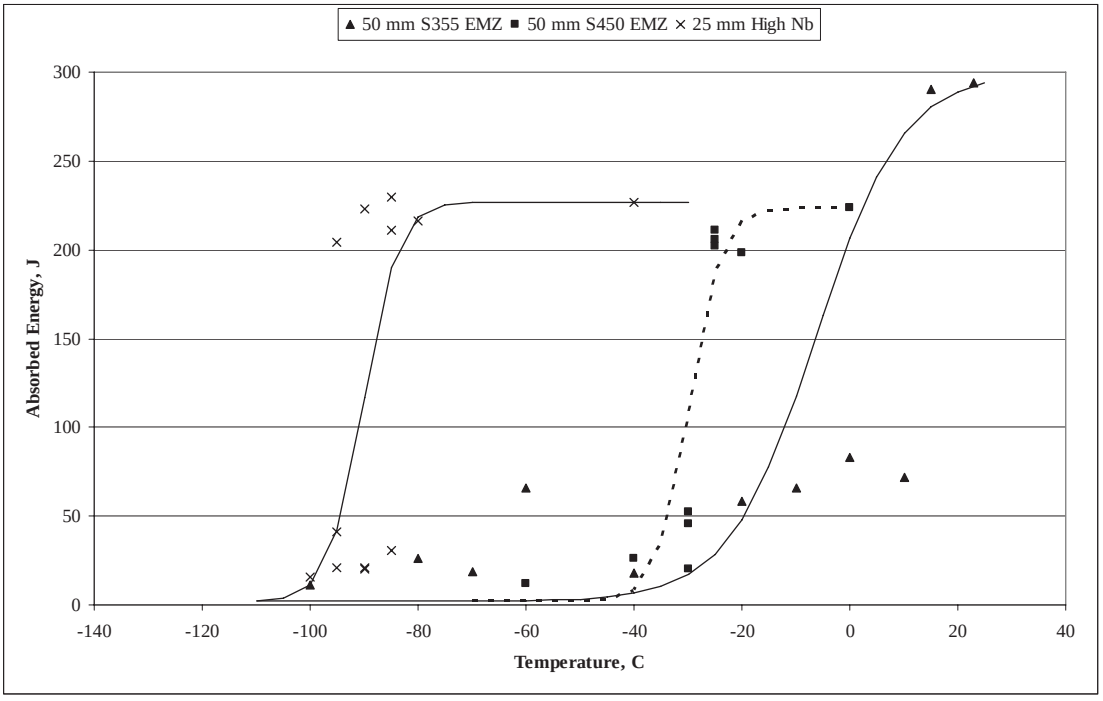

Figure 77: Impact transition curves for reduced pressure electron beam welds at fusion line + 0.5 mm

6.4.4.1.3 Laser welds

Samples were machined from the 25.4 mm plate to give 9 mm plates to produce an autogenous laser bead-on-plate weld and a hybrid laser/MAG butt-weld. The notch locations for the Charpy specimens are shown in Figure 78. The welding procedures are shown in Appendix B6.

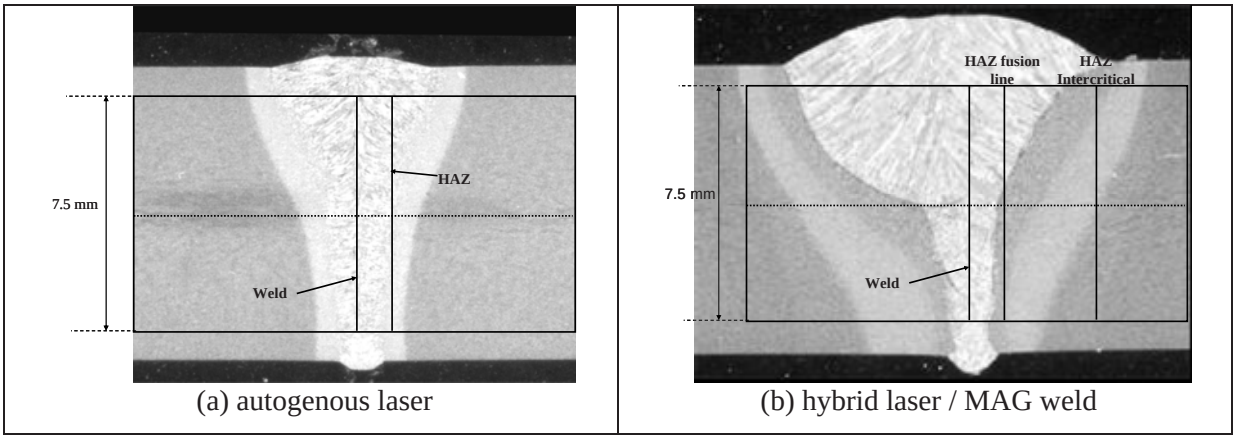

(a) autogenous laser (b) hybrid laser / MAG weld

Figure 78: Notch locations in Charpy specimens for 9 mm thick laser welds

The impact transition curves are shown in Figure 79 and Figure 80.

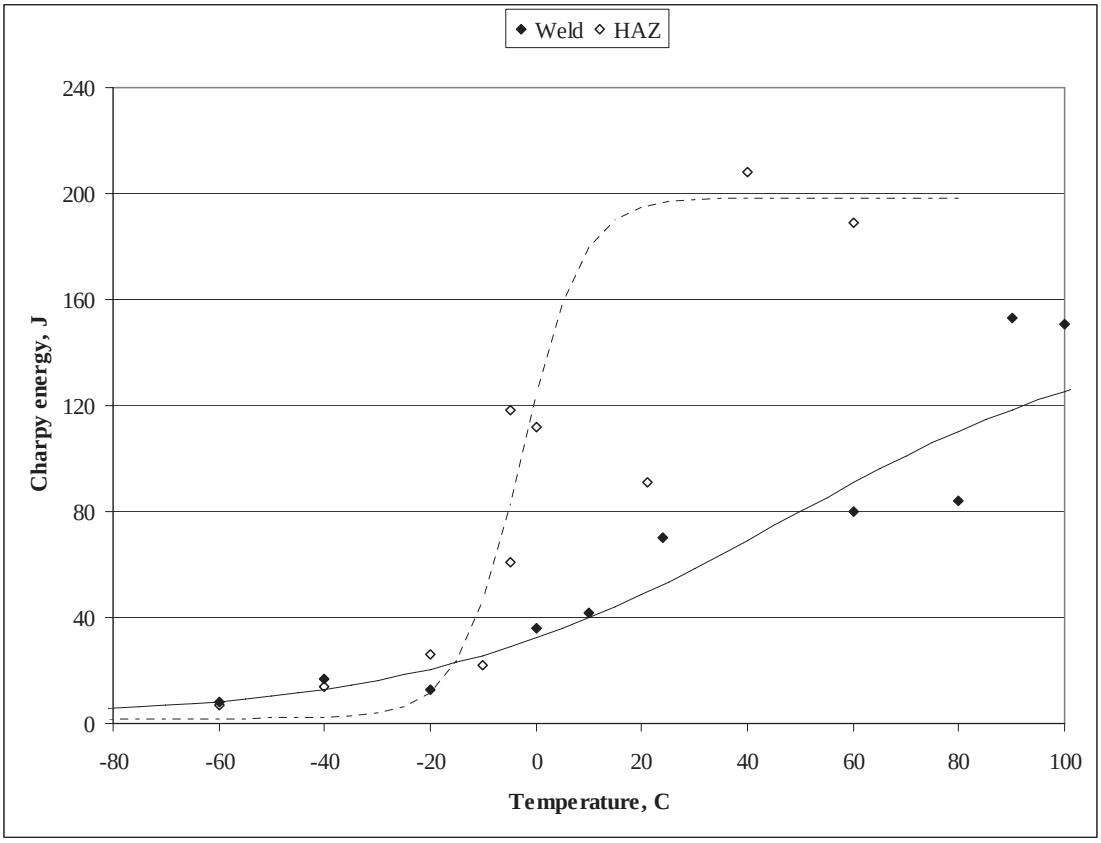

Figure 79: Impact transition curves for the weld and HAZ of 9 mm thick autogenous laser weld

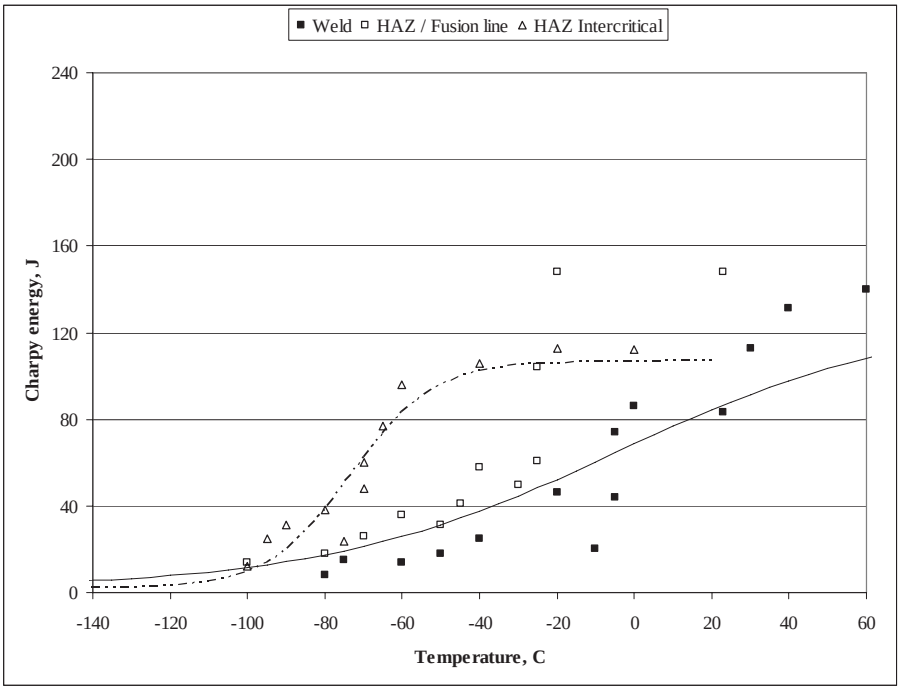

Figure 80: Impact transition curves for 9 mm thick hybrid laser/MAG weld

6.4.4.2 Weld simulation

Samples from casts 16685, 30257 and 81913, were also evaluated after weld simulation carried out by reheating to 1250°C followed by controlled cooling through the range 800 - 500°C, using times of 8 s and 30 s. Charpy impact transition curves were determined for these conditions and the hardness values at + 20°C are shown in Figure 81 and the absorbed energy values are in Figure 82.

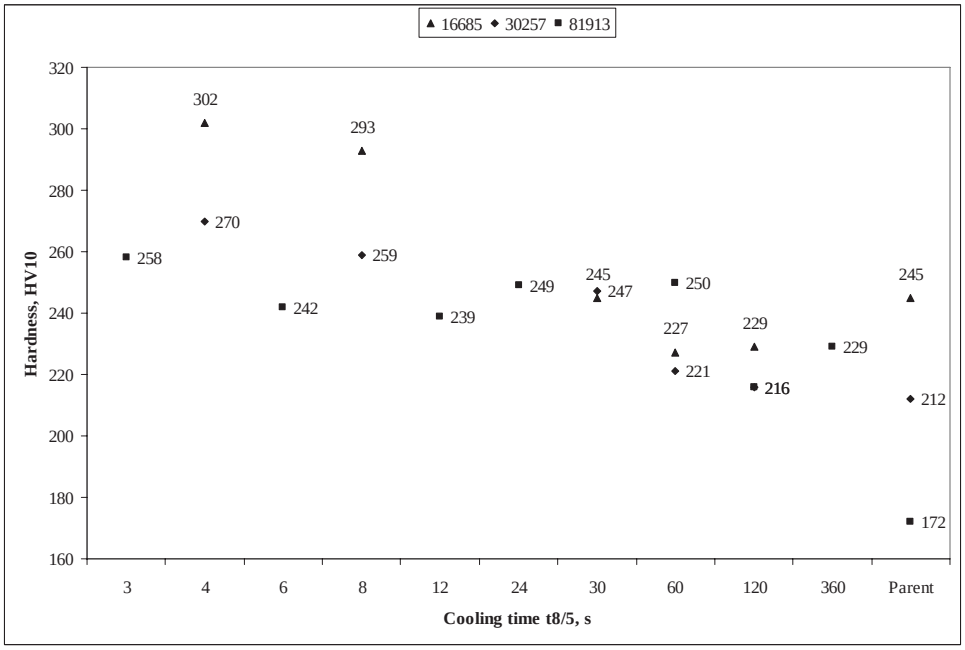

Figure 81: Hardness values at +20°C on simulated welds

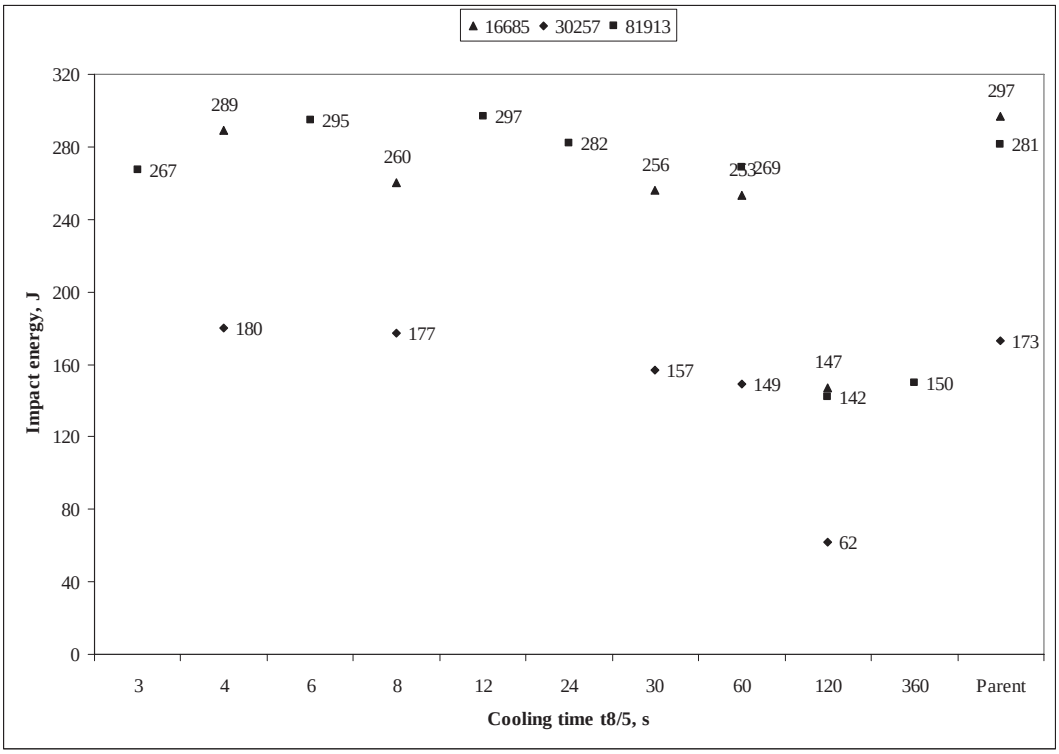

Figure 82: Charpy impact energy values at + 20°C on simulated welds

Impact transition curves for these three steels, Figure 83, show that the simulated weld at 30 s tends to have the highest transition temperature and that this is usually higher than that found in real welds, Figure 84. It can be concluded that the simulated weld with a 30 s cooling time gives a conservative estimate of the properties of real welds.

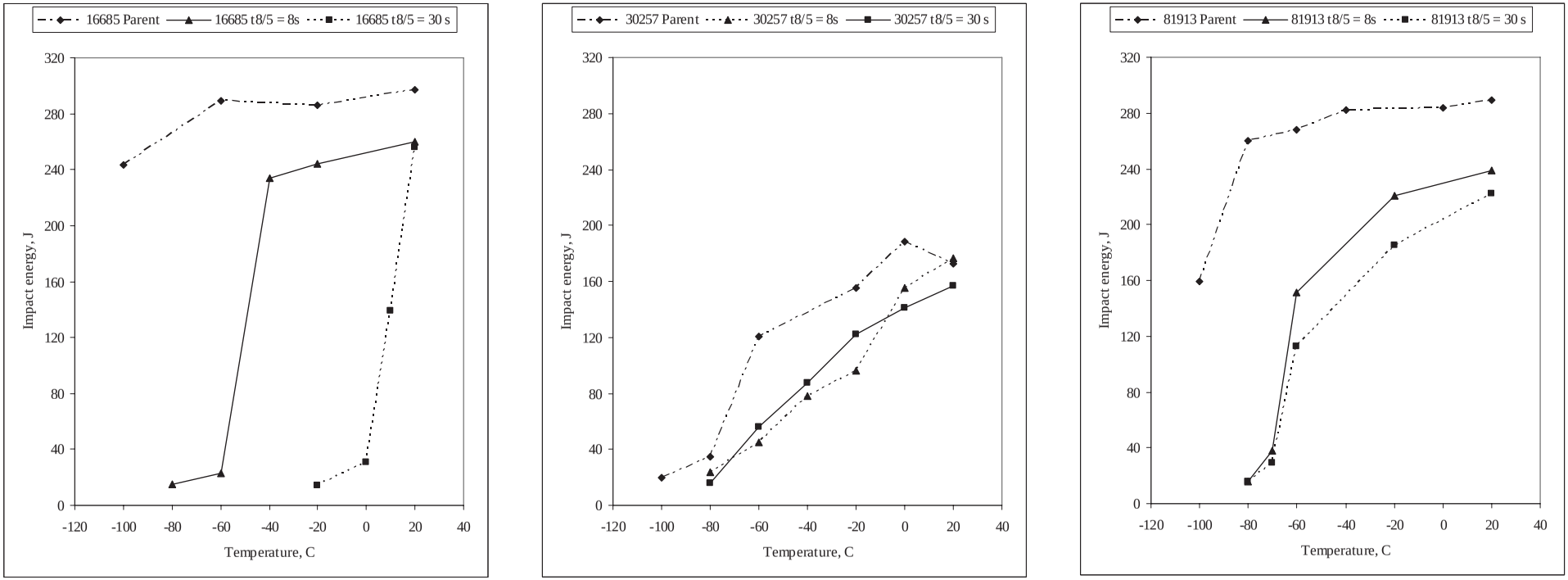

Figure 83: Comparison of Charpy impact transition curves for hot rolled product and simulated welds

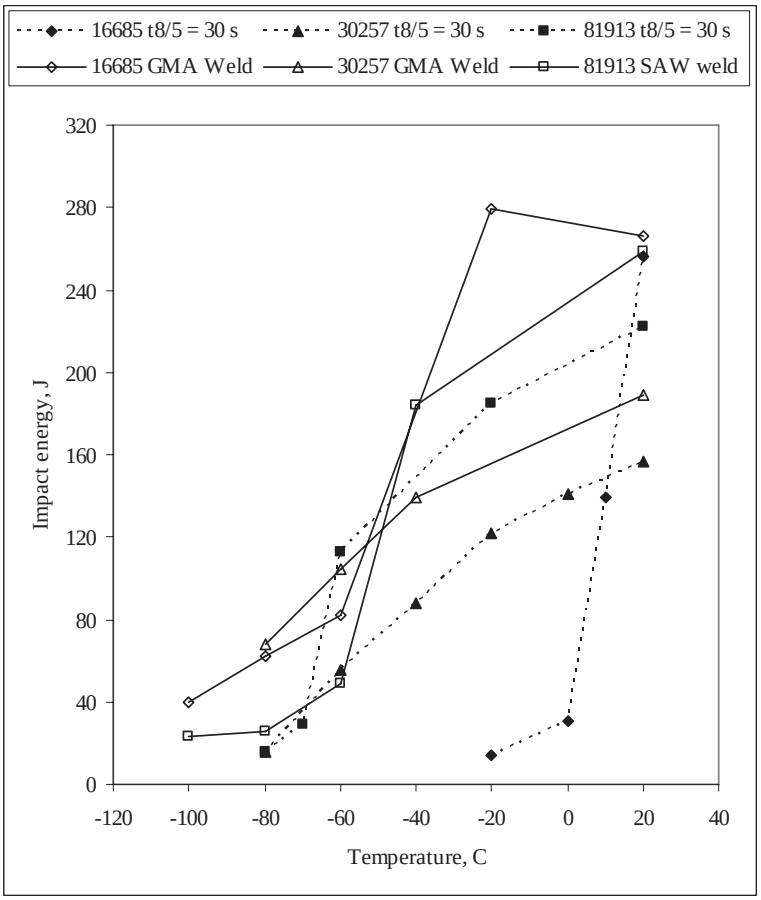

Figure 84: Comparison of impact transition curves for real and simulated welds

6.4.5 Downstream process considerations

A number of issues were identified as being of concern in the downstream processing of steel and, in order to address these, tests were carried out to demonstrate the through thickness ductility, strain ageing response, and post weld heat treatment response of steels for structural use.

6.4.5.1 Through thickness ductility

The through thickness ductility of three commercially rolled products has been measured, Table 90.

Table 90: Through-thickness reduction of area Z according to EN 10164

Tested steel	D_o (mm)	D_u (mm)	Z (%)	Z (%) mean	R_m (MPa)
Strip SO 466,coil 246063, t=14.1 mm	9.92	5.28	72	75	748
	9.89	4.90	75		734
	9.80	4.57	78		731
Plate PC 943 t=25.4 mm	9.91	4.61	78	66.8	543
	9.98	7.54	43		539
	9.95	4.58	79		538
Plate GR184 t=50 mm	10.01	6.33	60	61	510
	10.00	6.48	58		511
	10.00	5.91	65		508

6.4.5.2 Strain ageing

The strain ageing response was assessed following the approach described by Bannister [20] by determining the Charpy impact toughness transition curves for steel 81913 in the strained and the strained and aged conditions. Two samples of the 14.6 mm thick plate were strained in tension to 10% strain in the rolling direction. One of the samples was then artificially aged by holding it at 250°C for 30 minutes. Transverse Charpy specimens were extracted with the Charpy V notch oriented through the thickness and in the rolling direction (TL samples). The mean results of three tests at each temperature are shown in Figure 85.

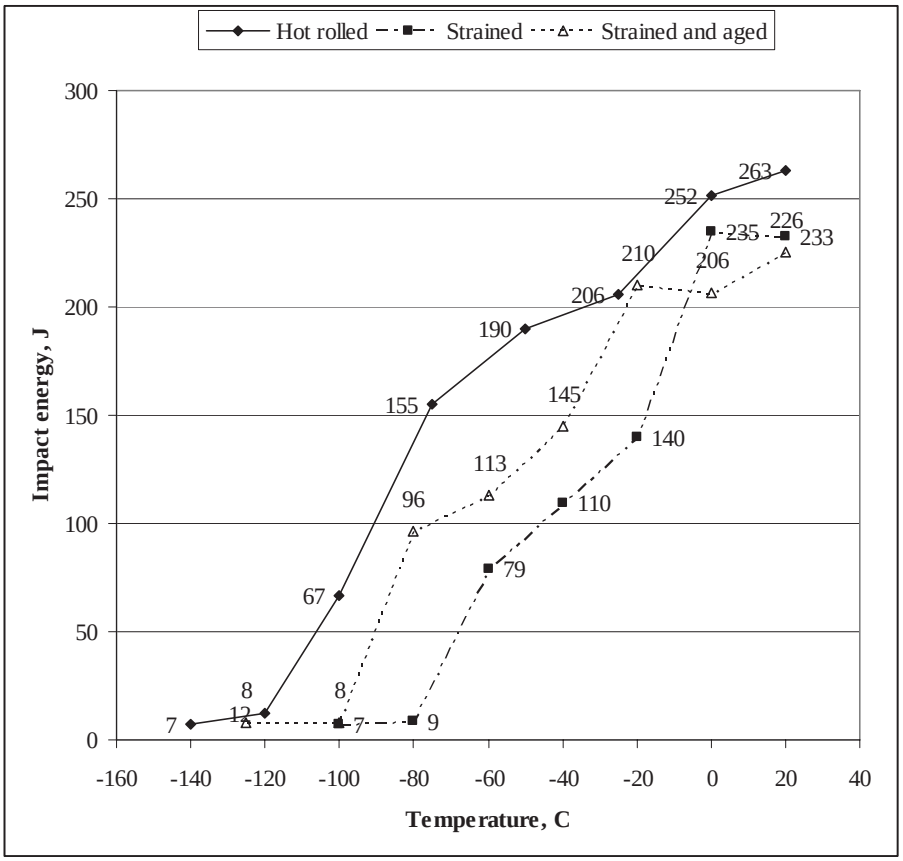

Figure 85: Charpy V transition curves for untreated, strained, and strained and aged material

The curves were fitted using the modified procedure of Oldfield [21] and the characteristic values of upper and lower shelf energy, ITT 27J, and ITT 0.5Kvmax were used to determine the effects of straining and of ageing as shown in Table 91.

Table 91: The effect of strain ageing on the transverse Charpy V transition curves of the high Nb low C commercial cast 81913 processed to 14.6 mm thick plate

	Untreated	10% strained	10% strained and aged 30min for 250°C
USE (J)	263	235	226
LSE (J)	7	7	7
ITT 27J (°C)	-126	-104	-107
ΔT ITT 27J (°C)		22	19
ITT 0.5Kvmax (°C)	-73	-52	-60
ΔT ITT 0.5Kvmax (°C)		21	13

USE = upper shelf energy, LSE = lower shelf energy, T27J = temperature at which a Charpy impact toughness value of 27J obtained, ΔT27J= shift in T27J with reference to the untreated condition, T50%

= temperature at which a Charpy impact toughness value equal to 50% USE is obtained, ΔT50% = shift in T50% with reference to the untreated condition.

6.4.5.3 Post weld heat treatment

The effect of post weld heat treatment was evaluated on two steels; one was a cast similar in composition to cast 81913, which had been supplied and welded before this project began as 12 mm thickness plate from Oregon Steel, and the other was cast 16685 in 14.1 mm thick coil-plate. The 12 mm plate was welded with a two-pass procedure. The heat treatment was at 575°C for 30 minutes.

A two pass submerged arc weld, Figure 86 (a), was made in the 12 mm Oregon plate using welding consumables typical of those used for seam welds in linepipe. The weld preparation was a double 'V' with 90° and 100° included angles for first and second weld passes respectively. The root region was welded by a laser, to give a continuous weld tack. Weld heat inputs for side 1 and 2 were 2.0 and 2.6 kJ/mm respectively as detailed in Appendix B7.

The effect of post weld heat treatment was assessed by determining the impact transition curves for the as welded and the heat treated conditions; steel 81913 curves are shown in Figure 86 and those for steel 16685 are shown in Figure 87.

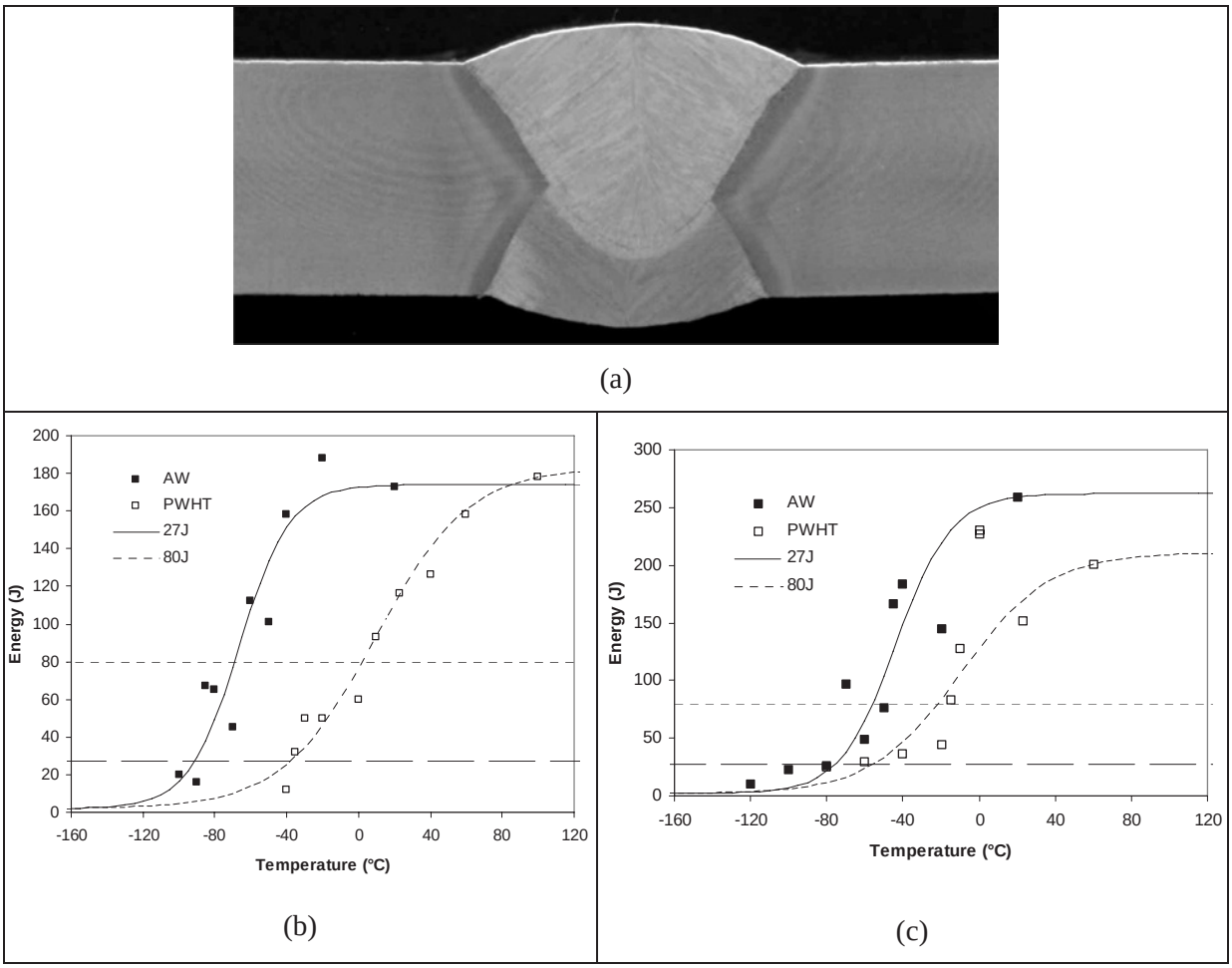

Figure 86: Charpy V impact toughness transition curves for two-pass submerged arc weld in 25.4 mm thick plate, number a) macroscopic image of weld, b) Charpy V impact transition curves for weld centre-line, c) Charpy V impact transition curves for the weld fusion line sampling 50% HAZ

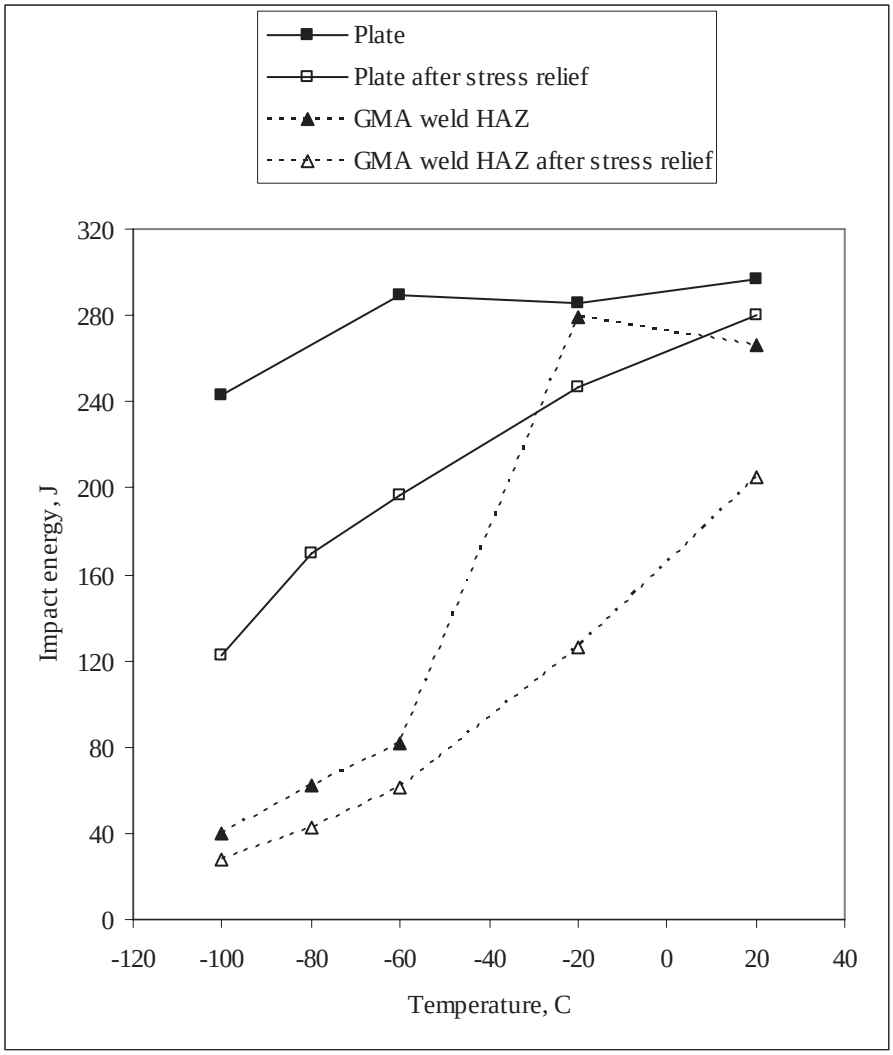

Figure 87: Effect of heat treatment on steel 16685

Both steels showed an increase in transition temperature after heat treatment with increases of 40 - 80^{o}C and these were associated with increases in hardness, of ~ 15 HV, thought to be due to precipitation of niobium during the heat treatment.

6.5 Industrial implementation

6.5.1 Commercially rolled product property predictions

The results of mechanical property tests on commercially rolled products have been compared with the properties predicted by the equations derived by linear multiple regression in the laboratory model. The product identities, processing conditions, measured and predicted properties used in the comparison are presented in Table 92 for tensile properties and in Table 93 for impact transition temperature values. The comparisons are shown for tensile properties, in Figure 88, and ITT values in Figure 89.

Table 92: Processing conditions and tensile properties for the commercially rolled products

Cast	Identity	log CR1	log CR2	RR	PS (MPa)	Predicted PS (MPa)	TS (MPa)	Predicted TS (MPa)
16685	246062	1.11	-2.65	3.4	532	626	641	701
16685	246063	1.13	-2.65	3.4	549	641	672	717
16685	246064	1.09	-2.65	3.4	546	637	657	713
16685	246065	1.07	-2.65	3.4	524	636	646	712
16685	246066	1.07	-2.65	3.4	535	636	646	712
16685	246067	1.04	-2.65	3.4	544	634	644	710
17721	41	1.26	-2.65	3.5	465	595	605	656
17721	51	1.20	-2.65	3.5	481	595	601	652
17721	21	1.18	-2.65	2.6	487	595	600	650
17721	21	1.18	-2.65	2.6	503	584	600	650
17721	69	1.11	-2.65	2.6	481	595	550	646
30257	Ruukki	1.11	-2.65	3.8	630	663	727	711
30257	783077	0.81	-2.65	3.5	569	642	663	689
30257	783078	0.79	-2.65	3.5	522	641	630	689
30257	783079	0.60	-2.65	3.5	547	630	645	675
30257	783080	0.68	-2.65	3.5	503	634	611	681
30257	937683	0.75	-2.65	3.8	613	639	708	685
30619	21	1.08	-2.65	3.0	501	587	604	655
30619	31	1.08	-2.65	3.0	484	587	576	655
30619	41	1.08	-2.65	3.0	490	587	596	655
30619	61	1.08	-2.65	3.0	488	587	593	655
30619	71	1.08	-2.65	3.0	492	587	599	655
30619	79	1.08	-2.65	3.0	495	587	603	655
51569	865787	0.76	-2.65	3.8	617	691	759	801
81351	41	1.59	-2.65	3.8	562	671	707	820
81351	61	1.51	-2.65	3.8	635	665	787	814
81351	31	1.52	-2.65	3.8	604	666	782	815
81351	51	1.38	-2.65	3.8	584	656	810	805
81913	PE111	-0.30	-1.10	3.7	439	475	533	567
81913	PB329	-0.35	-1.10	4.1	533	472	592	563
81913	PA665	-0.40	-1.10	3.1	479	468	541	560
81913	FO922	-0.35	-1.10	2.5	464	472	540	563
81913	GR184	-0.60	-1.10	2.2	410	455	521	546
81913	PA666	-0.35	-1.10	3.1	512	472	581	563
81913	7JE117	-0.30	-1.10	2.0	454	475	611	567

Table 93: Processing conditions and impact properties for the commercially rolled products

Cast	Strip	log CR1	log CR2	RR	CT, (°C)	27 J ITT, (°C)	Predicted 27 J ITT, (°C)	0.5Kvmax ITT, (°C)	Predicted 0.5Kvmax ITT, (°C)
16685	246062	0.92	-2.65	3.4	525	-115	-86	-93	-75
16685	246062	1.11	-2.65	3.4	390	-84	-59	-60	-34
16685	246062	1.22	-2.65	3.4	305	-86	-42	-74	-9
16685	246063	1.13	-2.65	3.4	390	-88	-59	-63	-34
16685	246064	0.89	-2.65	3.4	555	-80	-92	-73	-84
16685	246064	1.09	-2.65	3.4	440	-78	-69	-61	-49
16685	246064	1.15	-2.65	3.4	405	-70	-62	-59	-39
16685	246065	1.02	-2.65	3.4	470	-82	-75	-62	-58
16685	246065	1.07	-2.65	3.4	450	-83	-71	-69	-52
16685	246065	1.14	-2.65	3.4	445	-88	-70	-50	-51
16685	246066	0.93	-2.65	3.4	545	-81	-90	-64	-81
16685	246066	1.07	-2.65	3.4	460	-93	-73	-63	-55
16685	246066	1.17	-2.65	3.4	400	-81	-61	-63	-37
16685	246067	0.88	-2.65	3.4	560	-77	-93	-58	-85
16685	246067	1.04	-2.65	3.4	480	-79	-77	-59	-61
16685	246067	1.15	-2.65	3.4	400	-97	-61	-76	-37
17721	21	1.18	-2.65	2.6	510	-140	-87	-110	-69
17721	21	1.18	-2.65	2.6	510	-150	-87	-150	-69
17721	21	1.18	-2.65	2.6	540	-140	-93	-125	-78
17721	41	1.26	-2.65	3.5	482	-140	-99	-125	-75
17721	51	1.20	-2.65	3.5	553	-140	-114	-125	-96
17721	69	1.11	-2.65	2.6	580	-135	-101	-110	-90
17721	69	1.11	-2.65	2.6	570	-130	-99	-110	-87
17721	69	1.11	-2.65	2.6	480	-140	-81	-130	-60
30257	783077	0.74	-2.65	3.5	573	-39	-126	-31	-111
30257	783077	0.81	-2.65	3.5	544	-58	-120	-49	-102
30257	783077	0.82	-2.65	3.5	528	-73	-117	-54	-98
30257	783078	0.77	-2.65	3.5	604	-46	-132	-43	-120
30257	783078	0.75	-2.65	3.5	538	-60	-119	-44	-101
30257	783078	0.43	-2.65	3.5	553	-74	-122	-57	-105
30257	783079	0.60	-2.65	3.5	650	-60	-141	-44	-134
30257	783079	0.70	-2.65	3.5	588	-34	-129	-33	-116
30257	783079	0.64	-2.65	3.5	569	-50	-125	-39	-110
30257	783080	0.71	-2.65	3.5	560	-38	-123	-20	-107
30257	783080	0.70	-2.65	3.5	576	-43	-126	-24	-112
30257	783080	0.70	-2.65	3.5	568	-55	-125	-34	-110
30257	SZ	1.51	-2.65	3.8	570	-110	-131	-70	-115
30619	21	1.00	-2.65	3.0	600	-120	-123	-80	-111
30619	31	1.00	-2.65	3.0	640	-120	-131	-80	-123
30619	41	1.00	-2.65	3.0	550	-140	-113	-95	-96
30619	61	1.00	-2.65	3.0	530	-120	-109	-110	-90
30619	71	1.00	-2.65	3.0	570	-120	-117	-90	-102
30619	79	1.00	-2.65	3.0	590	-120	-121	-90	-108
81351	31	1.52	-2.65	3.8	579	-80	-101	-60	-87
81351	41	1.59	-2.65	3.8	600	-135	-105	-100	-93
81351	51	1.38	-2.65	3.8	550	-80	-95	-40	-78
81351	61	1.51	-2.65	3.8	580	-100	-101	-65	-87
81351	61	1.51	-2.65	3.8	550	-110	-95	-65	-78

81913	PA666	-0.30	-1.10	3.1	550	-90	-121	-75	-110
81913	PB329	-0.30	-1.10	4.1	550	-100	-141	-85	-126
81913	PC943	-0.30	-1.10	4.1	550	-140	-141	-140	-126
81913	PE111	-0.30	-1.10	3.7	550	-110	-133	-90	-120
81913	YBRM3	-0.30	-1.10	3.1	550	-90	-121	-75	-110
81913	YBRP2	-0.30	-1.10	4.1	550	-100	-141	-85	-126
81913	YBWA1	-0.30	-1.10	3.7	550	-110	-133	-90	-120
81913	FO922	-0.30	-1.10	2.5	550	-130	-109	-90	-101
81913	GR184	-0.50	-1.10	2.2	550	-110	-103	-70	-96

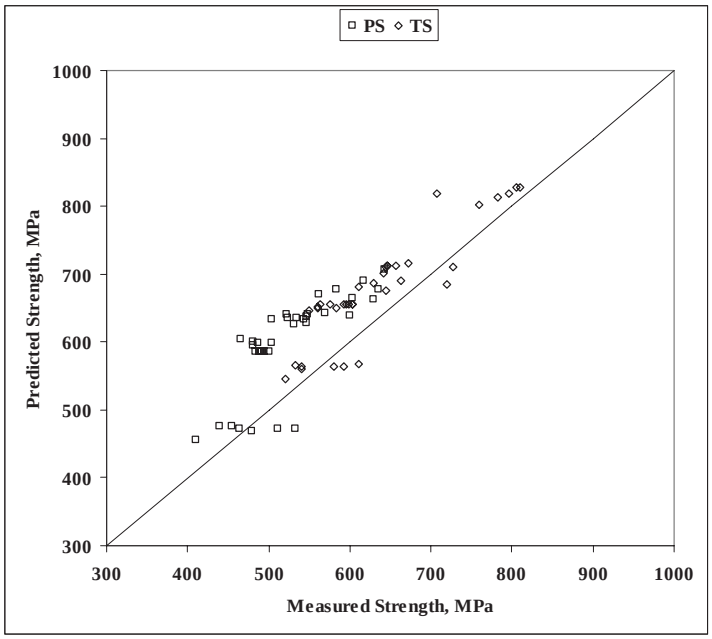

Figure 88: Comparison of predicted and measured tensile properties on commercially rolled products

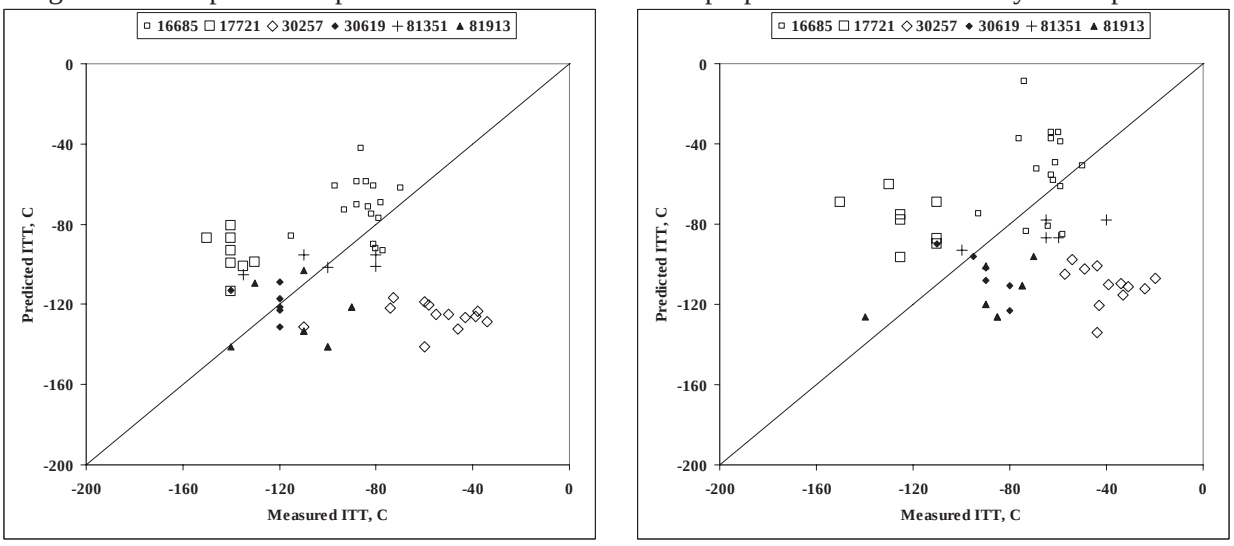

(a) 27 J ITT (b) 0.5Kvmax ITT

Figure 89: Comparison of predicted and measured ITT values on commercially rolled products

The prediction of the tensile strength was good, but predictions of the proof stress tended to be higher than the measured values. Predictions of the impact transition temperature were poor for cast 30257, with measured values being higher than the predictions, and cast 17721 where the measured values were lower than the predictions.

The regression equations have been used to predict the results presented by Piette et al [22] and Yakubtsov and Boyd [23] on low carbon niobium bearing steels processed in the laboratory, and the comparisons are shown in Figure 90 and Figure 91.

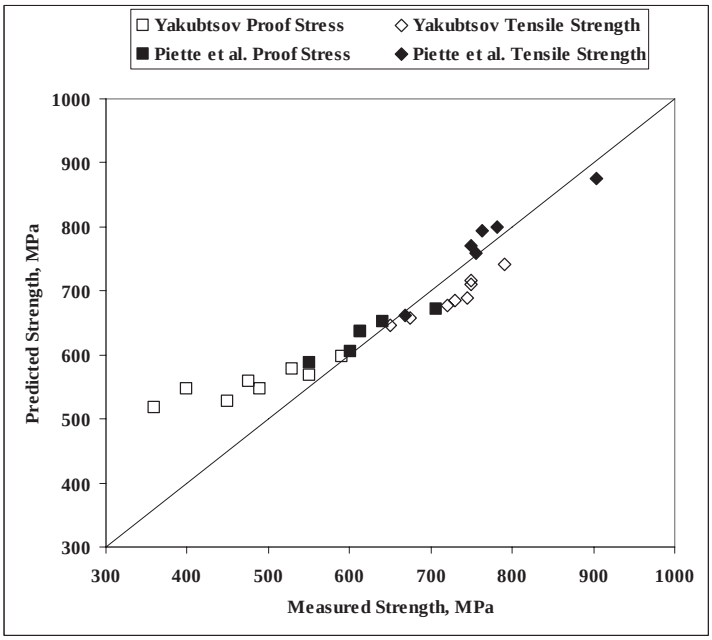

Figure 90: Comparison of predicted strengths for steels in published papers

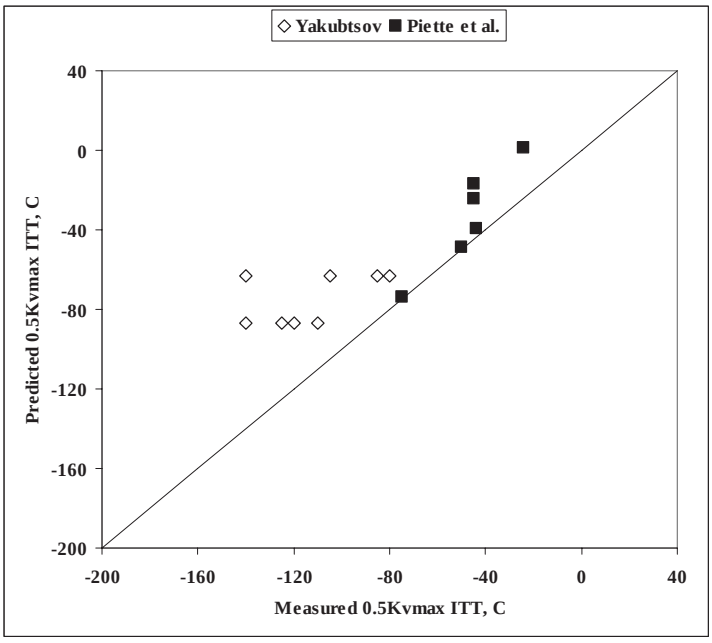

Figure 91: Comparison of predicted 0.5Kvmax ITT for steels in published papers

The details extracted from these papers are shown in Table 94, for the compositions, and Table 95, for the processing and properties.

Table 94: Steel compositions from published papers

Steel	C	Mn	Al	Ti	Nb	Ni	Mo	Cu	Cr	B
NC4	0.037	1.76	0.015 to 0.034	0.017	0.042	0	0.19	0	0.21	0.0001
NC5	0.040	1.87		0.017	0.040	0	0.50	0	0.50	0.0001
NC6	0.039	2.07		0.016	0.040	0	0.51	0	0.50	0.0001
NC8	0.073	1.63		0.014	0.039	0	0.20	0	0.50	0.0001
NC10	0.068	2.05		0.016	0.050	0	0.20	0	0.22	0.0001
NC11	0.071	2.03		0.016	0.040	0	0.50	0	0.51	0.0001
1	0.07	1.7	0.035	0.008	0	0.3	0.16	0	0	0.0001
2	0.07	1.7	0.035	0.008	0.02	0.3	0.16	0	0	0.0001
3	0.07	1.7	0.035	0.008	0.06	0.3	0.16	0	0	0.0001
4	0.07	1.7	0.035	0.008	0.10	0.3	0.16	0	0	0.0001

Table 95: Processing and properties for steels in published papers

Steel	log CR1	log CR2	RR	PS (MPa)	Predicted PS (MPa)	TS (MPa)	Predicted TS (MPa)	0.5Kvmax ITT (°C)	Predicted 0.5Kvmax ITT (°C)
NC4	1.40	-1.10	4	551	589	668	662	-75	-74
NC5	1.40	-1.10	4	613	639	750	771	-50	-49
NC6	1.40	-1.10	4	641	651	781	800	-44	-40
NC8	1.40	-1.10	4	601	602	756	760	-45	-24
NC10	1.40	-1.10	4	614	637	763	794	-45	-17
NC11	1.40	-1.10	4	707	672	903	876	-24	2
1	1.10	-1.10	4	400	548	720	677	-125	-87
2	1.10	-1.10	4	475	558	745	690	-110	-87
3	1.10	-1.10	4	530	578	750	716	-140	-87
4	1.10	-1.10	4	590	598	790	742	-120	-87
1	0.65	-1.10	2.5	360	518	650	646	-140	-63
2	0.65	-1.10	2.5	450	528	675	659	-80	-63
3	0.65	-1.10	2.5	490	548	730	685	-105	-63
4	0.65	-1.10	2.5	550	568	750	711	-85	-63

The prediction of properties appears to be good for steels processed in the laboratory, but less good on the commercially processed steels, where perhaps the values for processing conditions may be less certain.

6.5.2 Cost benefit analysis

With escalating raw material costs, steel mills are intensely pursuing lean alloying and minimized operational cost. Simultaneously, end users are demanding structural components with even better strength, toughness, formability and weldability characteristics. Consequently, new process and physical metallurgy challenges face today's steel producers. The change in economic climate has created a compelling situation that requires producers to consider a change in their grade development approach. High-alloy compositions are becoming prohibitively expensive for the end user under the current economic climate. This grade development strategy links a low-carbon, low-alloy, low-cost steel approach that balances the chemistry of the steel with the process metallurgy capabilities of the mill at a competitive price. A more economic production (avoiding major additions of alloying elements such as Mo, Ni, etc.) of HSLA steel with (partial) bainitic microstructure became possible with the introduction of accelerated cooling after thermo-mechanical rolling. Thanks to the finer grain size and the higher dislocation density of this type of bainite compared to polygonal ferrite, this microstructure leads to yield strength levels above 500 MPa, while air cooling can produce yield strengths above 420 - 460 MPa.

The past practice of passing on high raw material and operational costs to end-users is not sustainable for the long term. The current global competitive environment of the integrated and mini-mill steel

industry necessitates a thorough understanding of the economics of process and physical metallurgy changes made within the ironmaking, steelmaking and rolling processes as well as their effects on product margins, deliveries and overall customer performance. Under current economic conditions, the future grade development trend will focus upon five areas:

- Low-carbon low-alloy grades
- Fine-grained microstructures
- Application of cost - benefit analyses
- Increased capital spending on mill power and accelerating cooling upgrades
- Grade consolidation

The economic balance of the process metallurgical practices including the melting, rolling, chemistry development and thermal rolling practices with end user mechanical property demands has become an even bigger challenge for steel developers due to several factors. These factors include escalating raw material and energy prices that result in significant challenges for steel producers trying to meet or exceed end-user demands and expectations at globally competitive prices. The production of value-added microalloyed niobium-bearing steels can be realized through the synergistic development of appropriate steel chemistries along with the proper melting and alloy addition practices, slab reheating furnace practices and specific hot rolling practices to successfully obtain fine-grained, homogeneous microstructures. Cost - benefit analyses need to go beyond just the consideration of raw material costs to include production practices and overall operational and metallurgical costs. As shown below, the incorporation of low-carbon lean-alloy (LCLA) grades offers attractive cost benefits. Further benefits can be also realised by end-users, such as producers of pipe, steel structures or automotive components.

A Cost Benefit Analysis has been performed to assist the design and production of new low-carbon lean-alloy (LCLA) steels. The entire supply chain is integrally connected from raw materials to the finished component. Drivers such as the actual cost of raw materials, substitute materials, productivity/quality indices, operational and indirect costs are key components to be considered and evaluated.

The primary drivers of the total cost per ton of steel comprise the following components:

- Alloying cost
- BOF/EAF conversion cost
- Reheat furnace gas consumption
- Plate mill/hot strip mill conversion cost
- Electrical energy consumption
- Cobbles and diverts

It is evident that the actual operational cost varies significantly between different steel mills depending on their layout and capability of equipment. In order to allow a general analysis the costs of different mills were averaged to synthesize budget costs for individual processing steps such as steel making, continuous casting and hot rolling as shown in Table 96. These data are based on average costs of the year 2007 and refer to a standard CMn grade with 0.1% carbon. Also estimated are specific cost effects related to the production of LCLA steel such as carbon reduction below 0.1%, slab-conditioning costs due to crack forming during continuous casting, and cost penalties due to cobbles and diverts. On the contrary a cost saving is possible when hot charging of the slabs into the reheating furnace is possible.

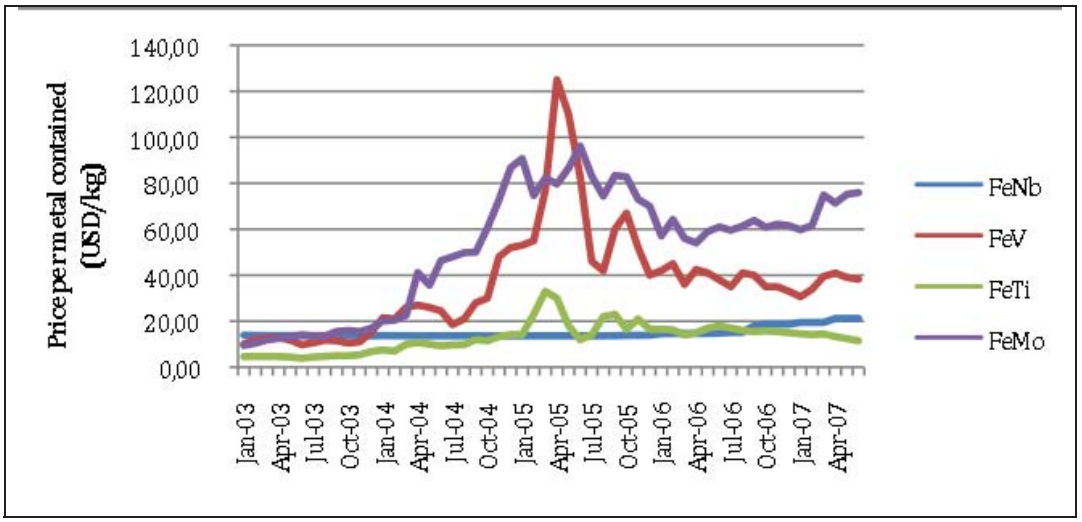

Figure 92: Evolution of relevant ferro-alloy costs

Table 1: Budget costs for relevant process steps used in the cost-benefit-analysis

Pig iron		190 €/t
Steelmaking	Standard CMn grade (0.1% C)	70 €/t
	Carbon reduction (per 0.01%)	+5 €/t
Continuous casting		15 €/t
	Slab conditioning (scarfing)	+20 €/t
HRM conversion cost	No TMCP	55 €/t
	Hot charging (cost saving)	-3 €/t
	Production time TMCP	+15-45 €/t
	Cobbles (per 1%)	+0.75 €/t
	Diverts (per 1%)	+1.70 €/t

6.5.2.1 Alloying cost analysis

The alloying cost can be very volatile, as recent years have shown. Price changes in the order of several hundred percent have been noticed for some relevant alloying elements, Figure 92. In order to make comparisons transparent, average ferro-alloy prices of the year 2007 are taken in the current analysis, Table 97. These data are used to evaluate the alloying cost changes when switching from traditional alloying concepts to the low-C high-Nb alloying concept.

Table 97: Average ferro-alloy costs over the year 2007

Ferro-alloy	MC FeMn	FeSi	FeTi	FeV	FeNb	FeMo	FeCr	Ni	Cu
Average price (€/alloy kg contained)	1.42	0.90	8.1	27.9	17.3	53.4	4.9	27.6	5.3

The particular focus of the project was high-Nb alloying (1 kg Nb per ton of steel); the specific alloying cost for that element is around 17.3 EUR per ton of steel. However, since Nb is already a standard alloying element in more conventional high strength steel alloy design, albeit in lower concentration (0.04 wt. %), it is reasonable to take 10.4 EUR per ton of steel as the actual cost increase related to high-Nb alloying.

Table 98 shows the cost of various alloy concepts for X70 and X80 hot-strip material. Compared to the traditional Nb-V alloying concept for X70, the HIPERC high Nb-Cr concept offers an alloying cost saving of around 5 EUR per ton. Within the HIPERC project an alternative alloying concept for X70

with a Nb content reduced to 0.06% was also investigated. This alloying concept would comply with current Nb limitations in the EN specification. A combination of Cr, Cu, and Ni was used to achieve the strength. Although the production of X70 hot strip is technically feasible, the additional alloying cost for this concept is around 60 EUR per ton compared to the low-C – high Nb concept.

Table 98: Alloying cost of various hot rolled strip concepts for X70 and X80 pipe skelp

Alloying concept	X70 coil	X70 coil HIPERC	X70 coil HIPERC 30619	X80 coil HIPERC 16685	X80 coil ERW	X80 coil HIPERC 81351	L555MB	X80 AF coil 2nd WEGP
(wt. %)	Salzgitter	Generic	14.0 mm Ruukki	14.1 mm Salzgitter	9.0 mm Bluescope	11.0 mm Ruukki	Ruukki	18.5 mm Chinese mills
C	0.10	0.05	0.04	0.05	0.08	0.04	0.06	0.04
Mn	1.70	1.80	1.81	1.75	1.60	1.96	1.75	1.85
Si	0.30	0.30	0.30	0.30	0.30	0.20	0.37	0.25
Cr		0.20	0.21	0.27		1.01		0.20
Cu			0.21			0.21		0.20
Ni			0.20			0.22		0.15
Mo				0.07	0.20		0.30	0.25
Nb	0.04	0.10	0.06	0.10	0.05	0.10	0.06	0.08
V	0.10						0.07	
Ti		0.02	0.01	0.02	0.02	0.01	0.02	0.02
Ferro-alloy cost	62.35€	56.98€	116.17€	96.02€	142.09€	169.36€	217.25€	239.24€

While X70 is a standard grade for many pipeline projects the use of X80 became significant only in the recent years. A major project was Cheyenne Plains in the USA, which is 617 km long and involved low-C high-Nb steel with either Cr or Mo as additional alloying element. Both alloying concepts were rolled on Steckel mills. More recently, the first mega project for X80 has been started in China. The 2nd West-to-East gas pipeline consists of roughly 5400 km X80 grade of which the larger part is made from coiled plate (spiral pipe). The specified requirements (AF microstructure, high toughness, strain based design) for that pipeline as well as the high gage (18.5 mm) necessitated a quite rich alloying concept leading to a high alloying cost. A more conventional CMnNbMo concept has been developed for thin gage ERW welded tube. The low-C high-Nb alloys qualified for X80 within the HIPERC project appear to be rather cost competitive. The cheapest alloying concept uses a moderate Cr and Mo addition. The Mo-free alloy design works with a relatively high Cr addition and further applies Ni and Cu alloying. The latter concept will be competitive against alloys containing at least 0.2% Mo.

6.5.2.2 Process cost analysis

6.5.2.2.1 Steelmaking

High-Nb steel concepts require the carbon content to be reduced to 0.05% or less. This translates into increased processing cost in the steelmaking shop compared to peritectic steel such as a 0.10%C Nb-V grade traditionally used for X70. This cost is budgeted to 5 EUR per ton and per 0.01% carbon reduction. However, many high-strength steel grades used today for either line pipe or structural applications do have reduced carbon contents to a level of around 0.08% anyway. This is due to the better toughness, lower transition temperature and improved weldability at reduced carbon content. Thus the steelmaking process cost surplus of replacing a traditional Nb microalloyed steel grade by a low carbon – high niobium grade can be estimated to be less than 25 EUR per tonne.

6.5.2.2.2 Continuous casting

For the behaviour of a steel grade during continuous casting the carbon content is of fundamental importance. As indicated in Figure 93 slab cracking is likely to occur when the carbon content is in the

peritectic range, i.e., from 0.10% to 0.16% C. Most harmful in medium carbon steels is the interdendritic enrichment during the peritectic reaction. During this reaction, additional shrinkage occurs due to the formation of face centred cubic austenite from the body centred cubic delta ferrite and liquid rest melt that is enriched in alloying elements is trapped in the interdendritic pools. This structural inhomogeneity, as well as the coarse grain size of the austenite formed at the high peritectic temperature, enhances the susceptibility of slabs to surface cracking. It has been reported, [24], that surface cracking is avoided when lowering the carbon content to about 0.05% or less. Lower carbon contents reduce the dendritic segregation due to a smaller solidification interval and a larger δ-ferrite interval. Homogenisation is enhanced because the diffusion coefficient of solute elements in δ-ferrite is 100 times that in austenite at the same temperature.

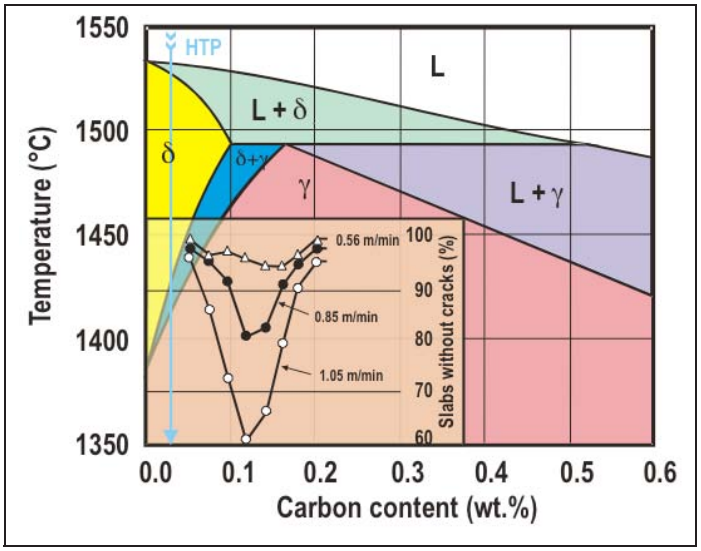

Figure 93: Peritectic range of the iron-carbon diagram and influence on the slab surface condition in continuous casting [24]

Typical casting speeds are in the range of 1.0 to 1.6 m/min. This means that near peritectic steels (0.08-0.10%C) have a substantial risk of cracking. Hence the slabs must be repaired by flame scarfing. Reducing the casting speed to low values where cracking is reduced, see Figure 93, is not a practical option due to loss of productivity and technical constraints of the casting machine. Production experience with a near peritectic Nb-V pipeline grade revealed an average slab repair cost of in the order of 20 EUR/tonne. Trial production experience within the HIPERC project as well as industrial production elsewhere have demonstrated that slab repair will be obsolete with the low-C – high-Nb alloying concept.

Crack-free slabs after continuous casting also offer the possibility of hot charging into the reheating furnace of the hot rolling mill. In this way, the energy necessary for soaking can be significantly reduced. The enthalpy for heating steel from room temperature (20°C) to soaking temperature (1250°C) is estimated to 815 MJ/t. By heating the steel from a charging temperature of 700°C the necessary enthalpy is reduced to 430 MJ/t. With an assumed combustion efficiency of 65%, the energy saving by hot charging is calculated to be around 600 MJ/t. With an average natural gas price (2007, Henry Hub) of 5.27 EUR/MMBTU the cost saving achieved by hot charging at about 700°C can be estimated to around 3 EUR/t.

6.5.2.2.3 Hot rolling

One of the important characteristics of the low-C high-Nb steel alloy design is its high recrystallisation stop temperature, which is 50-100°C higher than that of conventional TMCP alloy designs. Accordingly, since non-recrystallising rolling can be done at higher temperature and hence at lower flow stress of the material, the designation “high temperature processing” (HTP) alloy was given. The

original idea of allowing weaker powered rolling mills to produce TMCP steel may be less relevant today. However, TMCP rolling at increased temperature offers the possibility of a more compact rolling schedule and thus higher productivity of a hot strip mill. Figure 94 demonstrates the impact of the HTP concept on the hot rolling schedule. Both, the running-in (RIT) and the finish-rolling (FRT) temperature are significantly higher compared to a conventional alloying concept with lower recrystallisation stop temperature (T_{NR}). It is also obvious that the processing window of the HTP alloy is much larger. Typically finish rolling is 20-70°C above A_{r3} for the HTP alloy whereas it is only 5-15°C for a conventional alloy.

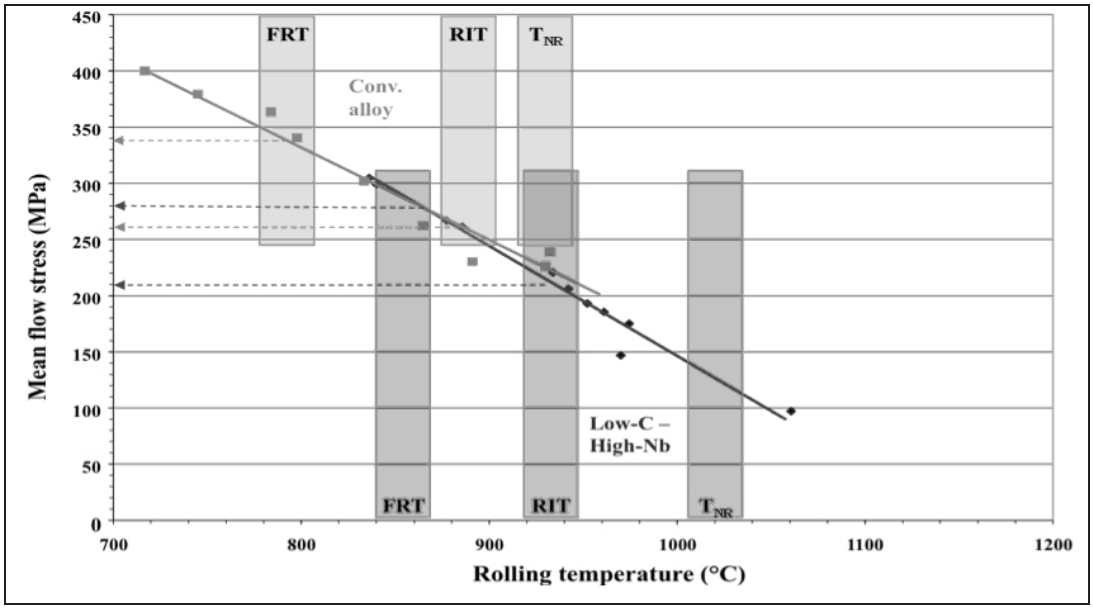

Figure 94: Comparison of conventional and high-Nb alloy TMCP schedule and mean flow stress

Some other advantages of the high-Nb alloy concept have also been seen during trial and industrial production of hot strip [25]:

- In comparison to the conventional alloy concepts, the high-Nb concept allows sizing in the sizing press up to a width reduction of 300 mm due to its high delivery temperatures after discharging from the furnace.
- Using the high-Nb concept can decrease the number of passes. Due to the high re-crystallization-stop temperature roughing can be done in a compact way, resulting in high delivery temperatures to the finishing train. Transfer bar oscillation can be omitted.
- Due to the higher delivery temperature of the transfer bar, the crop shear is facing lower resistance and the drives and bearings of the finishing stands are exposed to lower rolling forces reducing wear for the equipment involved.

Figure 95 summarises the actual production cost data of three different scenarios whereby the total production cost of a conventional (NbV) X70 is set as 100%. The high-Nb X80 concept can be produced at only 95% of the reference cost, i.e., it is cheaper than the lower grade with the conventional alloying concept. The more expensive alloying concept of the X80 is compensated by the absence of slab finishing (scarfing) cost and reduced production cost during hot rolling. If the high-Nb alloying concept is reduced to give only X70 as maximum strength, the total production cost would further shrink to around 87% of the reference.

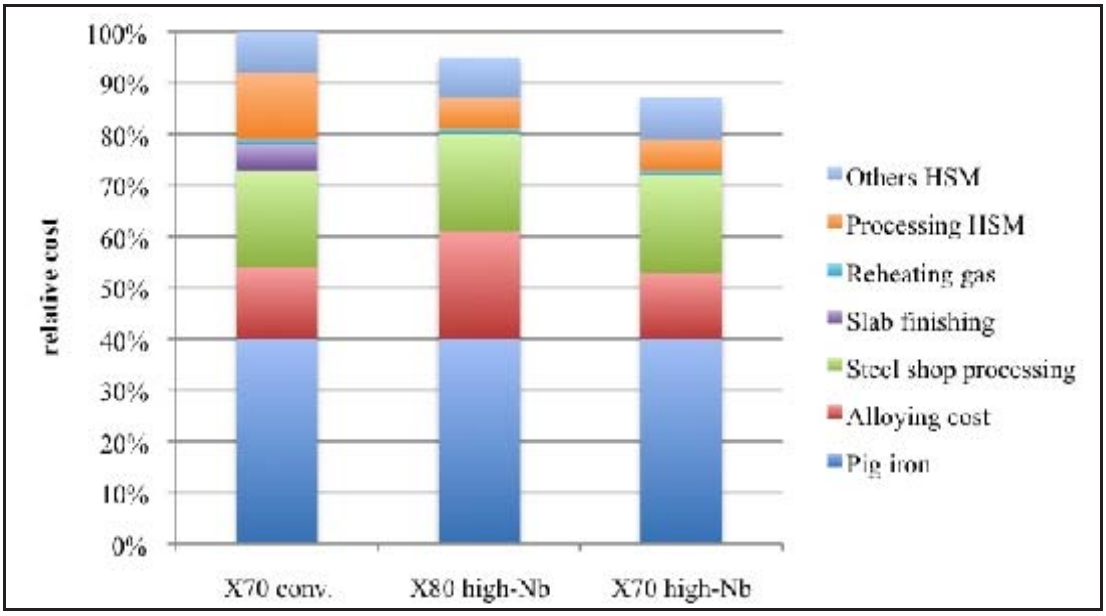

Figure 95: Cost analysis of different X70 and X80 hot strip concepts for pipe

Similar analysis can be done also for a plate mill process as shown in Figure 96. Here, different alloying concepts for S500 plate steel using different cooling strategies according to Table 99 are compared.

Table 99: Examples of alloying concepts for S500 plate material under different cooling conditions

	C	Mn	Cu	Ni	Cr	Mo	Nb	Ti	Cooling
Traditional alloy	0.09	1.80	0.30	0.25	0.25	0.15	0.05	0.010	Air
LCLA Cu-Nb	0.04	1.50	0.50	-	-	-	0.10	0.015	Accelerated
LCLA Nb	0.04	1.50	-	-	-	-	0.10	0.015	Heavy accelerated

The production cost of the three steel concepts shown in Table 99 is being compared by using control data of the individual production steps for one specific steel mill [26]. The reference is the LCLA Nb grade. The conventional alloy grade produced via air-cooling is 57% higher in cost as compared to the LCLA composition using accelerated cooling. As before in the strip mill examples, alloying, steelmaking and hot mill conversion costs are the major cost drivers. It is evident from Figure 96 that the alloying cost makes the biggest difference between the three concepts and that a powerful cooling device clearly allows for the cheaper alloying concept.

In all investigated cases it became obvious that potential costs or savings related to electrical power consumption, cobbles and diverts will have a negligible influence on the decision making process for the high-Nb alloy concept.

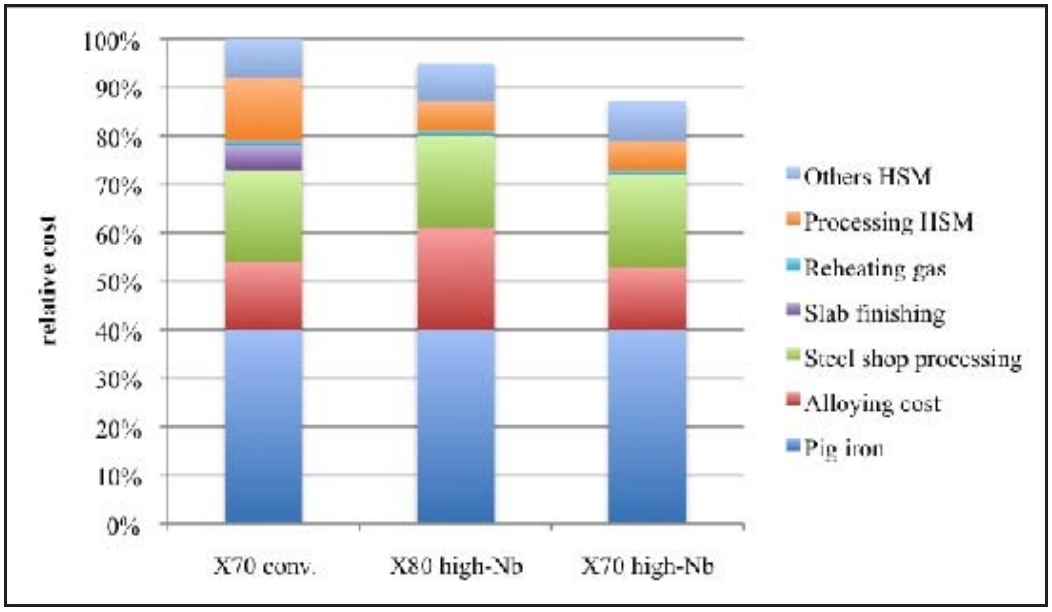

Figure 96: Cost analysis of different concepts for S500 grade plate material (AC air cooled, ACC accelerated cooled, HACC heavy accelerated cooling)

6.5.2.3 Other benefits of the high-Nb alloying concepts

6.5.2.3.1 Stability of mechanical properties

Besides pipe skelp and plate, as well as structural plate, the high-Nb alloying concept is also being used to produce thinner gauged hot-rolled band, for instance in automotive applications. In this case a high-Nb Cr alloy very similar to the HIPERC X70 pipe skelp, shown in Table 98, is applied. Depending on the run-out table conditions of cooling speed and coiling temperature, a ferritic or bainitic microstructure can be produced. Due to the high amount of Nb in solid solution at the moment of coiling it is possible to obtain substantial precipitation hardening by very fine NbC particles. This effect can provide a yield strength increase of up to 250 MPa. Since higher coiling temperatures promote precipitation hardening and lower ones rather promote dislocation hardening (bainite formation), the high-Nb alloying concept provides remarkably low scattering of mechanical properties even if the temperature profile over the strip is not stable on the run-out table. This is demonstrated in Figure 97 for 5 mm gauge hot strip of grade S550 MC [27]. Although there was a considerable temperature drift during coiling from 480°C at the coil head to 590°C at the coil tail, the yield strength varies only little and the tensile strength is practically unaffected. Compared to the conventional alloying concept (0.09%C, 0.70%Mn, 0.10%Si, 0.13%Ti), the high-Nb alloy is much more stable under mass production conditions as shown by the distributions of yield strength measured over several hundred production coils in Figure 98. This not only helps to reduce diverts significantly but also improves the down-stream processing.

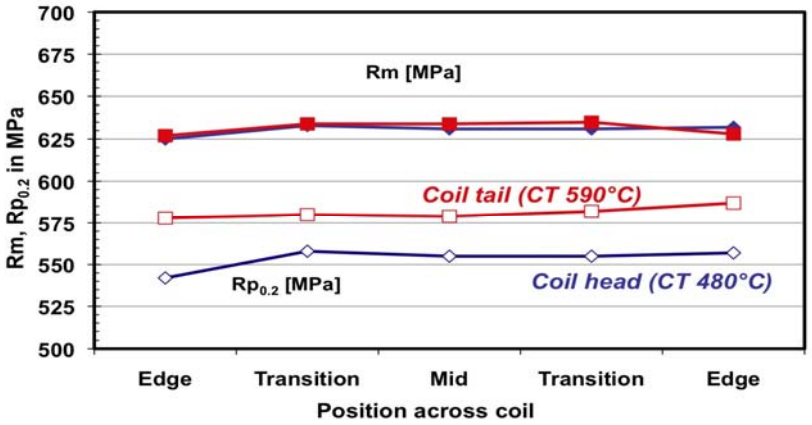

Figure 97: Variation of strength along and across a hot rolled high-Nb and high-Ti strip steel of 5 mm gauge [27]

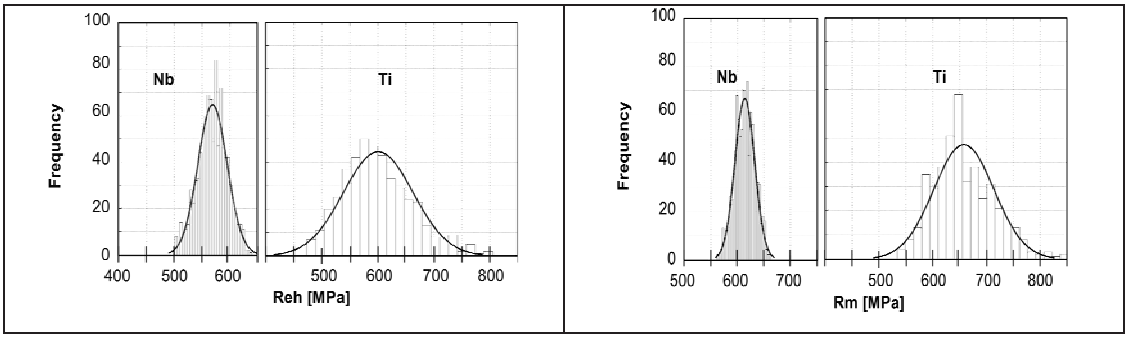

Figure 98: Statistical evaluation of strength in hot rolled high-Nb and high-Ti steel coils of 5 mm gauge [27]

6.5.2.3.2 Welding

One of the most important fabrication technologies for steel is welding. Depending on the final application very different welding techniques are being applied such as SAW used in pipe production, GMAW for mechanized field welding or laser welding often used in the vehicle industry. The various processes operate with quite different heat inputs and cooling rates. Especially low heat input and fast cooling rate tend to induce hard microstructures (martensite) with poor ductility and toughness. To avoid cold cracking the maximum permissible hardness should not exceed 350 HV and under increased hydrogen conditions this limit may be lowered to 300 HV. The ideal high strength steel would thus be as insensitive as possible towards varying heat input and cooling rate and would not produce phases harder than 350 HV. This potential is given by the alloy designs developed in this project. The low carbon content principally limits the hardness of martensite. Furthermore under low heat input welding conditions, the content of martensite is reduced as shown in Figure 99.

The welding CCT diagram for a low-C high-Nb pipe steel is shown in Figure 100 (a) [28]. The diagram comprises a very wide bainite field covering practically the entire range of technically relevant cooling speeds. This reflects excellent weld toughness, which is clearly superior to more traditional alloy concepts with higher carbon content Figure 100 (b).

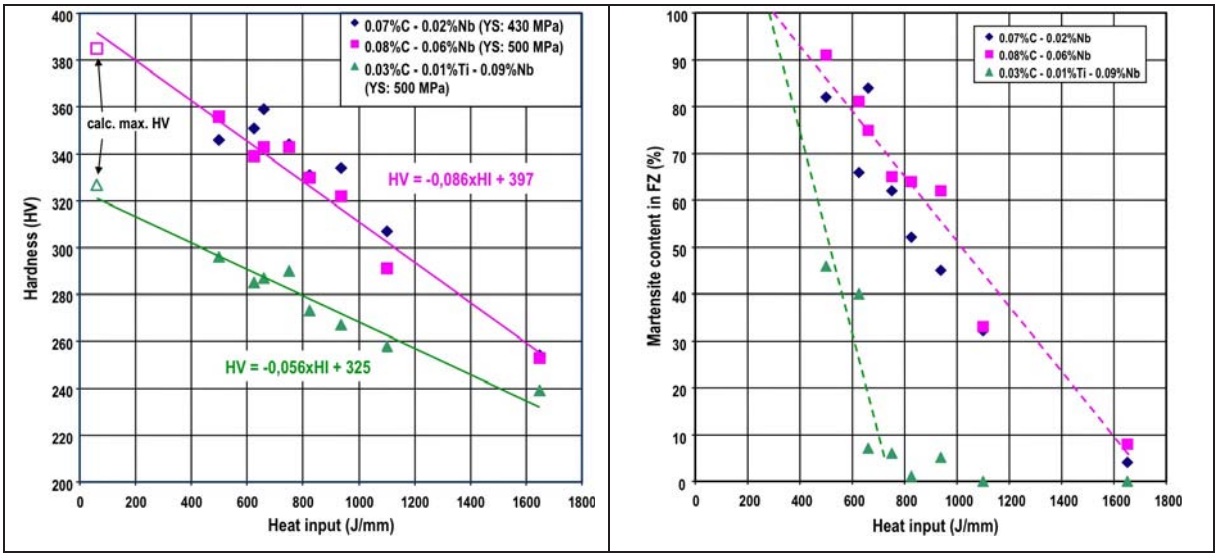

Figure 99: Influence of weld heat input (simulation: 1300°C peak temperature and heating rate 200°C/s) on weld metal hardness and martensite content

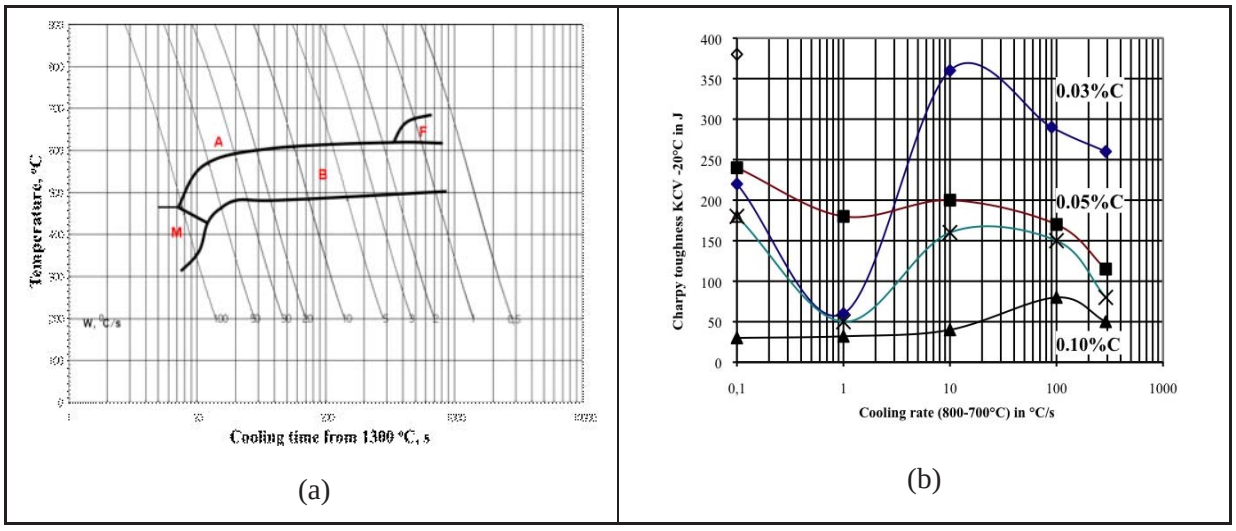

(a) (b)

Figure 100: Welding simulation (1300°C peak temperature and heating rate of 200°C/s); (a) CCT diagram of 0.05%C-1.8%Mn-0.10%Si-0.20%Ni0.25%Cr-0.25%Mo-0.09%Nb-0.01%Ti steel; (b) Charpy V-notch toughness at -20°C for different cooling rates and carbon contents.

The favourable welding behaviour of low-C high-Nb steel has the potential to optimise welding procedures and reduce welding cost. For instance, preheating could be omitted and welding speed could be increased. The use of that potential, however, will much depend on the actual practices of the weld contractor, available equipment, training and discipline of welders and boundary conditions specific to the project.

The following welding procedure [29] has been applied to field welding of the Cheyenne Plains X80 pipeline using low-C high-Nb steel (0.04%C, 1.6%Mn, 0.15%Si, 0.15%Ni, 0.10%Nb, 0.01%Ti):

- Root bead: E6010 (3.2 mm – 4.0 mm dia.)
- Hot Pass: E9010-P1 (4.0 mm – 4.8 mm dia.)
- Fill and Cap Passes: E9018M and/or E101T1-GM (1.1 mm dia., 75/25% Argon/CO2)
- Preheat: 65 °C; Repair Preheat: 120 °C
- Interpass Temperature: 230 °C maximum

The 11.8 mm mainline required two low hydrogen fill passes plus a cap pass. While the 16.9 mm crossing pipe required three to four low hydrogen passes plus a split (2 pass) cap. The resulting SMAW/FCAW weld properties were as follows:

- Cross-weld Tensile Tests (UTS): 683-759 MPa
- Weld Metal Centreline CVN@ -5 °C: 45-114 J
- HAZ CVN@-5 °C: 58-214J
- VHN10kg: 162 – 278 Parent Metal-HAZ-WM Traverses

To ensure that a quality weld root would be achieved for the manual welding process, a key requirement was that cellulosic welding materials could be used only for the root and hot pass welds, with higher than usual preheat requirements employed to reduce the probability of hydrogen assisted cold cracking (HACC). A low hydrogen welding process, consumables and procedure would be required for the remainder of the weld. Such a requirement was made to mitigate the potential for HACC during production and tie-in welding while still maintaining the strength and toughness properties of the weld zone.

Travel speeds for the low hydrogen welding processes were typically between 50 and 150 mm/min. FCAW provided the higher welding speeds with an additional advantage that the operating factor was two to four times that of SMAW, resulting in a considerable improvement in production speeds. The deposition rate, deposition efficiency and operating factor were considerably higher than for cellulosic welding techniques.

6.5.2.4 Summary

The cost benefit analysis of producing high strength steel using a low-C high-Nb alloying concept has revealed the following:

- Overall alloying costs can be reduced by using high niobium low carbon rather than somewhat higher carbon and lower niobium contents to produce pipe and structural steel grades with minimum specified yield strengths in the range of 485 to 555 MPa (S500, X70 & X80 grades).
- The surface quality of slabs is particularly good so that slab conditioning by flame scarfing becomes obsolete. The resultant cost saving is approximately 20 €/t.
- Due to the good slab surface quality hot charging to the reheating furnace is possible. The cost saving effect is, however, limited and estimated to be less than 3 €/t.
- Hot rolling under TMCP conditions in the strip mill can be done faster and with a wider processing window than for a conventional TMCP alloying concept. Due to generally higher finish rolling temperatures the novel steels are softer thus mechanical loads on the equipment involved are lower and maintenance will be consequently reduced. The resultant potential cost saving is in the order of 30 €/t.
- The alloying concept can be applied to pipe, plate, and both heavy and thin gauge hot strip, and over a wide range of yield strengths. It thus principally offers a good potential for grade consolidation reducing metallurgical and logistical complexity in the mill.
- Weldability of the steel is excellent due to the low carbon equivalent and stability of the HAZ microstructure over a wide range of cooling speeds. This allows optimising weld practices to become more economical.

6.5.3 Justification for changes to Euronorms

6.5.3.1 Euronorms concerned and related standards

An important objective of the HIPERC project has been to justify changes to the Euronorms related to high-strength steels for linepipe and structural applications. As shown earlier, the yield strength levels of the steels studied here range from 420 to above 700 MPa. Therefore, for structural steels, the Euronorm of interest is EN 10025-4 [30] (Thermomechanically rolled structural steels). This standard

covers steel grades with minimum specified yield strengths of 275, 355, 420 and 460 MPa and specified minimum impact toughness down to -20°C (designated M) or -50°C (designated ML). Steels are designated as SxxxM or SxxxML, where xxx is the yield strength concerned.

Though not specifically studied here, the steels covered by EN 10028-5 [31] (Thermomechanically rolled pressure vessel steels) are closely related to the structural steels in EN 10025-4 and are similarly affected by the results of this project.

As explained in EN 1993-1-12 [32], EN 1993 (Eurocode 3, Design of steel structures) also recognises the use of high yield strength, thermomechanically rolled steel for cold forming as covered by EN 10149-2 [33], which are also widely used in steel structures. Being intended for cold forming, the steels are 1.5 - 20 mm thick for yield strengths up to and including 460 MPa and 1.5 - 16 mm for the yield strength range 500 - 700 MPa.

High-strength steel for pipelines transporting combustible fluids is covered in EN 10208-2. Considering the processing conditions studied in HIPERC and the strength levels achieved, the thermomechanically processed grades designated L415MB, L450MB, L485MB and L555MB are concerned here.

To some extent, the above Euronorms have equivalents on other continents or within the ISO system. Tables 100 - 102 show some relevant details from some of the various standards. It can be seen that in the Euronorms for thermomechanically rolled structural steels, Table 100, and steels for pipelines, Table 102, niobium microalloying is limited to a maximum of about 0.05%. However, the maximum carbon levels allowed are about 0.16%. For structural steels, a similar situation is found in ASTM A572, though there even higher levels of carbon are allowed.

Table 100: Some details from standards related to hot-rolled high-strength structural steels

Standard	Product area	Designation	YS	C	Mn	Nb	V	Ti	(Nb+V+Ti)
			MPa	max	max	max	max	max	max
EN 10025-4	Hot rolled products of structural steels: Thermomechanically rolled	S355M/ML	355	0.14	1.6	0.05	0.10	0.05	-
		S420M/ML	420	0.16	1.7	0.05	0.12	0.05	-
		S460M/ML	460	0.16	1.7	0.05	0.12	0.05	-
EN 10149-2 (ISO 6930-1)	Thermomechanically rolled steels for cold forming	S315MC	315	0.12	1.3	0.09	0.2	0.15	0.22
		S355MC	355	0.12	1.5	0.09	0.2	0.15	0.22
		S420MC	420	0.12	1.6	0.09	0.2	0.15	0.22
		S460MC	460	0.12	1.6	0.09	0.2	0.15	0.22
		S500MC	500	0.12	1.7	0.09	0.2	0.15	0.22
		S550MC	550	0.12	1.8	0.09	0.2	0.15	0.22
		S600MC	600	0.12	1.9	0.09	0.2	0.22	0.22
		S650MC	650	0.12	2.0	0.09	0.2	0.22	0.22
		S700MC	700	0.12	2.1	0.09	0.2	0.22	0.22
ISO 4951-3	High yield strength steel bars and sections thermomechanically-rolled steels	E355M/ML	355	0.16	1.6	0.05	0.10	0.05	-
		E420M/ML	420	0.18	1.7	0.05	0.12	0.05	-
		E460M/ML	460	0.18	1.7	0.05	0.12	0.05	-
ASTM A572	High strength low alloy niobium vanadium structural steel	Grade 50	345	0.23	1.35	0.05	0.15	0.04	-
		Grade 55	380	0.25	1.35	0.05	0.15	0.04	-
		Grade 60	415	0.26	1.35	0.05	0.15	0.04	-
		Grade 66	450	0.23	1.65	0.05	0.15	0.04	-

Table 101: Some details from standards related to hot-rolled high-strength steels for pressure purposes

		Grade	YS	C	Mn	Nb	V	Ti	(Nb+V+Ti)
			MPa	max	max	max	max	max	max
EN 10028-5	steels for pressure purposes thermomechanically rolled	P355M/ML1/ML2	355	0.14	1.6	0.05	0.10	0.05	0.15
		P420M/ML1/ML2	420	0.16	1.7	0.05	0.10	0.05	0.15
		P460M/ML1/ML2	460	0.16	1.7	0.05	0.10	0.05	0.15

Table 102: Some details from standards related to steels for pipelines [a]

		Grade	YS	C	Mn	Nb	V	Ti	(Nb+V+Ti)
			MPa	max	max	max	max	max	max
EN 10208-2	Steel pipes for	L415MB	415	0.16	1.60	0.05	0.08	0.06	0.15
NEN, DIN	pipe lines for			*0.12*	*1.80*	*0.05*	*0.08*	*0.06*	*0.15*
2008	combustible fluids	L450MB	450	0.16	1.60	0.05	0.10	0.06	0.15
	class B			*0.12*	*1.80*	*0.05*	*0.10*	*0.06*	*0.15*
	welded pipes	L485MB	485	0.16	1.70	0.06	0.10	0.06	0.15
	t <= 25 mm			*0.12*	*1.90*	*0.06*	*0.10*	*0.06*	*0.15*
		L555MB	555	0.16	1.80	0.06	0.10	0.06	0.15
				0.12	*2.00*	*0.06*	*0.10*	*0.06*	*0.15*
API 5L /	Specification	L415M or X60	415	0.12	1.60	-	-	-	0.15
				0.09	1.75				
ISO 3183	for line pipe	L450M or X65	450	0.12	1.60	-	-	-	0.15
				0.09	1.75				
Oct. 2008	Product specification	L485M or X70	485	0.12	1.70	-	-	-	0.15
				0.06	2.00				
	level 2	L555M or X80	555	0.12	1.85	-	-	-	0.15
				0.06	2.00				
	Welded pipe	L625M or X90	625	0.10	2.10	-	-	-	0.15
				0.08	2.20				
	t <= 25 mm	L690M or X100	690	0.10	2.10	-	-	-	0.15
				0.08	2.20				
		L830M or X120	830	0.10	2.10	-	-	-	0.15
				0.08	2.20				

[a] *Numbers in italics show that increased levels of Mn are allowed when C max is reduced*

In the following sections, arguments are given in support of changing the Euronorms EN 10025-4, EN 10028-5 and EN 10208-2 with respect to the upper limit of niobium allowed in thermomechanically rolled steels. Sections 8.5.3.2 to 8.5.3.9 are mainly addressed at the structural steel standard EN 10025-4 while section 8.5.3.10 deals with EN 10208-2.

6.5.3.2 Issues related to niobium microalloying

The reasons for the current limitations on niobium microalloying in the above Euronorms are unknown. Therefore, when proposing any increase in the maximum level of niobium allowed in thermomechanically rolled structural and pipeline steel, it is necessary to address the possible objections that might be raised on the basis of current knowledge about niobium microalloying. Areas of concern might be the properties and behaviour of the plate (1) as delivered, (2) after arc welding, or (3) after cold bending.

Considering the steel as delivered, standards require basic strength, ductility and impact toughness properties that the steelmaker must achieve irrespective of the chemical composition of the steel. Therefore, the basic mechanical properties of the steel in its delivery condition should not be a cause for concern. Through-thickness ductility, which is not covered by 10025-4, is considered in section 6.5.3.3.

Another technological property that should be considered is the influence of niobium on tendency to strain ageing as this changes the ductility and toughness of the steel from that of the delivery condition. The influence of niobium on the technological properties of the steel in the workshop or pipe mill is also important. Strain ageing is an issue when cold forming is used. In addition, the influence of niobium on hydrogen cracking susceptibility needs to be considered as does the influence of niobium on weld metal and heat affected zone toughness both as-welded and after post-weld heat treating.

Of course, one of the most important issues to consider is the benefit to be gained by allowing higher levels of niobium. These have been demonstrated in the other work packages of this project and they are treated in the cost benefit analysis of work-package 5.

6.5.3.3 Through-thickness ductility

In work-package 3, coarse particles containing niobium were occasionally found on the centre-lines of continuously cast slabs. These were assumed to be the result of the eutectic reaction L => Fe + NbC in interdendritic centre-line segregation. Such eutectic particles have been identified elsewhere in cast material containing niobium. Heikkinen and Packard [34] showed that for 0.06 - 0.24% C a small amount of Fe + NbC eutectic is formed for all niobium contents in the range 0.02 - 0.17%, with the amount of eutectic increasing with increasing amounts of niobium and carbon. It was also showed that eutectic NbC remains un-dissolved during typical simulated slab reheating of 3 h at 1240 ^{o}C and become elongated stringers during the rolling process.

Un-dissolved eutectic NbC particles can conceivably reduce the through-thickness ductility of thick structural plate. Matsui, Sato and Tanaka [35] showed that for 0.11 to 0.26% C and 0.02 to 0.07% Nb, the sum (% C + 2.5x%Nb) must exceed a critical level for eutectic NbC to appear. The critical level was found to be dependent on the cooling rate through the liquidus - solidus range, but independent of other alloying elements such as Si, Mn, Cr, Ni, V, and Mo.

EN 10025-4 currently accepts 0.05 Nb in combination with 0.16 C giving %C + 2.5x%Nb = 0.285. The same tendency for eutectic NbC to appear would be given by 0.10 Nb together with 0.035 C. However, interdendritic segregation is smaller when C < 0.10 % compared to C > 0.1%, due to the absence of the peritectic reaction and fast back diffusion in ferrite. Therefore, the factor 2.5 in the Matsui “carbon equivalent” is likely to decrease for very low carbon levels, allowing even higher additions of Nb before eutectic NbC appears in appreciable amounts.

In the case of structural plates subjected to through-thickness loading, through-thickness ductility properties as specified in EN 1993-1-10 [36] and EN 10164 [37] should be specified, in which case steelmakers will be required to choose combinations of carbon and niobium that can meet the required Z quality class (Z15, Z25, Z35). Consequently, it is unnecessary to limit niobium in the material standard on the basis of the possible presence of un-dissolved eutectic NbC. Table showed that very good through-thickness ductility was obtained in the case of the steels studied here.

6.5.3.4 Strain ageing

Strain ageing is caused by the diffusion of free carbon and nitrogen to dislocations introduced during cold deformation, such as in straightening or bending operations. If the steel contains free nitrogen, ageing can occur at room temperature due to the diffusion of nitrogen to dislocations. If the steel temperature is raised to about 200^{o}C or more, for example as a result of welding, strain ageing occurs rapidly due to the diffusion of very small quantities of free carbon even in the absence of free nitrogen. Often, nitrogen-induced strain ageing is controlled by the presence of nitride formers such as titanium or aluminium. However, the presence of some free carbon (10-20 ppm) cannot be avoided except in special circumstances in the case of interstitial free deep drawing sheet steels. Strain ageing results in an increase in strength, a reduction in elongation to fracture and an increase in ductile-brittle transition temperature, which appears as a reduction in impact and fracture toughness. These property changes are also brought about by straining alone: the effects increase with increasing cold deformation. They are usually further increased by subsequent ageing. Such is the situation for all structural and, for that matter, pipe line steels.

As a result of the unavoidability of strain ageing, EN 1993 restricts the extent of welding close to cold-formed areas. Table 4.2 in EN 1993-1-8 [38] shows that for nominal degrees of cold forming up to 5% (r/t >= 10) there is no restriction on welding in cold-formed areas provided the steel is fully killed. Welding close to cold-formed areas is acceptable provided the material is not thicker than a critical limit (t < 6 - 24 mm) dependent on the degree of cold forming (r/t = 1 - 3). Details are given in Table. Cold bending together with welding is widely used, for example in structures containing the low-carbon cold-formable steels specified in EN 10149, see Table. These low-carbon steels (max 0.12%C) can contain up to 0.09% Nb and are successfully used in welded cold-formed structures.

Table 103: Limitations on welding near cold-formed regions according to EN1993-1-8.

r/t	Cold deformation strain %	Maximum thickness allowed without restrictions, mm		
		In general		Fully killed
		Static load	Fatigue load	Al>=0.02%
>=25	<=2	no limit	no limit	no limit
>=10	<=5	no limit	16	no limit
>=3.0	<=14	24	12	24
>=2.0	<=20	12	10	12
>=1.5	<=25	8	8	10
>=1.0	<=33	4	4	6
No welding in the shaded region below if thickness limitations are exceeded				

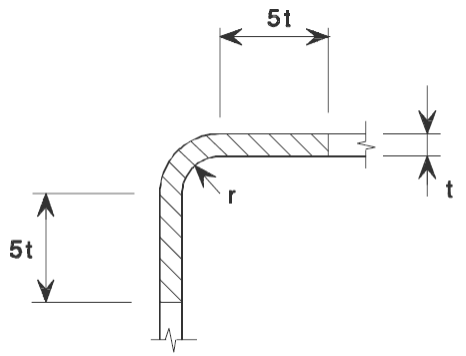

The transition temperature shifts brought about by strain ageing are taken into account in EN 1993-1-10 [38], which require the degree of cold forming to be considered when selecting the impact toughness of the base plate. The transition temperature is assumed to increase by 3 degrees Celsius for each percentage unit of nominal bending strain, given by 100/(1+2r/t). The shift is independent of steel chemistry and processing route.

The use of higher levels of niobium than 0.06% in low-carbon thermomechanically rolled steels is not expected to have a detrimental effect on strain ageing behaviour. The steels under consideration for higher niobium alloying have even lower maximum carbon contents than specified in EN 10149, where 0.09%Nb is already allowed. Also, it has been shown in work packages 1, 2, 3, and 4 that the low-carbon high-niobium concept results in very good combinations of yield strength and impact transition temperature. The toughness reserve provides additional safety against straining and ageing.

The above conclusion is supported by the results presented in Figure 85, where it was seen that the effects of strain ageing in cast 81913 were small: the transition temperature shifts caused by the combined effects of straining and ageing were less than the 3°C/strain percent considered as typical for the effect of straining alone in EN 1993-1-10. Indeed, Table 91 showed that for this steel, all of the transition temperature shift was caused by straining alone, with no additional shift due to ageing.

In conclusion, the strain ageing behaviour of high-niobium low-carbon steels is not a reason for limiting the niobium content of low-carbon high-strength structural steels or steels for pipelines.

6.5.3.5 Hydrogen cracking

EN 1011-2 Welding. Recommendations for welding of metallic materials. Part 2: Arc welding of ferritic steels [39] contains an informative annex with procedures for estimating preheat requirements based on steel chemistry. Two methods are given. One is based on the IIW carbon equivalent CEV and the other on another equivalent, CET. Neither equivalent takes account of niobium as such, but both methods are restricted to a maximum of 0.06%Nb. In addition, manganese is limited to 1.7% max for CE and 1.9% max for CET. Consequently this standard will not be appropriate for evaluating preheat requirements of the current high-niobium low-carbon steels.

EN 10025-4 specifies maximum values for carbon equivalents according to the IIW formula:

$$CEV = C+Mn/6+(Cu+Ni)/15+(Cr+Mo+V)/5.$$

The formula is based on work originally done by Dearden and O'Neill [40] using C and C-Mn steels with carbon contents in the range 0.10 - 0.31%. It provides a means of limiting alloy additions to keep heat affected zone (HAZ) hardness below 350 HV for a given heat input in the controlled thermal severity (CTS) test. Consequently, CEV is a measure of HAZ hardenabilty.

Susceptibility to hydrogen cracking depends on the susceptibility of the HAZ microstructure to cracking under the contraction stresses that develop during welding, which is not the same as HAZ hardness. Even ignoring this fact, CEV does not include the effect of niobium, nor is it likely to work well for very low carbon contents. Indeed, Yurioka et al [41] have shown that the carbon equivalent Pcm is better for C <=0.16% while CEV is valid for C >=0.20%. Their study covered 0.034% =< C <= 0.254%. They proposed a new carbon equivalent, CEN, that was close to Pcm for low carbon and closer to CEV for high carbon:

$$CEN = C + A \{ Si/24 + Mn/6 + Cu/15 + Ni/20 + (Cr + Mo + V + Nb)/5 + 5B\}$$

$$\text{Where } A = 0.75 + 0.25 \tanh\{20(C-0.12)\}$$

Factor A changes from 0.98 to 0.53 as the carbon contact decreases from 0.20 to 0.05 wt. %

CEN and CEV are almost the same for C > 0.16%, provided the niobium content is zero, Figure 101.

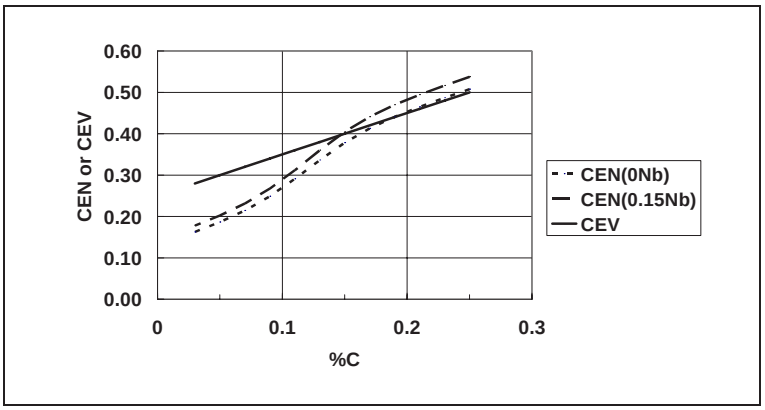

Figure 101: The influence of carbon content on CEV and CEN

However, the term A weakens the effect of alloying elements as the carbon content decreases. The formula also includes the effect of niobium. Due to the term A, the effect of niobium depends on the carbon content. The relative effects of C and Nb on hydrogen cracking are as follows:

$C = 0.20\%$ $\quad CEN = C + Nb/5 + \ldots$

$C = 0.10\%$ $\quad CEN = C + Nb/7.5 + \ldots$

$C = 0.05\%$ $\quad CEN = C + Nb/10 + \ldots$

Graville [42] has shown that for C < 0.11%, hydrogen cracking sensitivity can be described by the formula:

$$CEs = C + Mn/16 - Ni/50 + Cr/23 + Mo/7 + Nb/8 + V/9$$

that is C < 0.11% CEs = C + Nb/8 + …

which indicates a similar influence of Nb and C to that derived from the Yurioka CEN formula.

The current restrictions on carbon and niobium for the higher strength grades in EN 10025-4, Table, are C max 0.16 and Nb max 0.05. Should the niobium limit be raised from 0.05% to 0.15%, the above formulae suggest that it would be compensated by reductions in the carbon content of (0.15 - 0.05)/5 to (0.15 - 0.05)/10, i.e. 0.02 to 0.01. The steels of interest here have carbon contents of less than 0.08%, i.e. 0.08 lower than the current limit, more than necessary to compensate for higher levels of Nb.

The Tekken test results also showed that the current high-strength low-carbon compositions are very resistant to hydrogen cracking in the Tekken test. No preheating was required for welding with normal levels of hydrogen and only moderate preheating in the case of welding with cellulosic electrodes.

It can be concluded that higher levels of niobium can be allowed without increasing the risk of hydrogen cracking when carbon is limited to lower levels.

6.5.3.6 Weld metal toughness

Weld metal toughness depends on the chemistry of the weld metal and the cooling rate of the weld. Due to dilution, higher niobium contents in the base plate lead to higher levels in the weld metal, especially in high-dilution welding processes such as submerged arc welding, where the level of dilution can be as high as 70%. However, it is clear from the HIPERC results in work packages 2 - 4 that good weld metal toughness can still be obtained when the base plate contains approximately 0.10% Nb even using submerged arc welding. While the high niobium content of the present steels is detrimental to weld metal toughness under conditions of high dilution, their low carbon content counteracts the effects of niobium by giving lower levels of carbon in the weld metal, which is beneficial for toughness.

Similar results have been found elsewhere. For example, Signes and Baker [43] showed that submerged arc welding of 19 mm thick low-carbon high-niobium plates produced good weld metal toughness at -46^{o}C using three different wire - flux combinations. The steels studied contained 0.08 C 1.5 Mn and 0.03 - 0.15 Nb. They concluded that weld metal toughness should not be a limiting factor even for the highest niobium content.

Bersch and Kaup [44] studied 18 mm thick steels containing 0.09 C 0.2 Si 1.45 Mn 0.05 Al and 0 - 0.18%Nb. They showed that for manual metal arc and MAG welding impact toughness was unchanged at -20^{o}C even for an addition of 0.18% Nb to the base plate; the reason being that even then the base plate only contributes 0.01% Nb to the weld metal. In the case of multipass SAW, they showed that weld metal impact toughness at -20^{o}C was reduced by higher levels of niobium, but that sufficiently high values could be maintained even for 0.18% Nb. For higher-dilution two-pass SAW, which is commonly used in spiral pipe welding, good impact toughness could be obtained in the weld metal provided suitable welding consumables were selected.

Taking the HIPERC results together with other results from the literature, it can be seen that low-carbon steel (C =< 0.09%) with niobium levels in the range 0.10 to 0.18% can be welded with good weld metal toughness at -20^{o}C or lower even in the case of high-dilution SAW.

6.5.3.7 Heat affected zone and fusion line toughness

The results from work packages 2 - 4 showed that very good impact toughness can be obtained on the fusion line and in the HAZ for the high-niobium low-carbon compositions studied as industrial heats. In work package 1, it was shown that, for the range of laboratory compositions studied, there are no statistically significant detrimental effects of niobium on the 27 J or 50% upper shelf energy transition temperatures of simulated coarse-grained HAZs. This result is valid for 0.05 - 0.12 % Nb and 0.02 - 0.07 %C. The low carbon content of the present steels is however beneficial to HAZ toughness: decreasing carbon from 0.09% to 0.04% reduces the 50% upper shelf energy transition temperature for the coarse-grained HAZ by about 25°C for t8/5 = 30 s.

Similar results have been obtained in earlier research. Figure 102 shows the toughness of simulated coarse-grained HAZs for a wide range of cooling rates, comparing two pipe steels based on 0.09 %C 0.035 %Nb 0.08 %V on the one hand and 0.03 %C 0.10 %Nb on the other [45]. Typical weld cooling rates range from about 10 - 60 °C/s (corresponding $t_{8/5}$ values of roughly 30 - 5 s). shows that the use of lower carbon produces large improvements in HAZ toughness even in the presence of high niobium..

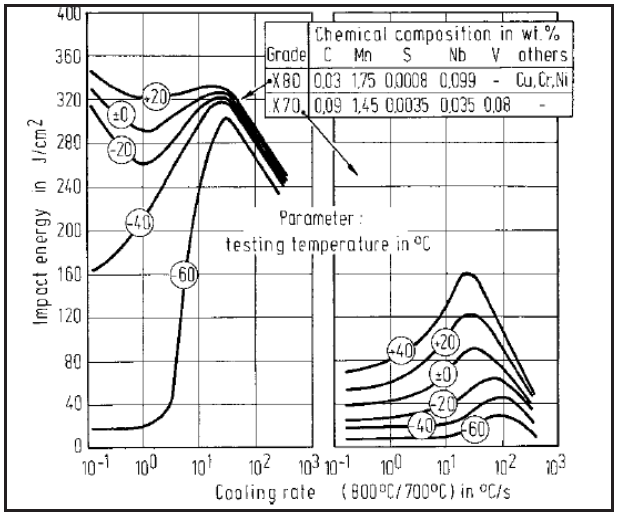

Figure 102: The Charpy V impact toughness of the simulated coarse-grained HAZ for a range of cooling rates. Peak temperature of 1350°C

Bersch and Kaup [44] also showed that good HAZ impact toughness at -20°C can be obtained in two-pass tandem SAW of 18 mm thick steel containing 0.09C 0.2 Si 1.45 Mn 0.05 Al and up to 0.18 Nb. Similar results were reported by Hulka and Heisterkamp [46].

Signes and Baker [43] studied the weldability of 19 mm thick plate made from 4 heats with 0.08 C, 1.5 Mn and Nb at 0.03, 0.06, 0.12 and 0.15%. Plate yield strengths were in the range 440 - 490 MPa. They used tandem SAW with one pass per side at an arc energy of 3 kJ/mm. Fusion line Charpy V impact toughness (50% weld metal/50% HAZ) at -46°C actually improved with increasing levels of Nb, see Figure 103.

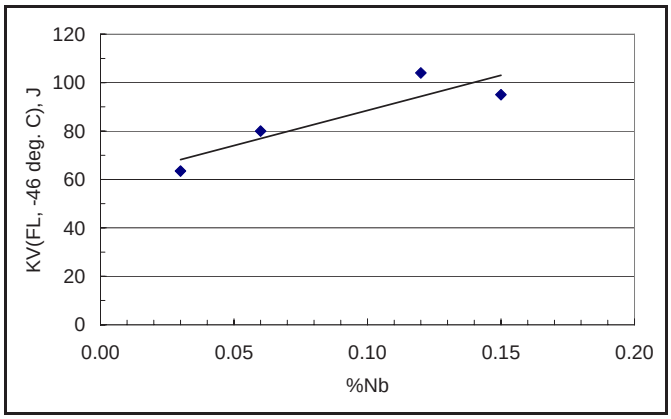

Figure 103: Fusion line Charpy V toughness vs. niobium content for 0.08%C 1.5%Mn 19 mm thick plate welded with one pass per side at 3 kJ/mm (60 - 65% dilution)

Signes and Baker also showed that there is a strong interaction between carbon and niobium as regards fusion line impact toughness at -46°C: as carbon content decreases over the range 0.18 - 0.08, the effect of niobium on FL toughness changed from being negative to positive. The negative effect of niobium on fusion line and HAZ toughness at high carbon contents may explain the limitation of Nb to a maximum of 0.05 - 0.06 in most standards since the standards have been designed to allow the use of carbon up to 0.16%. As shown above, the situation is very different in the case of carbon contents of

about 0.08% and below, in which niobium contents even up to 0.18% can still be welded with good HAZ impact toughness.

6.5.3.8 Weld toughness after post-weld heat treatment

Post-weld heat treatment (PWHT) is usually not used in structural or pipeline applications. Therefore, normally the properties of welds after PWHT will not be a limiting factor when considering the limits on niobium microalloying in standards for structural steel or pipeline applications. It may be appropriate, however, for standards to mention the fact that PWHT will reduce the toughness of the weld metal and HAZ in the case of high levels of niobium microalloying combined with low levels of carbon. Assessment of the effect of post weld heat treatment on the impact transition behaviour of two steels was shown in Figure 86 and Figure 87, and these showed that impact transition temperatures were shifted to higher temperatures, by 40 – 50 ^{o}C, but they were still good at about - 40 ^{o}C. It is thought that the shift in transition temperature was due to precipitation hardening, which also raised the hardness of the weld and HAZ by 10 – 30 HV.

Bersch and Kaup [44] showed that for two-pass submerged arc welds in 0.09 C steels PWHT for 2 h at 550^{o}C caused an increasing reduction in weld metal Charpy toughness with increasing levels of base plate niobium over the range 0 to 0.18%. At 0.18% Nb the Charpy V toughness in the weld metal was less than 27 J at -20^{o}C. The drop in toughness was accompanied by an increase in weld metal tensile strength and both were attributed to precipitation of NbC due to the presence of substantial amounts of niobium in solution in the weld metal in the as-welded state.

The effect of PWHT on weld toughness is not solely an issue for high niobium contents: HAZ toughness is also known to be impaired in the case of vanadium microalloying for similar reasons.

6.5.3.9 High-niobium low-carbon steel in pipelines

In work packages 2 and 3 it has been shown that the low-carbon high-niobium concept can be used to make UOE and spiral welded pipe in strength classes X65 - X80. It has been shown that the pipes have good combinations of strength and toughness as measured using Charpy V and drop weight tear testing. The girth weldability of the pipes was good and the pipe samples performed well in wide-plate tests. X80 pipes made according to the low-carbon high-niobium concept are currently in use in 600 km of pipe in the USA and there have been no reported problems with the use of these steels [29].

Steels for pipe lines are specified in EN 10208-2, which currently limits the level of niobium to 0.06% in all of the higher strength grades, as shown in

Table. This is unfortunate because it leads to unnecessarily expensive steels by forcing steelmakers to use more expensive alloying elements such as molybdenum where high niobium levels would suffice. The resultant solutions can be more expensive both financially and environmentally.
In contrast to EN 10208-2, the recently harmonised API 5L/ISO 3183 standards recognise that higher levels of niobium can be used to advantage when carbon is less than 0.12-0.10% and only limit the total level of microalloying through Nb+V+Ti =< 0.15, which allows niobium to be alloyed up to 0.15% in the absence of other microalloying elements.

6.5.3.10 Manganese levels in low-carbon structural and line pipe steels

Work-package 1 showed that good combinations of mechanical properties could be obtained in the present low-carbon steels with manganese contents at least up to 2.1%. Indeed, the results showed that better combinations of yield strength and toughness are obtained by increasing manganese and reducing carbon; the regression formulae show that increasing strength by 1 MPa using Mn raises the transition temperature by 0.4^{o}C compared to 1.4^{o}C when the increase is brought about using C. This fact is also recognised in the line pipe steel standards EN 10208-2 and API 5L/ISO 3183, which allow higher upper limits for manganese in the case of lower carbon contents, see Table 102. In higher carbon steels, manganese is limited to lower levels because of the risk of strong centre-line segregation when the steel

solidifies to austenite. When C < 0.12% solidification takes place mainly to delta-ferrite, which leads to lower levels of segregation thereby allowing higher manganese levels. The structural steel standard EN 10025-4 needs revising, however, as it limits manganese to a maximum of 1.7% irrespective of carbon content.

6.5.4 Conclusions and recommendations

HIPERC has been concerned with the use of relatively high levels of niobium in very-low-carbon steels. Laboratory-scale heats and pilot rolling trials simulating air and water-cooled plate production as well as hot-rolled strip production have been made. On the basis of measured mechanical properties, regression models for strength, toughness and weldability have been developed allowing the design of thermomechanically rolled structural and pipe steel in yield strength classes from 420 to 700 MPa. These equations have been verified by the full-scale production of structural steels and linepipe using plate mills and hot-strip mills. Both laboratory and full-scale trials have shown that excellent combinations of strength, toughness and weldability can be obtained using carbon contents in the range 0.02 – 0.07 wt. % and niobium contents in the range in 0.05–0.12 wt. %.

It has been demonstrated that a low-carbon, high-niobium chemistry allows the full-scale production of S420ML in 50 mm thickness and S460ML in 20 mm thickness plate using lower levels of controlled rolling and with air-cooling. The project has also demonstrated that the same approach allows the properties of L450MB - L555MB to be achieved in a cost-effective way without the use of more expensive alloying elements such as molybdenum and vanadium.

On the basis of these results together with the literature review above, it is suggested that the Euronorms EN 10025-4 and EN 10208-2 should be changed to enable the use of higher levels of niobium, up to a maximum of 0.15%, in the case of low carbon contents. Furthermore, in the case of low carbon contents, it is recommended that higher levels of manganese are allowed in the structural steel standard EN 10025-4.

The recommended changes to EN 10025-4 are as follows:

add a footnote to the current limits on niobium for all grades stating: “For each 0.01% reduction of the maximum carbon content, the maximum specified niobium content is increased by 0.01%, up to a maximum of 0.15%”

add a footnote to manganese stating: “For each 0.01% reduction of the maximum carbon content, the maximum manganese content is increased by 0.05% up to a maximum of 2.1%.”

Examples of the above recommendations are given in Table.

EN 10208-2 can be changed to follow the harmonised API 5L / ISO 3183 with regard to the levels of microalloying allowed. The current separate limitations on niobium, vanadium and titanium should be replaced by Nb+Ti+V =< 0.15%.

Furthermore, it is recommended that EN 10028-5 is changed in accordance with the above recommendation for EN 10025-4, together with an additional footnote stating that special care should be taken to ensure that toughness requirements are met in welds if post-weld heat treatment is prescribed in the case of high levels of microalloying.

Table 104: Proposed upper limits on C, Mn and Nb for S420M/ML and S460M/ML in EN 10025-4

C max	Mn max	Nb max
0.16	1.7	0.05
0.14	1.8	0.07
0.12	1.9	0.09
0.10	2.0	0.11
0.08	2.1	0.13
0.06	2.1	0.15

7. Figures and Tables

8. References

[1] EN ISO 4063: 2000, Welding and allied processes - Nomenclature of processes and reference numbers

[2] W. J. Liu and M. G. Alben, Can Metall. Q., 26 (1987), 145

[3] M. Pérez-Bahillo, B. López, A. Martín-Meizoso, Effect of rolling schedule in grain size of steels with high niobium content, X th Spanish National Congress on Materials 18-20 June, 2008 in San Sebastian

[4] J. Brozda and M. Zeman, Weldability of micro-alloyed steel with higher niobium content, Biuletyn Instytutu Spawalnictwa W Gliwicach, Nr. 5/2008, Rocznik 52, ISSN 0867-853X

[5] Atlas for Bainitic Microstructures Vol. 1, ed. T. Araki et al, Bainite Committee of Iron & Steel Institute of Japan, ISIJ 1992.

[6] R. Bengochea, B. López and I. Gutiérrez, ISIJ International, Vol. 39 (1999), No.6, pp. 583-591

[7] R. W. K. Honeycombe: Steels Microstructures and Properties, Edward Arnold Pub. Ltd., London, (1980)

[8] M. Thomson, M. Ferry, P.A. Manohar, ISIJ Int. 41, (2001), 891-899

[9] S. Zajac, T. Siwecki, B, Hutchinson and M. Attlegard: Metall. Trans., 22A (1991), 2681

[10] H.J. Jun, J.S. Kang, and D.H. Seo, Mat. Sci. Eng. A422 (2006), 157-162

[11] D. Q. Bai, S. Yue, W. P. Sun and J. J. Jonas, Effect of Deformation Parameters on the No-Recrystallisation Temperature in Nb-Bearing Steels, Metallurgical Transactions A, Vol. 24 (1993), p. 2151.

[12] M. Djahazi, X. L. He, J. J. Jonas and W.P. Sun: Metall. Trans. A, 23A (1992), 2111.

[13] X. L. He, M. Djahazi, J. J. Jonas, J. Jackman: Acta Metall. Mater. 39 (1991), 2295.

[14] D. Q. Bai, S. Yue, T. Maccagno and J. J. Jonas, ISIJ Int. 36 (1996), 1084.

[15] K. Wallin, Modified Tanh fitting algorithm for Charpy impact data, ECOPRESS Research Seminar on economical and safe application of modern steels for pressure vessels, 19th and 20th of May 2003, Aachen, Germany

[16] S. Cumming and H. Triel, 24” and 42” welding procedures for the University of Gent, Smart Engineering BV. Technical report 08081-UGT-SC-Rev 00, 20 pages, 2008

[17] G. Knauf and P. Hopkins, EPRG Guidelines on the Assessment of Defects in Transmission Pipeline Girth Welds, 3R International, 35 Jahrgang, Heft 10-11/1996, s. 620-624.

[18] R. M. Denys, W. De Waele, A. Lefevre and P. De Baets, An Engineering Approach To The Prediction Of The Tolerable Defect Size For Strain Based Design, Proc. of the Fourth Int. Conference on Pipeline Technology, Volume 1, Oostende, pp. 163-182, 2004.

[19] R. M. Denys, Weld metal strength mismatch: past, present and future, invited lecture Osaka University

[20] A.S. Bannister, M. Skalidakis, A. Pariser, P. Langenberg, F. Gutierrez-Solana Salcedo, L. Sanchez, D. Pesquera, and W. Azpiazu, Performance criteria for cold-formed structural steels, Contract number 7210-PR/246

[21] W. Oldfield, Fitting impact test data - a statistical procedure, ASTM Standardizations News, 1975, p. 24.

[22] M. Piette, E. Dubrelle-Prat, Ch. Perdrix, V. Schwinn, A. Streisselberger, and K. Hulka, Effect of 0 - 0.1 % Nb additions on mechanical properties of plates processed by thermomechanically controlled processing and accelerated cooling, Iron and Steelmaking, 2001, Vol. 28, No. 2, pp 175 – 179.

[23] I. A. Yakubtsov and J. D. Boyd, Effect of alloying on bainitic high strength plate, Materials Science and Technology, 2008, Vol. 4, No. 2, pp 221 – 227.

[24] J. Fröber, Stahl und Eisen no. 98 (1978), pp. 1092-1098

[25] S. Bremer, V. Flaxa and F.M. Knoop, A novel alloying concept for thermo-mechanical hot-rolled strip for large diameter HTS (helical two step) linepipe, Proceedings of IPC2008, September 29-October 3, 2008, Calgary (Canada), paper IPC2008-64678.

[26] S. G. Jansto, Cost Effective Microalloy Structural Steel Balance of Process Metallurgy and Materials Engineering, International Symposium on Materials Engineering for Structural Applications, Materials Science and Technology (MS&T) 2008, October 5-9, 2008, Pittsburgh, Pennsylvania, pp. 1289-1301.

[27] W. Haensch and C. Klinkenberg, Low carbon niobium-alloyed high strength steel for automotive hot strip, 2nd International Conference on Thermomechanical TMP'2004 Processing of Steels, Liège, Belgium, 2004, pp. 115-120.

[28] Y. D. Morozov, L. I. Efron and Y. I. Matrosov, Welding simulation for comparative analysis of steels for main pipelines, International Symposium on Microalloyed Steels for the Oil and Gas Industry, The Minerals, Metals & Materials Society, 2007, pp. 441-449.

[29] W. J. Fazackerley, P. A. Manuel, L. Christensen, First X-80 HSLA Pipeline in the USA, International Symposium on Microalloyed Steels for the Oil and Gas Industry, The Minerals, Metals & Materials Society, 2007, pp. 353-366.

[30] EN 10025-4 Hot rolled products of structural steels. Part 4: Technical delivery conditions for thermo-mechanical rolled weldable fine grain structural steels.

[31] EN 10028-5 Flat products made of steels for pressure purposes. Part 5: Weldable fine grain steels, thermomechanically rolled.

[32] EN 1993-1-12, Eurocode 3. Design of steel structures. Part 1-12: Additional rules for the extension of EN 1993 up to steel grades S 700

[33] EN 10149-2, Hot-rolled flat products made of high yield strength steels for cold forming. Part 2: Delivery conditions for thermomechanically rolled steels.

[34] V. K. Heikkinen and R. H. Packwood, Scand J Metall 6 (1977) 170-175

[35] S. Matsui, S. Sato and T. Tanaka, 102 nd ISIJ meeting, Nov. 1981, Lecture 1214.

[36] EN 1993-1-10 Eurocode 3: Design of steel structures. Part 1-10: Material toughness and through-thickness properties.

[37] EN 10164, Steel products with improved deformation properties perpendicular to the surface of the product. Technical delivery conditions.

[38] EN 1993-1-8 Eurocode 3: Design of steel structures. Part 1-8: Design of joints.

[39] EN 1011-2 Welding. Recommendations for welding of metallic materials. Part 2: Arc welding of ferritic steels

[40] J. Dearden and H. O'Neill, Trans. Inst. Weld., 3 Oct., 1940, 203 - 214.

[41] N. Yurioka, H. Suzuki, S. Ohshita and S. Sato, Determination of necessary preheating temperature in steel welding, Weld. J., June 1983, 147s-153s.

[42] B. A. Graville, in Proc. Conf. Welding of HSLA (microalloyed) structural steels, Rome, 9-12 Nov., 1976, ASM and Associazione Italiana di Metallurgia.

[43] E. G. Signes and J. C. Baker, Effect of Columbium and Vanadium on the weldability of HSLA Steels, Weld. J., 1979, 58 (6), 179s-187s.

[44] B. Bersch and K. Kaup, Effect of niobium on the welding behaviour of thermomechanically rolled steels, 3R International, 22 (10), October 1983, 484-492.

[45] K. Hulka, J. M. Gray and F. Heisterkamp, Metallurgical Concept and Full Scale Testing of a High Toughness, H2S Resistant 0.03%C-0.10%Nb Steel, Niobium Technical Report, NbTR 16/90, CBMM, Sao Paulo, Brazil, 1990).

[46] K. Hulka and F. Heisterkamp, Physical metallurgy, properties and weldability of pipeline steels with various niobium contents, in Proc. Int. Conf. Technology and Applications of High Strength Low Alloy (HSLA) Steels, ASM Congress, Philadelphia, 3-6 Oct., 1983, ASM, 190-191.

9. Appendix A – CCT Diagrams

0.038C 1.5Mn 0.11Nb 0.48Cu Steel A027

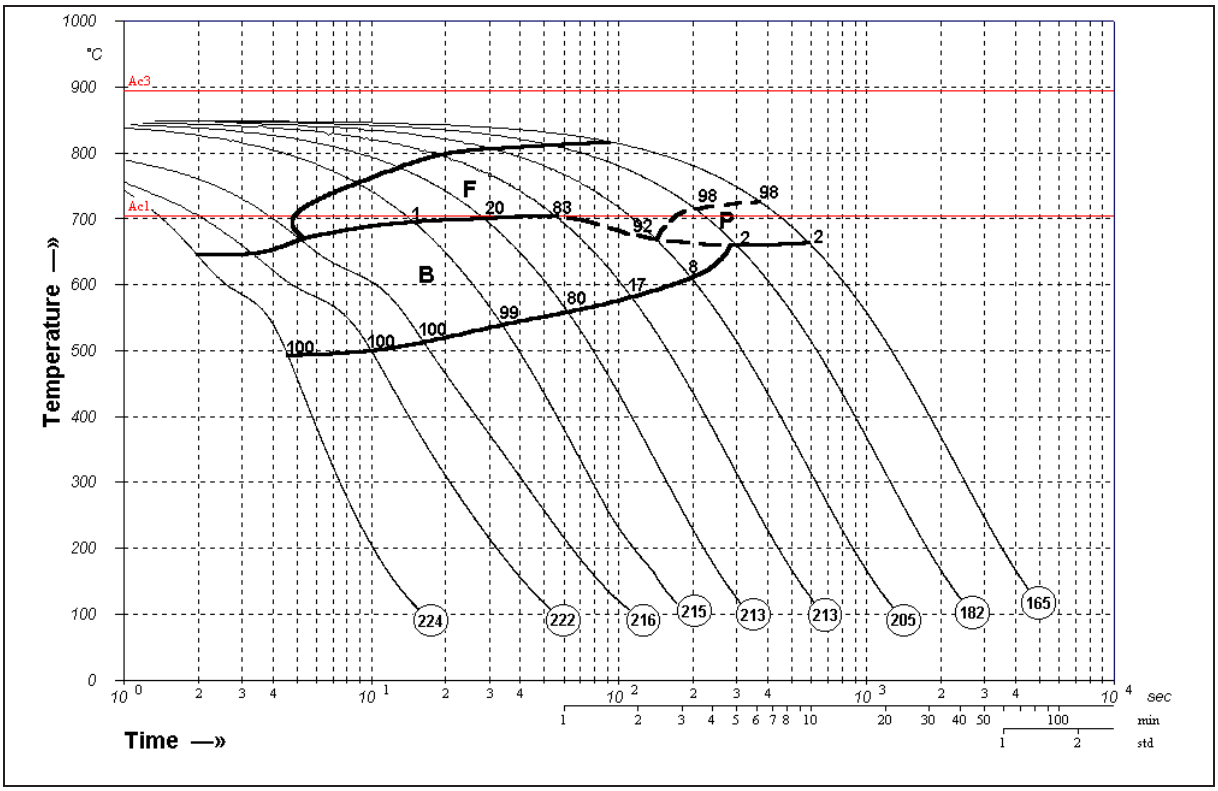

0.042C 1.5Mn 0.11Nb 0.44Ni Steel A028

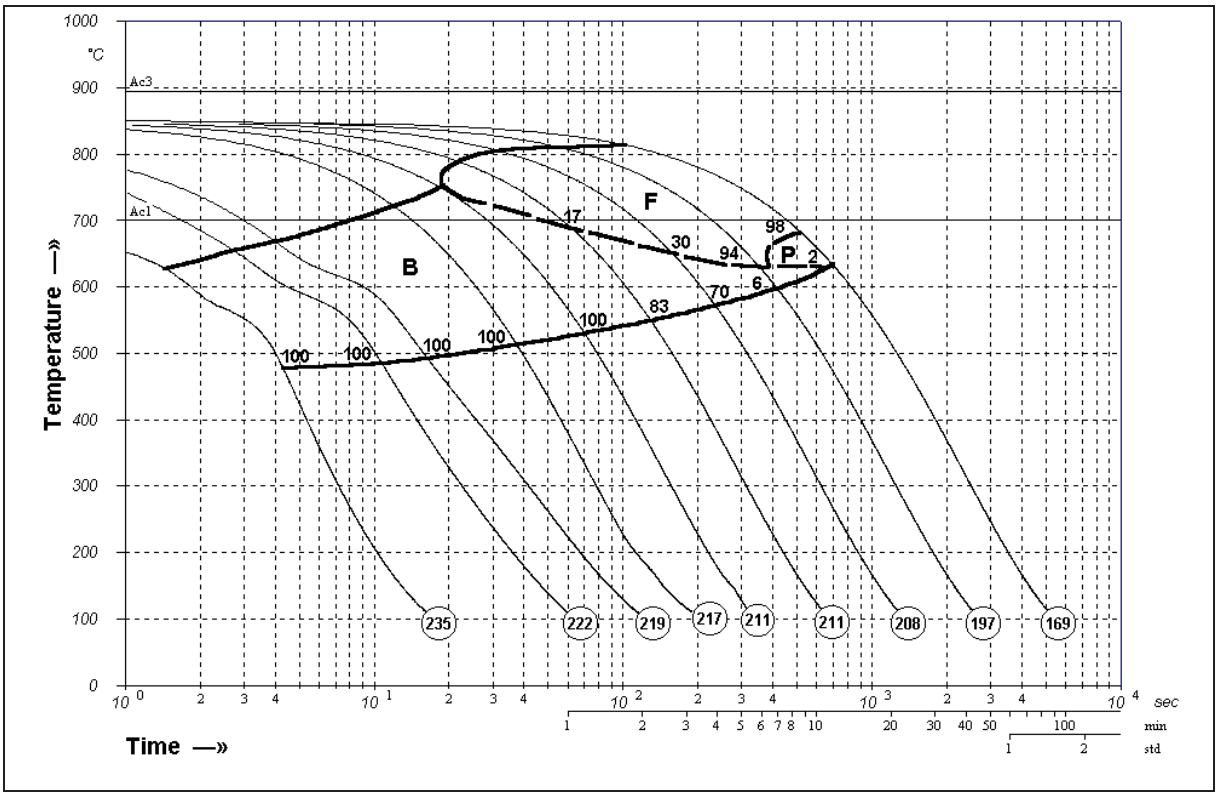

0.038C 1.4Mn 0.10Nb 0.32Mo Steel A029

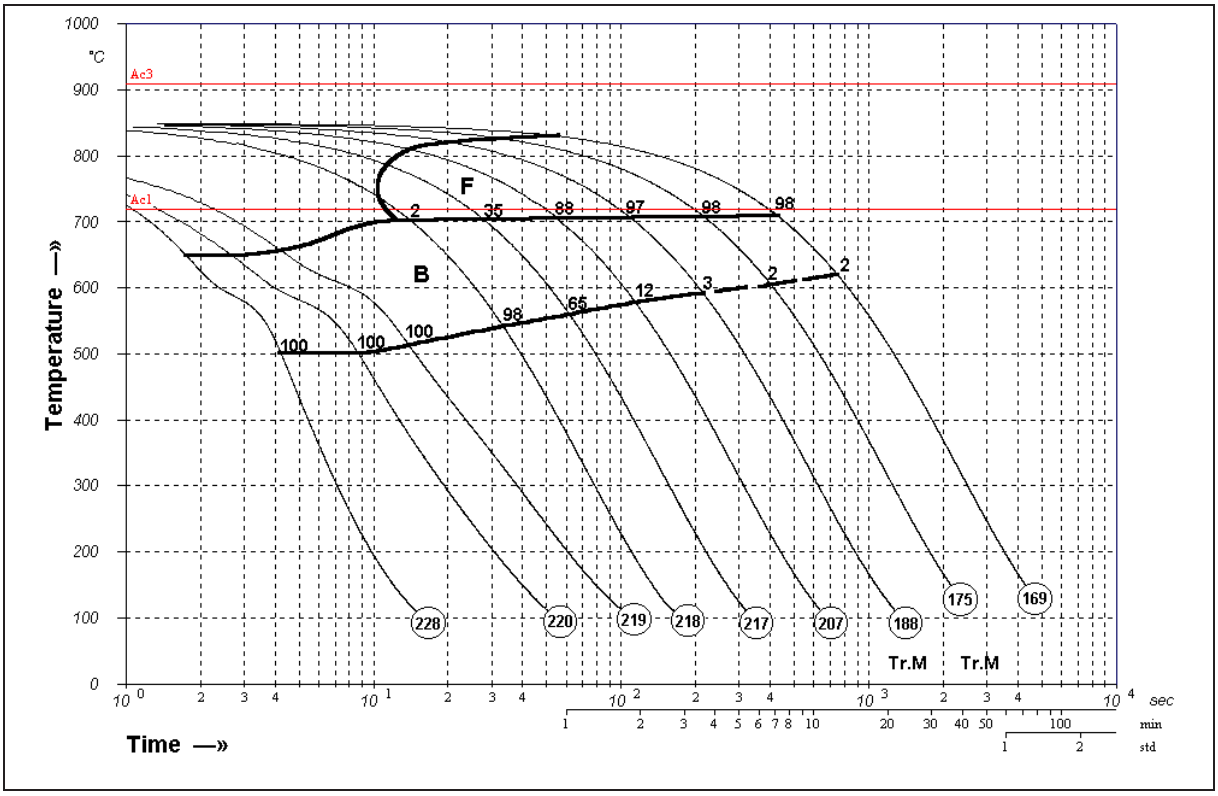

0.047C 1.5Mn 0.11Nb 0.44Ni 0.34Mo 0.049Cu Steel A030

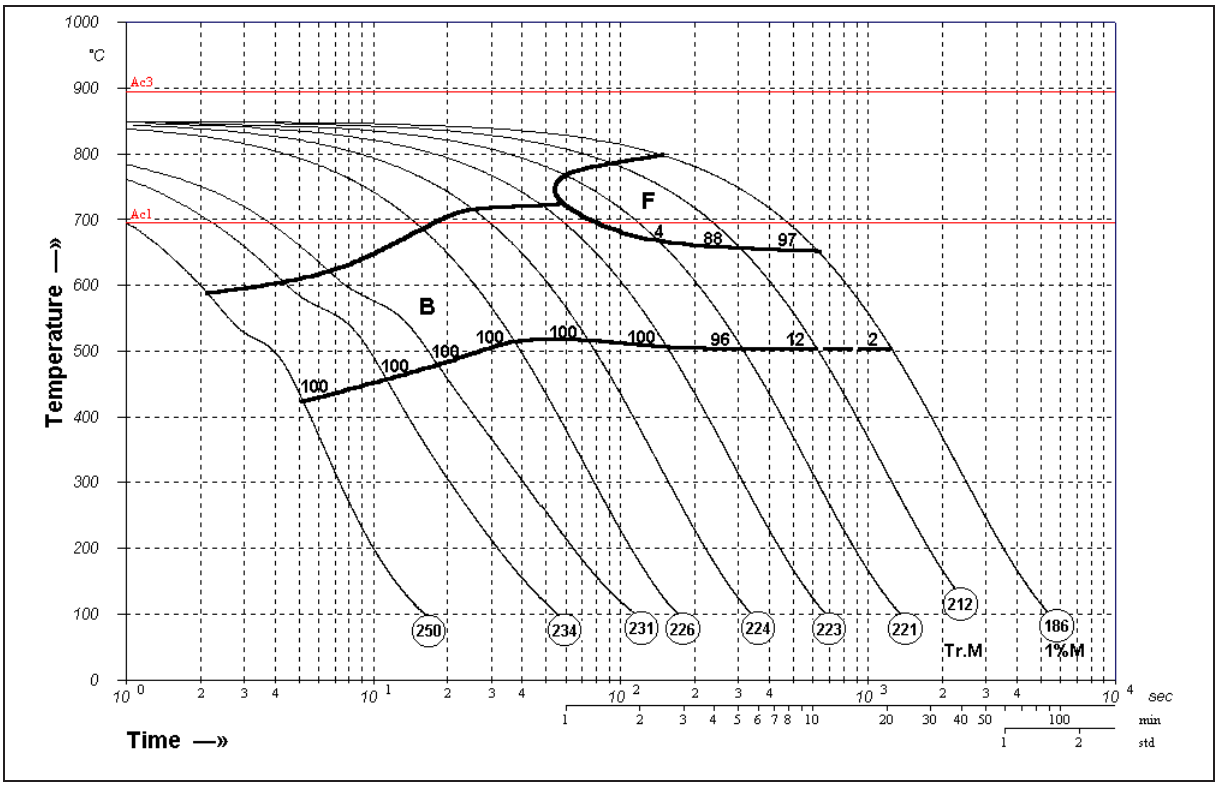

0.041C 1.5Mn 0.11Nb 0.47Cr Steel A031

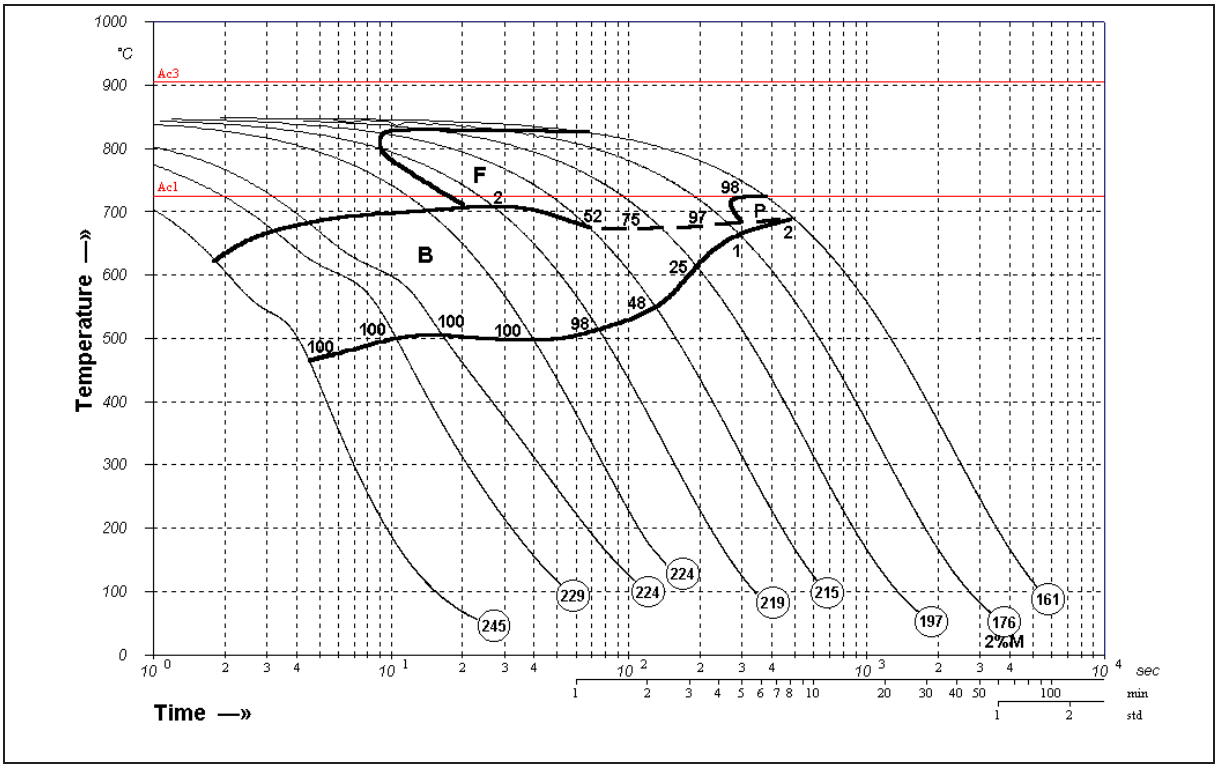

0.042C 1.5Mn 0.11Nb 0.44Ni 0.48Cu 0.51Cr Steel A032

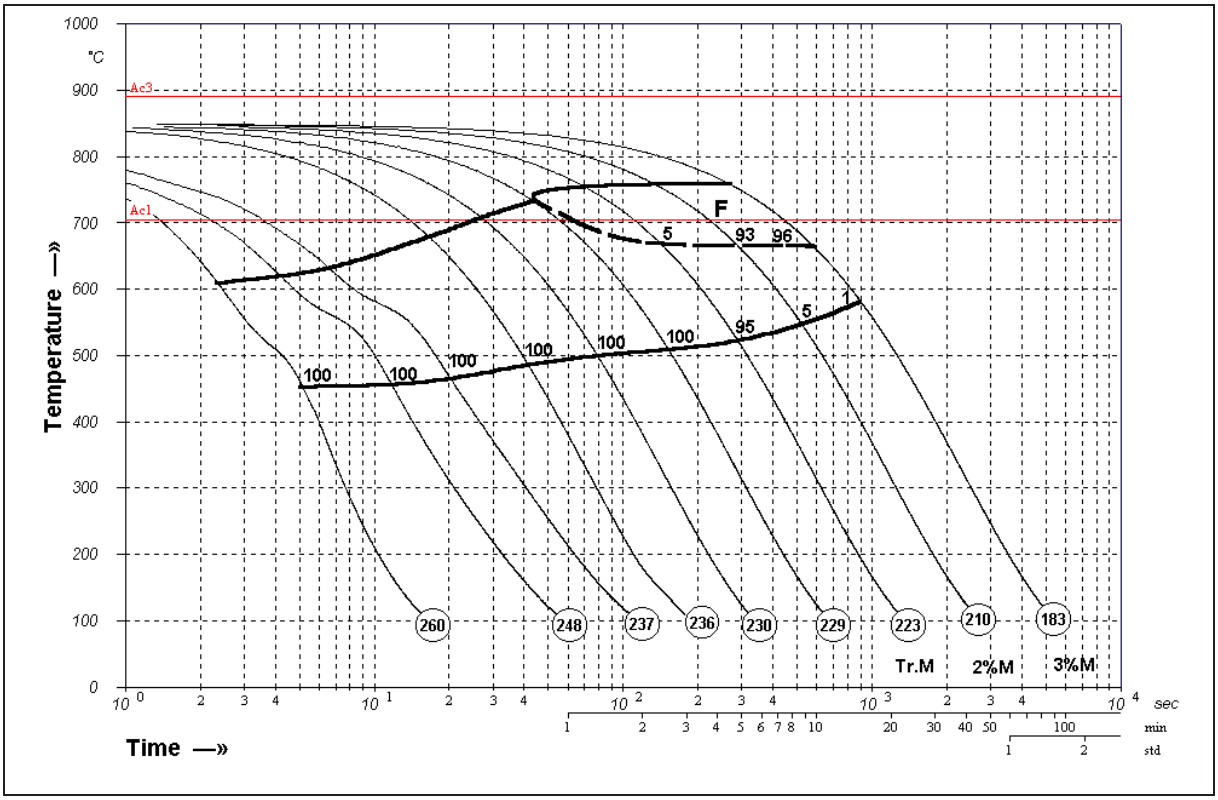

0.041C 1.5Mn 0.11Nb 0.35Mo 0.47Cu 0.50Cu Steel A033

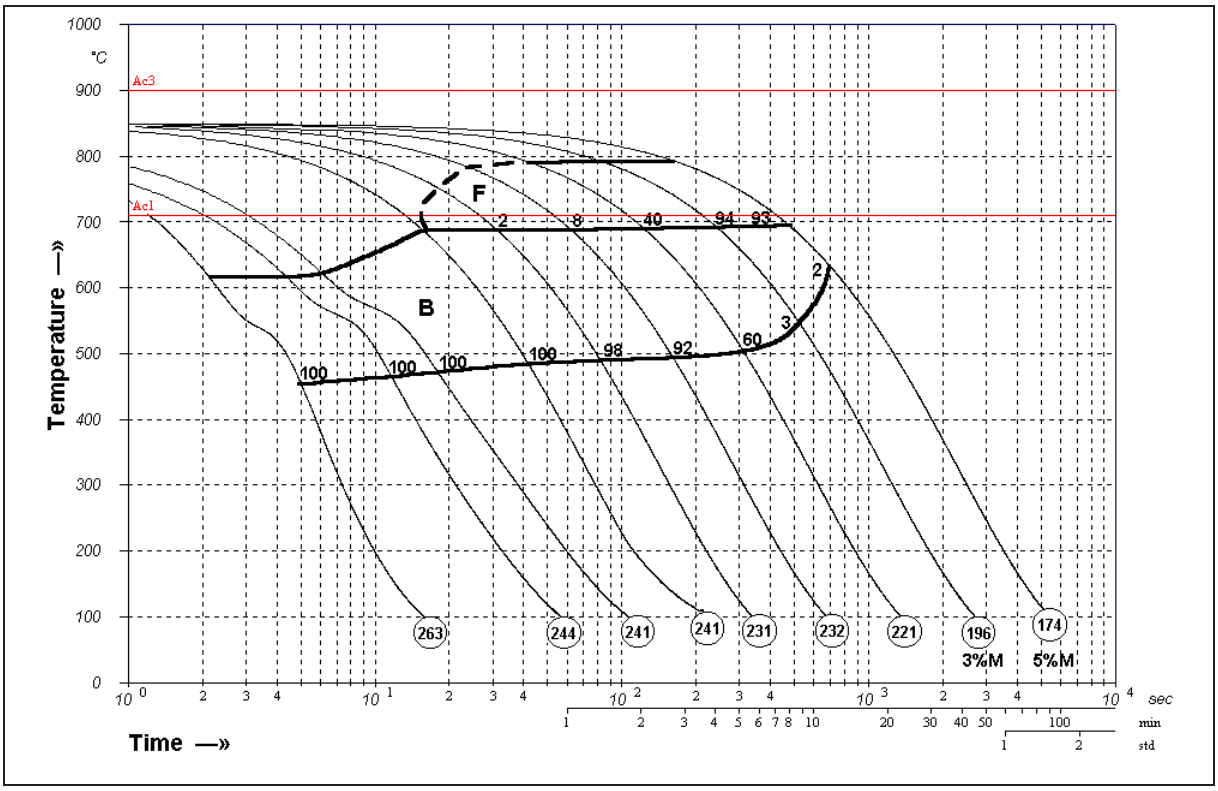

0.042C 1.5Mn 0.10Nb 0.43Ni 0.35Mo 0.52Cr Steel A034

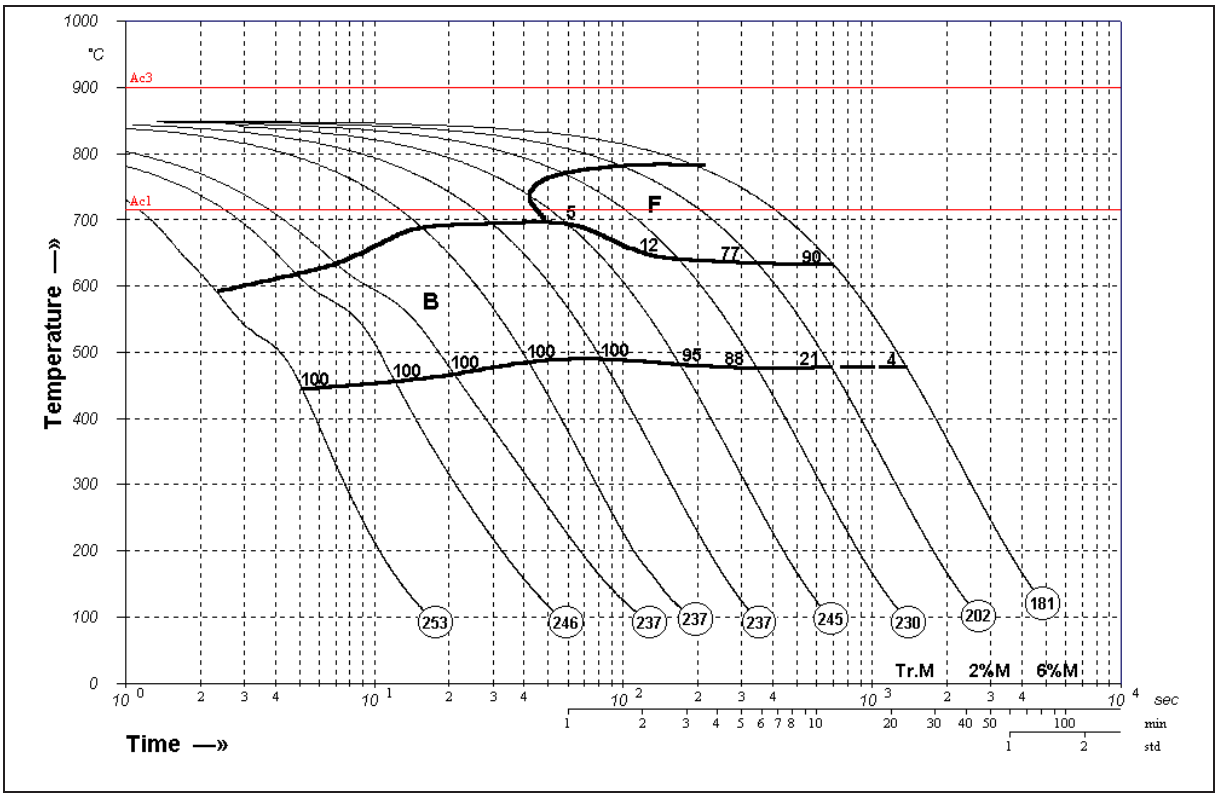

0.043C 2.0Mn 0.10Nb Steel A035

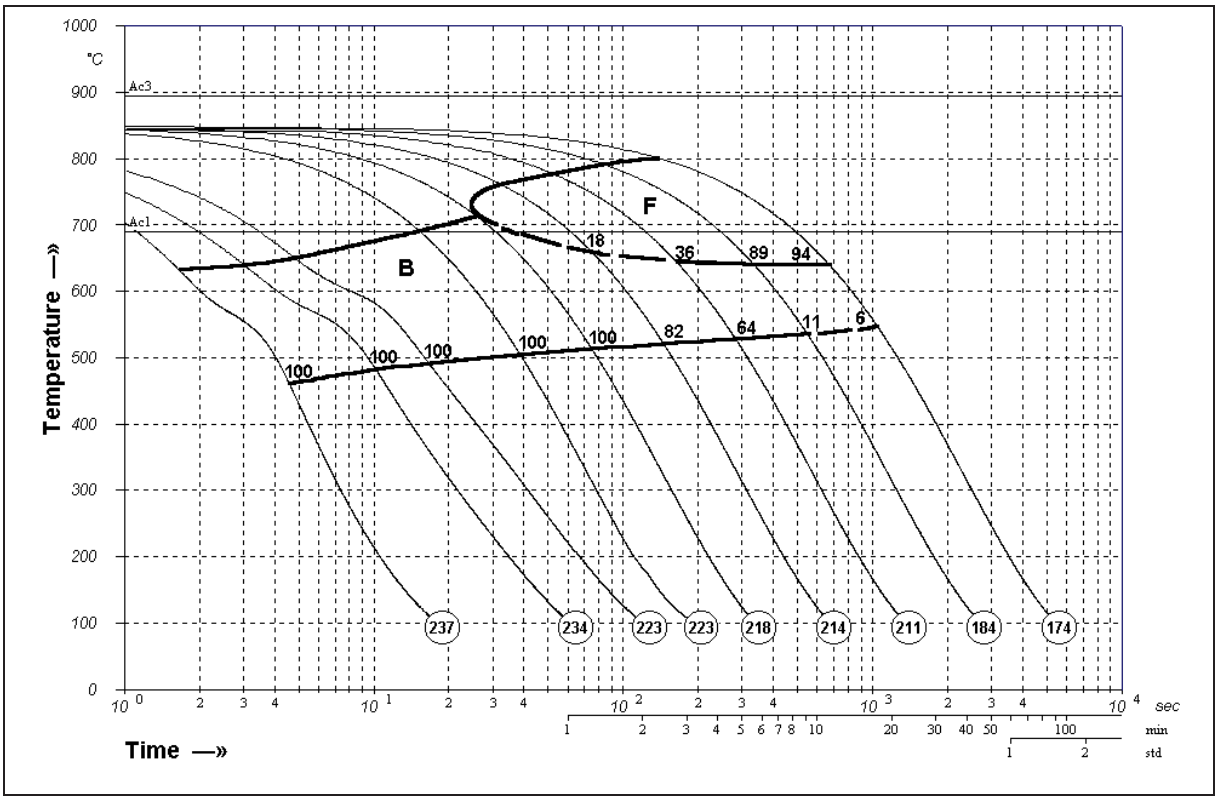

0.043C 2.1Mn 0.11Nb 0.43Ni 0.50Cu Steel A036

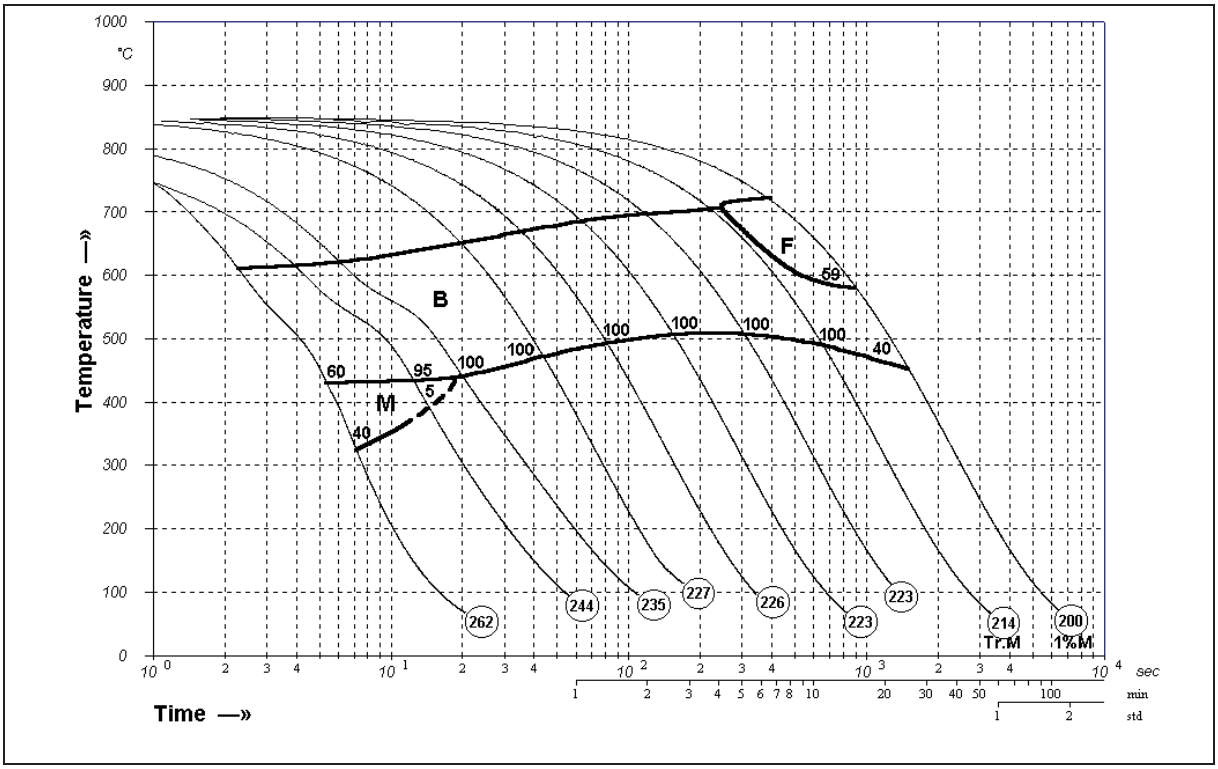

0.042C 2.1Mn 0.11Nb 0.35Mo 0.49Cu Steel A037

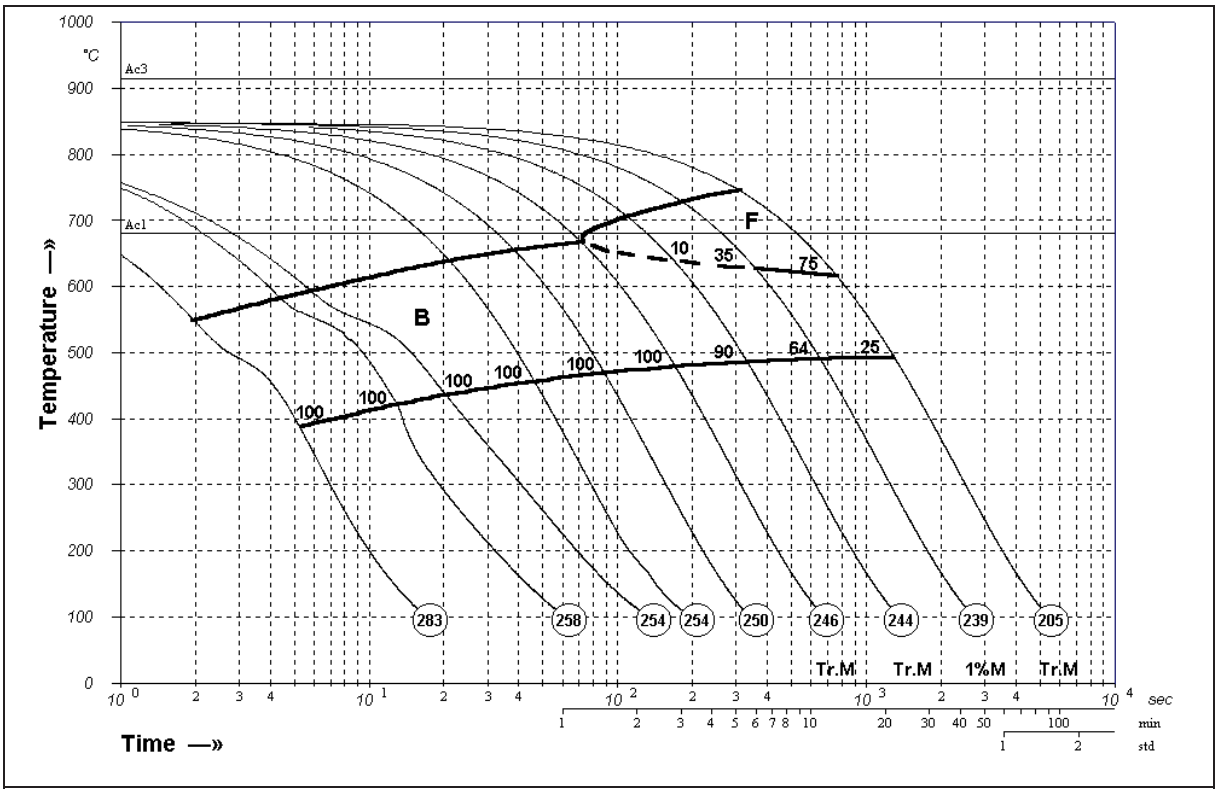

0.041C 2.0Mn 0.12Nb 0.51Ni 0.33Mo Steel A038

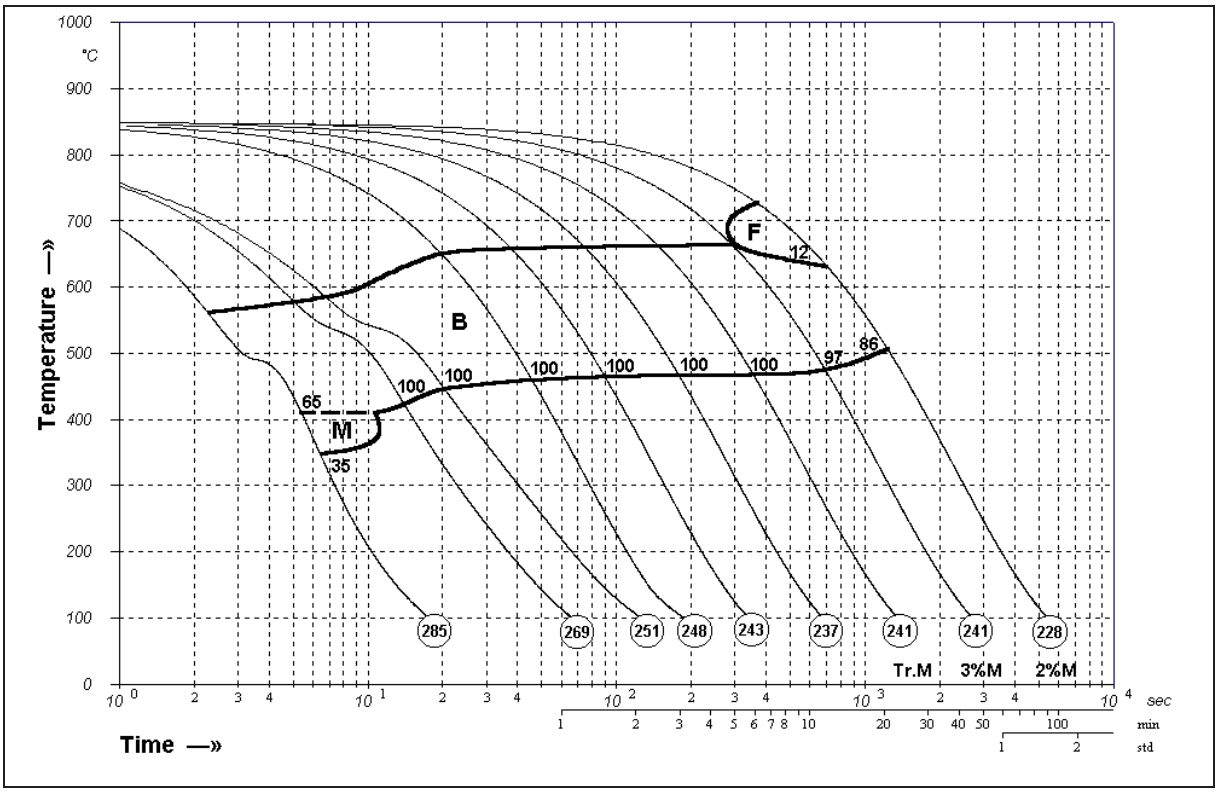

0.043C 2.1Mn 0.12Nb 0.56Cu 0.48Cr Steel A202

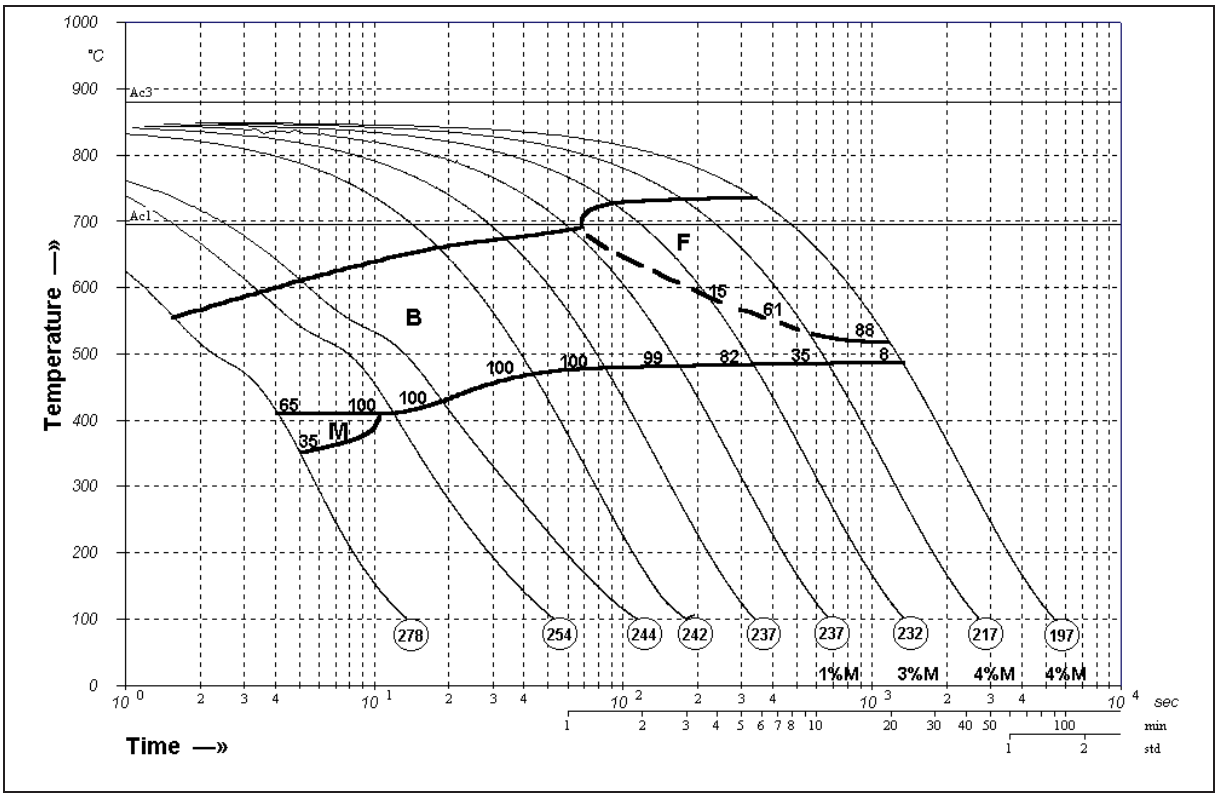

0.042C 2.1Mn 0.12Nb 0.49Ni 0.49Cr Steel A203

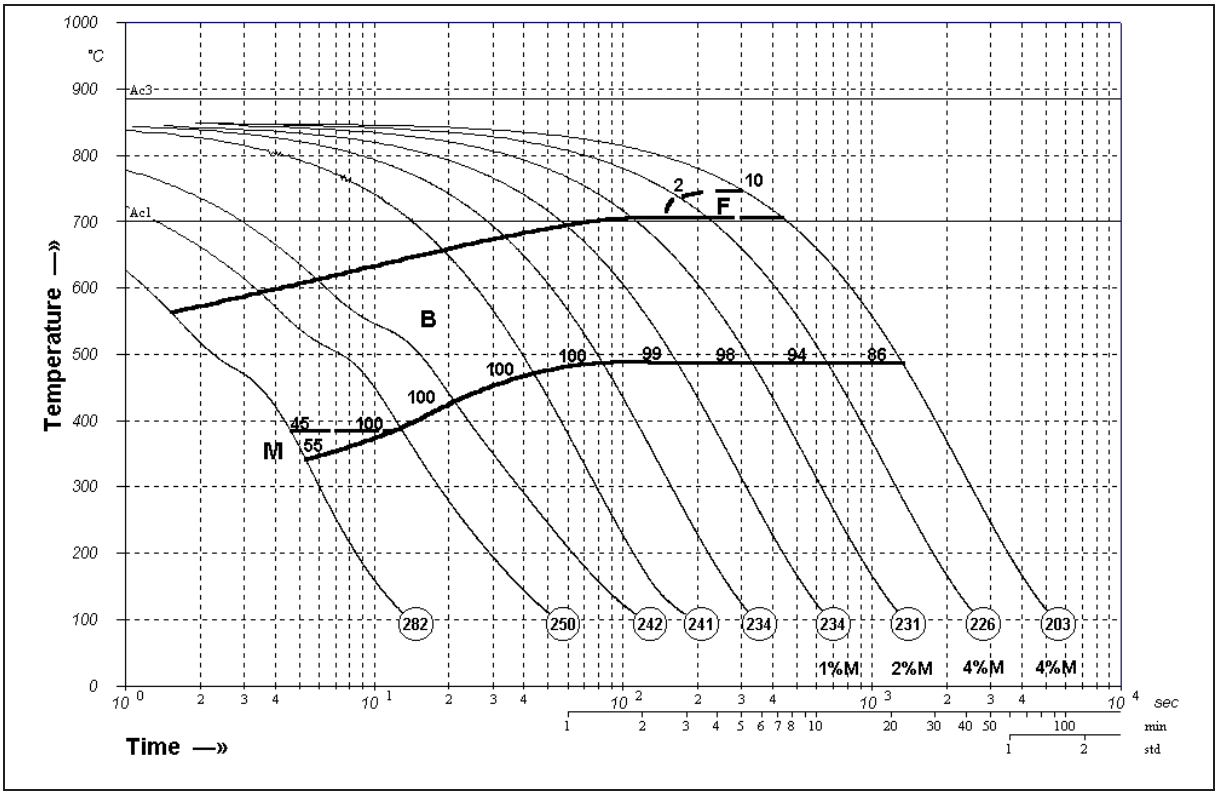

0.041C 2.0Mn 0.12Nb 0.33Mo 0.49Cr Steel A041

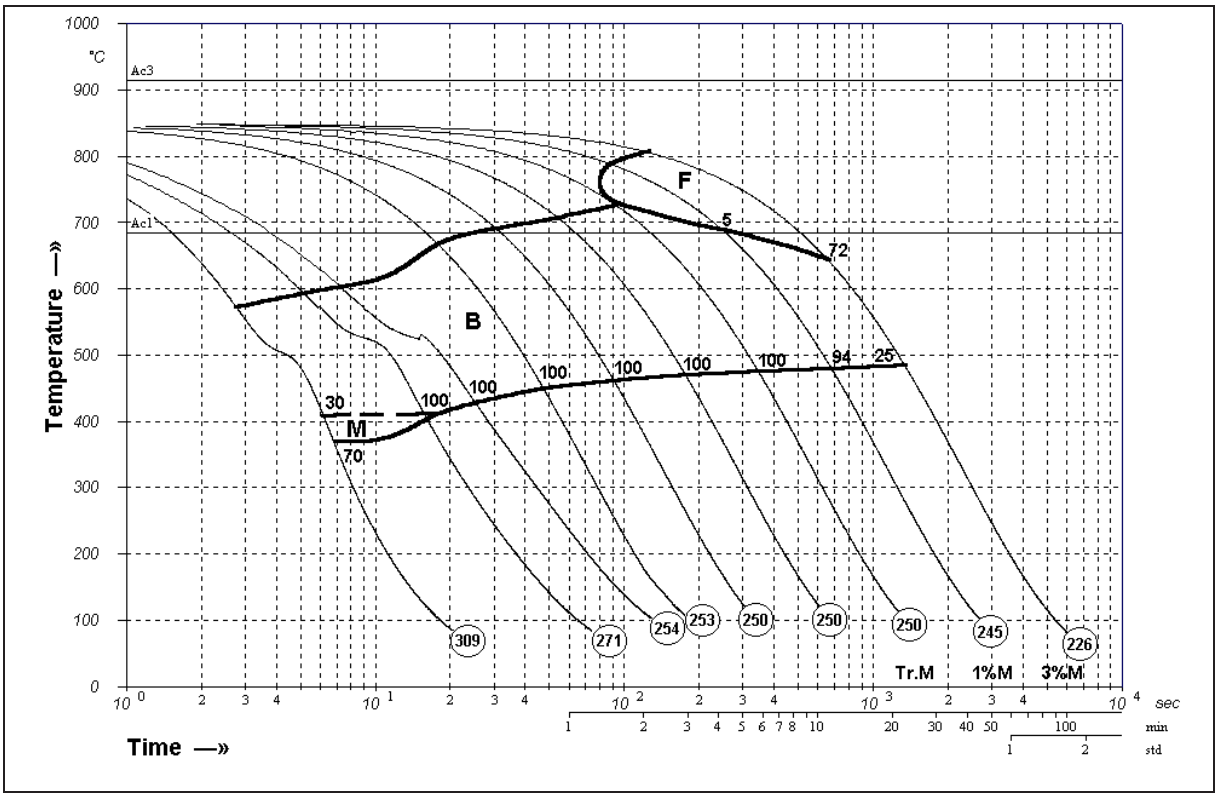

0.042C 2.1Mn 0.11Nb 0.45Ni 0.34Mo 0.53Cu 0.51Cr Steel A042

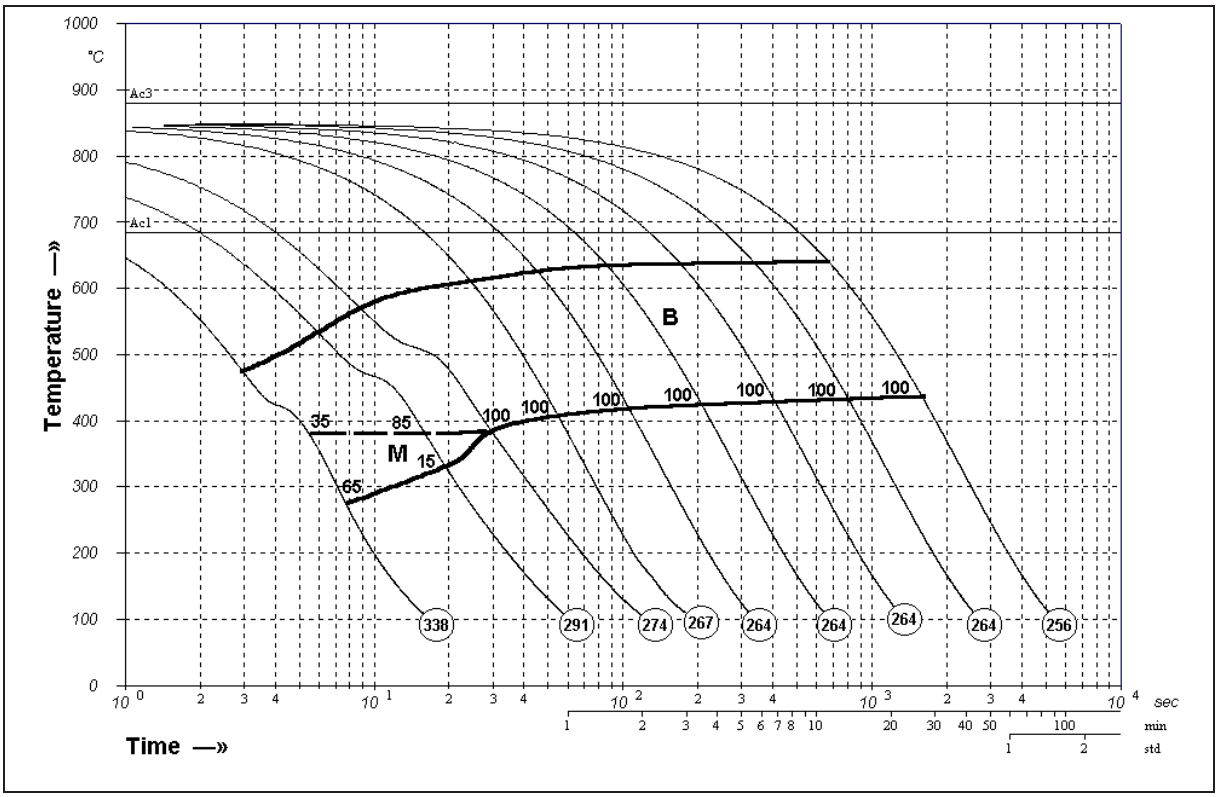

0.025C 1.8Mn 0.05Nb 0.24Ni 0.17Mo 0.27Cu 0.25Cr Steel A043

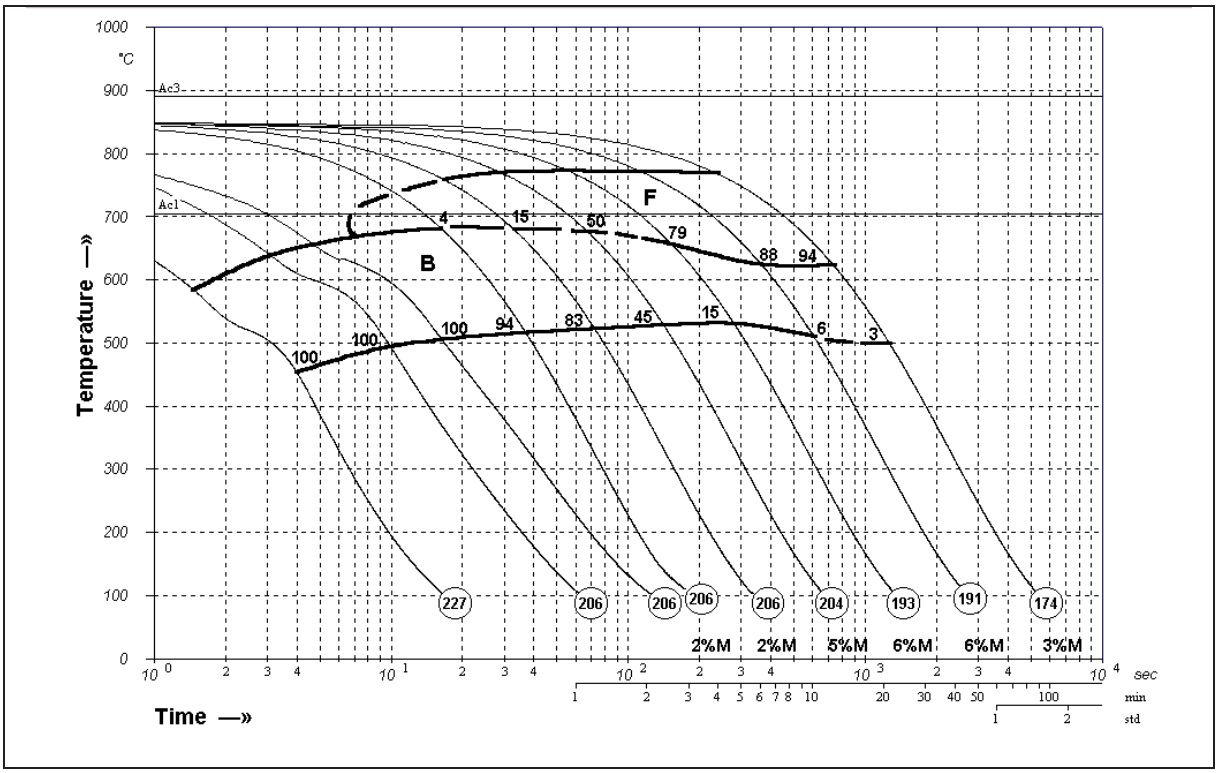

0.019C 1.8Mn 0.08Nb 0.24Ni 0.17Mo 0.29Cu 0.24Cr Steel A044

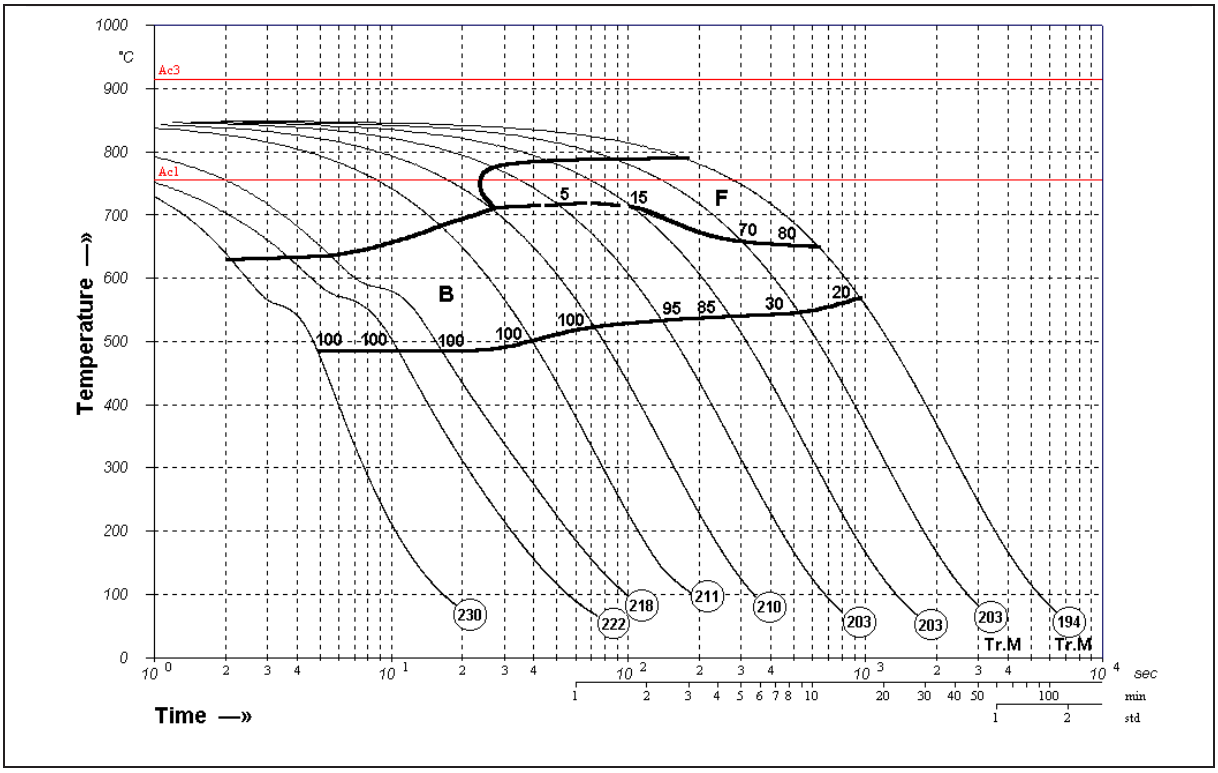

0.092C 1.8Mn 0.05Nb 0.24Ni 0.16Mo 0.30Cu 0.25Cr Steel A045

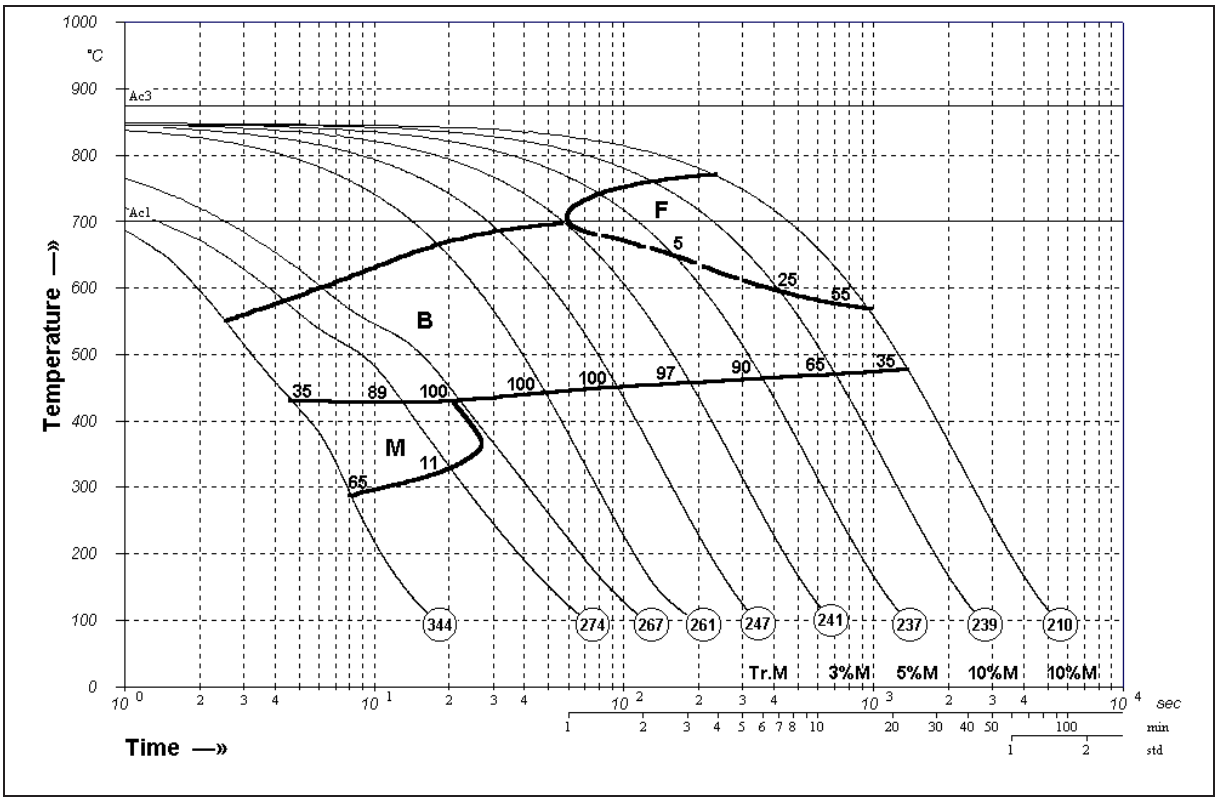

0.070C 1.8Mn 0.08Nb 0.23Ni 0.18Mo 0.28Cu 0.24Cr Steel A046

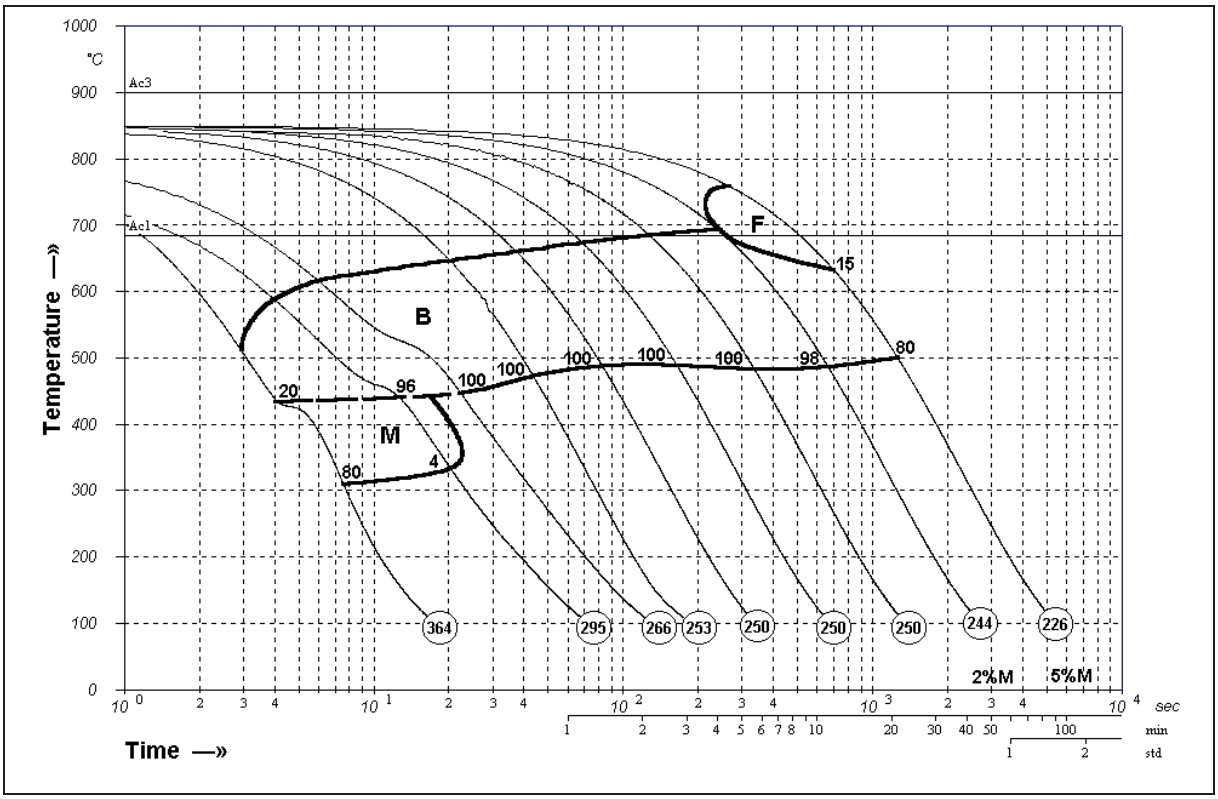

0.042C 1.8Mn 0.12Nb 0.25Ni 0.16Mo 0.30Cu 0.25Cr Steel A047

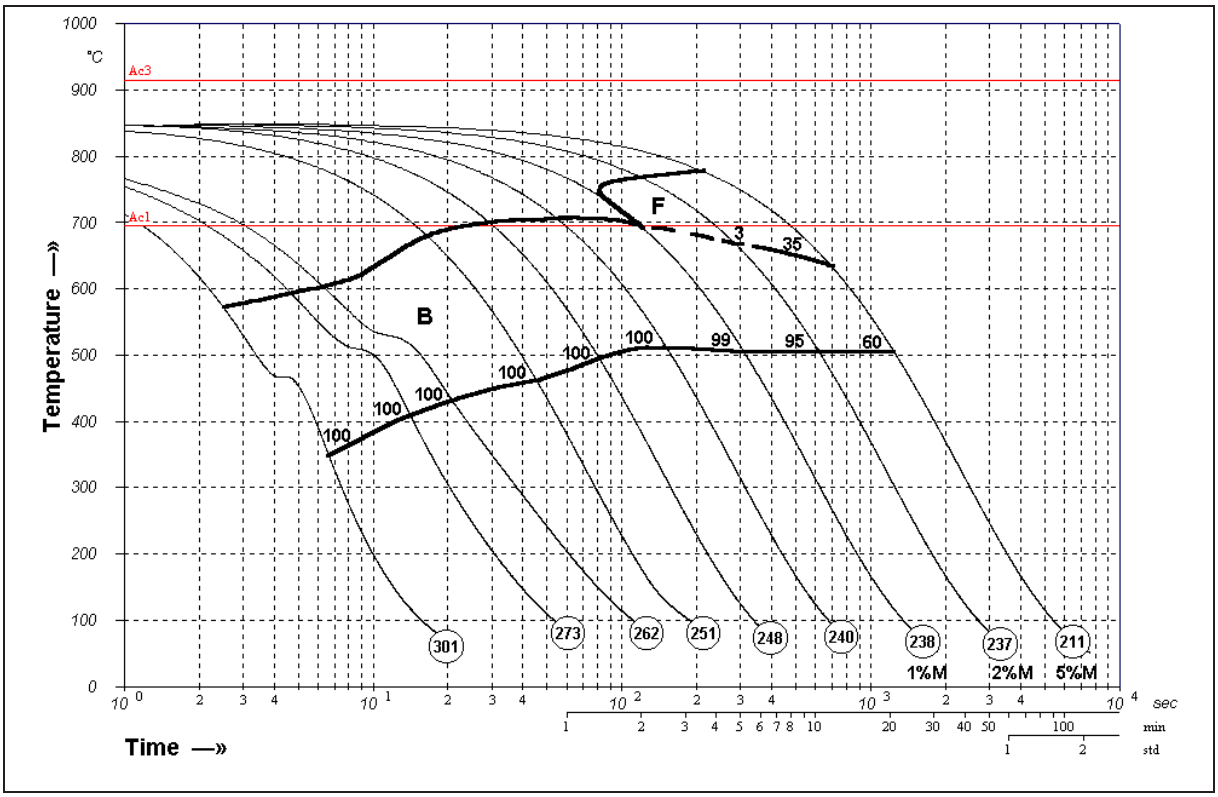

0.043C 1.8Mn 0.11Nb 0.23Ni 0.17Mo 0.30Cu 0.24Cr 0.0030B Steel A048

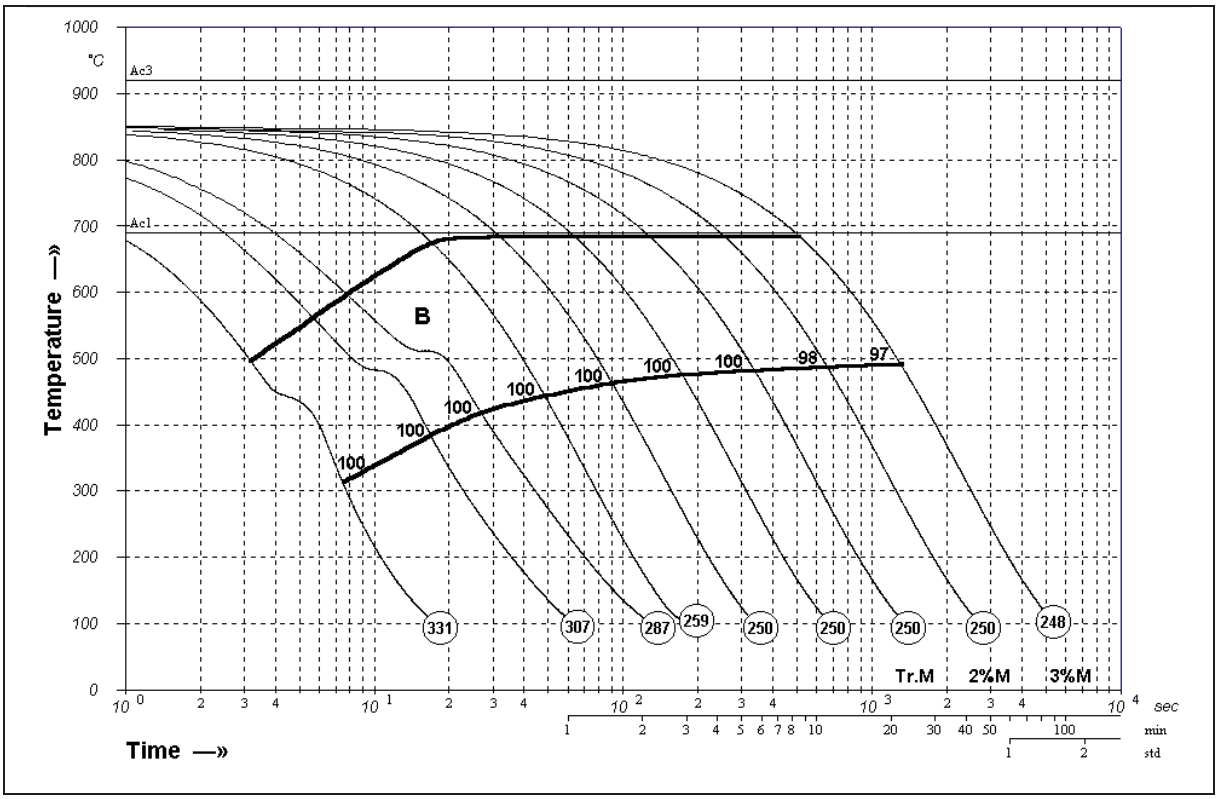

0.042C 1.8Mn 0.12Nb 0.24Ni 0.16Mo 0.30Cu 0.25Cr 0.0006B 0.022Ti Steel A049

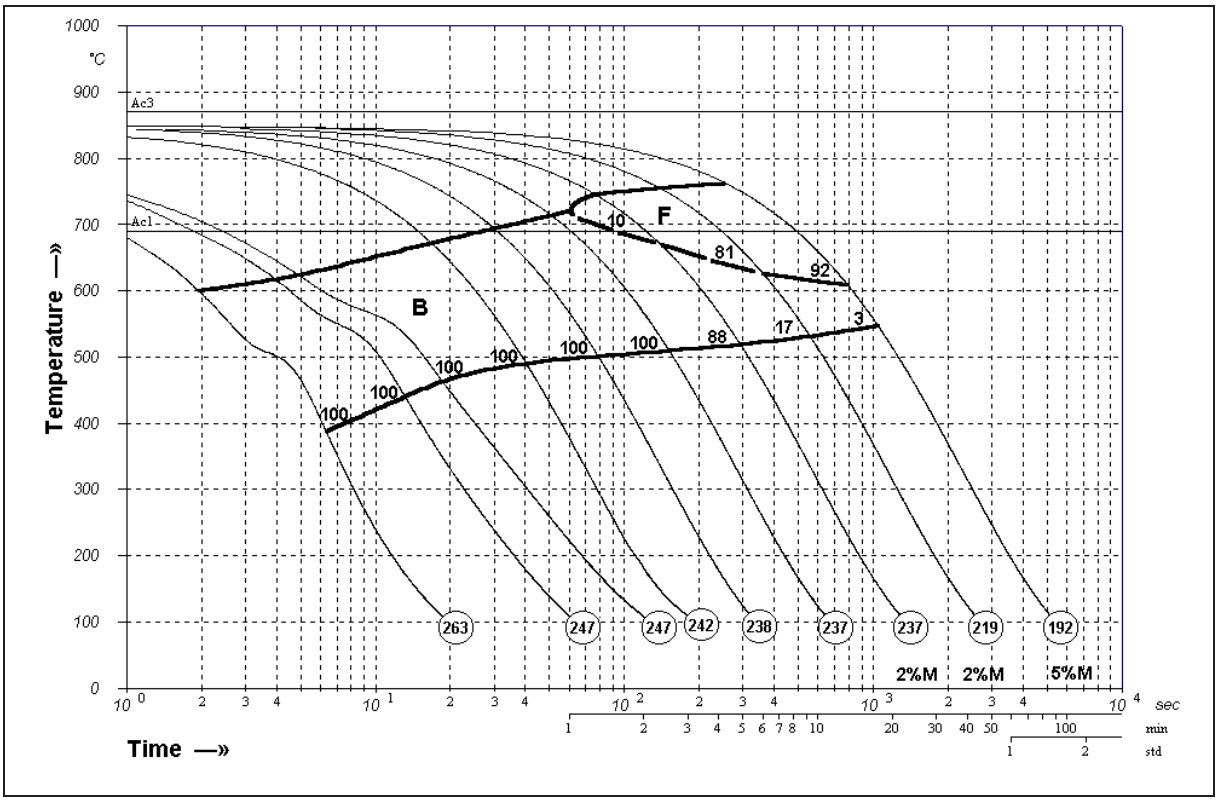

0.042C 1.9Mn 0.11Nb 0.23Ni 0.16Mo 0.29Cu 0.24Cr 0.0028B 0.021Ti Steel A050

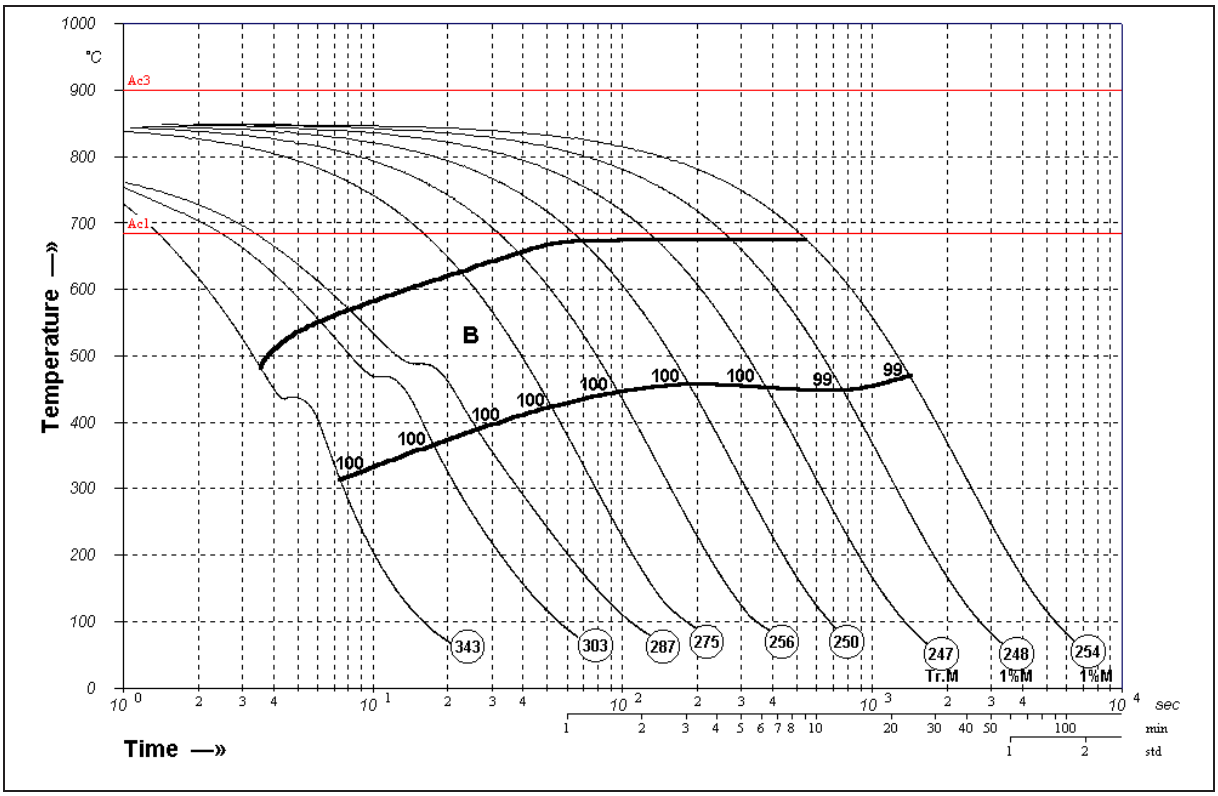

0.092C 2.1Mn 0.11Nb 0.50Cu 0.50Cr Steel A039

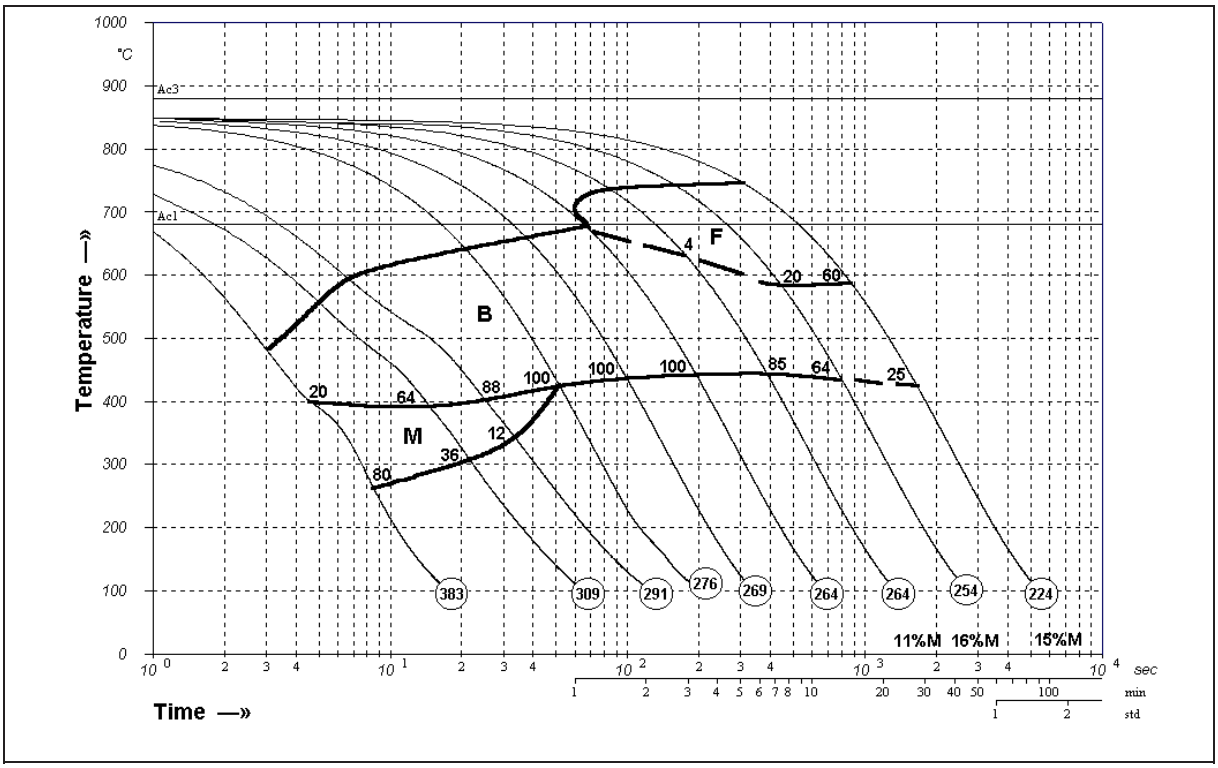

0.091C 2.0Mn 0.12Nb 0.53Ni 0.50Cr Steel A040

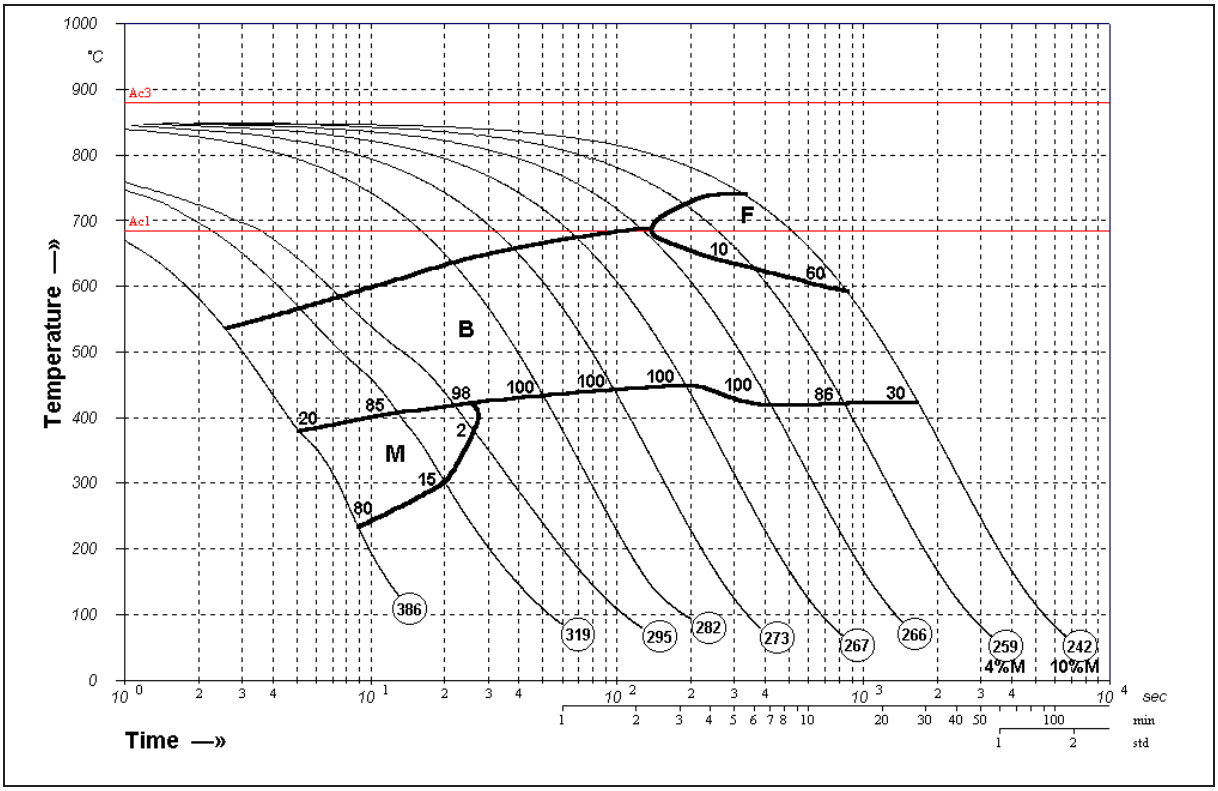

0.042C 1.97Mn 0.10Nb 0.21Ni 0.21Cu 0.98Cr Steel 81351

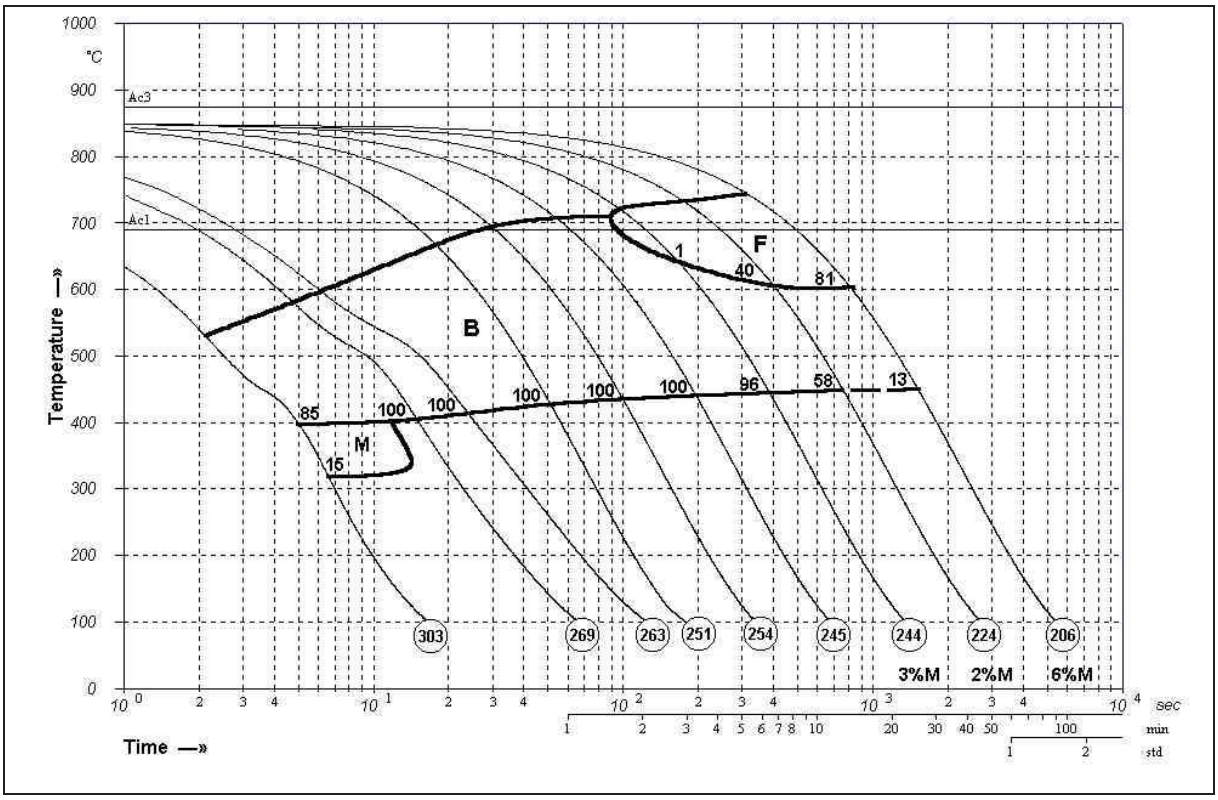

0.047C 1.73Mn 0.10Nb 0.04Ni 0.07Mo 0.04Cu 0.27Cr Steel 16685

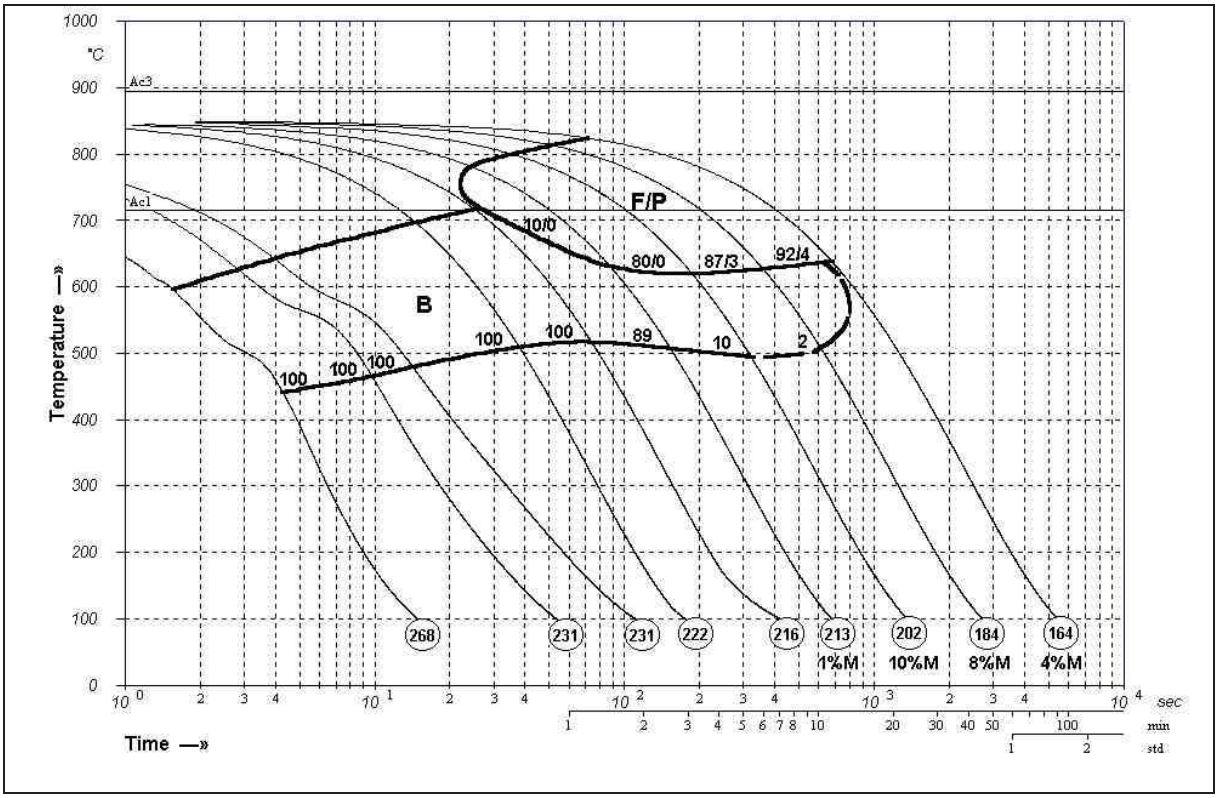

0.053C 1.59Mn 0.10Nb 0.17Ni 0.23Cu 0.26Cr Steel 81913

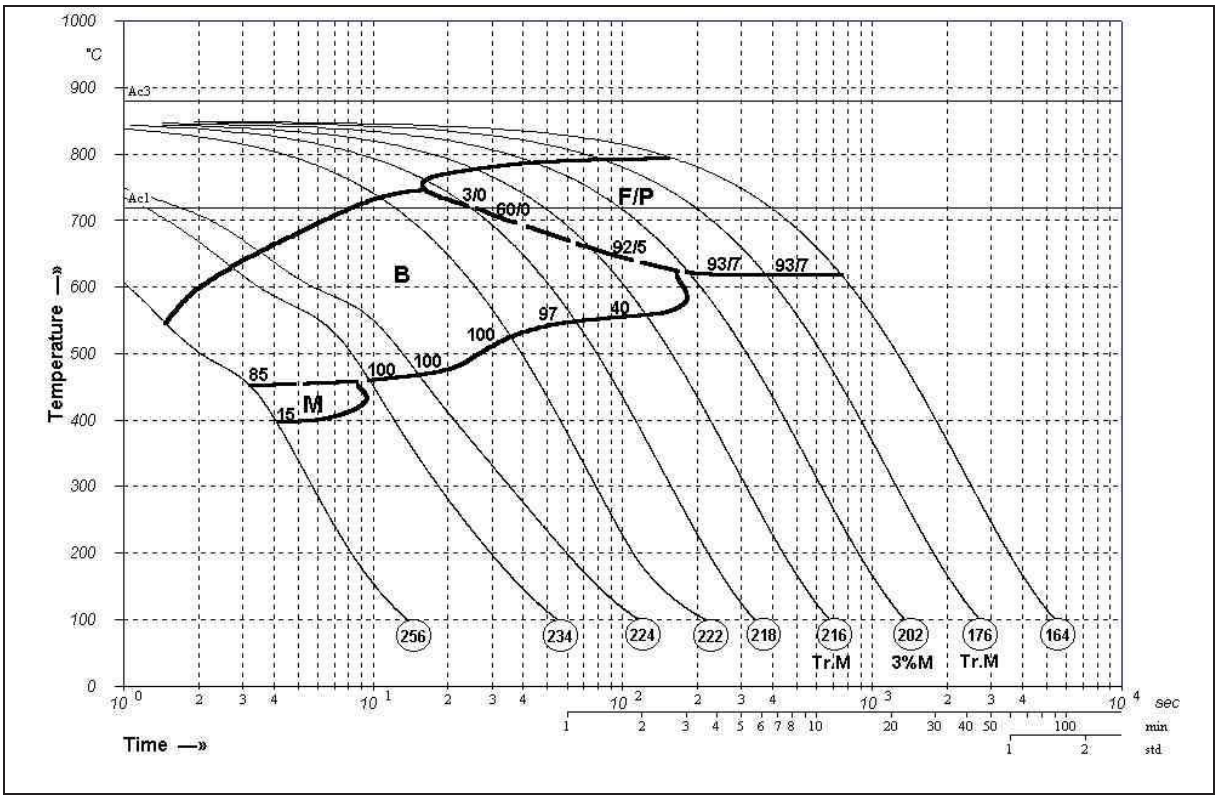

Appendix B: Welding Procedures

B1 Welding procedure for girth-welding of 14.6 mm thick, 610 mm diameter pipe, YBWA1.

MULTI METAAL

WELDING PROCEDURE SPECIFICATION pWPS

Ref.Codes: Stoomwezen, ASME IX, EN 288, NEN 3650, CSW-01-N | No.: **305-4** | Rev.no.: **3**

Customer : **SMART ENGINEERING B.V.**
Project : **TEST WELDING P.O.08081-08133** No.: **080198**

Material : **> API5LGrX70 or equivalent**

Application :
Matr.group : **EN11.1**
Diameter : **24"** Wall thickness : **15 mm**

Weld shape : **V60°±5°**
Weld joint prep.: **Flame cutting/Machining/Grinding**
Opening : **3mm ±0.5mm** Root face : **2mm ±0.5mm**

TACKWELDING	SHOP	FIELD
Preheat tack weld	>150°C by gasburner. Mat.bullet S235JRG2	
Place	In the top of meltingzone	
Welding process	FCAW	-
Consumables	E101T1-K3MJ-H4/T554ZPM1H5	
Manufact./type	LINCOLN OUTERSHIELD 550-H	
Wire thickness	1.2 mm	
Shielding gas	AR90%,CO2-7%,O2-3%	WELDOX 7
Flow rate	10-15 ltr/min.	

PROCES	GTAW/FCAW
Application	Shop welds
Tack welding	Totally removed before actual welding.

WELD.SEQUENCE	1.Root	2.Hot +Fill passes	3.Cap passes
Welding process	GTAW(141)	FCAW(136)	FCAW(136)
Welding position	PG (5GU)	PG (5GU)	PG (5GU)
Current mode	DC-.	DC+	DC+
Voltage	11-14 V.	20-25 V.	20-24 V.
Amperage	115-130 A.	145-210 A.	180-210 A.
Welding rate	4,3-12,9 cm/min	12-27 cm/min	12-27 cm/min
Heat input	5-16 kJ/cm.	7,5-18,5 kJ/cm.	7,5-17 kJ/cm.
Consumables	W42 6W3Ni1	T55 4ZPM1 H5	T55 4ZPM1 H5
Manufacturer	LINCOLN	LINCOLN	LINCOLN
Type	LNTNi1	OUTERSHIELD 550-H	OUTERSHIELD 550-H
Wire thickness	2,4 mm	1,2 mm	1,2 mm
Shielding gas	ARGON 99,998%(I1)	AR90%,CO2-7%,O2-3%	AR90%,CO2-7%,O2-3%
Flow rate	12-15 ltr./min.	10-14 ltr/min.	10-14 ltr/min.
Backing rate	-	-	-
Flow rate	-	-	-
Cleaning	Grinding	Grinding	Brushing
Inter pass temp.	max. 150°C.	max. 150°C.	max. 150°C.
Consum.stored	Org.Package	Org.Package	Org.Package

GENERAL : **Maxium sweepwide is 6x wire diameter**

PREHEATING : **>100°C, control by dig.thermometer.**

HEAT TREATMENT: **n.a.**

REMARKS : **Cooling down under blanket.**

PQR acc. : **EN15614-1/NEN3650;1992**

Minimum number of welding passes per weld			
Wallthickn.	Weld passes	Wallthickn.	Weld passes
2	1	18	8
3 t/m 6	2	21	9-10
7 t/m 9	3	23	10-12
11	5	26	13-15
13	6	28	15-17
15	6	32	19-21

The last pass should always be welded in the middle of the weld.

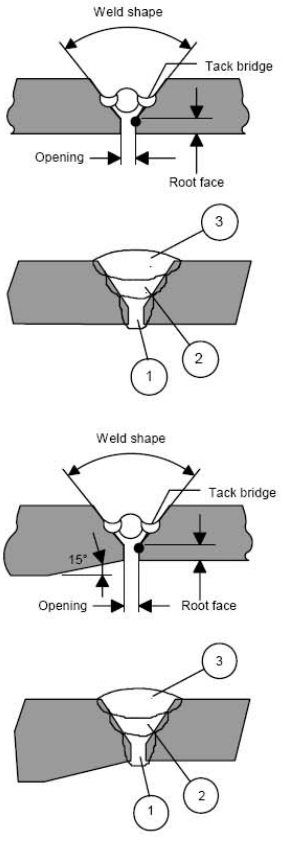

Manufacturer	Customer	Insp.Authority
Acc.: P.L.B.M.Klamer IWI NL IWI-C-007	Acc.:	Acc.:
Date : 10-9-2008	Date :	Date :

B2 Welding procedure for girth-welding of 14.2 mm thick, 1067 mm diameter pipe, 925332.

MULTI METAAL

WELDING PROCEDURE SPECIFICATION pWPS

Ref.Codes: Stoomwezen, ASME IX, EN 288, NEN 3650, CSW-01-N | No.: **301-5** | Rev.no.: **2**

Customer : **SMART ENGINEERING B.V.**
Project : **TEST WELDING P.O.08081-08133** No.: **080198**

Material : **> API5LGrX70 or equivalent**

Application :
Matr.group : **EN11.1**
Diameter : **42"** Wall thickness : **14,1 mm**

Weld shape : **V60°±5°**
Weld joint prep.: **Flame cutting/Machining/Grinding**
Opening : **1mm ±0.5mm** Root face : **2mm ±0.5mm**

TACKWELDING	SHOP	FIELD
Preheat tack weld	>150°C by gasburner. Mat.bullet S235JRG2	
Place	In the top of meltingzone	
Welding process	FCAW	-
Consumables	E101T1-K3MJ-H4/T554ZPM1H5	
Manufact./type	LINCOLN OUTERSHIELD 550-H	
Wire thickness	1.2 mm	
Shielding gas	AR90%,CO2-7%,O2-3%	WELDOX 7
Flow rate	10-15 ltr/min.	
PROCES	FCAW	
Application	Shop welds	
Tack welding	Totally removed before actual welding.	

WELD.SEQUENCE	1.Root	2. Hot +Fill passes	3.Cap passes
Welding process	FCAW(136)	FCAW(136)	FCAW(136)
Welding position	PG (5GU)	PG (5GU)	PG (5GU)
Current mode	DC+	DC+	DC+
Voltage	20-22 V.	20-25 V.	20-24 V.
Amperage	125-150 A.	145-210 A.	180-210 A.
Welding rate	12-15 cm/min	12-27 cm/min	12-27 cm/min
Heat input	9-13 kJ/cm.	7,5-18,5 kJ/cm.	7,5-17 kJ/cm.
Consumables	T55 4ZPM1 H5	T55 4ZPM1 H5	T55 4ZPM1 H5
Manufacturer	LINCOLN	LINCOLN	LINCOLN
Type	OUTERSHIELD 550-H	OUTERSHIELD 550-H	OUTERSHIELD 550-H
Wire thickness	1,2 mm	1,2 mm	1,2 mm
Shielding gas	AR90%,CO2-7%,O2-3%	AR90%,CO2-7%,O2-3%	AR90%,CO2-7%,O2-3%
Flow rate	14-18 ltr/min.	10-14 ltr/min.	10-14 ltr/min.
Backing rate	-	-	-
Flow rate	-	-	-
Cleaning	Grinding	Grinding	Brushing
Inter pass temp.	max. 150°C.	max. 150°C.	max. 150°C.
Consum.stored	Org.Package	Org.Package	Org.Package

GENERAL : **Maxium sweepwide is 6x wire diameter**
PREHEATING : **>100°C, control by dig.thermometer.**
HEAT TREATMENT: **n.a.**
REMARKS : **Cooling down under blanket.**
PQR acc. : **EN15614-1/NEN3650;1992**

Minimum number of welding passes per weld

Wallthickn.	Weld passes	Wallthickn.	Weld passes
2	1	18	8
3 t/m 6	2	21	9-10
7 t/m 9	3	23	10-12
11	5	26	13-15
13	6	28	15-17
15	6	32	19-21

The last pass should always be welded in the middle of the weld.

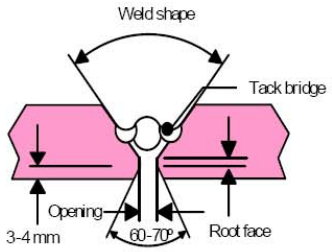

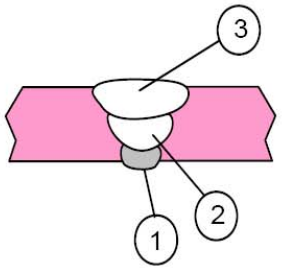

After "inside" root layer, Front side grinding before filling layer.

Manufacturer	Customer	Insp.Authority
Acc.: P.L.B.M.Klamer IWI NL IWI-C-007	Acc.:	Acc.:
Date : 10-9-2008	Date :	Date :

B3 Welding procedure for 25.4 mm Corus plate PA665

This plate was butt-welded in 5 passes using the submerged arc welding (SAW) process, reference number 121, at a heat input of 4.5 kJ/mm.

TRA JON 500 CD02 (Issue 1)

Page 1 of 1

Corus UK Limited
Swinden Technology Centre
Moorgate, Rotherham, S60 3AR
Telephone: 01709 820166
Fax: 01709 825337

corus

WELDING PARAMETERS

Authorised Signature	J.McCSden J.MARSDEN					Date	28/4/06	
Weld No.	6WA56	Project No.	949004	Operator	D. STUART	Date	26 - 4 - 06	
Weld Process	SUBMERGED - ARC	Plate QA No.	5YH1A+B	Thickness	25			
Preparation Method	FLAME CUT	Flux Type	OP121	Batch No.	400101			
Weld Position	FLAT	Gas Type		Flow Rate				
Weld Orientation	RD	Electrode No.	One	Two	Three	Four	Five	
Back Gouge/Grind	NO	Electrode Type	SD3					
Preheat (°C)	100							
Stickout (mm)	35	Cast Number	HEAG 44					
Flux Depth (mm)	45							
Wire Feed Speed		Coil Number	1441					

Weld Preparation

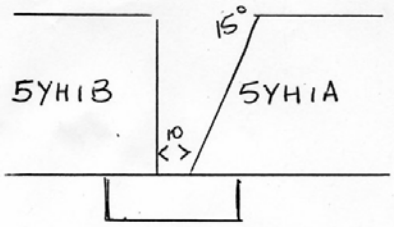

Weld Run Sequence

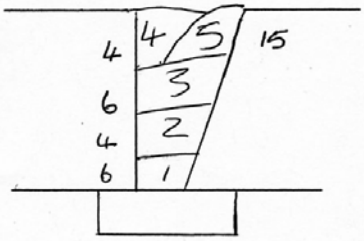

Run No.	Polarity	Dia.	Amps	Volts	Interpass Temperature	ROL (mm)	Time (s)	Weld Length	Welding Speed	Arc
1TO 5	DC+	3.2	700	30	150	1300		1000	280	4.5

Comments:

B4 Welding procedure for 50 mm thick Corus plate GR184

This plate was butt-welded in 21 passes using the submerged arc welding (SAW) process, reference number 121, at a heat input of 3.5 kJ/mm.

TRA JON 500 CD02 (Issue 1)
Page 1 of 1

Corus UK Limited
Swinden Technology Centre
Moorgate, Rotherham, S60 3AR
Telephone: 01709 820166
Fax: 01709 825337

corus

WELDING PARAMETERS

Authorised Signature	J.Marsden J.MARSDEN					Date	13/8/07	
Weld No.	7WA59 A + B	Project No.	1015715	Operator	D. STUART	Date	13 - 8 - 07	
Weld Process	SUBMERGED - ARC	Plate QA No.	6JE67	Thickness	50mm			
Preparation Method	FLAMECUT	Flux Type	0P121	Batch No.	538354			
Weld Position	FLAT	Gas Type		Flow Rate				
Weld Orientation	RD	Electrode No.	One	Two	Three	Four	Five	
Back Gouge/Grind	NO	Electrode Type	SD31Ni 0.25 MO					
Preheat (°C)	AMBIENT							
Stickout (mm)	35	Cast Number	FNALO25					
Flux Depth (mm)	55							
Wire Feed Speed		Coil Number	1476					

Weld Preparation

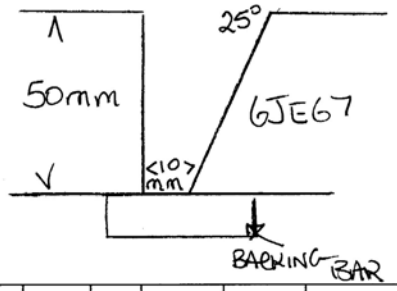

Weld Run Sequence

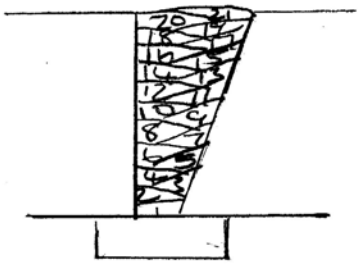

Run No.	Polarity	Dia.	Amps	Volts	Interpass Temperature	ROL (mm)	Time (s)	Weld Length	Welding Speed	Arc
1 TO21	DC+	4	700	33	250	1260		1000	396	3.5

Comments:

B5 Welding procedures for 50 mm thick S355EMZ and S450EMZ submerged arc butt-welds.

Preheat: 100°C

Interpass: 250°C

Joint Details: 45° Inclusive; Root Gap = 0 mm; Root Face = 0-3 mm

Wire Separation = 25 mm; Lead Wire 90°; Trail Wire 75/80° from horizontal

Run no.	Process	Consumable type	Wire size (mm)	Current (A)	Voltage (V)	Polarity	Travel speed (mm/s)
ROOT	MCAW	ESAB 1517	1.2	180-200	32/33	DC+ve	3.8 - 4
FILL	SAW (Tandem)	ESAB 12.32 + Ok 10.62 flux (Lead Wire)	4.0	500-670	26/33	DC+ve	7 -10
		(Trail Wire)	4.0	520-650	32/33	AC	
CAP	SAW	ESAB 12.32 + Ok 10.62 flux	4.0	550-600	32/33	DC+ve	8 - 8.5
BACK	SAW	ESAB 12.32 + Ok 10.62 flux	4.0	600-650	32/33	DC+ve	8 - 8.5

B6 Welding procedure for laser welds

Plate (mm)	Weld Type	kW	Speed (m/min)	Focus/ FL (mm)	Gas Flow (lpm)
9	Bead On Plate	11	0.7	508	80
9	Hybrid butt-weld	9	0.4	504	60

MAG welding parameters

Wire - Coromig 58
Diameter - 1.2 mm
Wire feed speed - 3.6 m/min
Stick out - 15 mm
Programme No. - 19
Gas - Special Mix
Separation - 4 mm
Current (Average) - 128 to 143 Amps
Voltage (Average) - 24.3 to 26.2 Volts

Chemical composition of the welding wire.

C	Si	Mn	P	S	Cr	Ni	Cu	Al	sol. Al	N	Nb	Ti	O
0.068	0.58	1.41	0.011	0.008	0.02	0.02	0.02	ND	ND	ND	ND	ND	ND

B7 Welding procedure for 12 mm Oregon steel plate

This plate was butt-welded in 2 passes using the submerged arc welding (SAW) process, reference number 121, at a heat input of 2.0 kJ/mm in pass 1 and 2.6 kJ/mm in pass 2.

TRA JON 500 CD02 (Issue 1)

Page 1 of 1

Corus UK Limited
Swinden Technology Centre
Moorgate, Rotherham, S60 3AR
Telephone: 01709 820166
Fax: 01709 825337

corus

WELDING PARAMETERS

Authorised Signature	J. Marsden J. MARSDEN					Date	23/2/05	
Weld No.	5WK7	Project No.	949004	Operator	D. STUART	Date	23 - 2 - 05	
Weld Process	SUBMERGED - ARC	Plate QA No.	Y4H1	Thickness	12 mm			
Preparation Method	machined prep	Flux Type	995N	Batch No.	F1FX20115			
Weld Position	FLAT	Gas Type	weldap20	Flow Rate	15lpm			
Weld Orientation		Electrode No.	One	Two	Three	Four	Five	
Back Gouge/Grind	NO	Electrode Type	LNS 140TB					
Preheat (°C)								
Stickout (mm)	35	Cast Number	F1SW205 04					
Flux Depth (mm)	45							
Wire Feed Speed		Coil Number						

Weld Preparation

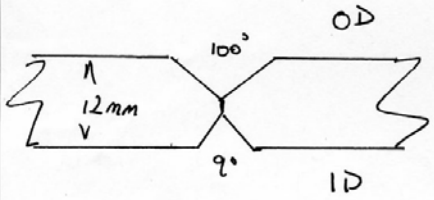

Weld Run Sequence

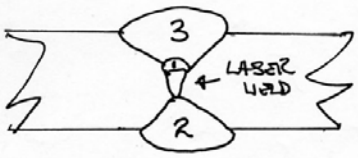

Run No.	Polarity	Dia.	Amps	Volts	Interpass Temperature	ROL (mm)	Time (s)	Weld Length	Welding Speed	Arc
1	DC+	1.2	140	19						
2	DC+	4	850	41					1050	2
3	DC+	4	900	40					830	2.6

Comments:

European Commission

EUR 24209 — HIPERC: A novel, high performance, economic steel concept for linepipe and general structural use

L. Drewett, J. Brozda, S. Bremer, B. Zeislmair, M. Liebeherr, H. Morbacher, W. De Waele, D. Porter, A. Martin-Meizoso, N. Gubeljak

Luxembourg: Publications Office of the European Union

2009 — 187 pp. — 21 × 29.7 cm

Research Fund for Coal and Steel series

ISBN 978-92-79-14438-7

doi 10.2777/86748

ISSN 1018-5593

Price (excluding VAT) in Luxembourg: EUR 8